

Three-Dimensional Nonlinear Dynamics of Cantilevered Cylinders in Axial Flow

by

Ahmad Jamal

Department of Mechanical Engineering
McGill University
Montréal, Quebec, Canada

April 2014

A thesis submitted to McGill University
in partial fulfillment of the requirements of the degree of
Doctor of Philosophy

© Ahmad Jamal 2014

Abstract

This thesis deals with the theoretical study of the linear and nonlinear dynamics of a slender flexible cantilevered cylindrical structure subjected to external axial water and air flows, of interest because of several important practical applications such as nuclear reactor fuel-element bundles, double pipe heat exchangers, and angioplasty. Lack of knowledge to account for the three-dimensional behaviour, important in the above-mentioned practical applications, was the motivation behind the present work. The theoretical results were obtained in the form of the amplitudes and frequencies of the instabilities, as well as the critical flow velocities at which these instabilities occurred.

Experiments were conducted to validate and complement the theoretical results for water flow. The results obtained from the experiments were presented in the form of dimensionless mean displacements, their corresponding root mean square values, and frequencies as a function of dimensionless flow velocity. Finally, the path traced by the oscillating cylinder was mapped.

In fluid-structure interaction problems, the fluid forces such as the inviscid hydrodynamic forces, the frictional or viscous forces, and the hydrostatic or pressure forces acting on the flexible structure play a vital role in defining the dynamics of the system. Therefore, a precise calculation of the force coefficients, such as longitudinal and normal viscous coefficients, base drag coefficient, and zero-flow normal force coefficient present in the equations of motion associated to the above mentioned fluid forces, is imperative. These presently calculated force coefficients were then incorporated in the linear and nonlinear equations of motion and solved to obtain the response of the cylinder in water flow. The response of the system from the linear model in air flow was also obtained. The effect of confinement on the linear dynamics was also studied.

A nonlinear three-dimensional cantilevered cylinder model was also created and simulated in a commercially available finite element modeling and simulation package, namely ADINA, in order to complement the results obtained from the linear and nonlinear models. The results of the ADINA simulations were obtained in water as well as air flows.

Experimental results validated the analytical and numerical model results. The results, thus obtained, are expected to play an important role in improving the above-mentioned engineering and medical applications to ensure operation below critical flow conditions.

Sommaire

Cette thèse traite de la dynamique linéaire et non linéaire d'une structure mince et flexible dans un écoulement axial d'eau ou d'air. Ce sujet a des applications importantes, par exemple en ce qui concerne les vibrations des faisceaux d'éléments combustibles dans les réacteurs nucléaires, les échangeurs de chaleur et l'angioplastie. Le manque de connaissances sur le comportement tridimensionnel de la structure mince dans les applications mentionnées ci-haut a motivé la recherche présentée dans cette thèse. Les résultats théoriques donnent les vitesses d'écoulement critiques pour le déclenchement des instabilités fluide-élastiques, ainsi que les amplitudes et fréquences associées à ces instabilités.

Des expériences ont été menées afin de valider et de compléter les résultats théoriques pour des écoulements d'eau. Les résultats obtenus à partir des expériences sont présentés sous la forme de moyennes de déplacements adimensionnels 'root-mean-square', et les fréquences en fonction de la vitesse d'écoulement adimensionnelle. Enfin, la forme tracée par le cylindre oscillant a été cartographiée.

Dans les problèmes d'interaction fluide-structure, les forces de fluide, telles que les forces hydrodynamiques non visqueuses, les forces associées au frottement, et les forces hydrostatiques et de pression agissant sur la structure souple jouent un rôle vital sur la dynamique du système. Par conséquent, un calcul précis des coefficients de ces forces est impératif dans les équations de mouvement associés aux forces fluides mentionnées ci-dessus, tels que les coefficients longitudinales et normales visqueux, le coefficient de traînée de base, et le coefficient de force normale dans un fluide stagnant. Ces coefficients de force actuellement calculés ont ensuite été intégrés dans les équations linéaires et non linéaires du mouvement, et les équations ont été résolues pour obtenir la réponse du cylindre dans l'écoulement d'eau. La réponse du système à partir du modèle linéaire d'un écoulement d'air a également été obtenu. L'effet du confinement sur la dynamique linéaire a aussi été étudié.

Un modèle de cylindre en porte à faux tridimensionnel non linéaire a également été créé et simulé dans un logiciel de modélisation par éléments finis et de simulation un logiciel commercial, à savoir ADINA, afin de compléter les résultats obtenus à partir de modèles linéaires et non linéaires. Les résultats des simulations de ADINA ont été obtenus pour des écoulements d'eau, ainsi que des écoulements d'air.

Les résultats expérimentaux ont validé les résultats des modèles analytique et numérique. Les résultats ainsi obtenus sont appelés à jouer un rôle important dans l'amélioration des techniques et applications industrielles et médicales mentionnées ci-dessus pour assurer un fonctionnement au dessous des conditions d'écoulement critiques.

Acknowledgements

I would like to express my deepest gratitude to my supervisor, Professor Michael P. Païdoussis, for his endless support, sincere and invaluable guidance, and constant encouragement throughout the years. His professional approach and genuine commitment to both his research and his students truly inspired me. I feel privileged to have had the opportunity to work with Him. Very special thanks go to Professor Luc G. Mongeau for his co-supervision of this work, his help with experimental methods and results analysis, and his suggestions during our discussions and on this thesis.

I am grateful to the Faculty of Engineering of McGill University for a McGill Engineering Doctoral Award (MEDA) to support in my PhD studies.

I would like to extend my appreciation to my colleagues, past and present, in the Fluid-Structures Interaction group at McGill University for their assistance and constructive discussions: Konstantinos Karagiozis, James Wang, Liaosha Tang, Dana Blake Giacobbi, Mojtaba Kheiri, Mehdi Paak, Mergen Hajghayesh, Kyriakos Moditis, Stéphane Jamin, and the visiting students Wensheng Zhao and Gabriel Aulard. I would also like to thank Yasser Rafat, Alireza Najafi-Yazdi, Jong Park, Rani Taher, Hani Bakhshae, and Salman Khan for their useful suggestions and moral support.

I am further indebted to Gary Savard, Tony Micozzi, Andy Hofman, Mario Iacobaccio, and George Tewfik of McGill University for their technical assistance during the course of my research work, and without whom my experiments would never have been completed. I am also grateful to Mrs. Mary Fiorilli-St-Germain and Mrs. Joyce Nault for their help with the administrative tasks.

I also thank Calcul Quebec for the use of their high performance computational resources to perform numerical simulations on Mammouth and Guillimin clusters.

Finally, very special thanks go to my parents, my wife, and all family members for their great moral support, encouragement, and patience during the course of my degree. My special love and thanks to my children Afiyah Ahmad, Hadiyah Jamal, and Muhammad Abdullah Jamal for their love and unmatched patience, and so I dedicate this work to them.

Contributions to Original Knowledge

The linear and nonlinear dynamics of a slender flexible cantilevered cylinder subjected to axial water and air flows is the subject of this thesis. To the author's best knowledge, this is the first time that a study on such a system in water and air flows has been undertaken from both a linear and a nonlinear point of view, both theoretically and experimentally. Below is a summary of the main contributions of this thesis to original knowledge.

1. In fluid-structure interaction problems, the fluid forces such as the inviscid hydrodynamic forces, the frictional or viscous forces, and the hydrostatic or pressure forces acting on the flexible structure play a vital role in defining the dynamics of the system. Therefore, a precise calculation of the force coefficients such as longitudinal and normal viscous coefficients, base drag coefficient, and zero-flow normal force coefficient associated to these forces present in the equation of motion is imperative. In the calculation of these force coefficients, the physical parameters of the experiments are used. This was done so as to be able to compare the theoretical results to those pertaining to the experimental system. A unique method is developed involving the use of a finite element modeling and simulation package, namely ADINA to calculate these coefficients. These are then incorporated in the linear and nonlinear equations of motion.
2. The linear and nonlinear dynamics of cantilevered cylinder in air flow was investigated. The model in air flow develops a different dynamics than that in water flow.
3. A nonlinear three-dimensional cantilevered cylinder model in axial flow is created and simulated in ADINA. One of the multiphysics capabilities of ADINA is Fluid-Structure Interaction (FSI). ADINA offers FSI capabilities in one single program for the solution of problems where the fluids are fully coupled to structures that can undergo highly nonlinear response due to large deformations and contact with the surrounding boundaries. In addition, the ADINA simulations consider the fluid forces in all three-directions and the resulting dynamics can be visualized as three-dimensional.

Contents

Abstract	i
Sommaire	ii
Acknowledgements	iii
Contributions to original knowledge	iv
Nomenclature	ix
Chapter 1: Introduction and Literature Review	1
1.1. Introduction	1
1.2. Literature review	3
1.2.1. Experimental studies on slender flexible cylinders in axial flow	3
1.2.2. Theoretical studies on slender flexible cylinders in axial flow	4
1.2.2.1. Linear models	4
1.2.2.2. Nonlinear models	10
1.3. Motivation of present work	11
1.4. Objectives	13
1.5. Outline of the thesis	14
Chapter 2: Experiments on Cantilevered Cylinder in Axial Flow	17
2.1. Introduction	17
2.2. Physical description	18
2.3. Calibrations of laser-optical sensors	18
2.4. Flexural rigidity of cylinder	19
2.5. Logarithmic decrements	20
2.6. Damping constants	21
2.7. Flow velocity measurement calibration	22
2.8. Flow velocity profile inside the test-section	23
2.9. Cylinder dynamics	26

2.9.1. Set-up for divergence	27
2.9.2. Set-up for flutter	28
2.10. Path traced by the oscillating cylinder	29
2.11. Summary	30
Chapter 3: Linear Analysis	71
3.1. Introduction	71
3.2. Problem description	72
3.3. Linear equation of motion	72
3.3.1. Boundary conditions	73
3.4. Dimensionless parameters	74
3.5. Method of solution	75
3.6. Model in water flow with previously used force coefficients	78
3.6.1. Adequacy of the linear solution	78
3.6.2. Analytical results	78
3.7. Model in air flow	79
3.7.1. Analytical results	79
3.8. Effect of confinement	80
3.8.1. Model in water flow	80
3.8.2. Model in air flow	81
3.9. Force coefficients	81
3.9.1. Longitudinal viscous coefficient, c_T	82
3.9.2. Normal viscous coefficient, c_N	84
3.9.3. Base drag coefficient, c_b	86
3.9.4. Zero-flow normal coefficient, c	88
3.10. Model in water flow with presently calculated force coefficients	90
3.10.1. Adequacy of the linear solution	90
3.10.2. Analytical results	90
3.11. Effect of confinement	91
3.12. Comparison of the results	91

3.13. Summary	93
Chapter 4: Nonlinear Analysis	126
4.1. Introduction	126
4.2. Nonlinear equation of motion	127
4.3. Boundary conditions	128
4.4. Dimensionless parameters	128
4.5. Method of solution	129
4.6. Model in water flow with previously used force coefficients	131
4.6.1. Adequacy of the nonlinear solution	131
4.6.2. Results	131
4.7. Model in water flow with presently calculated force coefficients	133
4.7.1. Adequacy of the nonlinear solution	133
4.7.2. Results	133
4.8. Comparison of the results	134
4.9. Summary	135
Chapter 5: Numerical Simulations	157
5.1. Introduction	157
5.2. Validation of ADINA	158
5.2.1. Two-dimensional pipe flow model	158
5.2.2. Backward facing step model	159
5.2.3. Point load deflection model	160
5.2.4. Three-dimensional point load deflection model	160
5.3. Model description	161
5.4. CFL condition	162
5.5. Model in water flow	163
5.5.1. Adequacy of the numerical solution	163
5.5.2. Numerical results	163
5.6. Model in air flow	166
5.6.1. Numerical results	166
5.7. Comparison of the results	168

5.8. Summary	168
Chapter 6: Comparison of the Models	191
6.1. Introduction	191
6.2. Comparison of the linear and the nonlinear models in water and air flows with previously used force coefficients	191
6.3. Comparison of the Models in water and air flows with presently calculated force coefficients	192
6.4. Summary	195
Chapter 7: Conclusions	200
7.1. Overview	200
7.2. Summary of the work	200
7.3. Suggestions for future work	206
References	208
Appendix A	217
A.1. Determination of end-shape factor, f	217

Nomenclature

Alphabetic Symbols

A	cylinder uniform cross-sectional area, m^2
$B(\eta)$	boundary condition
b	height of two-dimensional horizontal beam model, m
C	Courant number
C_{max}	maximum value of Courant number
c	normalized zero-flow normal coefficient
C_b	base drag coefficient
c_b	normalized base drag coefficient
C_D	zero-flow normal coefficient, m/s
C_f	friction drag coefficient
c_f	normalized friction drag coefficient
C_N	normal friction coefficient
c_N	normalized friction coefficient in the normal direction
c_o and c_L	rotational spring constant, N.m/rad
C_T	tangential friction coefficient
c_T	normalized friction coefficient in the tangential direction
$[C]$	damping matrix
C^+	a constant in the expression for the logarithmic law of the wall for turbulent flow
D	cylinder diameter, m
D_{ch}	channel diameter, m
D_h	hydraulic diameter, m
D_i	inner diameter of a pipe, m
D_o	outer diameter of a pipe, m
dy/dx	slope of the angle of inclination

E	Young's modulus, N/m ²
E^*	viscoelastic constant
EI	flexural rigidity of the cylinder, N.m ²
F	resultant force, N
F_L	viscous force per unit length in the longitudinal direction, N/m
F_N	viscous force per unit length in the normal direction, N/m
F_{px}	hydrostatic force in the x -direction, N
F_{py}	hydrostatic force in the y -direction, N
$F(\eta)$	equation of motion
f	end-shape factor
$f_{cr,fln}$	dimensional frequency at the critical flow velocity for the n^{th} mode flutter, Hz
f_D	Darcy-Weisbach friction coefficient
f_{fln}	dimensional flutter frequency in its n^{th} mode, Hz
f_n	natural frequency of the cylinder in its n^{th} mode, Hz
g	gravitational constant, m/s ²
h	ratio of the cylinder diameter and the hydraulic diameter of the channel
h_{Hg}	height of mercury column, m
I	second moment of area, m ⁴
$[I]$	unit matrix
$[K]$	stiffness matrix
k	Von Karman constant in the expression for the logarithmic law of the wall for turbulent flow
k_o and k_L	translational spring constants, N/m
L	total length of the cylinder including the end-piece, m
L_{ch}	length of channel, m
L_{eff}	effective length of cylinder, m
L_{ent}	entrance length, m
l	length of the cylinder end-piece, m
l_{beam}	length of two-dimensional horizontal beam model, m
M	added (virtual) mass of the fluid per unit length, kg/m
$[M]$	mass matrix

m	mass of the cylinder per unit length, kg/m
n	number of desired cylinder modes
n_{max}	highest desired cylinder mode
\bar{p}	mean value of pressure, N/m ²
p_L	pressure at the sides of the cylinder, N/m ²
p_b	base pressure, N/m ²
Δp	pressure gradient, N/m ²
Q	lateral shear force, N
\bar{Q}	a constant
$\{Q\}$	eigenvector
$\{q\}$	vector of generalized coordinates
$\{\dot{q}\}$	first order time derivative of the generalized coordinate vector
$\{\ddot{q}\}$	second order time derivative of the generalized coordinate vector
$q_r(\tau)$	generalized coordinates in the transverse direction
R	radius of cylinder
r	refractive index
R_{ch}	radius of the channel
R_{fit}^2	goodness of fit
Re	Reynolds number
S	cylinder cross-sectional area
$[S]$	resulting matrix of the eigenvalue problem
Stk	Stokes number
s	cylinder axial distance, m
s_h	backward facing step height, m
T	axial tension, N
T_c	kinetic energy, J
\bar{T}	externally imposed uniform tension, N
t	time, s
Δt	time step in numerical simulations, s
U	uniform dimensional flow velocity, m/s

u	dimensionless flow velocity
$u_{cr,dn}$	critical flow velocity for the onset of divergence in n^{th} mode
$u_{cr,fn}$	critical flow velocity for the onset of flutter in n^{th} mode
u_{rn}	re-stabilization of cylinder from n^{th} mode
u^+	dimensionless velocity in the expression for the logarithmic law of the wall for turbulent flow
u^*	frictional velocity, m/s
V_c	potential energy, J
W	vertical concentrated point load, N
δW	virtual work by the fluid-related forces acting on the cylinder, J
x	axial distance, m
Δx	axial distance increment, m
x_e, s_e	parameter representing the axial variation in the end-piece cross-sectional area, m
\bar{x}_e, \bar{s}_e	parameter representing the axial variation in the end-piece diameter, m
$y(x, t)$	cylinder displacement in the transverse direction at any longitudinal distance and time, m
y^+	dimensionless wall coordinate in the expression for the logarithmic law of the wall for turbulent flow
z	displacement in z -direction, m

Greek Symbols

γ	gravity parameter
γ_c	confinement parameter
$\phi_r(\xi)$	eigenfunctions of cantilevered cylinder
$\delta(\xi-1)$	Dirac's delta function
$\bar{\delta}$	ratio of inner to outer diameters of a pipe
δ_{max}	maximum deflection of the cylinder or beam end, m
δ_n	logarithmic decrement of the cylinder of its n^{th} mode
δx	element of the cylinder with minuscule length in longitudinal direction, m

ρ	density of fluid, kg/m ³
ν	Poisson's ratio
ν_k	fluid kinematic viscosity, m ² /s
χ	confinement factor
ζ	dimensionless distance in the x -direction
η	dimensionless distance in the transverse direction
$\eta(1)_{\text{r.m.s.}}$	r.m.s. value of the dimensionless cylinder tip amplitude
$\eta^*(1)$	dimensionless mean cylinder tip displacement
τ	dimensionless time
λ_r	beam eigenvalues
α	ratio of channel and cylinder diameters
$\bar{\alpha}^*$	viscoelastic damping constant
β	mass ratio
Γ	dimensionless externally imposed uniform tension
ε	slenderness factor
Π	dimensionless mean pressure
χ_e	dimensionless parameter representing the variation in the end-piece cross-sectional area
$\bar{\chi}_e$	dimensionless parameter representing the variation in the end-piece diameter
λ_r, λ_j	eigenvalues of cylinder in r th or j th mode
θ	angle of inclination of the cylinder to the incoming fluid flow
Ω	radian frequency, rad/s
Ω_n	radian frequency of cylinder in its n^{th} mode, rad/s
ω	dimensionless frequency
$\omega_{cr,fln}$	dimensionless flutter frequency of cylinder at the critical flow velocity in its n^{th} mode
ω_{fln}	dimensionless flutter frequency of cylinder in its n^{th} mode
\mathcal{L}	Lagrangian of the system
$\bar{\mu}^*$	hysteretic damping constant

Chapter 1

Introduction and Literature Review

1.1. Introduction

The dynamics of flexible cylindrical structures in fluid flow (cross-flow and axial flow) is rather complex. To simplify the problem, an assumption is usually made that the flow is either purely normal to the axis of the structure (cross-flow) or purely axial (axial flow) (Modarres-Sadeghi 2006). A structure interacting with fluid in cross-flow and axial flow collectively is studied so extensively that a distinct field has emerged namely Fluid-Structure Interaction (FSI). FSI is the interaction of a deformable structure with an internal or external fluid flow (Bungartz and Schäfer, eds. 2006). Cylinders in cross-flows exhibit significant dynamic deformations and oscillations. This problem has retained much attention from researchers and designers in the past, due to its important industrial applications such as heat exchanger tube banks (Chen 1978), as shown in Fig. 1.1, feed-water heater (Kaneko et al. 2008), and chimney stacks (Zdravkovich 2003). In contrast, cylindrical structures in axial flow undergo relatively smaller transverse vibrations. The importance of this problem was not immediately felt, resulting in relatively less extensive research work in this area.

Cylindrical structures in axial flow can be categorized into unconfined and confined flows. When the cylinder is isolated in the ocean or in a fairly large flow channel, such that the pressure-drop within the outer flow is very small, the cylinder is considered to be in unconfined flow. When the cylinder is in close proximity to adjacent cylinders or to the flow-containing channel, such that pressure drop is clearly not negligible, the cylinder is then considered to be in confined flow. There are many important engineering applications in the second category. An axial flow induces smaller- amplitude transverse vibrations in cylindrical structures than that a cross-flow. The amplitudes are so small that, in some cases, they might be of little concern. They can become worrisome in applications such as in nuclear reactor fuel-element bundles, monitoring tubes, and control rods and in double pipe heat exchangers where the flow is mainly axial. In both cases, the problem originates from either close spacing between the cylindrical elements or between the cylindrical elements and intermediate supports; therefore, even small amplitude vibrations result in impact, resulting in accelerated wear and with time, might cause

the rupture of the cylindrical elements (Païdoussis 2004). Thus, unlike cross-flow-induced vibration problems, low-amplitude axial-flow-induced vibration problems usually become prominent after long period of time, causing fatigue and cracking due to cyclic stresses. Another important reason for interest in axial-flow-induced vibration is that some systems are inherently very flexible because of their material, support configuration, or length. These systems are prone to larger amplitude vibrations (Païdoussis 2004). According to Païdoussis (2004), most of the interest as early as 1958 in the low amplitude vibration of cylindrical structures in axial flow was directly related to the power industry and related work was carried out for one of the following reasons: (a) measurement of the amplitude of vibration of particular cylindrical structure configurations, e.g., modeling nuclear reactor components such as fuel rods, monitoring tubes, and tubular cylindrical elements in the steam generator and the flow conditions; (b) comprehending the reasons of vibration; (c) development of mechanisms for foreseeing the vibration amplitudes.

One of the practical examples of cylindrical structures in axial flow is seismic receiver arrays. Seismic sonars are often used to survey the undersea geological deposits such as oil and gas below the seafloor. Sound pulses generated from a sonar transmitter attached to a vessel travel through the water and into the sea bed. The reflected pulses are recorded by the seismic receiver arrays also attached to the same vessel. These seismic arrays are extremely long, neutrally buoyant, and slightly submerged in water (Païdoussis 2004). The reflected pulses are then analyzed to detect the presence of any mineral deposits lying under the sea floor (AML Oceanographic 2013). In order for the system to work effectively, the dynamical behaviour of the slender cylinder-like arrays in the water needs to be understood.

Another practical application, in biomedical science, is ‘catheterization’. This technique is used to open a blocked or narrowed coronary artery due to substantial buildup of fatty matter. A long narrow flexible guide wire called a ‘catheter’, equipped with a small deflated balloon and a stent (a stainless steel mesh tube), is inserted into the artery and reaches where blockage has occurred. The balloon is then inflated and it fixes the stent to keep the artery open. Another way of widening the artery passage is by using a balloon catheter. A deflated balloon on a catheter is passed into the narrowed locations and then inflated to a fixed size. The balloon crushes the fatty deposits, opening up the blood vessel to improve flow; the balloon is then collapsed and withdrawn (Morgan and Walser 2010). Dynamic instability of catheters can become substantially

critical for the successful completion of the above mentioned procedures and patient health recovery. The instability in terms of dynamic buckling or whipping action of the catheter is one of the reasons for coronary or vascular perforation that may lead to severe complications or even death. It has been reported as a result of the study taken place in Columbia University where, between April 2004 and October 2008, 13,466 angioplasties were performed and out of these, 33 (0.245%) coronary perforation cases were documented with 26 (78.8%) angiographically severe cases. Among the fifteen patients who were treated using a single catheter, there were three deaths (20%), two surgical explorations (13.3%), eight emergent pericardiocentesis (53.3%), and one event of severe anoxic brain damage (6.7%) (Ben-Gal et al. 2010). Therefore, understanding the dynamics of such system becomes very important.

1.2. Literature Review

In this section, a review of the representative previous studies on the system of a slender cylinder subjected to axial flow will be presented, starting from the studies done on unconfined flow, followed by studies on confined flow.

1.2.1. Experimental Studies on Slender Flexible Cylinders in Axial Flow

One of the early experimental studies on the dynamics of slender flexible cylinders in unconfined axial flow was conducted by Païdoussis (1966b). He conducted experiments on horizontally positioned cantilevered and simply supported cylinders in axial water flow. To remind the reader, cantilevered cylinder has one of its ends clamped/ fixed while the other end is free. Simply supported cylinder has both its ends pinned to a rigid support. He fixed a smoothly tapered rigid end-piece at the free downstream end of the cantilevered cylinder, whereas made both the ends of the simply supported cylinder tapered over a very short distance. The experiments served as a means to compare and validate the theoretical model of similar system also developed by him (1966a). Païdoussis et al. (1980b) examined, experimentally, the dynamical behaviour of the flexible slender cylinder in axial flow, perturbed harmonically in time. They compared the experimental results with those of theory (Païdoussis et al. 1980a) and found good agreement between them.

For solitary cylinder, Païdoussis and Pettigrew (1979) conducted experiments to study the dynamics of flexible cylinder in an axisymmetric confined axial fluid and two-phase flows. They also compared the results qualitatively and quantitatively with theoretical predictions and found that the agreement was qualitatively good and quantitatively fair. Later, Gagnon and Païdoussis (1994b) studied, experimentally, the coupling characteristics of cluster of cylinders clamped at both ends in turbulent axial flow. Two, four, and twenty eight cylinder clusters were used for the experiments with a maximum of four flexible instrumented cylinders in the cluster. The rest of the cylinders were rigid. They recorded the vibration amplitudes of the cylinders in two orthogonal directions. They presented the results for the clusters in the form of Power Spectral Density (PSD), coherence plots, and inter-cylinder phases. They also conducted experiments on four-cylinder cluster to see the effect of inter-cylinder gap. They used the experimental results to support the theory for similar system developed by them (1994a).

1.2.2. Theoretical Studies on Slender Flexible Cylinders in Axial Flow

1.2.2.1. *Linear Models*

One of the earliest studies on the dynamics of slender flexible structures in axial flow was undertaken by Hawthorne (1961). He reported the designing, fabrication, and experimental testing of many designs of towed flexible barge all made of flexible material. Dracone is a slender flexible container towed behind a small ship, used to transport lighter-than-sea-water liquids such as gasoline, kerosene, and fresh water. After delivery of the cargo, the Dracone is either rolled and carried on the ship or filled with air and towed back to land (Païdoussis 2004). He was concerned with the directional stability of the towed Dracone system in order to avoid excessive stresses that might develop while towing the system in water.

Following Hawthorne's work on towed flexible structures, Païdoussis (1966a) studied the dynamics of slender flexible cylinders in unconfined axial flow. This was a two-part study comprising of (i) the development of linear analytical model of the flexible cylinder dynamics for different boundary conditions and (ii) experiments to compare and validate the theory. The experimental part is described in Section 1.2.1. The boundary conditions considered for the cylinder were either clamped or pinned at both ends of the cylinder, or clamped at the upstream end and free at the other end. The two-dimensional linear model accounted for small, free, lateral

motions of the cylinder immersed in fluid flowing parallel to the axis of the cylinder. He did not account for the damping in the material of the cylinder. He used the standard boundary conditions for the cylinder supported at both ends. However, in case of the free downstream end, he considered a rigid end-piece at the free end the cross-sectional area of which was assumed to be tapered smoothly to zero over a short distance such that $l/L \ll 1$. Here, L is the total length of the cylinder including the end-piece and l is the length of the end-piece. He applied the time- and velocity-dependent boundary condition at this free end. He observed that the inviscid force contributed considerably in the cylinder response.

This study, however, contained an error in completely specifying the forces causing the vibration in the cylinder. The error arose due to the absence of the term $F_L (\partial y / \partial x)$ in the y -direction (transverse direction) force balance equation. This error was carried forward, undetected, to others' work, for example, Orloff & Ives (1969), Pao (1970), and Chen & Wambsganss (1972). The model itself was later extended and corrected, leading to the most complete linear model of Païdoussis (1973). Furthermore, a linear analytical model pertaining to the case of a cluster of cylinders or a solitary cylinder in confined flow was also developed in this work. The model took gravity and pressurization into account, and determined the frictional forces in a systematic way.

Later, Païdoussis (1974) studied the small amplitude vibration, termed sub-critical vibration, induced in cylindrical structures by turbulence in the axial flow. Sub-critical vibrations are small amplitude vibrations occurring at flow velocities lower than the critical flow velocities at which fluid-elastic instabilities develop in the cylinder. Considering the range of axial flow velocities pertaining to most industrial systems, the vibration amplitudes were small. In this work, based on the theory developed for cylindrical structures in axial flow (Païdoussis 1973), he developed an analytical model to predict the dynamics of slender flexible cylinder in unconfined and confined axial flows. Furthermore, he derived an empirical relation to predict the sub-critical vibration amplitudes. He also explained the mechanisms of sub-critical vibrations in the cylindrical system. He categorized the sub-critical vibrations as forced, parametric, or self-excited. He also discussed other analytical models developed by other researchers such as Quinn's (1962) self-excited vibration model, Reavis's (1969) and Chen & Wambsganss's (1972) forced-vibration models, Gorman's (1969, 1971) two-phase flow forced-vibration model, and Chen's (1970a,b) parametric vibration model. Hannover and Païdoussis (1978) examined the

dynamics and stability of cylindrical tubular beams conveying fluid and simultaneously subjected to axial external flow by deriving and solving the equation of motion while taking into account the boundary-layer thickness on the cylinder due to the external flow, internal dissipation, and gravity effects. They also conducted experiments on similar system in order to support the theoretical predictions.

Païdoussis et al. (1980a) investigated, theoretically, the dynamical behaviour of a solitary flexible slender cylinder in pulsating flow. They first conducted the theoretical analysis of the system in steady and unperturbed flow for various sets of boundary conditions, and established (i) the eigenfrequencies of the system at any given flow velocity and (ii) the critical flow velocities that mark the onset of system instabilities. Then they did the analysis of the system in pulsating flow, establishing the existence of parametric resonances. They also looked into the effects of the mean flow velocity, boundary conditions, dissipative forces, and virtual (hydrodynamic) mass on the extent and location of the parametric instability zones. Païdoussis (1983) reviewed the two classes of flow-induced vibrations encountered in nuclear reactors and reactor peripherals, vibration of cylindrical structures induced by cross-flow and by axial flow. In view of the importance of safety for reactor plant in order to safeguard the potentially very delicate environment and people, this study highlighted the potential causes of reactor damage due to flow-induced vibrations and their underlying mechanisms. The review encompassed buffeting, often referred to as subcritical vibration, in a solitary cylinder subjected to axial flow, flow periodicity, as well as fluid-elastic instabilities in cylinder also subjected to axial flow.

De Langre et al. (2007) investigated the effect of length on long flexible cylinders in axial flow. Following Païdoussis (1973) and Païdoussis et al. (2002), they modelled the cylinder as beam. They proposed a new dimensionless form of the equation of motion governing lateral vibrations to make it appropriate for the analysis of the effect of the length. They also found a limit regime where the length of the cylinder did not affect the characteristics of the instability and the deformation was confined to a finite region close to the downstream end. Wang and Ni (2009) reviewed the linear dynamics of different flexible structures as a result of interaction with fluid flow. They considered the fundamental case scenarios of the fluid-induced instabilities in structures such as straight pipes conveying fluid, nano-tubes conveying fluid, tubular beams subjected to both internal and external axial flows, cylindrical shells subjected to axial flow, plates in axial flow, and slender structures in axial flow or axially towed in quiescent fluid.

Considerable work has been done on the dynamics of clusters of flexible cylinders in axial flow and solitary cylinder in annular axial flow; both are cases of confined flow. One early study is by Païdoussis (1979). A linear theory of the dynamics of clusters of independently supported flexible cylinders in axial flow was developed and an extensive discussion of the behaviour of such systems with increasing flow velocity was presented, with emphasis on the modal forms of free coupled motions of the cylinders and on the onset of the instabilities. Results of an experimental study, involving systems of two, three, or four cylinders with different inter-cylinder gaps and support conditions were also presented and compared with theoretical results. Related to the earlier work, Païdoussis et al. (1983a, b) in a two part study analyzed the dynamics of a cluster of three structurally interconnected cylinders in vacuum in part 1. The interconnection was modeled through translational and rotational linear springs. The knowledge and experience gained in the first part was later utilized to analyze the dynamics of the same system in axial flow.

Païdoussis (1993) delivered the Calvin Rice lecture in which he covered the topics of the stability of pipes conveying fluid and of cylinders in axial flow. He mentioned that although much of the research work on these topics is curiosity driven and little or no application was in mind, unexpected uses and applications materialized in the following years. He indicated that the applications ranged from a marine propulsion system to the dynamics of deep water risers. He described the dynamics of thin pipes (shells), cantilevered pipes, and pipes with supported ends conveying fluid, and cylinders and shells in axial flow and leakage flow. Later on, Gagnon and Païdoussis (1994a) developed a random vibration theory to study the fluid coupling characteristics and turbulence-induced response of a four-cylinder cluster system. The work was motivated by the practical application in nuclear power plants in which vibration may be induced by the axial flow in the nuclear fuel elements stacked in a cluster leading to serious consequences. They developed the random vibration theory based on the work of Reavis (1967, 1969) and Païdoussis and Curling (1985). They also used the updated form of the mean flow theory developed by Païdoussis and Suss (1977). The mean flow theory provides the free-vibration lateral deflection characteristics of cluster of cylinders subjected to steady axial flow. In the same work, they combined both the theories (random vibration theory and mean flow theory) into a global multi-degree of freedom random vibration model. The distinguishing features of this model are the capability of predicting the response of the mixed rigid-flexible

cylinders cluster, changing frequencies, and modal characteristics with varying mean flow velocity.

Concerning fluid-elastic vibration, Païdoussis (1981) presented a critical assessment of the state-of-the-art for flow induced vibrations of cylinder arrays in cross and axial flows. He discussed different mechanisms that were recognized previously as potentially capable of giving rise to vibrations in cross and axial flows including small-amplitude vibrations induced in cylinder arrays in axial flow. He presented an empirical relation governing the forced vibrations in axial flow and discussed the underlying mechanisms of forced vibration, hydrodynamic coupling, parametric resonances, and fluid-elastic instabilities in cylinder arrays also in axial flow.

Considerable work has been done on the dynamics of rigid cylindrical structures in unsteady flows inside narrow annuli. For brevity, only some representative studies are mentioned. Mateescu and Païdoussis (1985) studied, analytically, the effect of unsteady potential flow in an axially variable annulus on the dynamics of oscillating rigid center-body. They extended the model to make it compatible with short center-body as well. Later, Mateescu and Païdoussis (1987) investigated the unsteady viscous effects on the annular-flow-induced instabilities of a rigid cylindrical body oscillating about a hinge in a coaxial narrow duct. For that, they extended the previously developed analytical model by Mateescu and Païdoussis (1985) to account for the unsteady viscous effects of a fluid flow in an approximate manner. They also compared the inviscid and viscous flow theories. Extending the formulation to flexible structures, the dynamics and stability of a flexible cylinder in annular flow was studied by Païdoussis et al. (1990). The principal contribution of this work was that firstly, they formulated the inviscid forces based on the potential flow theory and secondly, they formulated the unsteady viscous forces not by an adaptation of Taylor's expression but by a systematic application of the Navier-Stokes equations. They modified the linear model for a slender flexible cylinder in axial flow developed by Païdoussis (1973) to make it work for the flexible cylinder in annular flows subjected to unsteady viscous fluid forces by substituting the formulated inviscid and viscous force terms in the equation of motion. They also obtained the results for very narrow annuli.

There is a fair amount of research work on the dynamics of continuous flexible axisymmetric bodies in axial leakage flow. To remind the reader, when the fluid gap or annulus is narrow, the flow is considered to be a leakage flow. Fujita and Shintani (1999, 2001) studied

the flow-induced vibration instability of a long flexible axisymmetric rod due to axial leakage flow for different end boundary conditions. Unlike considering the axisymmetric rod as a rigid body and not a continuous body as in the previous studies, they considered the rod as a continuous flexible body. They analytically coupled the equations for the fluid and the structure. In the derivation of the analytical model, they obtained the expressions for the added mass, added damping, and added stiffness by considering unsteady pressure acting on the rod. They simplified the derived linear equation of motion into matrix form and then solved in MATLAB to obtain the complex eigenvalues. As a continuation of their work, Fujita et al. (2007) conducted experiments on a simply supported axisymmetric circular elastic beam subjected to laminar axial leakage flow. They also derived and analytically solved the coupled equations for similar system of fluid and beam structure for verification. They presented the analytical results in the form of complex eigenvalues. They, specifically, focused on explaining the generation of travelling waves and the energy balance for the distortion of vibration response in axial direction of the system at the transition from a lower predominant frequency to a higher one by means of experimental and analytical results. Later, Langthjem et al. (2006) bridged and extended the models developed by Li et al. (2002) and Fujita and Shintani (2001) to account for an eccentric simply supported flexible cylindrical rod undergoing static and dynamics instabilities due to annular laminar or turbulent leakage flow. For this, they derived the coupled fluid-structure equations and then discretized the equations using the Bubnov-Galerkin finite element method (Cook et al. 1989). They chose this discretization method because of its capability to handle various end boundary conditions and asymmetries in a very simple way by choosing the expansion functions 'once and for all'. Finally, they grouped the coupled equations into single matrix system and simplified it to 'extended' eigenvalue problem. The results they obtained were in the form of complex eigenvalues. Langthjem and Nakamura (2007) investigated the effect of swirl on the stability of slender flexible rod in axial annular leakage flow. They derived the analytical relations and analyzed the results. For the derivations, they assumed laminar fluid flow and vibrations of the rod in one plane. More recently, Fujita and Ohkuma (2010) used the already proposed analytical model by Fujuta and Shintani (2001) to investigate how the critical flow velocities for divergence and flutter vary for different end boundary conditions of an elastic beam in a narrow axial flow. They also conducted parametric studies of the effects of fluid

temperature, width of annular gap, viscosity of fluid, and structural damping on the critical flow velocities.

Some studies have specifically focused on the fundamental mechanisms and practical aspects of flow-induced instabilities of flexible structures in unconfined and confined flows together. In order to present the consequences of such instabilities, Païdoussis (1980) compiled many practical cases of flow-induced vibration problems in heat exchangers and nuclear reactors. Later, Païdoussis (1987) presented an abridged state-of-the-art review paper on flow-induced instabilities of cylindrical structures for the Fluid-Structure Interaction (FSI) categories mentioned above. This paper provides a brief and somewhat unified discussion of the subject matter. Naudascher and Rockwell (1990) also discussed, very briefly, the dynamics of slender bodies in axial flow pertaining to a rod (they referred to the flexible cylinder as a rod) in external axial flow, leakage flow, and multiple bodies in axial flow. They described the effect of confinement in case of multiple cylinders in an array on critical velocities. A more recent paper by Païdoussis (2008) discussed how the experience gained in studying the problem of pipes conveying fluid radiated into other areas of Applied Mechanics, particularly other problems in FSI involving slender structures and axial flows; specifically the dynamics of (a) Pipes conveying fluids; (b) slender cylinders in unconfined and confined axial flows; (c) cylindrical shells subjected to axial flow; and (e) plates in axial flow. It also provided a recap of equations and brief insight into the instability mechanisms in such problems.

1.2.2.2. Nonlinear Models

Through a linear model of a flexible cylindrical system in axial flow, one can reliably predict the occurrence of first instability, which is in most of the cases static often referred to as divergence, but post-divergence dynamics of the system needs to be validated through a nonlinear model (Païdoussis 1998, 2004; Modarres-Sadeghi 2006). This was done in 2002 when the first complete two-dimensional nonlinear analytical model governing the dynamics of cantilevered inextensible flexible cylinders in unconfined axial flow was developed. This work was a three-part study comprising (i) the physical dynamics (Païdoussis et al. 2002), (ii) the nonlinear equations of motion (Lopes et al. 2002), and (iii) the nonlinear dynamics (Semler et al. 2002). In first part, the physical dynamics of the system via experimental behaviour of elastomer cylinders in water flow and the energy transfer mechanisms were examined from a work-energy

perspective without obtaining the solution of the equations of motion. They experimentally determined the critical flow velocities for the onset of static and dynamic instabilities in a vertical flexible cantilevered cylinder enclosed in a relatively wider channel with axial flow and studied the effects of free-end shape, mass ratio, and surface roughness and slenderness on these critical velocities. In the second part, the nonlinear equation of motion was derived for the dynamics of a slender cantilevered cylinder in axial flow terminated by an ogival free end. In third part, the dynamics of the cantilevered cylinder in axial flow were explored by means of the equations of motion derived in part 2, and using the Finite Difference Method (FDM) and AUTO (a bifurcation software package) as numerical tools in order to obtain the solution of the discretized equations.

Modarres-Sadeghi et al. (2005) developed weakly nonlinear equations of motion for an extensible slender flexible cylinder with extensible centreline subjected to axial flow. They considered simply supported boundary conditions of the cylinder. The model comprised two coupled nonlinear equations describing the motions involving the longitudinal and transverse displacements. The derivation of the equations of motion was carried out in a Lagrangian framework. The equations were later transformed into a set of second-order ordinary differential equations using the Galerkin technique, which were finally solved numerically using Houbolt's finite difference method. The authors also analyzed the influences of frictional coefficients, externally imposed uniform tension, and dimensionless axial flexibility on stability and amplitude of the buckled solution. Later, Modarres-Sadeghi et al. (2007) presented a comparative study of the dynamics of a cylinder with simply supported and clamped-clamped (both the cylinder ends clamped) boundary conditions. Houbolt's Finite Difference Method (FDM) and AUTO were used to solve the equations of motion. With the combination of these methods, they could obtain the bifurcation diagrams and dynamic response of the cylinder over a wide range of flow velocity.

1.3. Motivation of Present Work

A comprehensive literature review indicates that earlier experiments on systems similar to the present one were conducted with different objectives in mind. For example, the experiments conducted by Païdoussis (1966b) were focused on studying the two-dimensional dynamics of a horizontal cylinder subjected to axial flow in order to validate and support the two-dimensional

linear theory of similar system developed by him (1966a). Other set of experiments conducted by Païdoussis et al. (1980b) were focused on studying the effect of harmonically perturbed axial flow pulsation frequency and amplitude on the parametric resonance oscillations in solitary cylinder clamped at its both ends. They used shorter and thinner cylindrical system than the one used in the present experimental study. Later, the experiments conducted by Païdoussis et al. (2002) on the vertical cantilevered cylinder in axial flow were intended to compare the experimental results with those of the two-dimensional nonlinear theory for similar system developed by them (Lopes et al. 2002). Hence the need remains to conduct the experiments on solitary cantilevered cylinder in axial flow to study the three-dimensional dynamics of the cylinder by determining the critical flow velocities, cylinder displacements and oscillation amplitudes, oscillation frequencies, and path traced by the oscillating cylinder, and also to validate and complement the three-dimensional nonlinear model results for similar system. The present experiments are also going to serve as a validation tool for the presently used two-dimensional linear and nonlinear models to study the dynamics of the same system.

In fluid-structure interaction problems, a precise calculation of the force coefficients such as longitudinal and normal viscous coefficients, base drag coefficient, and zero-flow normal force coefficient present in the equations of motion associated to the fluid forces acting on the cylinder surface is imperative. In the previous theoretical studies on cylindrical system in axial flow with different support boundary conditions (Païdoussis 1966a, 1973; Païdoussis et al. 1980a; De Langre et al. 2007), the force coefficients especially the viscous force coefficients in transverse and longitudinal directions were considered to be equal. Therefore, these force coefficients are calculated based on the parameters actually used in the experiments and theoretical models. It is expected that the implementation of these calculated coefficients in the linear model will enable the model to better predict the dynamics of the system.

As indicated earlier, a linear model can reliably predict the first point of instability of a flexible system in axial flow, which is most of the time a static instability commonly referred to as divergence. The dynamics of the system thereafter has to be verified via a nonlinear model (Païdoussis 1998, 2004; Modarres-Sadeghi 2006). From the literature review, it is noted that in the research work utilizing the nonlinear models to describe the system dynamics of a slender flexible system in axial flow (Païdoussis et al. 2002; Modarres-Sadeghi 2005, 2007), the force coefficients were either selected within a reasonable range or obtained based on some simple

relations. Therefore, an effort is undertaken to solve the nonlinear equation with the presently calculated force coefficients incorporated in it in order to better describe the nonlinear dynamics of the system.

Finally, a comprehensive literature review indicates that a three-dimensional coupled nonlinear model that governs the dynamics of cylindrical structures in axial flow has not yet been developed and studied. This, despite the fact that, in one of the aforementioned experiments (Païdoussis et al. 2002), three-dimensional dynamical behaviour was observed. In fact the path traced by the end of the cylinder was observed to be orbital. Lack of knowledge to account for the three-dimensional behaviour especially the non-symmetry found in the cylinder motion, important in the above-mentioned practical applications, is the motivation behind the present work, which is aimed at developing a three-dimensional coupled nonlinear model for a confined flexible cylindrical structure in axial flow in a Finite Element Method (FEM) based modelling and simulation package called ADINA in addition to experiments and other theoretical work done.

1.4. Objectives

The objectives, therefore, are to conduct experiments on a slender flexible cantilevered cylinder in axial flow, obtain and incorporate the presently calculated fluid force coefficients in the two-dimensional linear and nonlinear analytical models to study the linear and nonlinear dynamics of a cantilevered cylinder for a flow velocity range, investigate the effect of confinement on the dynamics of cylinder, develop three-dimensional nonlinear cantilevered cylinder model in ADINA, a specialized finite element modeling and simulation package, and investigate its response for a flow velocity range. The theoretical (linear and nonlinear) and numerical (created in ADINA) models are going to be validated with the help of experimental results. Finally, the results of the models are going to be compared together and presented at one place in order to observe the coherence of the results of the models and also to build a degree of confidence up to what beam mode, each model is capable of predicting the dynamics of the system.

1.5. Outline of the Thesis

In Chapter 1, a brief introduction of the subject area, its practical applications, and motivation behind the present work are given. In addition, a review of the previous studies on the dynamics of slender flexible structures in axial flow is also presented. This review includes earlier analytical and numerical studies on flexible cylinders in axial flow using linear and nonlinear models, for the cylinder in wide and narrow channels. It also includes the experimental studies done so far on similar systems. Finally, the objectives of the present study are presented.

In Chapter 2, procedures to calibrate the non-contacting laser-optical tracking systems used to measure the cylinder displacements and determine the essential parameters such as flexural rigidity, EI , logarithmic decrements, δ_n , hysteretic damping constant, $\bar{\mu}^*$, and the dimensionless viscoelastic damping constant, $\bar{\alpha}^*$ of the cylinder are presented. Then the fluid flow velocity profile inside the water tunnel test-section is also determined with the help of Laser Doppler anemometry (LDA). This chapter also includes descriptions of the LDA equipment and the experimental set-up to obtain these measurements. Description of the experimental set-up for the cantilevered cylinder with ogival end piece inside the vertical transparent test section of a water tunnel is then presented. Finally, the experimental results and quantitative analysis are presented.

In Chapter 3, the linear equation of motion of the flexible cylinder is considered. The linear partial differential equation is discretized by using the ‘extended Galerkin method’, resulting in a set of ordinary differential equations, solving them through a MATLAB code, and analyzing the results. The fluid forces such as inviscid forces, viscous forces, and hydrostatic or pressure forces acting on the surface of the cylinder contribute to the overall dynamics of the cylinder. Therefore, the coefficients associated to the viscous fluid forces such as longitudinal and normal viscous coefficients, base drag coefficient, and zero-flow normal coefficient are recalculated and incorporated in the linear model and the model is then solved to yield the dynamical behaviour of the cylinder with increasing flow velocities.

In Chapter 4, nonlinear equations of motion are solved using Houbolt’s Finite Difference Method (FDM) and the results employing the previously used coefficients by Semler et al. (2002) and the presently calculated ones are presented. Bifurcation diagrams, time histories, Fast Fourier Transform, Power Spectral Density, phase plots, Poincaré map, and mode shapes are

obtained to analyze the cylinder dynamics with increasing flow velocity. Finally, comparisons of the results in terms of the critical velocities for instabilities reported by Semler et al. (2002) and present model with previous and present force coefficients are presented.

In Chapter 5, the results of a three-dimensional model of a flexible cylinder enclosed in a channel created via a commercially available finite element modeling and simulation package, namely ADINA are presented. The simulations are performed at different water and air flow velocities and the vibration response of the cylinder is obtained. Finally, water and air flow results in terms of critical velocities marking the instabilities of the cylindrical system are compared.

In Chapter 6, the results in terms of the critical velocities, displacement magnitudes, and frequencies of linear and nonlinear models, experiments, and numerical model in water and air flows using the previous and present force coefficients are compared.

Finally Chapter 7 summarizes the thesis with the conclusions of the research work undertaken and suggestions for future work.

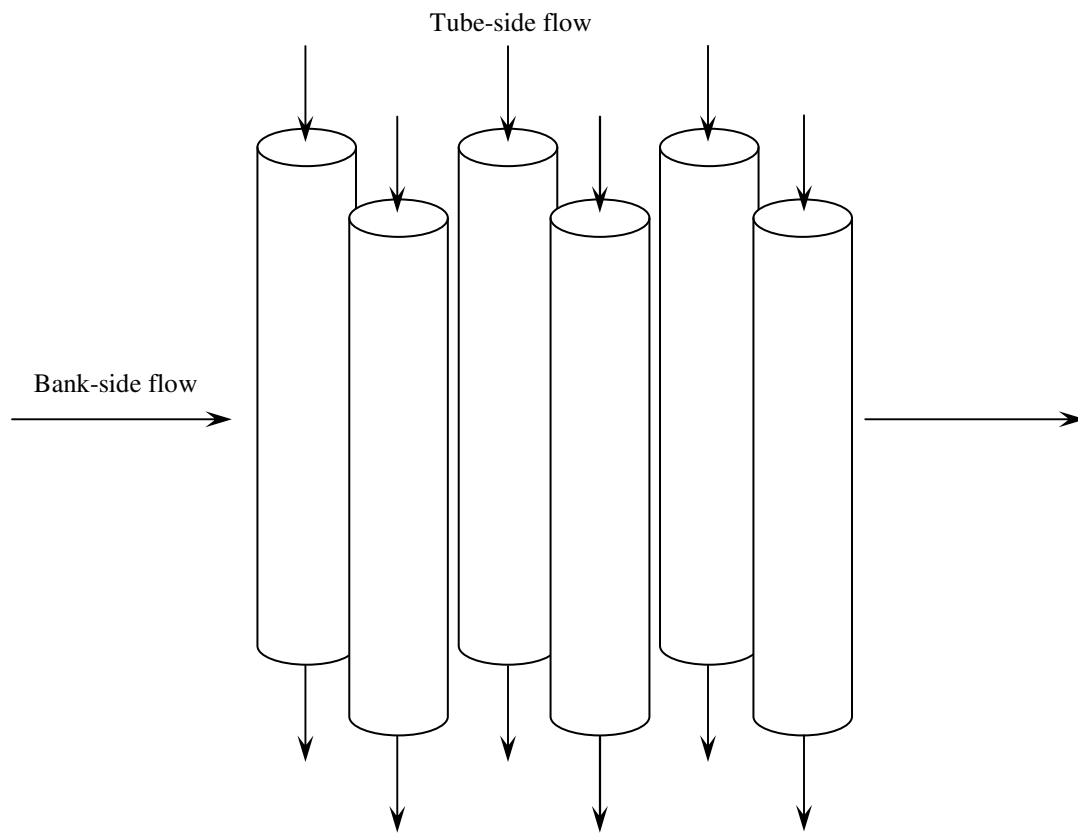


Fig. 1.1. Schematic of a heat exchanger tube bank.

Chapter 2

Experiments on Cantilevered Cylinder in Axial Flow

2.1. Introduction

As indicated in Chapter 1, earlier experiments on systems similar to the present one were conducted with different objectives in mind. The experiments conducted by Païdoussis (1966b) were focused on studying the two-dimensional dynamics of a horizontal cylinder subjected to axial flow in order to validate and support the two-dimensional linear theory of similar system developed by him (1966a). Using similar system to the 1966 experiments, Païdoussis et al. (2002) conducted experiments this time on a vertical cylinder in order to compare the experimental results with those of the two-dimensional nonlinear theory for similar system developed by them (Lopes et al. 2002). Other set of experiments conducted by Païdoussis et al. (1980b) were focused on studying the effect of harmonically perturbed axial flow on the parametric resonance oscillations in solitary cylinder. From the review of early experimental work, a need is felt to conduct experiments on the cantilevered cylindrical system in axial flow in order to study its three-dimensional dynamics and also to validate and complement the three-dimensional nonlinear numerical model results of similar system. The present experiments are also intended to compare the presently used two-dimensional linear and nonlinear models for their efficacy in predicting the dynamics of similar system.

This chapter gives an account of the experiments conducted on vertical flexible cantilevered cylinders in axial flow. The elastomer cylinder is made of *Silastic*® E RTV Silicone Rubber from Dow Corning. The cylinder casting is done using a two-part silicone rubber kit consisting of a base and a curing agent. The procedure is described by Païdoussis (1998) and Rinaldi (2009). Although they have given the procedure for a pipe, it is similar for cylinder. The only difference is that the mould for cylinder is of different length and diameter, and does not have the central rod, which is meant to make a hollow cylinder (i.e., a pipe) for internal axial flow. The upstream end of the cylinder is clamped and supported by four arms, which are rounded at the leading edge and pointed at the trailing edge as shown in Fig. 2.1 (a). The downstream free end of the cylinder is terminated by an ogival rigid end-piece as shown in Fig. 2.1 (b). The cylinder centreline is considered to be inextensible. The entire cylinder assembly is

enclosed in a vertical transparent plexiglas test-section of a closed loop water tunnel as shown in Fig. 2.2. The flow direction of the water inside the test-section is downwards. The objective of the experiments is to study the dynamics of the flexible cantilevered cylinder by determining the critical velocities for static and dynamic instabilities, as well as the effect of flow velocity on the amplitudes and frequencies of the unstable cylinder.

This chapter also includes the procedures to determine the structural and damping constants of the cylinder, calibrate the flow velocity and non-contacting one-dimensional optical displacement sensors used to record the cylinder motions, obtain the velocity flow profile inside the test-section, and the profile of the path traced by the oscillating cylinder.

2.2. Physical Description

The cantilevered cylinder has length, $L = 0.5265$ m, diameter, $D = 0.0254$ m, end-piece length, $l = 0.0346$ m, and tapering end-piece shape factor estimated to be $f = 0.8$ (see Appendix A). The vertical test-section ('channel'), made of plexiglas, has length, $L_{ch} = 0.77$ m and diameter, $D_{ch} = 0.203$ m. The confinement factor, χ is a measure of the confinement of a cylinder inside a channel or its proximity to the surrounding cylinders. It is defined by the expression (Païdoussis 2004)

$$\chi = \left(\frac{D_{ch}^2 + D^2}{D_{ch}^2 - D^2} \right). \quad (2.1)$$

Its value approaches 1 for a cylinder in unconfined flow and increases as the cylinder confinement is increased. Its value as calculated is 1.03. Water is circulated in the water tunnel by an Ingersoll-Rand type S horizontal split-case centrifugal pump with a discharge capacity of 2,200 gallons per minute. The maximum flow velocity achieved in the water tunnel is about 5.5 m/s corresponding to $u = 8.2$.

2.3. Calibrations of Laser-Optical Sensors

Two laser sensors have been utilized in the experiments. Therefore, before the experiment, calibrating both sensors is necessary. One is a Micro-Epsilon OptoNCDT 1400-200 non-contacting laser-optical displacement measurement sensor and the other is MEL M27L non-

contacting laser distance sensor. The calibration of these laser sensors enable the output voltages from the sensors to be converted to linear distances. The laser heads of both sensors are placed at a known distance, x , from some reference, say a rigid vertical plate. The laser heads are then moved gradually with known increments, Δx , towards the reference. At each location of the laser head, the DC voltage is recorded by a multimeter. The known distances, $x_1, x_2, x_3, \dots, x_n$ are then plotted against the output voltage for each sensor as shown in Figs. 2.3 and 2.4. Each of the figures shows that the output voltage varies linearly with the distance. The goodness of fit R_{fit}^2 for Figs. 2.3 and 2.4 come out to be 1 and 0.9998, respectively.

2.4. Flexural Rigidity of Cylinder

One of the essential quantities to know is the flexural rigidity of the cylinder, EI . The most convenient method to determine EI is by conducting planar free vibration experiments of a cantilevered cylinder hung vertically in air and excited in its first mode natural frequency. This can be achieved rather effortlessly by displacing and releasing the free end of the cylinder such that it oscillates in its first mode. The displacement of the cylinder is then measured using the Micro-Epsilon OptoNCDT 1400-200 non-contacting laser-optical displacement measurement sensor, which lies in the plane of oscillation, giving the output as a voltage. The resulting time signal is post-processed in a customized MATLAB code to obtain the Fast Fourier Transform (FFT) and Power Spectral Density (PSD) plots as shown in Fig. 2.5. FFT is an efficient algorithm to transform a discrete signal such as displacements of a structure in time domain into its discrete frequency domain (Strang 1994). PSD is a measure of the distribution of the power of a signal over the different frequencies (Miller and Childers 2004). From these plots, the first mode natural frequency, f_1 , is determined, which is 1.10 Hz. It is known that both the frequency and flexural rigidity depend on the gravity parameter, γ . Therefore, the expression given by Païdoussis and Des Trois Maisons (1969),

$$\frac{\gamma}{[\text{Re}(\omega_1)]^2} = \frac{g}{[\text{Re}(\Omega_1)]^2 L_{eff}}, \quad (2.2)$$

is used. Here, $\text{Re}(\omega_1)$ is the real part of dimensionless first mode natural frequency, g is the gravitational constant, L_{eff} is the effective length of cylinder, and $\Omega_1 = 2\pi f_1$ is the dimensional

first mode natural frequency in rad/s. Substituting the values of the parameters on right hand side of eq. (2.2) and using Table A.1 from Païdoussis and Des Trois Maisons (1969), the corresponding value of γ is found by linear interpolation. EI is then calculated from the expression

$$\gamma = \frac{mgL^3}{EI}, \quad (2.3)$$

given by Païdoussis and Des Trois Maisons (1971). Here, m is the mass of the cylinder per unit length. Equation (2.3) thus gives the value of $EI = 0.0719 \text{ N.m}^2$.

2.5. Logarithmic Decrements

The logarithmic decrements, δ_n , of the cantilevered cylinder in its first three modes are also determined experimentally by planar free vibrations of the cylinder hung in air and excited in its first, second and third modes. The first mode is, once again, excited manually, i.e., by displacing the free end of the cylinder in the plane of the measuring laser sensor. However, the second and third modes are excited mechanically with the help of a crank-slider mechanism. This mechanism consists of a DC motor attached to a rod through a crank that enables the rod to slide to and fro as shown in Fig. 2.6. The digital controller is used to control the r.p.m. of the motor, exciting the cylinder in the second and third modes.

When the DC motor is stopped abruptly, the cylinder oscillates, for a time, in only the desired mode. The decaying oscillations in the first, second and third modes are then recorded one by one with the help of the laser sensor. A MATLAB code with low-band, pass-band, and high-band Chebyshev type 1 filters of order 5 for first, second, and third mode cylinder oscillations, respectively, is used. Filters are used in order to remove any unwanted components, such as noise, from the signal. Figures 2.7 and 2.8 show the time histories, FFTs, and PSDs of the second and third modes, respectively.

The second and third mode frequencies, thus, determined are $f_2 = 4.52 \text{ Hz}$ and $f_3 = 11.96 \text{ Hz}$. The filtered signal of each mode is then used to obtain natural logarithm (\ln) of the cylinder displacement and plot it against time. Figure 2.9 shows a representative plot of $\ln(\text{Displacement})$ versus time of the first mode. The slope of the decaying peaks of $\ln(\text{Displacement})$ and the frequency of each mode are substituted in the expression

$$\delta_n = \frac{\text{slope}}{f_n} \quad (2.4)$$

to determine the logarithmic decrements, δ_n , which are $\delta_1 = 0.021$, $\delta_2 = 0.095$, and $\delta_3 = 0.558$. The reason of δ_3 being so high than δ_1 and δ_2 is due to system's rapid third mode oscillation decay.

2.6. Damping Constants

In order to consider the internal dissipation of the cylinder, a two-constant damping model is utilized. It is necessary to determine the hysteretic damping constant, $\bar{\mu}^*$, and the viscoelastic damping constant, $\bar{\alpha}^*$. The expression given by Païdoussis and Des Trois Maisons (1971), i.e.,

$$\delta_n^* = \frac{\delta_n}{\bar{\mu}^* + \bar{\alpha}^* \text{Re}(\omega_n)} \quad (2.5)$$

is used. The procedure to determine the damping constants begins with determining δ_n^* and $\text{Re}(\omega_n)$ for each mode. This is done by reading directly from Figs. 1 and 2 given by Païdoussis and Des Trois Maisons (1971) corresponding to γ calculated in Section 2.4. Substituting the known values of δ_n^* , $\text{Re}(\omega_n)$, and δ_n for each mode in eq. (2.5) gives rise to three independent linear equations. There are now two unknowns, i.e., $\bar{\mu}^*$ and $\bar{\alpha}^*$, and three equations. From these equations, three sets of two equations each are formed, i.e., sets of eq. (2.5) for first and second modes, first and third modes, and second and third modes. Each set is solved simultaneously to get $\bar{\mu}^*$ and $\bar{\alpha}^*$, thus obtaining three values of each damping constant. The average of each constant thus provides a good estimate to start fine-tuning the values and reaching values with minimum error in computing δ_1^* , δ_2^* , and δ_3^* from eq. (2.5) as a check. This fine-tuning is done in MATLAB using an optimization algorithm namely “*fmincon*”. *fmincon* finds minimum of constrained nonlinear multivariable function. It actually attempts to find a constrained minimum of a scalar function of several variables starting at an initial estimate x_o . The simplest of the syntaxes is $x = \text{fmincon}(\text{fun}, x_o, A, b)$. The algorithm starts at x_o and attempts to find a minimizer x of the function described in *fun* subject to the linear inequalities $A^* x \leq b$. The initial estimate x_o can be a scalar, vector, or matrix. A and b are the Linear constraint matrix and its

corresponding vector b , respectively (MATLAB help file 2010). Finally, the values obtained are $\bar{\mu}^* = 0.0272$ and $\bar{\alpha}^* = 0.000378$.

2.7. Flow Velocity Measurement Calibration

The water tunnel, used for the experiment, has a small bypass flow pipe for water circulation in addition to the main flow pipe. Venturi flow meters are fitted on both pipes. There are two differential-pressure transducers (Huba-692) across each of the Venturi meters, of which the readings are, respectively, displayed on two controllers (ATR141, used as read-out unit); one controller for each flow pipe. The controller ATR141 for the differential-pressure transducer (Huba-692) connected to the Venturi flow meter on the main flow pipe and the centrifugal pump speed in terms of r.p.m. are calibrated using a pitot-static tube and a mercury manometer. For calibration and actual experiments, the small bypass pipe is kept closed with the help of a choke valve and water is allowed to flow through the main pipe only. Therefore, the output panel shows the readings of only the Venturi meter of the main pipe. The pitot-static tube is inserted through the lower test-section window and its tip is carefully aligned with the centreline of the test section, as shown in Fig. 2.10. Thereafter, a mercury manometer is connected to the pitot-static tube. From the height of the mercury column, one can obtain the flow velocity using the relation, shown by Tang (2007)

$$U = \sqrt{2 \left(\frac{\rho_{Hg}}{\rho_{water}} - 1 \right) g h_{Hg}} , \quad (2.6)$$

where, ρ_{Hg} is the density of mercury, ρ_{water} is the density of water, and h_{Hg} is the height of mercury column.

The water tunnel is operated from its idle state to higher flow velocities by increasing the rotational speed of the pump by increments of 50 revolutions per minute (r.p.m.); the corresponding values of ATR141 readings from the output panel and the height of mercury column from the manometer being noted. Figure 2.11 shows the plot of height of mercury column in inches versus the ATR141 readings and the linear curve fit of the data with R_{fit}^2 equal to 0.997. The origin corresponds to $U = 0$ m/s, i.e., the pump being in idle state. Figure 2.12 shows the calculated flow velocity plotted against the ATR141 readings. The curve fit is via a

sixth order polynomial with $R_{fit}^2 = 0.9988$. This plot provides the calibration of the controller for the differential pressure transducer (Huba-692). Figure 2.13 shows the linearly fit flow velocity calibration curve for the r.p.m. of the pump with $R_{fit}^2 = 0.9996$.

2.8. Flow Velocity Profile inside the Test-Section

The flow velocity profile in the test-section is measured experimentally. For that, the cylinder model and support are removed from the test-section. The water tunnel is filled with water and operated at a target flow velocity. Since the actual experiment of studying the cylinder dynamics is done for a velocity range mostly in the turbulent flow regime, it has been ascertained that the velocity profile obtained experimentally is for turbulent flow. The water tunnel was operated at mean flow velocity of 1.9 m/s for the experiment. The corresponding Reynolds number, Re and volume flow rate are 3.842×10^5 and $0.0627 \text{ m}^3/\text{s}$, respectively.

Laser Doppler Anemometry (LDA) was used for the experimental procedure. LDA, also known as Laser Doppler velocimetry (LDV), is the technique of using the Doppler shift principle in a laser beam to measure the velocity of fluid flow in transparent or semi-transparent channel, or the motion of opaque or reflecting vibrating surfaces. Fluid flow measurement is undertaken from the Doppler shift effect on a beam scattered by very small reflecting spheres, called the seeding particles, moving within the fluid flow (Yeh and Cummins 1964). LDA passes two beams of parallel, monochromatic, and coherent laser light crossing at a point in the flow of the fluid being measured. These two beams are usually obtained by dividing a single beam, thus ensuring coherence between the two lasers. Lasers with wavelengths in the visible spectrum (390–750 nm) are usually used. A transmitting optics focuses the beams to intersect at the focal point of the laser beams, where they interfere and generate a set of fringes. As seeding particles moving in the fluid pass through these fringes, they reflect light that is then collected by a receiving optics and finally focused on a photodetector. The reflected light fluctuates in intensity, the frequency of which is corresponding to the Doppler shift between the incident and scattered light, and is thus proportional to the component of particle velocity which lies in the plane of the two laser beams. If the sensor is aligned to the flow in such a way that these fringes are perpendicular to the flow direction, the electrical signal generated at the photodetector will then be proportional to the seeding particle velocity inside the flow (Drain 1980).

Flowlite is an integrated laser-optics system developed by Dantec. The laser head stimulates Helium-Neon (He-Ne) laser beam with a focal length of 0.16 m. The seeding particles used in the flow are Iridine 100 silver pearl having size range of 10 to 15 μm . The flowlite system used gives one-dimensional flow velocity. It is designed for use with Dantec's signal processors and BSA Flow application post-processing software (Dantec Dynamics 2004). The output data appears in the software as a histogram of flow velocity probability distribution, as percent count. The software selects a range of flow velocity based on the data input from the laser-optics system. The data input contains the velocity components of the seeding particles in only the axial direction; if some particles flow at some angle to the cylinder axis, only the axial components of their velocities is recorded. In this way, a range of axial velocities are input to the software. These velocities are then quantized into uniform velocity ranges; each range being confined to a histogram bar. Each histogram bar is horizontally centered on the mean value of its velocity range. The histogram bar possessing the highest occurrences of its seeding particles' velocities exhibits maximum percent count in the histogram and its mean velocity is considered as the required velocity at that particular location. In other words, the flow velocity is quantized. The higher the percent count of one particular histogram bar as compared to the others, the more uniform is the flow. Furthermore, the larger the number of histogram bars, the more accurate is the velocity determination. In the present measurements, a histogram resolution of 0.01 m/s, which is 0.53 % of the mean water tunnel velocity, with 525 histogram bars is used.

The procedure starts by placing the laser head horizontally facing the test-section in such a way that the focal point of laser beams either reaches the inside centre of the test-section or closest to it. The data at that point is then recorded. The laser head is then moved away from the test-section with equal increments such that the focal point of beams inside the test-section moves towards its inner wall and data is recorded at each location. Two representative histograms and velocity plots are shown in Figs. 2.14 and 2.15. The histograms in these figures are not symmetric as the shape of the histogram depends on the distribution of the axial components of seeding particles' velocities in the histogram bars. The histogram also shows the normal velocity distribution.

Finally, the velocity profile obtained is shown in Fig. 2.16 with $R_{fit}^2 = 0.9908$. The curve is sixth order polynomial:

$U = -9 \times 10^7 y^6 + 3 \times 10^7 y^5 - 4 \times 10^6 y^4 + 2.38 \times 10^5 y^3 - 8.07 \times 10^3 y^2 + 1.35 \times 10^2 y + 1.167$. The y -axis marks the inner surface of the test-section. The solid circles represent the velocities at different locations. A curve fit of the velocity data shows the turbulent velocity profile. The figure also shows that there are no velocity data points at radial distances less than 0.0029 m. The reason is that it is very difficult to measure the velocity very close to wall. Therefore, the velocities at radial distances between 0 and 0.0029 m are resolved theoretically by the law of the wall for turbulent flow. One of commonly used models for law of the wall is the logarithmic log law model given as

$$u^+ = \frac{1}{k} \ln y^+ + C^+, \quad (2.7)$$

where, u^+ is the dimensionless velocity, k is the Von Karman constant, y^+ is the dimensionless wall coordinate, and C^+ is a constant. u^+ and y^+ are given by the expressions

$$u^+ = \frac{u}{u^*}, \quad (2.8)$$

and

$$y^+ = \frac{u^* y}{\nu_k}, \quad (2.9)$$

respectively. In these expressions, u is the mean flow velocity, u^* is the frictional velocity, y is the radial distance of the point, where velocity is to be determined, and ν_k is the kinematic viscosity of water. The known values are $k = 0.41$, $C^+ = 5.0$, and $\nu = 1.004 \times 10^{-6} \text{ m}^2/\text{s}$ (Schlichting and Gersten 2000). It is known that near the wall in turbulent flow, there are two adjacent layers, namely the inner layer and outer layer. The inner layer is further composed of a viscous sub-layer, which stretches in the range of $0 < y^+ \leq 5$, a buffer layer, which stretches in the range of $5 < y^+ \leq 30$ (White 2003), and an overlap layer also called log law region, which stretches in the range of $35 \leq y^+ \leq 350$ (White 1974). In the viscous sub-layer, the expression $u^+ = y^+$ is applicable. In the buffer layer, $u^+ \neq y^+$ and $u^+ \neq (1/k) \ln(y^+) + C^+$. However, for $0 \leq y^+ < 11$, $u^+ = y^+$ gives better results, whereas for $y^+ > 11$, eq. (2.7) gives better results, though neither are accurate at $y^+ = 11$ (Pope 2000). In the overlap layer, eq. (2.7) is applicable. The outer layer stretches beyond $y^+ = 350$ in the turbulent flow (White 2003). Substituting u^+ , y^+ , k , C^+ , and ν at

given $u = 1.9$ m/s and $R_{ch} = 0.1015$ (radius of the test-section) into eq. (2.7) gives an expression with u^* on both its sides. Through trial and error, the value of u^* is calculated, yielding 0.0712 m/s. The experimentally unresolved distance is divided into five equally distant segments and for each radial distance y , the flow velocity, u is now calculated using eq. (2.7). The experimentally measured and theoretical velocities are then plotted together, as shown in Fig. 2.17. The theoretical data curve fit is of fifth order polynomial $U = 1 \times 10^{14} y^5 - 1 \times 10^{12} y^4 + 4 \times 10^9 y^3 - 6 \times 10^6 y^2 + 4.16 \times 10^3 y + 1 \times 10^{-10}$. The velocities obtained by experimental and theoretical procedures at the common radial distance, i.e., $y = 0.0029$ m do not match having a discrepancy of 13.4%, which is quite understandable. Experimental errors include difficulty in controlling the seeding particles distribution in the flow, laser beam diffraction due to different media, and rounding off the data to some significant figures. The theoretical model does not give the exact true values of velocity due to the imprecise usage of the relations in the sub-layers, which do not have distinct boundaries.

The effect of the distance of the laser head from the test-section on the focal length is also investigated. The plexiglas of the test-section having refractive index, $n = 1.49$, changes the focal length of the laser beams passing through it, and any change in the distance of the laser head from the test-section also effects the focal length. Using n and some trigonometric relations, the focal length is calculated across the test section plexiglas wall. For that, a simple MATLAB routine is developed which gives the focal lengths by entering, as input, the perpendicular distances of the laser head from the test-section outer wall. Figure 2.18 shows this linear variation. It is also observed that the plexiglas, in general, extends the focal length of the laser beams passing through it.

Flow velocity and focal length results are quantitatively represented in Table 2.1. Table 2.2 quantitatively shows the logarithmic log law model velocity and y^+ results.

2.9. Cylinder Dynamics

The dynamics of the flexible cantilevered cylinder has been studied using the MEL M27L non-contacting laser distance sensor with two different set-ups. The first set-up is for estimating the critical flow velocity at which static instability, i.e., divergence, develops in the first and second cylinder modes, whereas the second set-up is for estimating the critical flow velocity at which a

dynamic instability, i.e., flutter, develops in second and third cylinder modes. Each set-up is dealt with in a separate sub-section.

2.9.1. Set-up for Divergence

In the first set-up, the MEL M27L non-contacting laser head is placed against the free downstream end of the cylinder just above the ogival end-piece at a vertical distance of 0.49 m (19.3 cylinder diameters) from the upstream cylinder support. The laser head is horizontally placed at its working mid-range from the cylinder surface. The schematic of the set-up is shown in Fig. 2.19.

The flow velocity of the water tunnel is gradually increased with increments of 50 r.p.m. The dimensional flow velocity in m/s is obtained by using the calibration curve of velocity versus r.p.m (Fig. 2.13) and later rendered dimensionless by using the expression given by Païdoussis (2004). Here, it is worth mentioning that the cylinder does not remain perfectly stationary even at very small flow velocities but rather exhibits localized small lateral motions, which persist until flutter develops. These motions can be easily observed by looking at the cylinder tip. Because of these localized motions, it is extremely difficult to record the mean DC output of the laser sensor using a multimeter. Therefore, the motions of the point on the cylinder surface where the laser is focused are recorded for 60 seconds using a LabVIEW program customized for the present measurements. The data is then time-averaged to obtain reasonably accurate single displacement value, \bar{y} , for each flow velocity. \bar{y} is made dimensionless by $\eta^* = \bar{y}/D$ and plotted against the dimensionless velocity, u , as shown in Fig. 2.20.

It is clear from the figure that divergence does not develop abruptly and hence cannot be identified easily. In order to estimate the critical flow velocity, $u_{cr,d1}$, a criterion of η^* surpassing a threshold of 0.5 is arbitrarily chosen. η^* is the dimensionless mean cylinder displacement. Physically, this criterion corresponds to about half the cylinder diameter. Therefore, the resulting $u_{cr,d1}$ is 1.87. With increasing flow, the divergence takes on a second beam-mode shape. Similarly, identifying the critical flow velocity for second mode divergence precisely is also very difficult; with increasing velocity, the first mode divergence transforms into second mode rather gradually. Therefore, the velocity at which the second mode shape becomes very obvious is considered to be $u_{cr,d2}$. Its value is approximately 4.66. This value is based on visual judgment, therefore, the symbol ' \approx ' is used in Fig. 2.20 and the tables in Chapter 6 to present the value of

$u_{cr,d2}$. The same set-up cannot be used to determine the critical flow velocity for flutter, $u_{cr,fl2}$, since at higher flow velocities, the cylinder amplitudes near the downstream end become too large for the laser to trace the full motion. For that, the second set-up is adopted, the details of which are described hereunder.

2.9.2. Set-up for Flutter

The second set-up involves placing the MEL M27L non-contacting laser head at a vertical distance of 0.09 m (3.5 cylinder diameters) from the upstream cylinder support. The laser head is horizontally placed at its working mid-range from the cylinder surface. The schematic of the set-up is shown in Fig. 2.21.

The flow velocity of the water tunnel is gradually increased beyond $u_{cr,d}$ by increasing the pump speed by increments of 50 r.p.m. For each u , the data, which is obtained as distance in mm, is rendered dimensionless by dividing by the diameter of the cylinder; r.m.s. values of the dimensionless displacements η are then obtained and plotted against u as shown in Fig. 2.22. At $u_{cr,fl2} = 5.92$, there is a sudden increase in the $\eta_{r.m.s.}$ value, signalling the onset of second mode flutter. The corresponding dimensional and dimensionless frequencies are $f_{cr,fl2} = 3.54$ Hz and $\omega_{cr,fl2} = 23.83$, respectively. A corresponding abrupt rise to $\omega_{cr,fl2}$ at $u_{cr,fl2}$ is depicted in Fig 2.23. The second mode oscillation is confirmed by comparing its frequency with the second mode free oscillation frequency, which is in its vicinity. At flow velocities beyond $u_{cr,fl2}$, the $\eta_{r.m.s.}$ values remain more or less constant until, at $u_{cr,fl3} = 7.70$, its value increases abruptly, indicating the onset of third mode flutter, as shown in Fig. 2.24. The critical flow velocity for third mode flutter, $u_{cr,fl3}$, is also confirmed by comparing the dimensionless flutter frequencies of the cylinder at increasing velocities as shown in Fig. 2.25. As observed in Figs. 2.24 and 2.25, a slight drop in $\eta_{r.m.s.}$ and ω at $6.7 \leq u \leq 7.5$ is due to the transition from second mode cylinder oscillation to third mode oscillation. At $u_{cr,fl3}$, the frequency increases from a mean second mode flutter frequency, $\omega_{fl2} = 23.27$ to $\omega_{cr,fl3} = 56.49$. The corresponding third mode dimensional frequency, $f_{cr,fl3}$, is 8.39 Hz. Similar to the second mode, third mode is also confirmed by visual inspection and comparing its frequency with the third mode free oscillation frequency in air, which is in its vicinity.

Figure 2.26 shows the time history, FFT, and PSD of cylinder second mode flutter at $u = 6.43$. The frequency, f_{fl2} , is the dominant and distinct second mode frequency. Its value is 3.51

Hz. $2f_{fl2}$, $3f_{fl2}$, $4f_{fl2}$, and $5f_{fl2}$ are the multiples of this fundamental frequency. Similarly, Figure 2.27 shows the time history, FFT, and PSD of cylinder third mode flutter at $u_{cr,fl3} = 7.70$. The dominant third mode frequency, $f_{cr,fl3}$, is 8.39 Hz. $2f_{cr,fl3}$ is the multiple of this fundamental frequency.

Figure 2.28 shows the cylinder stable and unstable conditions. The unstable conditions correspond to divergence in first mode in (b), flutter in second mode in (c), and flutter in third mode in (d).

2.10. Path Traced by the Oscillating Cylinder

The path traced by the fluttering cylinder is experimentally determined with the set-up shown in Fig. 2.29. In the figure, the top view shows the solid circle representing the equilibrium position of the cylinder, whereas the dotted circle represents the displaced position of the cylinder at any instant during flutter. The ‘+’ represents the cylinder centerline. The two laser sensor heads, i.e., OptoNCDT 1400-200 and MEL M27L, are placed in the vertical planes normal to each other at a vertical distance of 0.09 m from the upstream cylinder support. Each of the laser sensor heads is placed horizontally at its working mid-range.

The water tunnel is run at flow velocities higher than $u_{cr,fl2}$ in order to record the cylinder flutter in second and third modes using both laser heads. For each flow velocity, the cylinder displacements are recorded as function of time in both the planes using the laser sensors and the corresponding mean flutter amplitude is determined. Results show that the cylinder flutter in second and third modes does not follow a circular path but rather an elliptical path. The mean ratio of second mode flutter amplitudes recorded by OptoNCDT 1400-200 and MEL M27L sensors comes out to be 1.19. Representative results are presented here. Figure 2.30 shows the value of each of the upper bound and lower bound second mode flutter amplitudes for flow velocity, $u = 6.43$. The upper bound, bearing a positive value, represents the mean amplitude of all cylinder oscillations with distances greater than the distance of the equilibrium position of the cylinder from the laser head; the lower bound, bearing a negative value, represents the distances smaller than the distance of the equilibrium position of the cylinder from the laser head. It is obvious from the figure that there exists an asymmetry between the upper and lower bounds in oscillations recorded by the laser sensors. This asymmetry is due to the quasi-circular path the cylinder follows. It is in fact a kind of whirling ‘orbital’ motion.

Figure 2.31 shows the total peak to peak mean amplitude in each oscillation plane recorded by each of the laser sensors with respect to fixed zero reference at $u = 6.43$. It is very clear from the figure that the total mean amplitude in the plane recorded by OptoNCDT 1400-200 laser sensor is greater than that in the other plane recorded by MEL M27L laser sensor. Figures 2.32 and 2.33 are additional and perhaps clearer ways of representing the results by showing the values of total peak to peak amplitudes in the two planes and the approximate visualization of the elliptical path traced by the cylinder exhibiting second mode flutter, respectively.

Results also show that the asymmetry, i.e., quasi-circular path, of third mode cylinder flutter oscillations in the two orthogonal planes becomes more pronounced than that of the second mode. The mean ratio of third mode flutter amplitudes recorded by OptoNCDT 1400-200 and MEL M27L sensors is 1.48. This is depicted in Figs. 2.34-2.37 at $u = 7.95$.

2.11. Summary

Experiments were conducted to determine flexural rigidity, EI , logarithmic decrements δ_n , and hysteretic, $\bar{\mu}^*$, and viscoelastic, $\bar{\alpha}^*$, damping constants of a cantilevered cylinder. Then, an account of the calibration of the water tunnel flow velocity measurement was given in Section 2.7. In addition to this, the flow velocity profile inside the test section along a single plane was also experimentally constructed and presented in Section 2.8. Finally, some more experiments were conducted to map the path traced by the cylinder oscillating in second and third modes.

After the above experimental procedures, the main set of experiments was conducted to study the dynamics of the cantilevered cylinder having an ogival end-piece at the downstream free end. In order to determine the critical velocities for divergence, $u_{cr,d}$, the laser heads were placed horizontally near the free end of the cylinder and static displacements with time were recorded. As mentioned earlier, locating $u_{cr,d1}$ or $u_{cr,d2}$ was very difficult, because there was not distinct point to identify the onset of instability. Therefore, when the displacement increased substantially, the velocity corresponding to it was marked as $u_{cr,d1}$. Similarly, visual judgment was also involved to mark $u_{cr,d2}$. In order to determine the critical velocities for flutter, $u_{cr,fl}$, the laser heads were placed horizontally in the upper half of the cylinder length and for each flow velocity, displacements with time were recorded. The r.m.s. value of the dimensionless displacements for each velocity was obtained and plotted against u . In the case of flutter, the

substantial increase in r.m.s. value at flutter onset was quite distinct. Hence, the critical velocities for flutter in the second, $u_{cr,fl2}$, and third, $u_{cr,fl3}$, modes were determined. Finally, the paths traced by the cylinder in second and third modes were experimentally obtained. The mean cylinder oscillation amplitude was obtained for each laser sensor at each of the given flow velocities and then compared with the help of plots and drawn the path. Results showed that the cylinder did not follow a circular path but rather a quasi-circular one, i.e., a kind of whirling ‘orbital’ path.

Table. 2.1. Flow velocities and focal lengths at decreasing radial distances of the laser beams focal point.

Sr. No.	Distance from the laser head (m)	Distance inside the test-section, y (m)	Percent of the radius of the test-section	Focal length (m)	Flow velocity, U (m/s)
1	0.0847	0.0852	84.0	0.1873	2.049
2	0.0897	0.0786	77.4	0.1856	2.049
3	0.0947	0.0719	70.8	0.1839	2.03
4	0.0997	0.0652	64.2	0.1823	2.049
5	0.1047	0.0586	57.7	0.1806	2.03
6	0.1097	0.0519	51.1	0.1789	2.03
7	0.1147	0.0452	44.5	0.1773	2.03
8	0.1197	0.0385	38.0	0.1756	2.03
9	0.1247	0.0319	31.4	0.1739	2.011
10	0.1297	0.0252	24.8	0.1722	2.03
11	0.1347	0.0185	18.3	0.1706	2.03
12	0.1397	0.0119	11.7	0.1689	1.992
13	0.1429	0.0077	7.5	0.1679	1.783
14	0.1457	0.0039	3.8	0.1669	1.612
15	0.1464	0.0029	2.8	0.1667	1.479

Table. 2.2. Flow velocities and y^+ at decreasing radial distances of the laser beams focal point.

Sr. No.	Distance inside the test section, y (m)	Velocity, u (m/s)	y^+
1	0.0029	1.281	204.38
2	0.0023	1.242	163.51
3	0.0017	1.192	122.63
4	0.0012	1.122	81.75
5	0.0006	1.001	40.88
6	0.0000	0	0

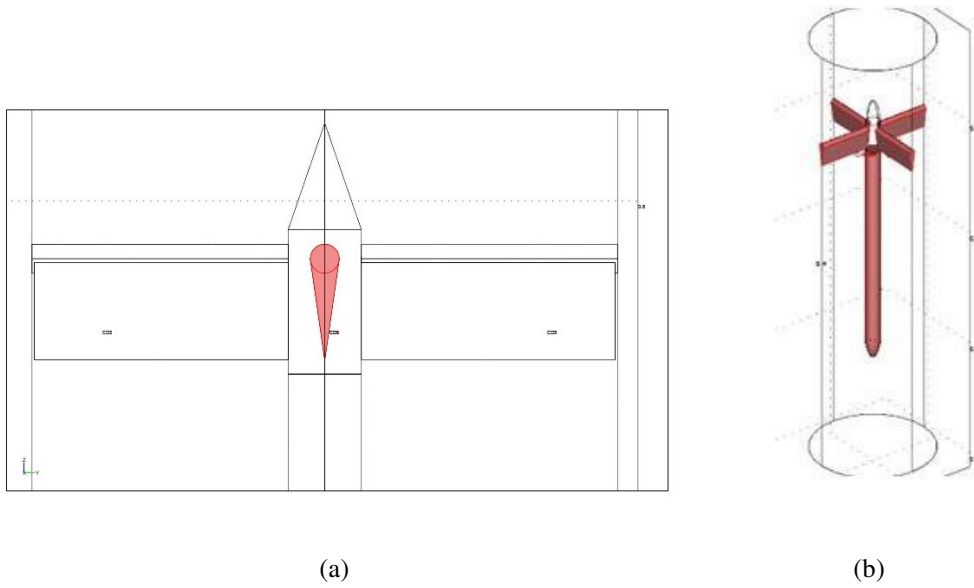


Fig. 2.1. (a) Schematics of the upstream support arms and (b) the entire cylinder assembly with the downstream ogival end-piece.



Fig. 2.2. Cantilevered cylinder enclosed in a transparent plexiglas test-section.

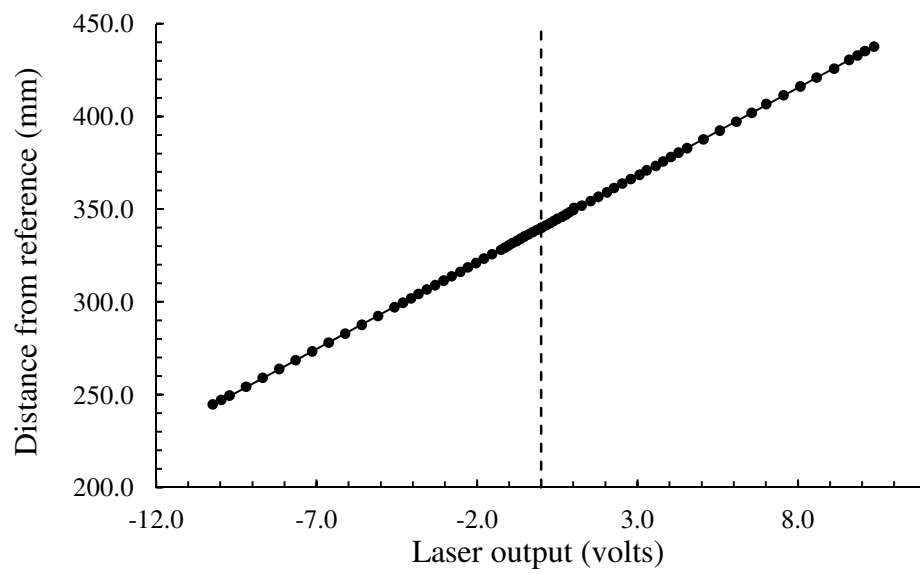


Fig. 2.3. Calibration curve for MEL laser distance sensor. — , linear curve fit.

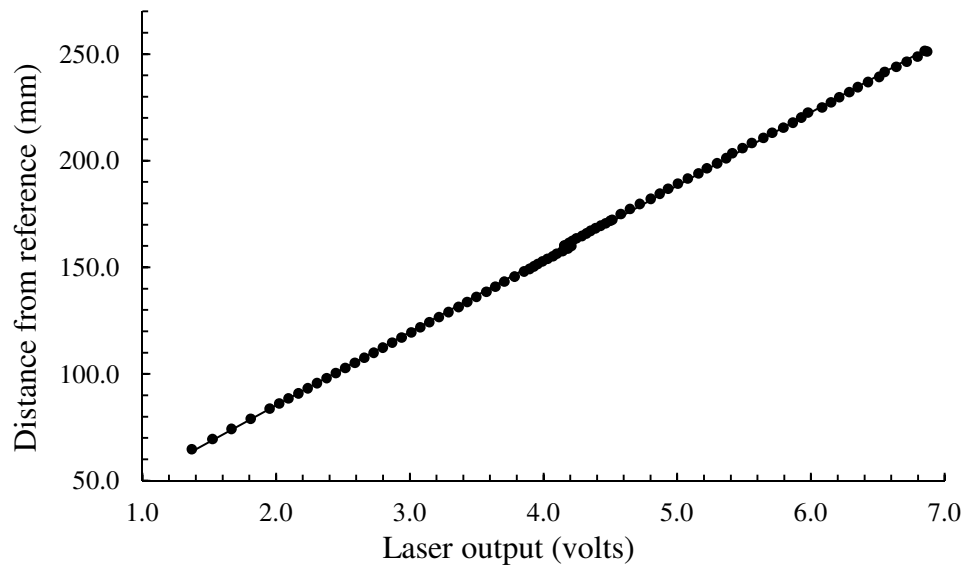


Fig. 2.4. Calibration curve for OptoNCDT 1400-200 laser distance sensor. — , linear curve fit.

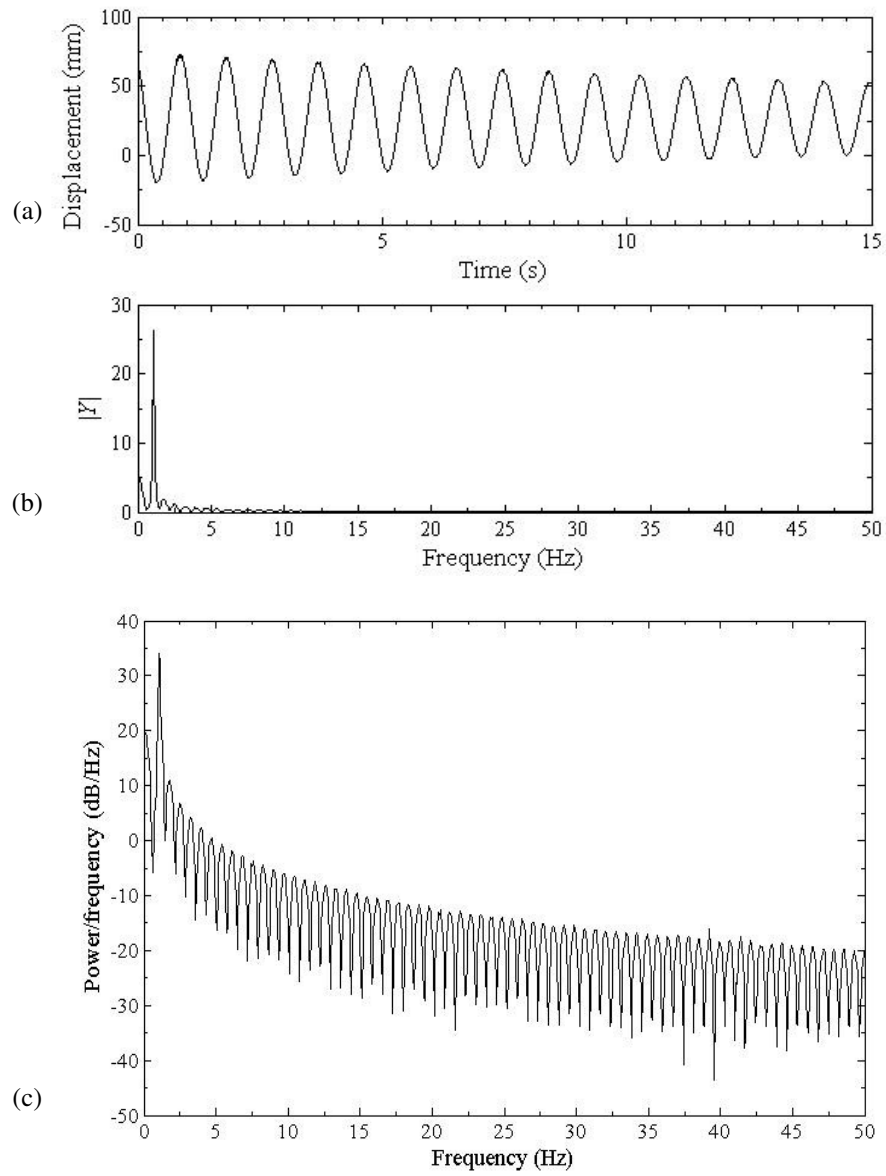


Fig. 2.5. (a) Time history, (b) FFT, and (c) PSD of first mode oscillation of cantilevered cylinder.

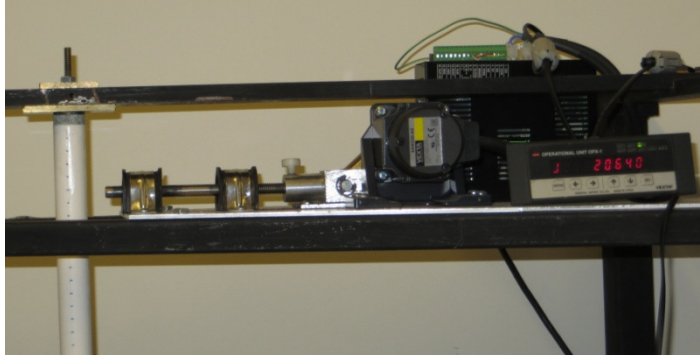


Fig. 2.6. DC motor and crank-slider mechanism with digital speed controller.

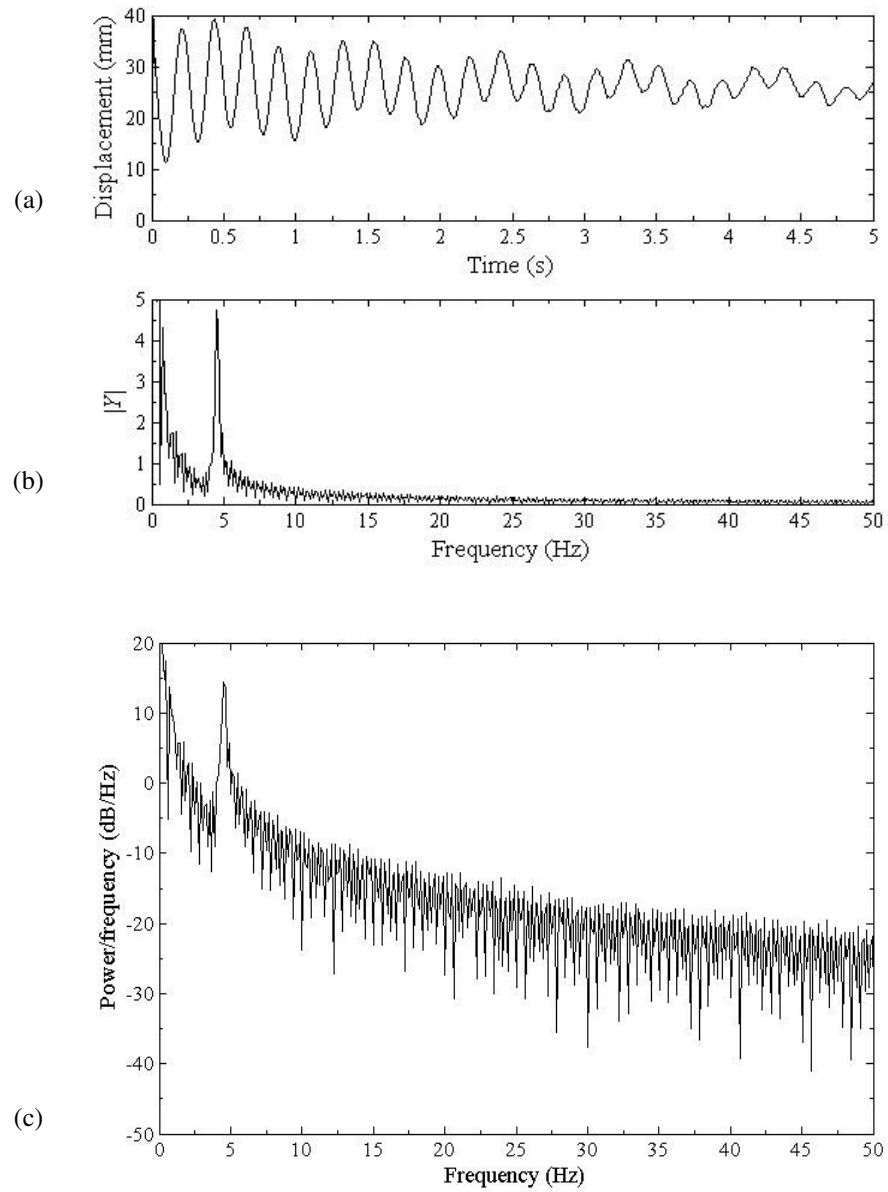


Fig. 2.7. (a) Time history, (b) FFT, and (c) PSD of second mode oscillation of cantilevered cylinder.

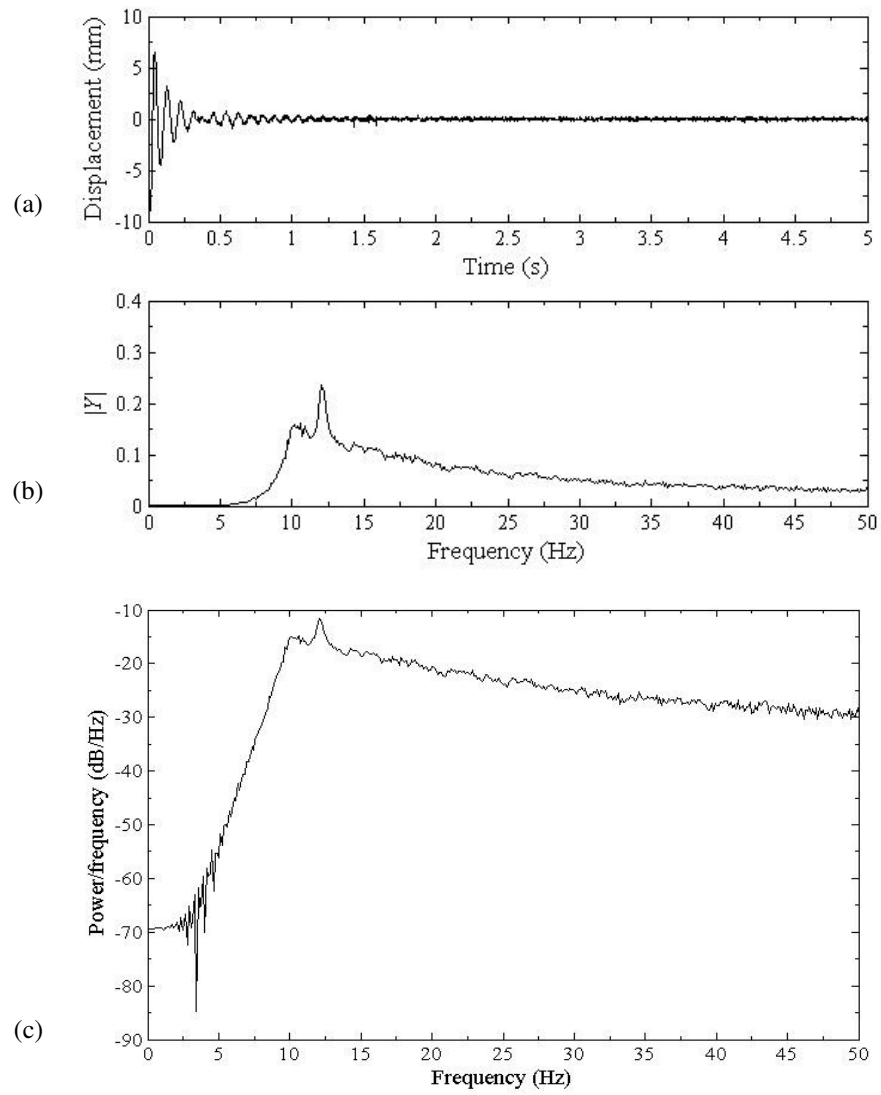


Fig. 2.8. (a) Time history, (b) FFT, and (c) PSD of third mode oscillation of cantilevered cylinder.

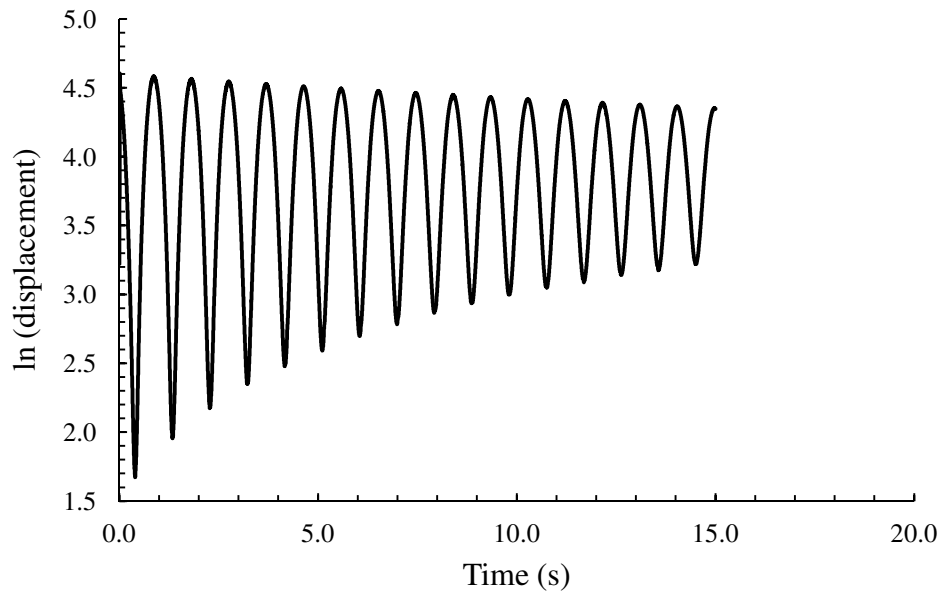


Fig. 2.9. Plot of $\ln(\text{displacement})$ versus time of first mode.



Fig. 2.10. Pitot-static tube and mercury manometer set-up for flow velocity calibration.

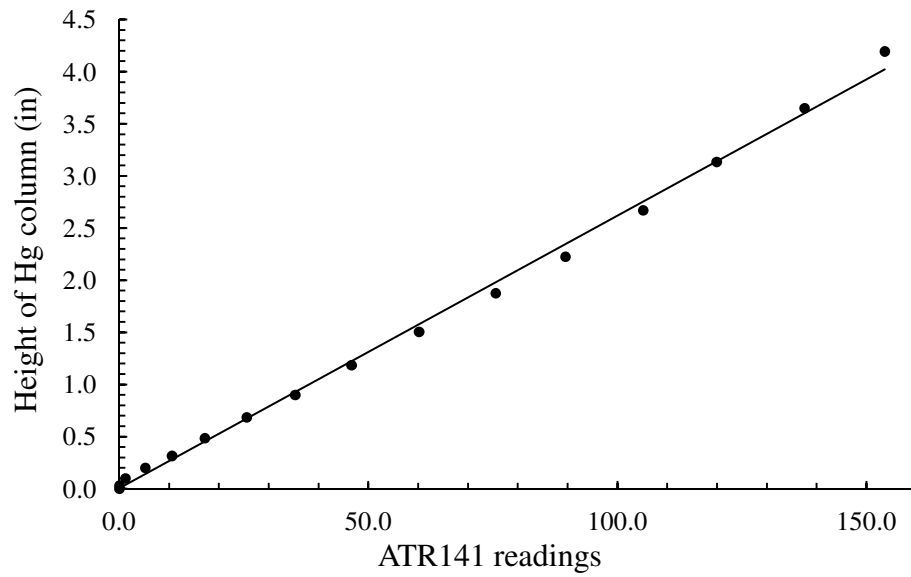


Fig. 2.11. Plot of height of mercury column versus ATR141 readings. —, linear curve fit.

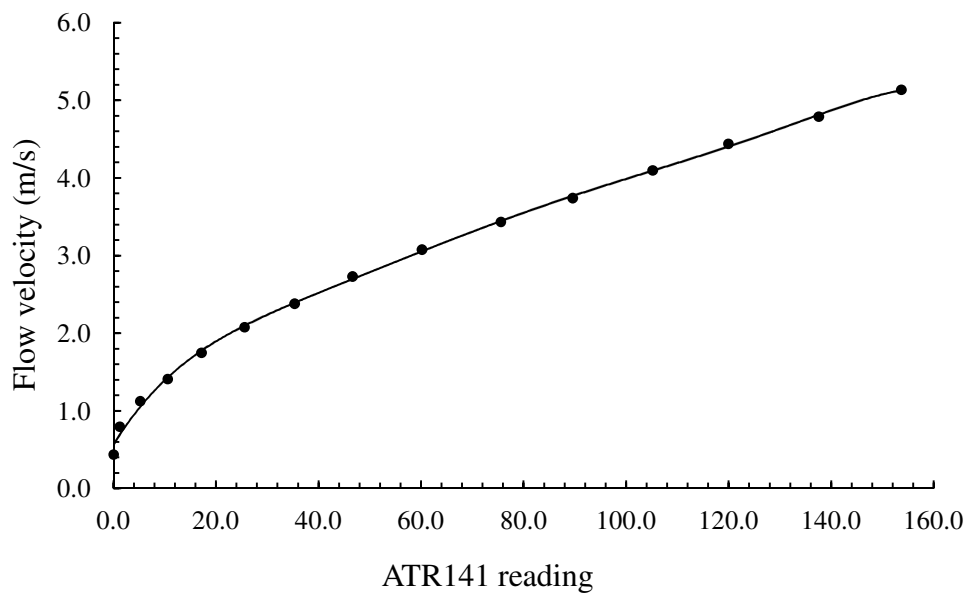


Fig. 2.12. Plot of flow velocity versus ATR141 readings. —, polynomial curve fit.

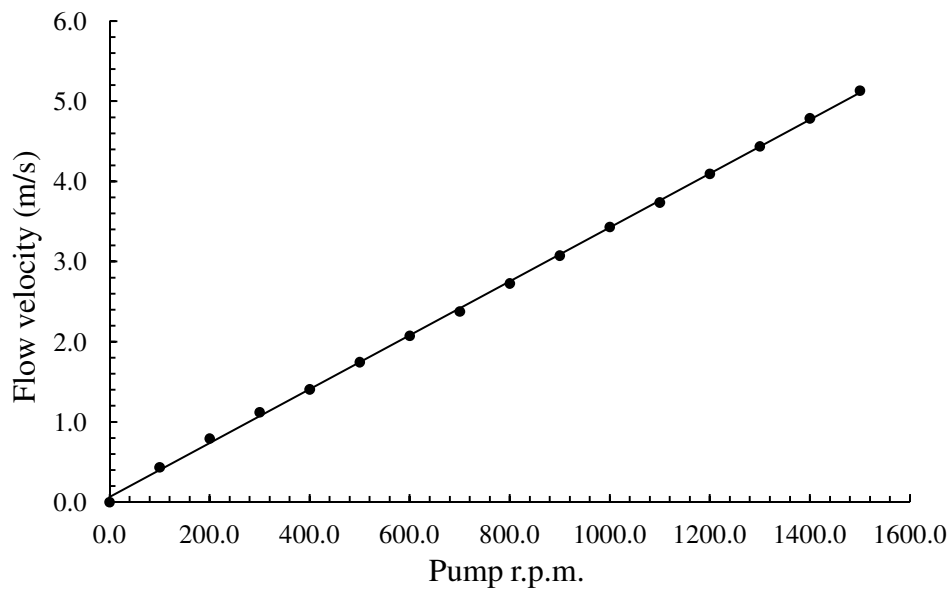


Fig. 2.13. Plot of flow velocity versus pump rotational speed. —, linear curve fit.

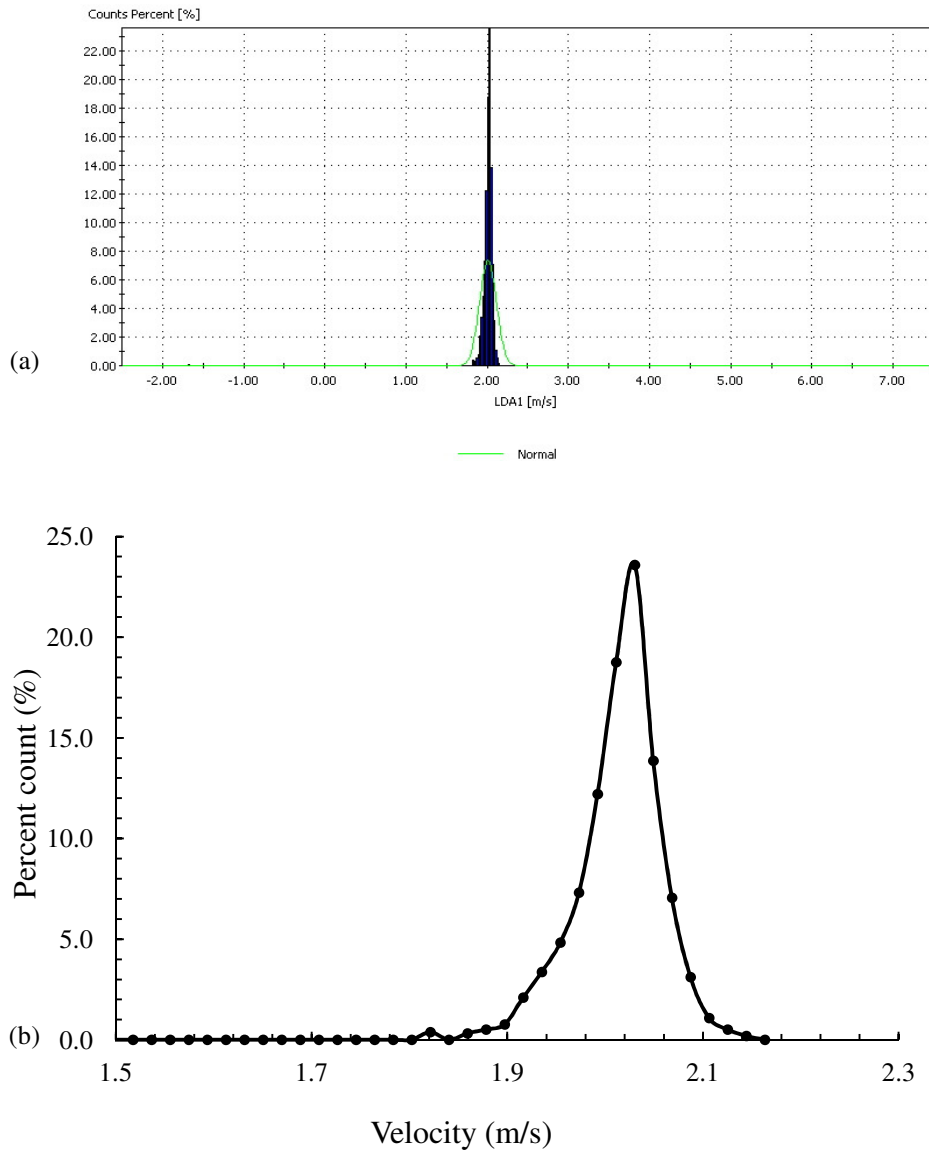


Fig. 2.14. (a) Histogram with normal velocity distribution; (b) mean velocity probability plot at radial distance of 0.0452 m.

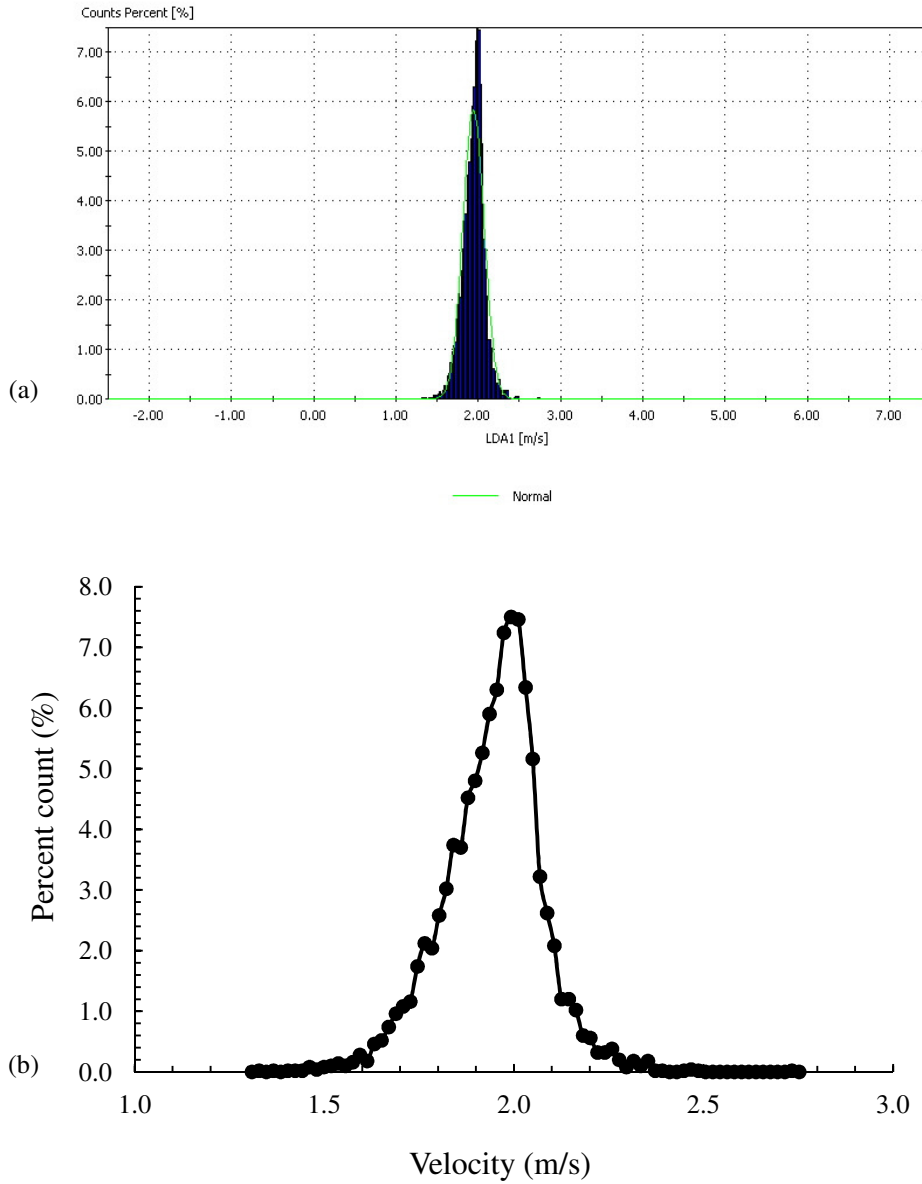


Fig. 2.15. (a) Histogram with normal velocity distribution; (b) mean velocity probability plot at radial distance of 0.0119 m.

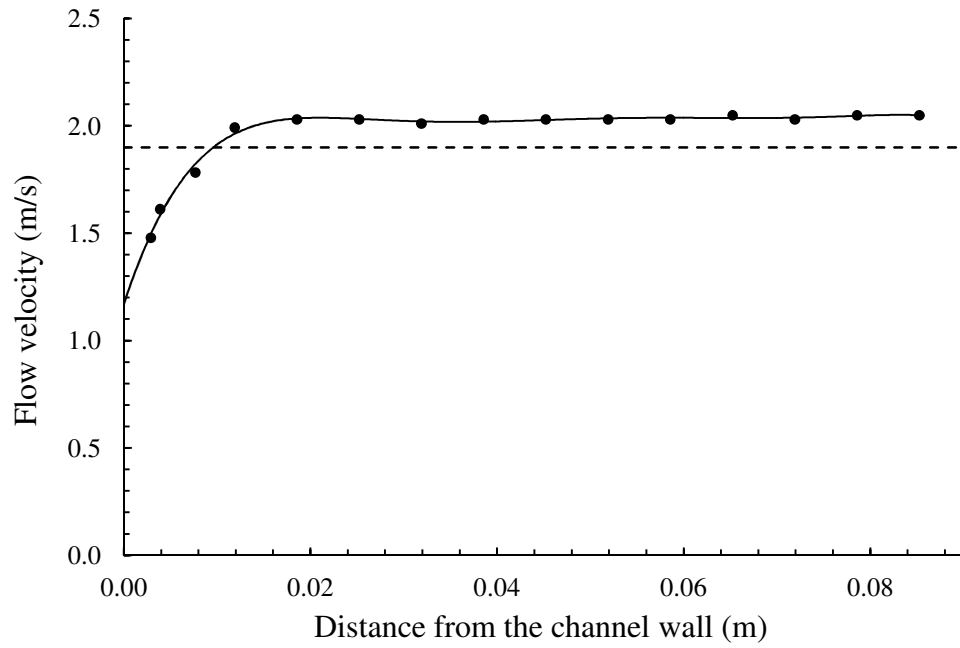


Fig. 2.16. Turbulent velocity profile inside the test-section. ●, LDA data; ----, mean flow velocity; —, polynomial curve fit of LDA data.

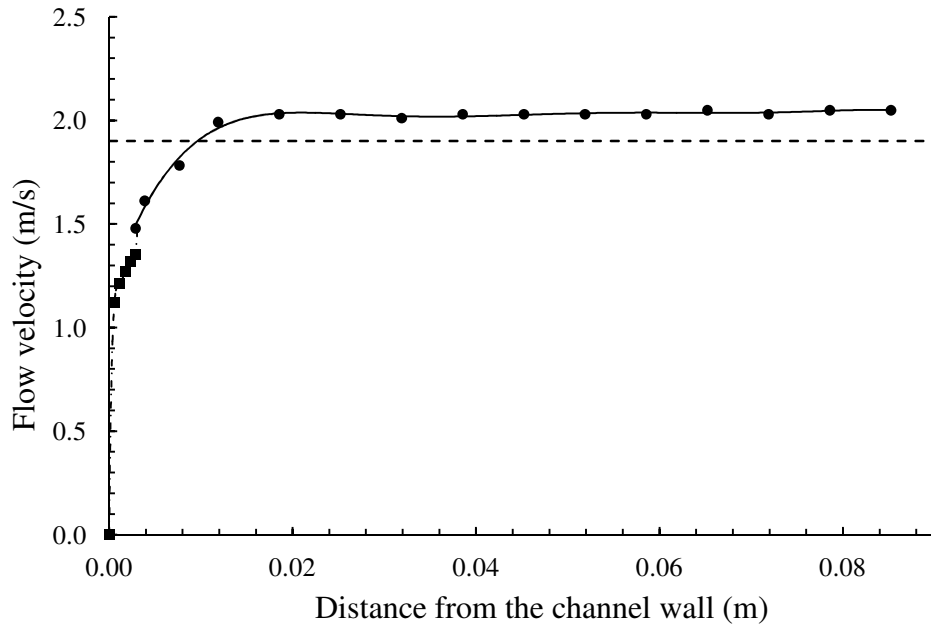


Fig. 2.17. Turbulent velocity profile obtained from the Flowlite system and logarithmic log law.

- , LDA data; ■ , logarithmic log law data; -----, mean flow velocity;
- , polynomial curve fit of LDA data; - - - - - , polynomial curve fit of logarithmic log law.

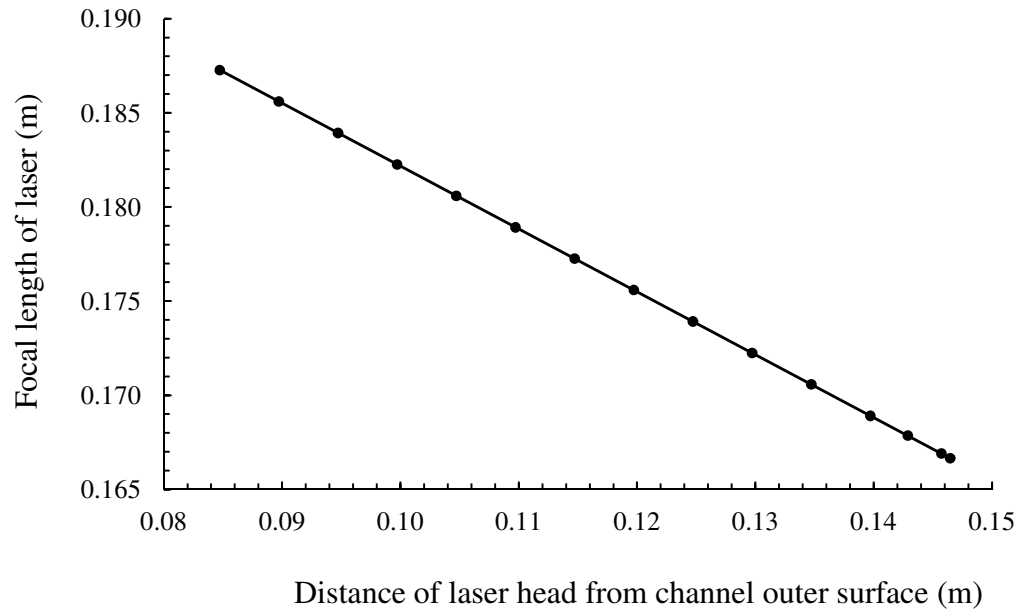


Fig. 2.18. Focal lengths of laser beams plotted against varying laser head distances from test-section outer wall.

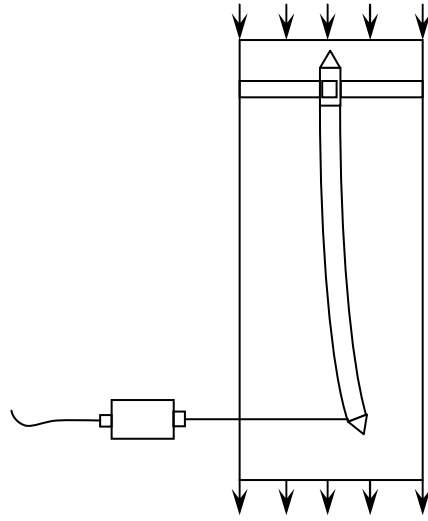


Fig. 2.19. Schematics of the set-up to estimate critical flow velocity for divergence.

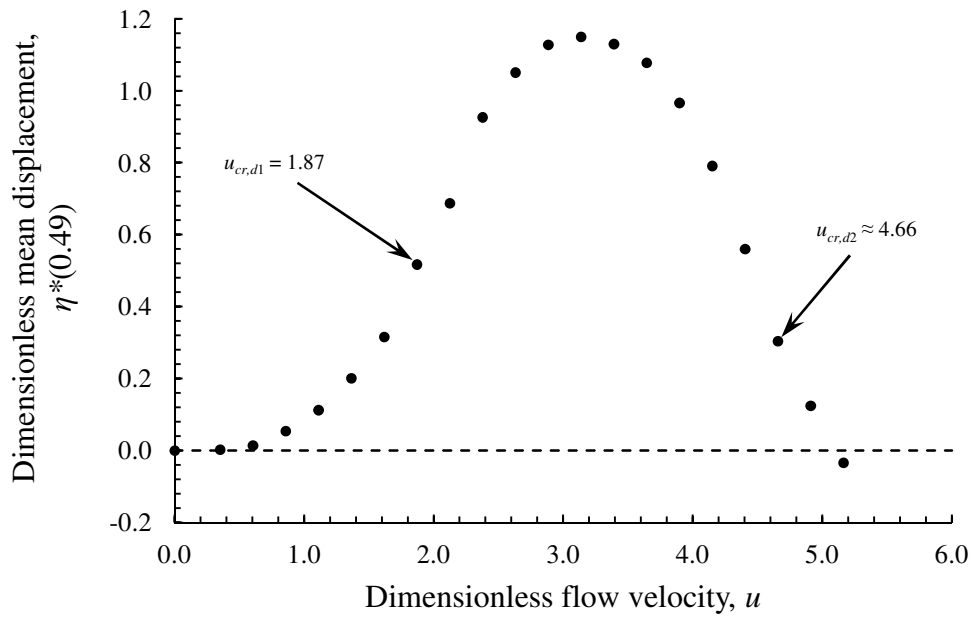


Fig. 2.20. Plot of dimensionless mean displacement, $\eta^*(0.49)$ versus dimensionless flow velocity, u .

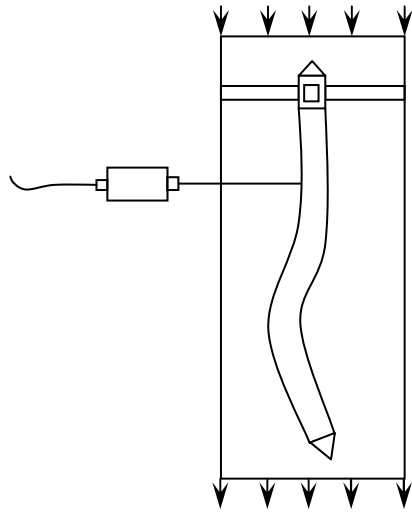


Fig. 2.21. Schematics of the set-up to estimate critical flow velocity for flutter.

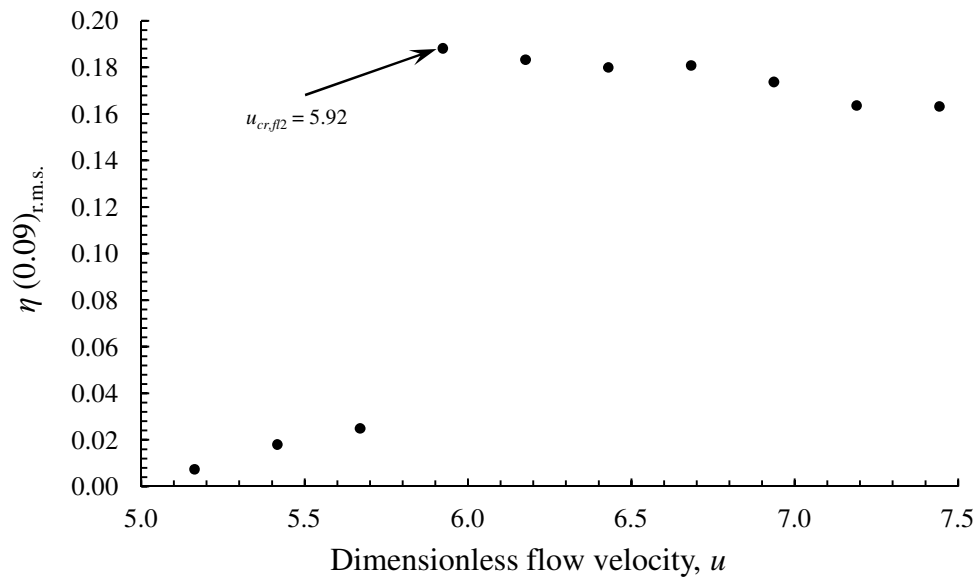


Fig. 2.22. The r.m.s. amplitude, $[\eta(0.09)]_{r.m.s.}$ versus u showing the onset of second mode flutter.

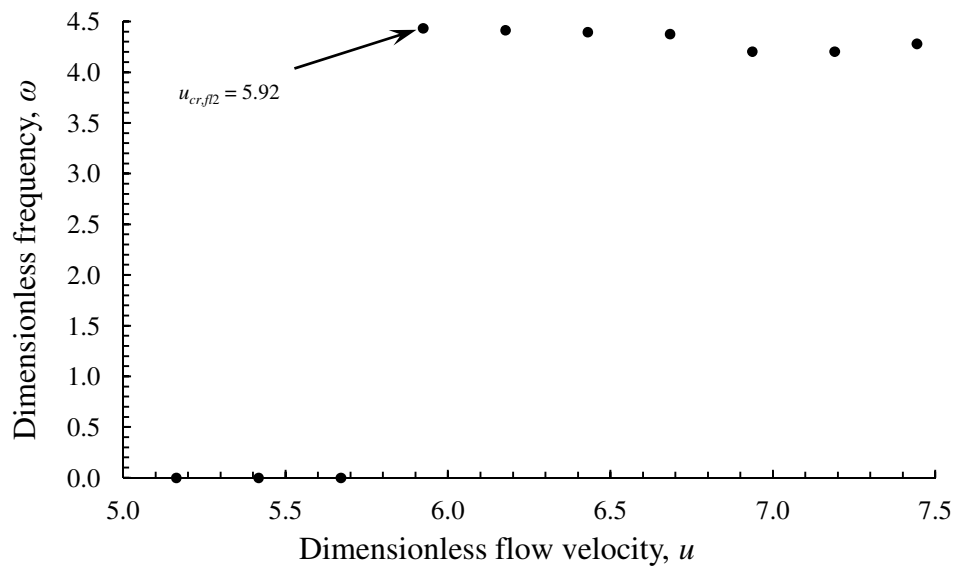


Fig. 2.23. Dimensionless frequency, ω versus u showing the onset of second mode flutter.

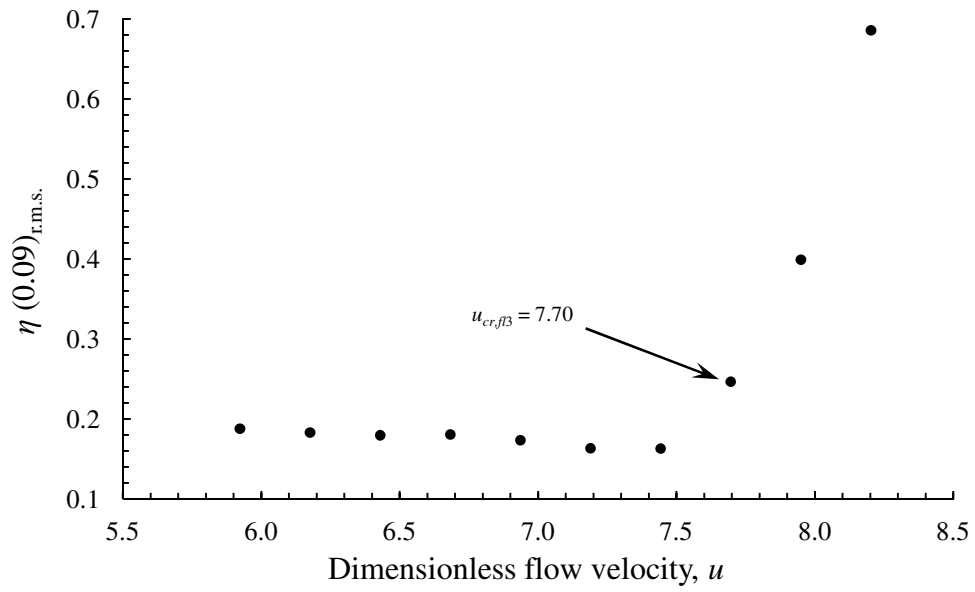


Fig. 2.24. The r.m.s. amplitude, $[\eta (0.09)]_{r.m.s.}$ versus u showing the onset of third mode flutter.

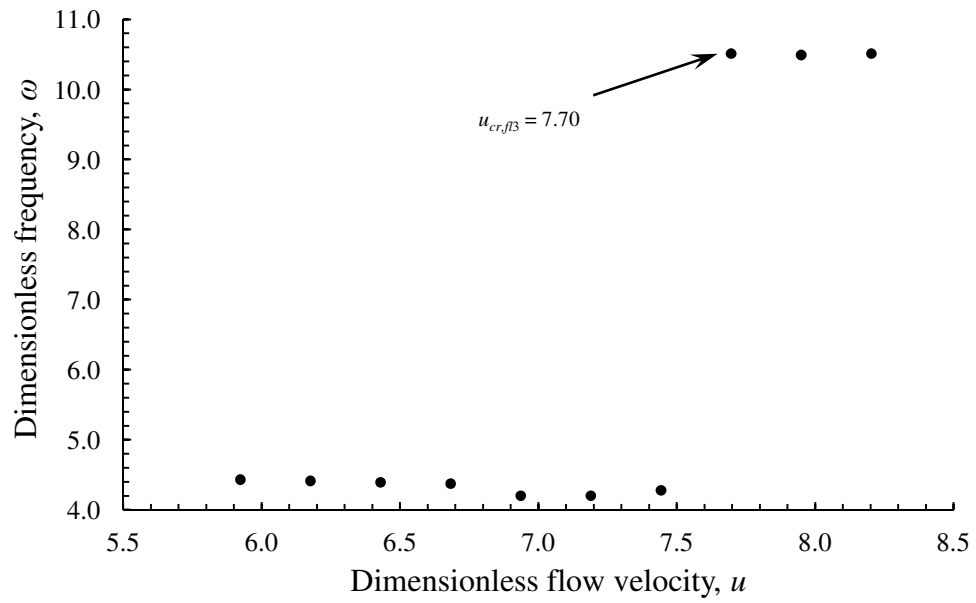


Fig. 2.25. Dimensionless frequency, ω versus u showing the onset of third mode flutter.

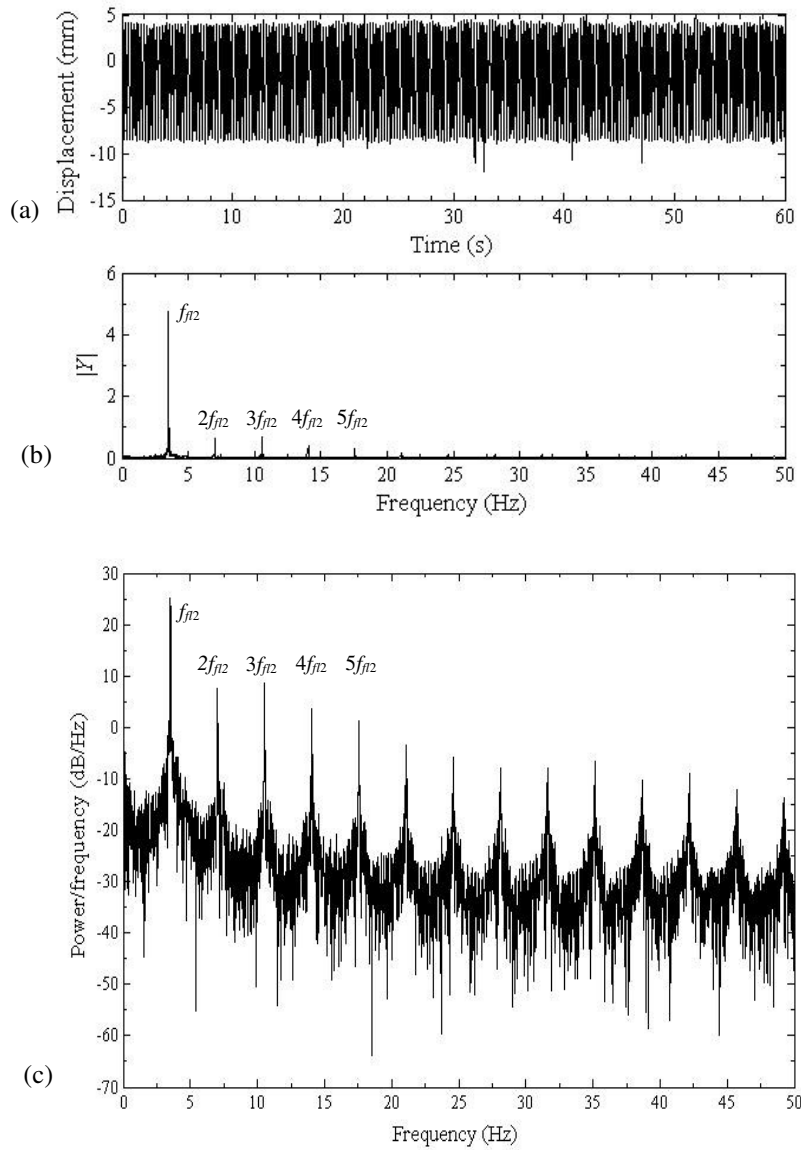


Fig. 2.26. (a) Time history, (b) FFT, and (c) PSD of second mode flutter of cantilevered cylinder at $u = 6.43$.

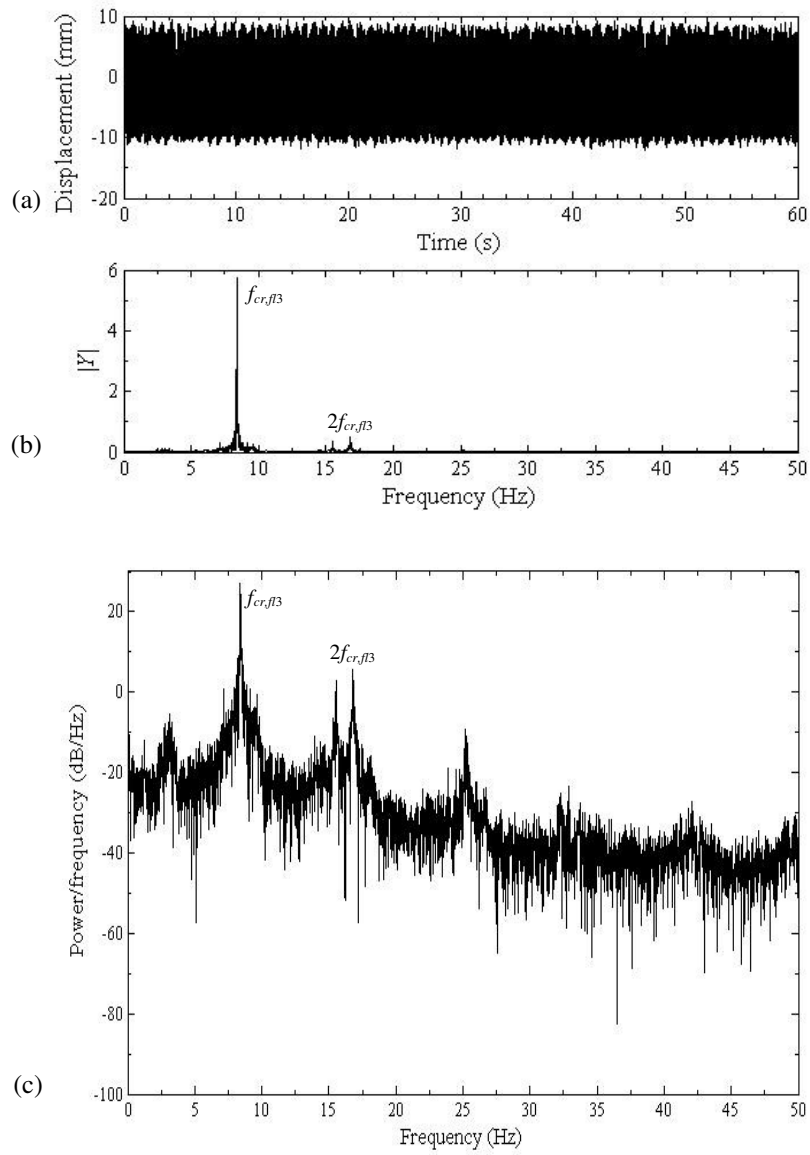


Fig. 2.27. (a) Time history, (b) FFT, and (c) PSD of third mode flutter of cantilevered cylinder at $u = 7.70$.

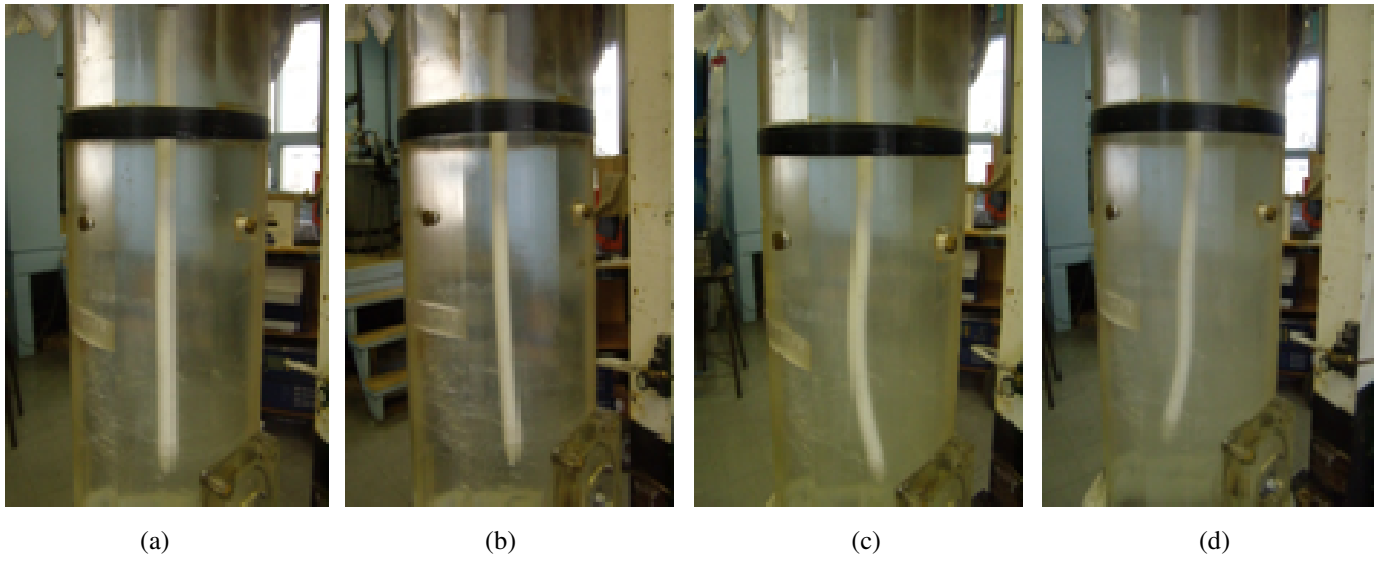


Fig. 2.28. Cylinder stable and unstable conditions: (a) stable cylinder; (b) divergence in first mode; (c) flutter in second mode; (d) flutter in third mode.

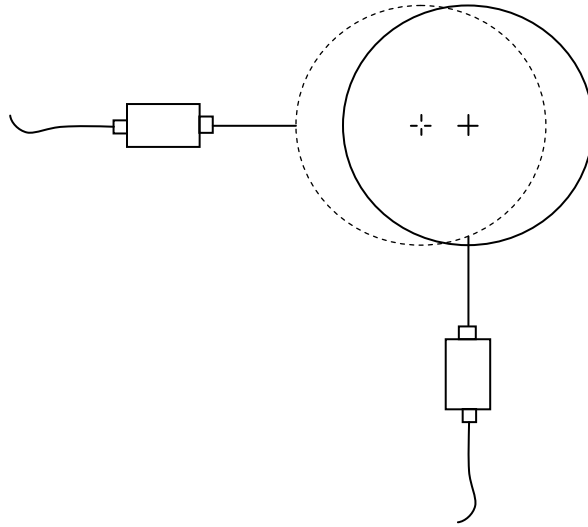


Fig. 2.29. Two laser set-up to determine the path traced by the oscillating cylinder.

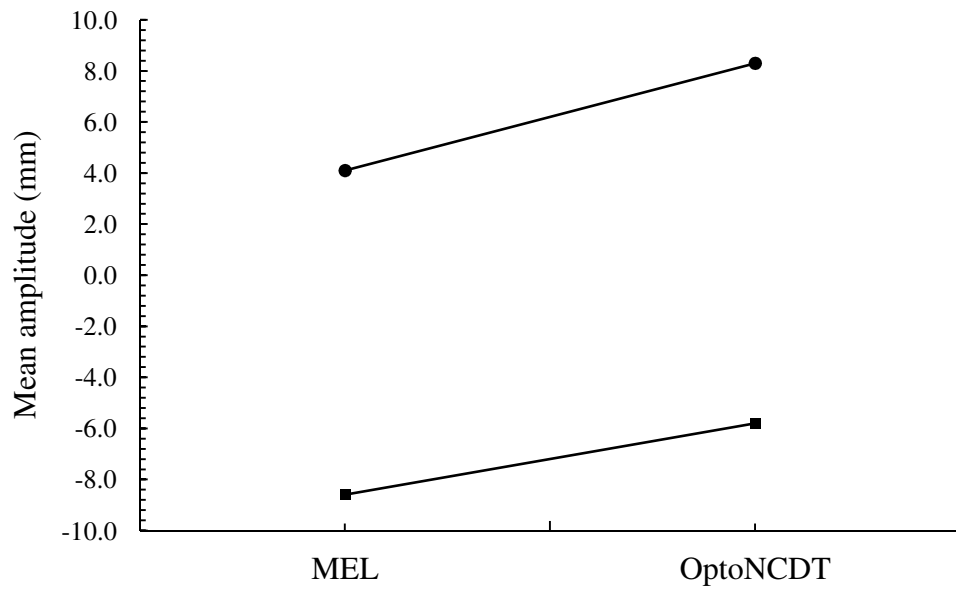


Fig. 2.30. Forward (upper bound) and backward (lower bound) motions of the cylinder about its mean position recorded by the two laser sensors at $u = 6.43$. \bullet , upper bound; \blacksquare , lower bound.

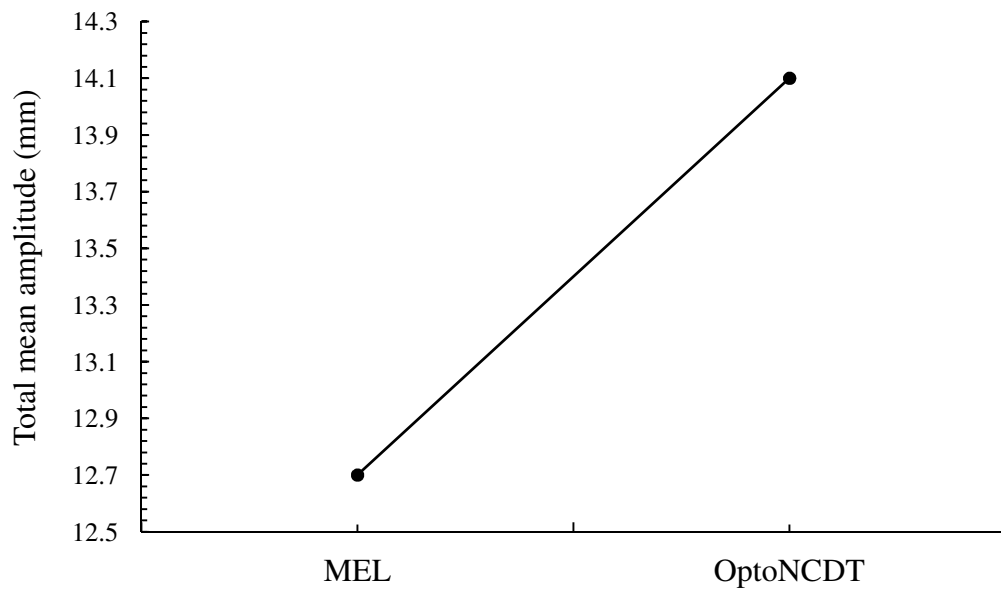


Fig. 2.31. Mean amplitudes recorded by the two lasers at $u = 6.43$.

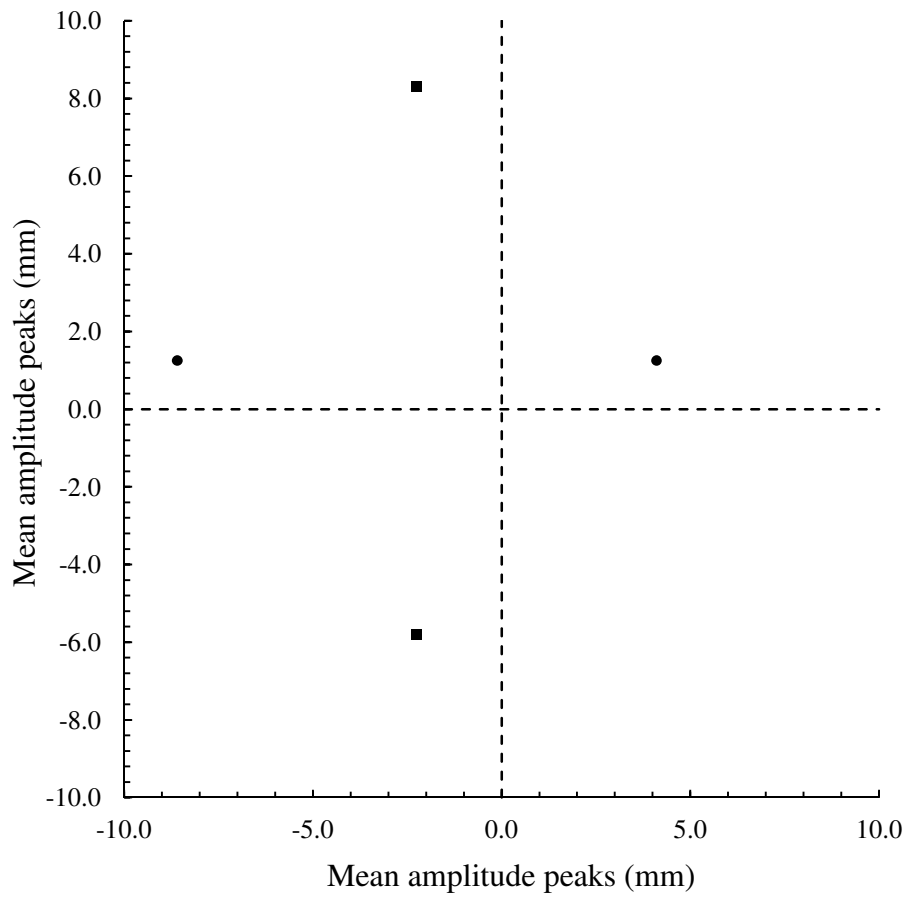


Fig. 2.32. Mean values of (positive and negative) amplitude peaks recorded by the two lasers at $u = 6.43$. • , MEL sensor; ■ , OptoNCDT 1400-200 sensor.

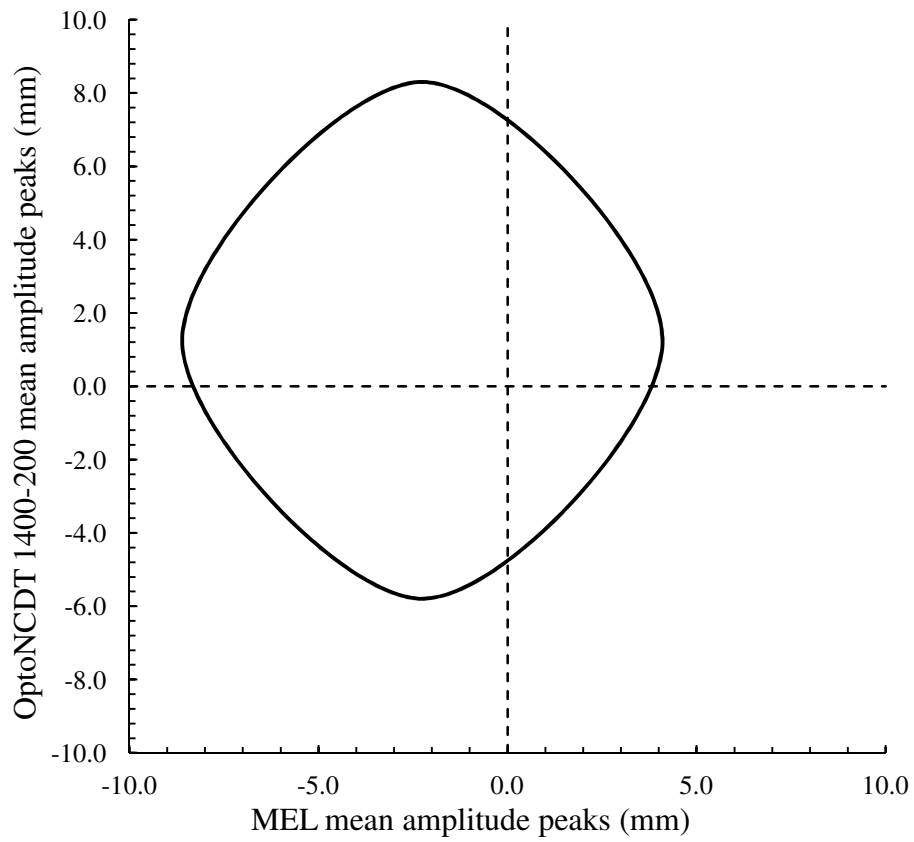


Fig. 2.33. Mean values of (positive and negative) amplitude peaks traced by the two lasers at $u = 6.43$.

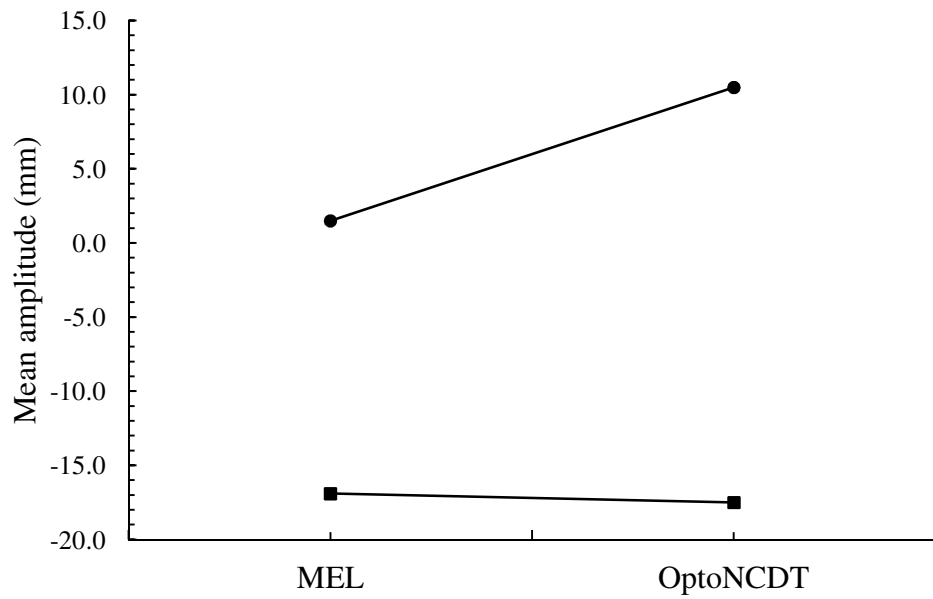


Fig. 2.34. Forward (upper bound) and backward (lower bound) motions of the cylinder about its mean position recorded by the two laser sensors at $u = 7.95$. \bullet , upper bound; \blacksquare , lower bound.

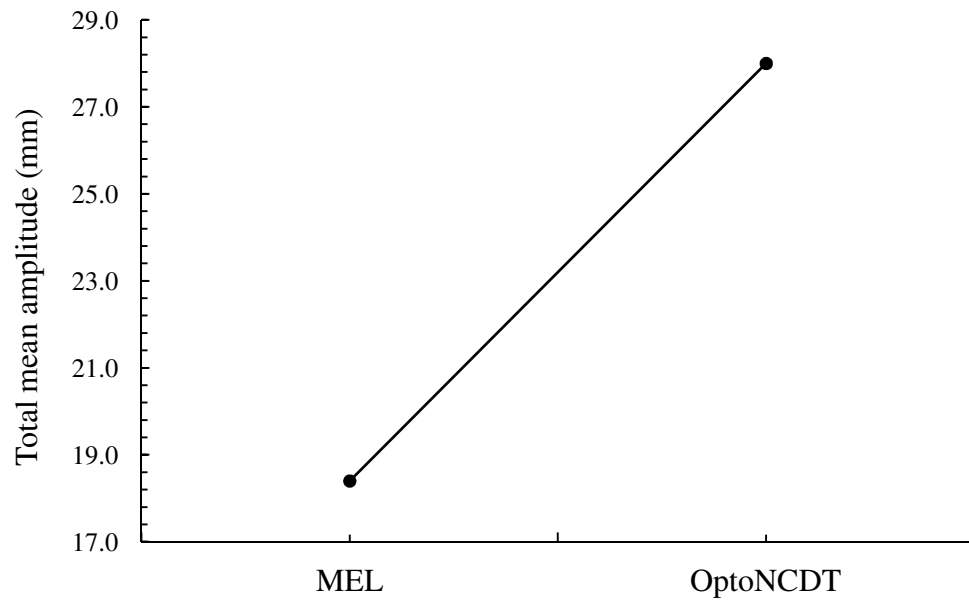


Fig. 2.35. Mean amplitudes recorded by the two lasers at $u = 7.95$.

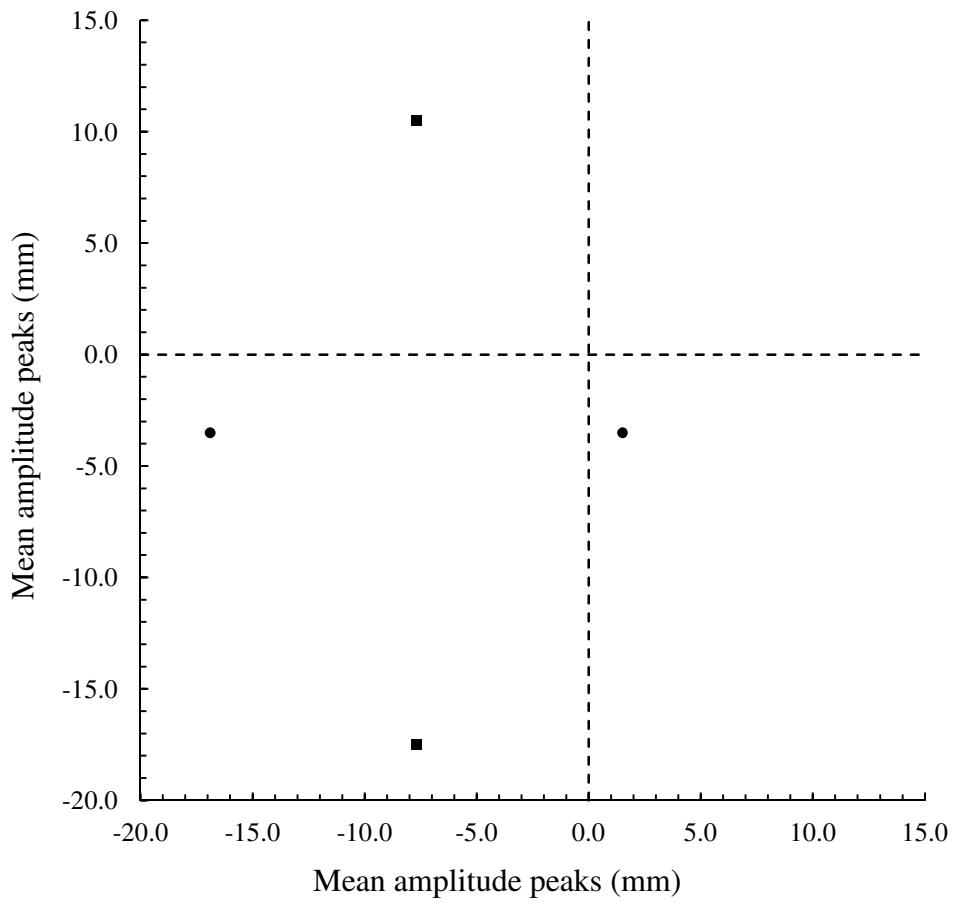


Fig. 2.36. Mean values of (positive and negative) amplitude peaks recorded by the two lasers at $u = 7.95$. • , MEL sensor; ■ , OptoNCDT 1400-200 sensor.

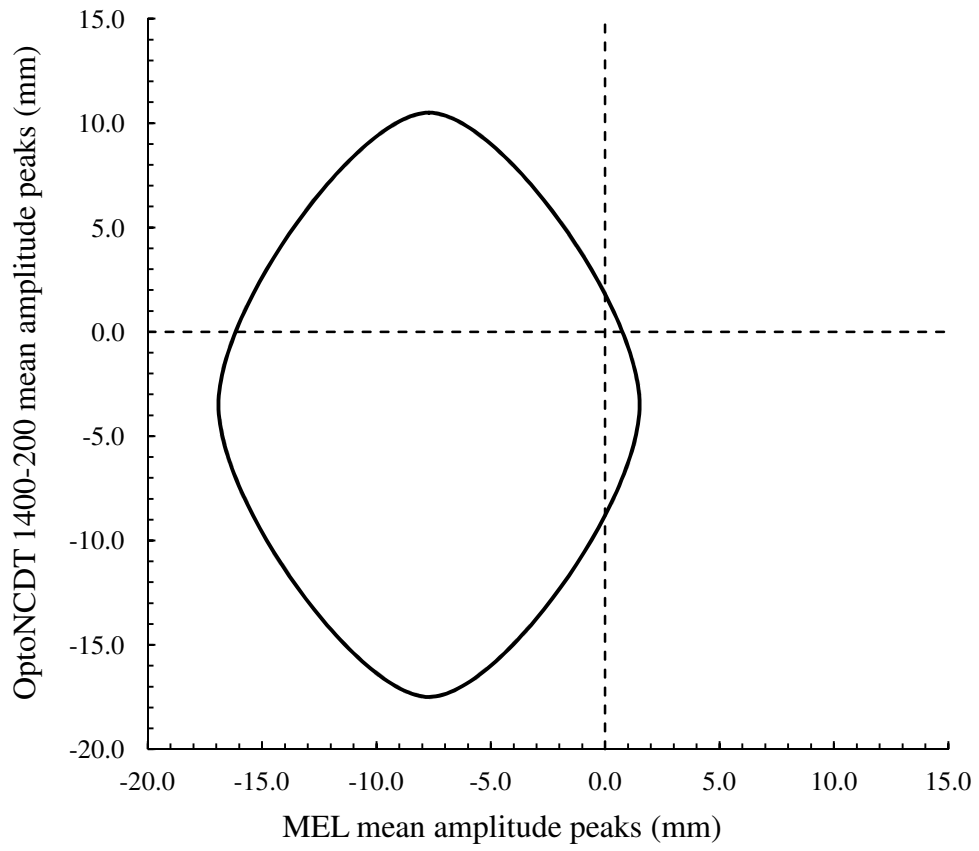


Fig. 2.37. Mean values of (positive and negative) amplitude peaks traced by the two lasers at $u = 7.95$.

Chapter 3

Linear Analysis

3.1. Introduction

In the previous theoretical studies on cylindrical system in axial flow with different lengths and support boundary conditions (Païdoussis 1966a, 1973; Païdoussis et al. 1980a; De Langre et al. 2007), the details of which are given in Chapter 1, they formulated the various fluid forces such as the inviscid forces, viscous forces, and hydrostatic or pressure forces acting on the cylinder. As a matter of fact, some of the viscous forces are semi-empirical and involve fluid force coefficients such as longitudinal and normal viscous coefficients, base drag coefficient, and zero-flow normal force coefficient. In most of the above cited work, they considered equal values for the longitudinal and normal viscous force coefficients, and considered the base drag coefficient varying linearly with the end-shape factor f . Hence there is need to re-evaluate these force coefficients based on the present problem and incorporate in the linear model. It is expected that the implementation of these calculated coefficients in the linear model will enable the model to better describe the dynamics of the system.

In addition to obtaining these force coefficients, this chapter also gives an account of the linear dynamics of a vertical cantilevered flexible cylinder in axial uniform water and air flows. In this connection, the effect of confinement on the dynamics of the cylindrical system, both in water and air flows, is also presented. The effect of confinement on the system with the calculated force coefficients is then presented. The present model results with the previously reported force coefficients are then compared with those by Païdoussis (1973) in order to establish the adequacy of the present solution method. In addition, the present results with previously used and presently calculated force coefficients are also compared together to see how these coefficients affect the overall dynamics of the system. Finally, the model results for water and air flows are compared together to understand the dynamics of the system in different flow media.

3.2. Problem Description

The system under consideration consists of a flexible cylindrical body of radius R , uniform circular cross-sectional area A , length L , flexural rigidity EI , and mass per unit length m , and centrally located in a rigid channel of radius R_{ch} as shown in Fig. 3.1 (a). The rigid channel contains an incompressible fluid of density ρ flowing with uniform flow velocity U parallel to the axis of the cylinder. The undeformed cylinder axis coincides with the x -axis, and since the system is vertical, the x -axis is along the same direction of gravitational force. The cylinder is considered to have cantilevered boundary conditions. The cylinder is generally fitted with an ogival end-piece at the downstream free end and considered to be short relative to the overall length of the cylinder as shown in Fig. 3.1 (b). Furthermore, the fluid is assumed to be contained by boundaries sufficiently distant from the cylinder to have negligible influence on its motion. The present problem of the dynamics of flexible cylinder in axial flow is a typical FSI problem. The basic assumptions made for the cylinder and for the fluid are that (a) the fluid is incompressible, (b) the mean fluid flow velocity is constant, (c) the cylinder is slender, so that Euler-Bernoulli beam theory remains applicable, (d) although the deflections of the cylinder may be large, strains are small, and (e) the cylinder centreline is inextensible (Païdoussis 2004).

3.3. Linear Equation of Motion

Let us consider small lateral motions of the cylinder about its equilibrium position at rest as shown in Fig. 3.1 (a). Various fluid forces act on the cylinder, the relations of which are determined as follows: the inviscid hydrodynamic force per unit length, F_A , is determined based on the theory developed by Lighthill (1960); the viscous forces in the normal and longitudinal direction, F_N and F_L , respectively, are determined based on Taylor's work (1952); the hydrostatic forces in the x - and y - direction, F_{px} and F_{py} , respectively, are determined by considering an element, δx , of the cylinder undergoing small oscillations, $y(x, t)$. The equation of motion of cylinder, given by Païdoussis (2004), can be written as

$$\begin{aligned}
& \left(E^* \frac{\partial}{\partial t} + E \right) I \frac{\partial^4 y}{\partial x^4} + \chi \rho A \left(\frac{\partial}{\partial t} + U \frac{\partial}{\partial x} \right)^2 y - \left\{ \begin{array}{l} \delta [\bar{T} + (1-2\nu)(\bar{p}A)] + \left[\frac{1}{2} \rho D U^2 C_T \left(1 + \frac{D}{D_h} \right) \right] \\ + (m - \rho A)g \end{array} \right\} \frac{\partial^2 y}{\partial x^2} \\
& \left[\left(1 - \frac{1}{2} \delta \right) L - x \right] + \frac{1}{2} \rho D^2 U^2 (1 - \delta) C_b \\
& + \frac{1}{2} \rho D U C_N \left(\frac{\partial y}{\partial t} + U \frac{\partial y}{\partial x} \right) + \frac{1}{2} \rho D C_D \frac{\partial y}{\partial t} + \left[(m - \rho A)g + \frac{1}{2} \rho D U^2 C_N \left(\frac{D}{D_h} \right) \right] \frac{\partial y}{\partial x} + m \frac{\partial^2 y}{\partial t^2} = 0, \quad (3.1)
\end{aligned}$$

where $\delta = 0$ indicates that the downstream end of the cylinder is free to slide axially, and $\delta = 1$ if the supports do not allow axial extension (Païdoussis 2004). In eq. (3.1), E is Young's Modulus, E^* is the corresponding viscoelastic constant, I is the second moment of area, \bar{T} is externally imposed uniform tension, ν is Poisson's ratio, \bar{p} is the mean value of pressure, p at $x = \frac{1}{2} L$, C_T and C_N are the tangential and normal friction coefficients, respectively, C_b is the base drag coefficient, C_D is form drag coefficient, and m is the mass of the cylinder per unit length. E^* is complex. The real part relates to the elastic behavior of the material and defines stiffness. The imaginary component relates to the material's viscous behaviour and defines the energy dissipation ability of the material. Mathematically, it can be defined as $E^* = E_1 + E_2 i = (\sigma_o / \varepsilon_o) e^{i\phi}$. The complete derivation of the linear equation of motion for a cylinder in axial flow may be found in Païdoussis (2004).

3.3.1. Boundary Conditions

A set of generalized boundary conditions for cylinders with supported ends is given by Païdoussis (2004) as

$$EI \frac{\partial^3 y}{\partial x^3} + k_o y = 0, \quad \text{at } x = 0 \quad (3.2a)$$

$$EI \frac{\partial^2 y}{\partial x^2} - c_o \frac{\partial y}{\partial x} = 0, \quad \text{at } x = 0 \quad (3.2b)$$

$$EI \frac{\partial^3 y}{\partial x^3} - k_L y = 0, \quad \text{at } x = L \quad (3.3a)$$

$$EI \frac{\partial^2 y}{\partial x^2} + c_L \frac{\partial y}{\partial x} = 0, \quad \text{at } x = L \quad (3.3b)$$

where, k_o and k_L are translational spring constants and c_o and c_L rotational ones, for $x = 0$ and $x = L$, respectively. From the above relations, the standard boundary conditions can be extracted accordingly as k_o, k_L, c_o, c_L are either zero or infinity.

In the case of a free downstream end, a more general boundary condition is considered to tackle cases of an ogival free end. The final form obtained is:

$$y = \frac{\partial y}{\partial x} = 0, \quad \text{at } x = 0 \quad (3.4)$$

$$\frac{\partial^2 y}{\partial x^2} = EI \frac{\partial^3 y}{\partial x^3} + fMU \left(\frac{\partial y}{\partial t} + U \frac{\partial y}{\partial x} \right) - (m + fM)x_e \frac{\partial^2 y}{\partial t^2} = 0 \quad \text{at } x = L, \quad (3.5)$$

where

$$x_e = \frac{1}{A} \int_{L-l}^L A(x) dx, \quad M = \chi \rho A; \quad (3.6)$$

f is the end-shape factor, which determines the slenderness of the end shape. Its value approaches 1 for an ideally slender end and 0 for a perfectly blunt end. M is the added (virtual) mass of the fluid per unit length and m is the mass of the cylinder per unit length. χ is defined in Chapter 2. A complete derivation of this boundary condition is given by Païdoussis (2004).

3.4. Dimensionless Parameters

In order to render the linear partial differential equation (3.1) and the ogival end-piece boundary conditions (eq. (3.5)) dimensionless, the following relations are used:

$$\begin{aligned} \xi = \frac{x}{L}, \quad \eta = \frac{y}{L}, \quad \tau = \frac{t}{L^2} \left(\frac{EI}{m + \rho A} \right)^{1/2}, \quad \alpha = \left[\frac{I}{E(\rho A + m)} \right]^{1/2} \frac{E^*}{L^2}, \quad \beta = \frac{\rho A}{\rho A + m}, \quad \gamma = \frac{(m - \rho A)gL^3}{EI} \\ \Gamma = \frac{\bar{T}L^2}{EI}, \quad \varepsilon = \frac{L}{D}, \quad u = \left(\frac{\rho A}{EI} \right)^{1/2} UL, \quad \Pi = \frac{\bar{p}AL^2}{EI}, \quad h = \frac{D}{D_h}, \quad c_f = \frac{4}{\pi} C_f, \quad c_N = \frac{4}{\pi} C_N, \quad c_T = \frac{4}{\pi} C_T \\ c_b = \frac{4}{\pi} C_b, \quad c = \frac{4}{\pi} \left(\frac{\rho A}{EI} \right)^{1/2} LC_D, \quad \chi_e = \frac{x_e}{L}. \end{aligned} \quad (3.7)$$

The equation of motion and the boundary conditions for a cantilevered cylinder are thus

$$\left(\alpha \frac{\partial}{\partial \tau} + 1\right) \frac{\partial^4 \eta}{\partial \xi^4} + \left\{ \begin{array}{l} \chi u^2 - \delta[\Gamma + (1 - 2\nu)\Pi] - \left[\frac{1}{2} \varepsilon c_T u^2 (1 + h) + \gamma \right] \left[\left(1 - \frac{1}{2} \delta\right) - \xi \right] \\ - \frac{1}{2} (1 - \delta) c_b u^2 \end{array} \right\} \frac{\partial^2 \eta}{\partial \xi^2} \\ + 2\chi\beta^{1/2} u \frac{\partial^2 \eta}{\partial \xi \partial \tau} + \left[\frac{1}{2} \varepsilon c_N u^2 (1 + h) + \gamma \right] \frac{\partial \eta}{\partial \xi} + \left[\frac{1}{2} \varepsilon c_N \beta^{1/2} u + \frac{1}{2} \varepsilon c \beta^{1/2} \right] \frac{\partial \eta}{\partial \tau} + [1 + (\chi - 1)\beta] \frac{\partial^2 \eta}{\partial \tau^2} = 0, \quad (3.8)$$

$$\eta = \frac{\partial \eta}{\partial \xi} = 0 \quad \text{at } \xi = 0, \quad (3.9)$$

$$\frac{\partial^2 \eta}{\partial \xi^2} = \frac{\partial^3 \eta}{\partial \xi^3} + \chi f u^2 \frac{\partial \eta}{\partial \xi} + \chi f \beta^{1/2} u \frac{\partial \eta}{\partial \tau} - \{1 + (\chi f - 1)\beta\} \chi_c \frac{\partial^2 \eta}{\partial \tau^2} = 0 \quad \text{at } \xi = 1. \quad (3.10)$$

For $\chi = 1$ and $h = 0$, eq. (3.8) will transform into the equation governing the dynamics of the flexible solitary cylinder in unconfined flow.

3.5. Method of Solution

The dimensionless equation (eq. (3.8)) is the general equation for the cylinder in external axial flow. The corresponding boundary conditions for a cantilevered cylinder (eqs. (3.9) and (3.10)) are applied for the solution. First, the solution of the linear equation of motion governing the dynamics of the cantilevered cylinder in unconfined flow is obtained. Assuming a solution of the form $\eta(\xi, \tau) = \sum_{r=1}^{\infty} \phi_r(\xi) q_r(\tau)$, with $\phi_r(\xi)$ the eigenfunctions of a cantilevered cylinder, all boundary conditions are satisfied with the exception of eq. (3.10). This boundary condition is time- and flow velocity-dependent and renders the solution more complicated. For this, the so-called ‘extended Galerkin method’ is used. This method embeds the equation of motion (eq. (3.8)) and the free end boundary condition (eq. (3.10)) in a single equation, expressed as

$$F(\eta(\xi, \tau)) + \delta(\xi - 1)B(\eta(\xi, \tau)) = 0, \quad (3.11)$$

where $F(\eta)$ is the equation of motion, $B(\eta)$ is the boundary condition, and $\delta(\xi - 1)$ is Dirac’s delta function. Applying the procedure leads to the following general form of the second order ordinary differential equation

$$[M]\{\ddot{q}\} + [C]\{\dot{q}\} + [K]\{q\} = 0, \quad (3.12)$$

where $\{q\}$ is the vector of generalized coordinates, and $\{\dot{q}\}$ and $\{\ddot{q}\}$ its time derivatives (Païdoussis 2004). The elements of the mass matrix $[M]$, damping matrix $[C]$, and stiffness matrix $[K]$ are

$$[M] = [1 + (\chi - 1)\beta]\delta_{rj} + \chi_e \{1 + (\chi^f - 1)\beta\}\phi_r(1)\phi_j(1), \quad (3.13)$$

$$[C] = \left(\alpha\lambda_r^4 + \frac{1}{2}\varepsilon c_N \beta^{1/2} u + \frac{1}{2}\varepsilon c \beta^{1/2} \right) \delta_{rj} + 2\chi\beta^{1/2} u b_{rj} - \chi^f \beta^{1/2} u \phi_r(1)\phi_j(1), \text{ and} \quad (3.14)$$

$$[K] = \lambda_r^4 \delta_{rj} + \left[\chi u^2 - \delta \{ \Gamma + (1 - 2\nu)\Pi \} - \left(\frac{1}{2}\varepsilon c_T (1 + h) u^2 + \gamma \right) \left(1 - \frac{1}{2}\delta \right) - \frac{1}{2}(1 - \delta) c_b u^2 \right] c_{rj} \\ + \left(\frac{1}{2}\varepsilon c_T (1 + h) u^2 + \gamma \right) d_{rj} + \left(\frac{1}{2}\varepsilon c_N u^2 (1 + h) + \gamma \right) b_{rj} - \chi^f u^2 \phi_r(1)\phi_j'(1), \quad (3.15)$$

respectively. Here,

$$b_{rj} = \int_0^1 \phi_r \phi_j' d\xi, \quad (3.16)$$

$$c_{rj} = \int_0^1 \phi_r \phi_j'' d\xi, \quad (3.17)$$

$$d_{rj} = \int_0^1 \xi \phi_r \phi_j'' d\xi, \quad (3.18)$$

$$\phi_r(1) = \cosh \lambda_r - \cos \lambda_r - \sigma_r (\sinh \lambda_r - \sin \lambda_r), \quad (3.19)$$

$$\phi_j(1) = \cosh \lambda_j - \cos \lambda_j - \sigma_j (\sinh \lambda_j - \sin \lambda_j), \quad (3.20)$$

$$\phi_j'(1) = \lambda_j [\sinh \lambda_j + \sin \lambda_j - \sigma_r (\cosh \lambda_j - \cos \lambda_j)], \quad (3.21)$$

$$\phi_j''(1) = \lambda_j^2 [\cosh \lambda_j + \cos \lambda_j - \sigma_r (\sinh \lambda_j + \sin \lambda_j)], \quad (3.22)$$

$$\sigma_r = \frac{\sinh \lambda_r - \sin \lambda_r}{\cosh \lambda_r + \cos \lambda_r}, \quad (3.23)$$

$$\sigma_j = \frac{\sinh \lambda_j - \sin \lambda_j}{\cosh \lambda_j + \cos \lambda_j}, \quad (3.24)$$

and

$$\delta_{rj} = \begin{cases} 1, & r = j \\ 0, & r \neq j \end{cases}. \quad (3.25)$$

Also $\lambda_r = \lambda_j$ are the eigenvalues of cylinder in r th or j th mode, r and j are the number of desired cylinder modes ranging from 1 to n_{max} , and n_{max} is the highest desired cylinder mode. The coefficients b_{rj} , c_{rj} , and d_{rj} depend on the boundary conditions and the method to evaluate them analytically. These are illustrated in Païdoussis (1998) as

$$b_{rj} = \begin{cases} \frac{4}{(\lambda_r/\lambda_j)^2 + (-1)^{r+j}}, & r \neq j \\ 2, & r = j \end{cases} \quad (3.26)$$

$$c_{rj} = \begin{cases} \frac{4(\lambda_j\sigma_j - \lambda_r\sigma_r)}{(-1)^{r+j} - (\lambda_r/\lambda_j)^2}, & r \neq j \\ \lambda_j\sigma_j(2 - \lambda_j\sigma_j), & r = j \end{cases} \quad (3.27)$$

$$d_{rj} = \begin{cases} \frac{4(\lambda_j\sigma_j - \lambda_r\sigma_r + 2)}{1 - (\lambda_r/\lambda_j)^4} (-1)^{r+j} - \frac{3 + (\lambda_r/\lambda_j)^4}{1 - (\lambda_r/\lambda_j)^4} b_{rj}, & r \neq j \\ \frac{1}{2} c_{jj}, & r = j \end{cases} \quad (3.28)$$

The model is then solved by converting the equation of motion (eq. (3.12)) into a set of first order ordinary differential equations and then eventually transforming the equation into matrix form. To solve this matrix equation, the following solution is considered:

$$Q = \bar{Q} e^{\lambda t}, \quad (3.29)$$

where \bar{Q} is a constant; it is eliminated during the simplification procedure, which ends up in the form of an eigenvalue problem, i.e., $(\lambda_r[I] - [S])\{Q\} = 0$. Here λ_r are the beam eigenvalues, $[I]$ is the unit matrix of order n , $\{Q\}$ is the eigenvector, and $[S]$ is the resultant matrix of the order of $2n \times 2n$

$$[S] = \begin{bmatrix} [0] & [I] \\ -[M][K] & -[M][C] \end{bmatrix}. \quad (3.30)$$

The eigenvalue problem is finally solved using MATLAB code for eigenfrequencies by considering the corresponding values of $[M]$, $[C]$, and $[K]$ for cantilevered cylinder. Six cylinder modes are considered in the Galerkin solution.

3.6. Model in Water Flow with Previously Used Force Coefficients

3.6.1. Adequacy of the Linear Solution

Adequacy of the linear solution is established by solving the linear equation especially for this purpose and comparing one of the linear solution results, for instance, critical flow velocity for the onset of first mode divergence, represented by $u_{cr,d1}$, with that obtained by Païdoussis (1973). The solution of the linear equation yields $u_{cr,d1} = 2.042$. The value of $u_{cr,d1}$ obtained by Païdoussis (1973) is 2.04. The difference is 0.1%, which shows a very good agreement. Complete comparison is presented in Section 3.12.

3.6.2. Analytical Results

In this section, the results obtained from the solution of linear equation of motion for cantilevered cylinder boundary conditions in water flow are presented. The fluid force coefficients and other dimensionless parameters used by Païdoussis (1973) are implemented in the present model. These are $\beta = 0.5$, $\varepsilon_{cN} = \varepsilon_{cT} = 1$, $f = 0.8$, $\chi = 1$, $\varepsilon = 20.276$, and $\delta = \alpha = \varepsilon c = c_b = \gamma = \Gamma = 0$. Figure 3.2 shows the Argand diagram, representing the dimensionless complex eigenfrequency, $\omega = \text{Re}(\omega) + i \text{Im}(\omega)$, of the cantilevered cylinder at dimensionless velocity, u ranging from 0 to 12 for the first three modes, obtained using $n = 6$. The y -axis represents the damping, i.e., $\text{Im}(\omega)$, whereas x -axis represents the dimensionless oscillation frequency, i.e., $\text{Re}(\omega)$. Cylinder motions caused by perturbation are damped at small u . At sufficiently high u , the cylinder first loses stability by divergence in its first mode, via a pitchfork bifurcation, at $u_{cr,d1} = 2.042$. The symbol cr represents the critical value for the onset of instability, d stands for static divergence and 1 represents the first mode shape. The system then re-stabilizes at $u_{r1} = 4.965$, and then loses stability by second mode flutter, via a Hopf bifurcation, at $u_{cr,f12} = 5.173$ with a corresponding dimensionless frequency, $\text{Re}(\omega_{cr,f12})$ of 10.47, since the first-mode locus

enters the unstable region at this critical flow velocity while $\text{Re}(\omega)$ (the real part of the complex eigenfrequency) remains positive. It then re-stabilizes at $u_{r2} = 8.677$, but, before that, it loses stability again via Hopf bifurcation at $u_{cr,fl3} = 8.311$ in the third mode by flutter. $\text{Re}(\omega_{cr,fl3})$ at this critical velocity is 32.46. It is worth reiterate that divergence is a static instability with no frequency whereas flutter is a dynamic instability with finite frequency.

Figures 3.3 and 3.4 show the dimensionless oscillation frequency, i.e., the real part of the complex eigenfrequency, and damping, i.e., the imaginary part of the complex eigenfrequency, respectively, for the first three cylinder modes as function of the dimensionless flow velocity u for a cantilevered cylinder. For the values of u in the range $0 \leq u \leq u_{cr,d1}$, the real part of eigenfrequency continues to decrease until, at a certain flow velocity, the eigenfrequency becomes purely imaginary, i.e., $\text{Re}(\omega)$ becomes zero. As u continues to increase, $\text{Im}(\omega)$ becomes negative and this is the critical value of u , i.e., $u_{cr,d1}$ at which the system loses its stability by divergence in its first mode. At an even higher velocity, i.e., $u_{cr,d1} \leq u \leq u_{cr,fl3}$, the system undergoes second and third mode flutter with non-zero values of $\text{Re}(\omega_{cr,fl})$, as shown in Figs. 3.3 and 3.4.

3.7. Model in Air Flow

3.7.1. Analytical Results

In this section, the results obtained from the solution of linear equation of motion for a cantilevered cylinder in air flow are presented. The generation and inclusion of the model subjected to axial air flow in this chapter is motivated as a limiting case by the motion of a long train with the last carriage having a tapered end inside a tunnel. The motion of the train in stationary air inside the tunnel produces the same effects of fluid forces on the train as for a stationary train subjected to axial air flow inside the tunnel. Cantilevered cylinder model is considered in air flow since this model is also going to be developed and simulated in other modeling software and then compared with the analytical results presented in this section. In order to make the code run for air flow, the value of mass ratio, β is the parameter to modify. It is dimensionless number and is defined as

$$\beta = \frac{\rho A}{\rho A + m}, \quad (3.31)$$

as given in Païdoussis (2004). Its value for air is 1.074×10^{-3} . Other input parameters are kept the same as for the cantilevered cylinder model in water flow. Figure 3.5 shows the Argand diagram, representing the dimensionless complex eigenfrequency, $\omega = \text{Re}(\omega) + i \text{Im}(\omega)$, of the cantilevered cylinder as a function of the dimensionless velocity, u , ranging from 0 to 12 for the first three modes in air flow. Cylinder motions are damped at low flow velocities. At sufficiently high flow velocity, the complex eigenfrequency of the first mode becomes purely imaginary, bifurcating on the $\text{Im}(\omega)$ -axis with $\text{Re}(\omega) = 0$. At $u_{cr,d1} = 2.042$, one of its branches becomes negative leading to the onset of divergence in first mode via a pitchfork bifurcation. As the flow velocity increases, the system losses stability in the second mode via a Hopf bifurcation at $u_{cr,fl2} = 3.470$ with dimensionless frequency, $\text{Re}(\omega_{cr,fl2}) = 13.57$. It is seen in the figure that with increasing flow velocity, the second mode in the unstable region bifurcates on the $\text{Im}(\omega)$ -axis at $u_{cr,d2} = 4.965$ marking divergence in the second mode. Later, the cylinder develops divergence in the third mode at $u_{cr,d3} = 9.541$. In the present model, $u = 4.965$ is marked as the beginning of the second zone of divergence.

A similar trend of the re-occurrence of divergence at high flow velocities for very small β was indicated by Semler et al. (2002). They solved the linear equation of motion with cantilevered boundary conditions for $0 < \beta < 1$. They observed that for $\beta < 0.38$, the system never re-stabilizes after divergence, but goes to second and higher mode flutter. On the basis of their results, they established a value of $u = 9.6$ representing the second zone of divergence. The difference between the flow velocity commencing the second zone of divergence in the present model ($u = 4.965$) and the one ($u = 9.6$) established by Semler et al. (2002) is due to different values of $\varepsilon_{cN}(0.5)$, $\varepsilon_{cT}(0.5)$, and $c_b(0.3)$ used by them, as compared to those used in the present model ($\varepsilon_{cN} = 1$, $\varepsilon_{cN} = 1$, and $c_b = 0$). Figures 3.6 and 3.7 show the dimensionless oscillation frequency and damping for the first three cylinder modes as function of the dimensionless flow velocity u for the cantilevered cylinder in air flow.

3.8. Effect of Confinement

3.8.1. Model in Water Flow

The effect of confinement on the critical value of u for the onset of divergence and flutter of cylinder in water flow is considered. It is recalled that the confinement factor is

$$\chi = \left(\frac{D_{ch}^2 + D^2}{D_{ch}^2 - D^2} \right). \quad (3.32)$$

Using eq. (3.32), values of χ are varied from 1.01 to 2.00. These values are obtained by keeping the cylinder diameter, D , fixed while reducing the channel diameter. Another useful parameter associated with confinement is α , the ratio of channel to cylinder diameters,

$$\alpha = \frac{D_{ch}}{D}. \quad (3.33)$$

Table 3.1 shows the values of α corresponding to those of χ . Higher values of α signify low confinement and vice versa. The critical values of the flow velocity for the onset of divergence and flutter vary with confinement, as shown in Figs. 3.8 - 3.10. With increasing confinement, viscous effects become more pronounced and the streamwise pressure drop acquires considerable value. This results in the divergence of the cylinder occurring earlier at lower velocity, as shown in Fig. 3.8. A similar trend is observed in second and third mode flutter instabilities as shown in Figs 3.9 and 3.10, respectively.

3.8.2. Model in Air Flow

Next, the effect of confinement on the critical value of u for the onset of divergence and flutter of cylinder in air flow is analyzed. Similar to the case for water flow, values of confinement factor, χ , are varied from 1.01 to 2.00. The results of the critical values of flow velocity for the onset of divergence and flutter varying with confinement are shown in Figs. 3.11 and 3.12, respectively. The general trend in both the figures show the occurrences of first mode divergence and second mode flutter at decreasing critical flow velocities with increasing confinement. This can be attributed to viscous effects and the stream-wise pressure drop becoming more pronounced with increasing confinement.

3.9. Force Coefficients

Equation (3.8) governs the dynamics of the flexible cylindrical system. Force coefficients in the equation, i.e., the longitudinal viscous coefficient, c_T , normal viscous coefficient, c_N , base drag coefficient, c_b , and zero-flow normal coefficient, c play vital role in the energy transfer and hence the system dynamics. Therefore, determining these force coefficients is imperative. These

are expected to be more precisely representing the fluid forces affecting the cylindrical system dynamics. Hence, these force coefficients, once calculated, are going to be used in the linear model instead of the previously used ones by Païdoussis (1973). This section provides a step-by-step procedure to calculate these coefficients for a given fluid and model geometry, and discusses the factors affecting these coefficients.

3.9.1. Longitudinal Viscous Coefficient, c_T

Viscous forces acting on slender inclined cylinders are discussed by Taylor (1952) in relation to the swimming of long narrow animals such as snakes, eels, and marine worms. He idealized the motion of these animals in water producing propulsion by considering the equilibrium of slender flexible cylinders having bending waves traveling down the cylinder at constant amplitude and speed in water. He formulated specifically the viscous fluid forces in transverse (N) and longitudinal (L) directions acting on the flexible smooth and rough cylinders inclined at certain angles to the flow direction. As limiting cases of a rough cylinder, he presented the expressions of transverse and longitudinal viscous forces for string like cylinders and cylinders with thin disks or plates set at right angles to the cylinder axis. He symbolized the force coefficients associated to the form and friction drag by $[C_D]_p$ and C_f , respectively.

In case of cylinder surface roughness, Taylor noticed that the boundary layer does not remain laminar and that the viscous forces rely on the nature of surface roughness (Païdoussis 2004). He proposed the longitudinal viscous force per unit length, F_L as

$$F_L = \frac{1}{2} \rho D U^2 C_f \cos i, \quad (3.34)$$

where D is the cylinder diameter, C_f is the coefficient associated with friction drag for a cylinder in cross-flow, defining i as

$$i = \tan^{-1}(\partial y / \partial x) + \tan^{-1}[(\partial y / \partial t) / U]. \quad (3.35)$$

For small motions, eq. (3.34) may be linearized and, using eq. (3.35), the viscous force may be represented by

$$F_L = \frac{1}{2} \rho D U^2 C_T, \quad (3.36)$$

where for the sake of generality, C_T is adopted in place of C_f . For the present study, C_T can be determined for a system of known cylinder diameter, fluid, and inlet flow velocity by using the equation

$$C_T = \frac{2F_L}{\rho DU^2}. \quad (3.37)$$

It is known that C_T decreases with increasing length (Païdoussis 2004). The parameter C_T is modified and L is rendered dimensionless by using the relations (Païdoussis 2004)

$$c_T = \frac{4}{\pi} C_T, \quad (3.38)$$

and

$$\varepsilon = \frac{L}{D}. \quad (3.39)$$

In the past, some researchers have determined the value of C_T (Heorner 1965; Hannover 1977; Ni & Hansen 1978; Lee & Kennedy 1985; Dowling 1988; Sudarsan 1997) and some have established a range in which its value is likely to lie (Chen and Wambsganss 1972; Païdoussis 2004). These researchers used different relations for different flow regimes and different surface roughness. Païdoussis (2004) proposed ‘a reasonable range’ for c_T as $0.010 < c_T < 0.025$.

Now consider a rigid circular cylinder at zero angle of inclination inside a circular channel with the input parameters $\rho = 998.2 \text{ kg/m}^3$, $D = 0.0254 \text{ m}$, and $U = 0.64 \text{ m/s}$ as shown in Fig. 3.13. The inlet flow velocity is rendered dimensionless by using the expression (eq. (3.7)) mentioned in Section 3.4, which yields $u = 1.0$. The Reynolds number Re is 1.3×10^5 . The only parameter to be determined is F_L . For this, the model is developed and simulated using a specialized finite element modeling and simulation package called ADINA. The total number of elements in the numerical fluid domain is 74294.

After obtaining F_L from the model simulation in ADINA for given $\varepsilon = 20.5$, C_T is calculated from eq. (3.37). The dimensionless value c_T is determined from eq. (3.38). Based on the knowledge that c_T is inversely proportional to the length of the structure, the analysis has been extended to establish the trend of the values of c_T with increasing ε . Values of ε varying

from 10 to 60 have been considered. Figure 3.14 shows the values of c_T varying with ε . The decreasing trend of c_T with ε can be described by the following fourth order polynomial

$$c_T = -3 \times 10^{-7} \varepsilon^4 + 6 \times 10^{-6} \varepsilon^3 - 3 \times 10^{-5} \varepsilon^2 - 2 \times 10^{-4} \varepsilon + 0.0259. \quad (3.40)$$

Finally, the mean value of c_T is 0.0234. This value is within the range prescribed by Païdoussis (2004).

3.9.2. Normal Viscous Coefficient, c_N

The normal viscous force per unit length as proposed by Taylor (1952) is

$$F_N = \frac{1}{2} \rho D U^2 (C_f \sin i + C_{Dp} \sin^2 i), \quad (3.41)$$

where C_{Dp} is the coefficient associated with form drag. For small motions, $\sin i \ll 1$, eq. (3.41), using eq. (3.35), may be linearized into the form

$$F_N = \frac{1}{2} \rho D U C_N \left(\frac{\partial y}{\partial t} + U \frac{\partial y}{\partial x} \right) + \frac{1}{2} \rho D C_D \frac{\partial y}{\partial t}. \quad (3.42)$$

Here again, C_N has been adopted in place of C_f for the sake of generality. In order to solve eq. (3.42) for C_N , consider a rigid cylinder enclosed in a channel of finite length and diameter. Since the cylinder is rigid, i.e., the cylinder does not move, $\partial y / \partial t$ becomes zero and the resulting equation is

$$F_N = \frac{1}{2} \rho D U^2 C_N \frac{dy}{dx}. \quad (3.43)$$

Modification of eq. (3.43) for C_N yields

$$C_N = \frac{2F_N}{\rho D U^2 (dy/dx)}. \quad (3.44)$$

Modifying C_N through the expression given by Païdoussis (2004) yields

$$c_N = \frac{4}{\pi} C_N. \quad (3.45)$$

Despite the consensus of researchers' view that $c_N \neq c_T$ at least for solitary cylinders, some have considered $c_N = c_T$ for their research work (Païdoussis 1966a 1973; Triantafyllou and Chryssostomidis 1985). Different values and ranges of c_N are found in the literature (Ortloff and Ives 1969; Chen and Wambsganss 1972; Lee and Kennedy 1985; Dowling 1988). Païdoussis (2004) proposed a range of c_N well suited to the pertaining research cases, in general as $0.005 < c_N < 0.040$.

The known input parameters of the model are $\rho = 998.2 \text{ kg/m}^3$, $D = 0.0254 \text{ m}$, and $U = 0.64 \text{ m/s}$. The corresponding dimensionless inlet flow velocity u and Reynolds number Re are 1.0 and 1.3×10^5 , respectively. In order to find the normal viscous force per unit length F_N , the cylinder needs to be inclined at an angle θ to the longitudinal axis of the channel, since F_N does not exist at zero angle of inclination. By doing this, the transverse inviscid hydrodynamic force or lift force also comes into play and becomes a part of the normal component of the viscous force; hence its effect should be removed. This is done by subtracting the inviscid force from the viscous force,

$$F = \text{viscous force} - \text{inviscid force} . \quad (3.46)$$

The normal component of the resultant force F is the normal viscous force per unit length, $F_N = F \sin \theta$. The model is developed and simulated in ADINA to find F_N . The total number of element in the numerical fluid domain is 71279. The cylinder with different angles of inclination to the fluid flow $\theta = 5^\circ, 10^\circ, 15^\circ, 20^\circ$ and slenderness factors, $\varepsilon = 5, 10, 15, 20, 30, 40, 50$ are considered. The ratio dy/dx is the slope of the angle of inclination. The model with inclined cylinder is shown in Fig. 3.15. The mean value of F_N for each θ has been substituted into eq. (3.44) to obtain C_N . The final mean value of c_N is 0.0041. It is slightly lower than the minimum suggested value by Païdoussis (2004), but still within acceptable range as used by other researchers.

Figure 3.16 shows the variation of F_N with ε at different angles of inclination of the cylinder with respect to channel axis. It is obvious from the figure that, with increasing ε , F_N also increases depicting that normal viscous force per unit length is more pronounced for longer or wider cylinders. A similar trend is shown in Fig. 3.17, in which F_N has been plotted against θ at different values of ε . Increasing the angle of inclination of the structure enhances the contribution of the normal viscous force component per unit length, i.e., F_N in the overall viscous force.

Figure 3.18 shows the normal viscous force coefficient, c_N plotted against the angle of inclination, θ . Contrary to F_N , c_N decreases with θ . The reason is that with increasing θ , the differential climb of dy/dx is greater than that of F_N . The trend for the variation of c_N with θ is described by the third order polynomial

$$c_N = -2 \times 10^{-4} \theta^3 + 2.6 \times 10^{-3} \theta^2 - 9.2 \times 10^{-3} \theta + 1.36 \times 10^{-2}. \quad (3.47)$$

3.9.3. Base Drag Coefficient, c_b

Consider the case of a cylinder either free to slide axially or completely free at $x = L$. Recalling that the pA term arises from the pressure on the sides of the cylinder, and considering a slice of the cylinder at $x = L$, one obtains

$$T_L = -p_b A, \quad (3.48)$$

where p_b is the base pressure. Hence

$$(T + pA)_L = (p_L - p_b)A, \quad (3.49)$$

where p_L is the pressure at the sides of the cylinder. Since $p_b < p_L$ generally, this is referred to as base drag, which may be expressed as (Païdoussis 2004)

$$(T + pA)_L = \frac{1}{2} \rho D^2 U^2 C_b. \quad (3.50)$$

Equating eqs. (3.49) and (3.50) yields

$$(p_L - p_b)A = \frac{1}{2} \rho D^2 U^2 C_b. \quad (3.51)$$

From this equation, a relation for C_b can be derived as

$$C_b = \frac{2A(p_L - p_b)}{\rho D^2 U^2}. \quad (3.52)$$

The modified form of C_b in eq. (3.7) given by Païdoussis (2004) is

$$c_b = \frac{4}{\pi} C_b. \quad (3.53)$$

Many researchers have calculated the base drag coefficient c_b for various base- and forebody-shapes in the past (Hoerner 1965; Idel' chik 1966; Blevins 1984). Based on the formulation of Hoerner (1965), Païdoussis (2004) obtained $c_b = 0.21$ for a blunt end forebody and 1.17 for a hemispherical end with no forebody. Based on the past obtained values of c_b , Païdoussis (2004) suggested a reasonable range as $0.1 < c_b < 0.7$.

Consider eq. (3.52) with known input parameters $A = 5.0671 \times 10^{-4} \text{ m}^2$, $\rho = 998.2 \text{ kg/m}^3$, and $D = 0.0254 \text{ m}$. The parameters such as p_L and p_b are determined by developing a rigid cylinder model at zero angle of inclination in ADINA as shown in Fig. 3.19. The total number of elements in the numerical fluid domain is 73483. Although Fig. 3.19 is similar to Fig. 3.13 but included for the sake of the representation of the model to determine pressures independent of the previous sections. Simulations are performed for $U \text{ (m/s)} = 0.321, 0.640, 0.960, 1.280, 1.603$ and $\varepsilon = 5, 10, 15, 20, 30, 40, 50$. The corresponding dimensionless flow velocities u are 0.5, 1.0, 1.5, 2.0, 2.5 and Reynolds numbers Re are $6.5 \times 10^4, 1.3 \times 10^5, 1.9 \times 10^5, 2.6 \times 10^5, 3.2 \times 10^5$. The values of p_L and p_b for each U and ε are substituted in eq. (3.52) to obtain C_b . The corresponding modified values of c_b are obtained by substituting the values of C_b in eq. (3.53). Finally, the mean value of c_b obtained is 0.2024, which is well within the suggested range by Païdoussis (2004).

Figure 3.20 shows the base drag coefficient, c_b , plotted against ε for different values of dimensionless flow velocity u . The general trend shows that with growing ε at a certain flow velocity u , c_b decreases. The possible reason for this trend is that, due to boundary layer development along the length of the cylinder, the average pressure at the sides of the cylinder decreases for larger ε , causing the difference between p_L and p_b to decrease. The eventual result comes in the form of reduced c_b . Figure 3.21 shows c_b versus u at different values of ε . Increasing the flow velocity, u at certain ε causes the average pressure at the sides of the cylinder to increase and eventually leads to widening the gap between the value of p_L and p_b . This causes the value of c_b to increase. In Fig. 3.20, a peculiar peak in the value of c_b at $\varepsilon = 1.5$ is quite obvious. From the results, it is observed that the base pressure first starts decreasing with increasing ε . From $\varepsilon = 10$ to 15, a sudden drop in the value of p_b is observed. After that p_b starts increasing. $(p_L - p_b)$, which is a major parameter in the determination of c_b results in a higher

value at $\varepsilon = 1.5$ due that sudden drop. It might be a threshold value of ε after that the base pressure starts increasing. But still the exact reason is not clear. Figure 3.22 shows the plot of average c_b versus u depicting this increasing trend.

It is important to note that all the plots in Sections 3.9.1, 3.9.2, and 3.9.3 cannot have smooth lines as the calculations involve the results from the ADINA simulations, which can be considered as numerical experiments generating discrete values.

3.9.4. Zero-Flow Normal Coefficient, c

Recalling eq. (3.42), the second term stands for a linear mean contribution of the quadratic viscous forces at no fluid flow velocity. This term is retained, since all other viscous force terms disappear at $U = 0$ (Chen and Wambsganss 1972). Here, C_D is not dimensionless (Païdoussis 2004); it has the units of velocity. The final form of eq. (3.42) thus obtained is

$$F = \frac{1}{2} \rho D C_D \frac{\partial y}{\partial t}. \quad (3.54)$$

The drag coefficient for a long cylinder oscillating in quiescent viscous fluid has been discussed by Païdoussis (1998). The viscous force per unit length is found to be given by

$$F = -C_d \Omega \rho A \left(\frac{dz}{dt} \right), \quad (3.55)$$

where z is the displacement, Ω the radian frequency, ρ the fluid density, A the cylinder cross-sectional area, and C_d the drag coefficient. Comparing eqs. (3.54) and (3.55) gives the expression for C_D as

$$C_D = \left(\frac{\pi}{2} \right) D \Omega C_d. \quad (3.56)$$

In order to render C_D dimensionless, Païdoussis (2004) derived the following expression

$$c = \frac{4}{\pi} \left(\frac{\rho A}{EI} \right)^{1/2} L C_D. \quad (3.57)$$

Païdoussis (2004) considered two cases in order to establish reasonable range of c . He obtained a lower value of c equal to 0.008 by considering a cylinder made of metal and a higher value equal to 0.06 by considering an elastomer cylinder. Sinyavskii et al. (1980) derived the expression for C_d as

$$C_d = \frac{2\sqrt{2}}{\sqrt{Stk}} \frac{1 + \gamma_c^3}{(1 - \gamma_c^2)^2}, \quad (3.58)$$

where γ_c is the confinement parameter given by the expression

$$\gamma_c = \frac{R}{R_{ch}}, \quad (3.59)$$

where R and R_{ch} are the cylinder and channel radii, respectively. Consider the case with no confinement. In this case, $\gamma_c = 0$ and the resulting expression for C_d obtained is

$$C_d = \frac{2\sqrt{2}}{\sqrt{Stk}}. \quad (3.60)$$

This is the same expression derived by Batchelor (1967); Stk is Stokes number given by

$$Stk = \frac{\Omega R^2}{\nu_k}. \quad (3.61)$$

In order to calculate Ω , the expression given by Païdoussis (2004) is used, which is

$$\omega = \left(\frac{\rho A + m}{EI} \right)^{1/2} \Omega L^2, \quad (3.62)$$

where ω is the dimensionless complex frequency and m is the mass of cylinder per unit length. Re-ordering of eq. (3.62) gives

$$\Omega = \frac{\omega}{L^2} \left(\frac{EI}{\rho A + m} \right)^{1/2}. \quad (3.63)$$

In order to determine ω , a MATLAB code to solve the linear equation of motion for a cantilevered cylinder with system parameters $D = 0.0254$ m, $\rho = 998.2$ kg/m³, $E = 2.76 \times 10^6$ Pa, $I = 2.0432 \times 10^{-8}$ m⁴, $L = 0.52$ m, $\nu_k = 1.004 \times 10^{-6}$ m²/s, and $m = 0.5675$ kg/m are employed. These parameters match the experimental ones. The iterative solution starts by considering an initial guess for c equal to zero in the code. From the solution, ω at the critical value of cylinder second mode instability, i.e., flutter, is obtained; ω is the real part of the complex eigenfrequency. The value of ω is substituted in eq. (3.63) to obtain Ω , which is, in turn, put in eq. (3.61) to get St . Hereafter, eqs. (3.60), (3.56) and (3.57) are used in order to obtain the value of c . The obtained value of c is plugged in the MATLAB code to obtain new values of ω , Ω , Stk , C_d , C_D , and finally c . This procedure is repeated until a converged value of c is obtained. From the above mentioned procedure, the value of c thus obtained is 0.0510, which is within the range $0.008 \leq c \leq 0.060$, proposed by Païdoussis (2004).

3.10. Model in Water Flow with Presently Calculated Force Coefficients

3.10.1. Adequacy of the Linear Solution

Adequacy of the linear solution with the presently calculated force coefficients is established by solving the linear equation especially for this purpose and comparing the critical flow velocity for the onset of first mode divergence, $u_{cr,d1}$, with the experimental one. The solution of the linear equation yields $u_{cr,d1} = 1.904$. The measured critical flow velocity, $u_{cr,d1}$, in experiments is 1.87 (Chapter 2). The difference is 1.81%, which is in good agreement.

3.10.2. Analytical Results

The presently obtained force coefficients are substituted in the linear equation of motion for cantilevered flexible cylinder in water flow and solved using MATLAB code. The values of these force coefficients and other parameters are: $\beta = 0.5$, $\varepsilon_{CN} = 0.0852$, $\varepsilon_{CT} = 0.4857$, $f = 0.8$, $\chi = 1$, $\varepsilon c = 1.0571$, $c_b = 0.2024$, $\varepsilon = 20.7283$, $\gamma = 1.23$, and $\delta = \alpha = \Gamma = 0$. The results (Fig. 3.23) show that cylinder motions if caused by perturbation are damped at small u . As velocity is increased, the complex frequency becomes purely imaginary with zero frequency but remains positive, indicating that the cylinder displacement is damped. At sufficiently high u , however, the cylinder first loses stability by divergence in its first mode, via a pitchfork bifurcation, at $u_{cr,d1} = 1.904$.

The critical velocity $u_{cr,d1}$ is marked by the imaginary branch of the complex frequency becoming negative along the $\text{Im}(\omega)$ -axis at zero frequency. At higher flow velocity, the cylinder re-stabilizes in its first mode at $u_{r1} = 5.237$. Before u_1 is reached, the cylinder second mode in stable region bifurcates on $\text{Im}(\omega)$ -axis at $u_{2,0} = 4.921$. The dimensionless flow velocity $u_{2,0}$ signifies the velocity corresponding to zero frequency of the second mode-shape locus along positive $\text{Im}(\omega)$ -axis in the stable region. At slightly higher velocity, $u_{1,2} = 5.243$, the positive branches of the first and second mode loci coalesce and leave the axis at a point where $\text{Im}(\omega) > 0$, indicating the motions damped out. Soon after, at $u_{cr,fl1,2} = 5.278$, the imaginary branches of the couple mode loci become negative, i.e., $\text{Im}(\omega) < 0$, at a finite frequency, indicating the onset of coupled-mode flutter. The corresponding value of $\text{Re}(\omega_{cr,fl1,2})$ is equal to 3.92. The cylinder does not become unstable in the third mode, even at higher velocities as high as $u = 12$. Figures 3.24 and 3.25 show the frequency and damping plotted against the dimensionless velocity u .

3.11. Effect of Confinement

Next, the effect of confinement on the critical value of u for the onset of divergence and flutter of cantilevered cylinder in water flow is analyzed with the presently calculated force coefficients substituted in the model's MATLAB code. The results of the critical values of flow velocity for the onset of divergence and coupled-mode flutter varying with confinement are shown in Figs. 3.26 and 3.27, respectively for $1.01 \leq \chi \leq 2.00$. With increasing confinement, viscous effects become more pronounced and the stream wise pressure drop acquires considerable value. This results in the divergence and coupled-mode flutter of the cylinder occurring earlier with increasing flow velocity.

3.12. Comparison of the Results

The results using the previously used force coefficients (Païdoussis 1973) are compared with those of Païdoussis (1973). Païdoussis (1973) solved the equations of motion by considering a solution of the form

$$\eta(\xi, \tau) = Y(\xi)e^{i\omega\tau}. \quad (3.64)$$

For a cantilevered cylinder, he expanded $Y(\zeta)$ in terms of a power series in ζ . The procedure to solve the present model has already been described above. Table 3.2 shows the comparison of cantilevered cylinder results with those of Païdoussis (1973). Results are in good agreement.

Table 3.3 presents the comparison of cantilevered cylinder critical velocities and the corresponding dimensionless frequencies with previously used force coefficients by Païdoussis (1973) and presently calculated ones. With the presently calculated force coefficients, lower $u_{cr,d1}$ are obtained than with the previous force coefficients; also coupled-mode flutter is obtained instead of a single mode flutter. The reason can be understood by considering the effects of f and c_b on the dynamics of the cylinder. According to theory, decreasing f stabilizes the system for divergence, while increasing c_b destabilizes it. Since the model with the present force coefficients has same value of f (0.8) and a higher value of c_b (0.2024) than the one with previous coefficients ($c_b = 0.0$), the results suggest that the effect of c_b makes the cylinder statically unstable at lower $u_{cr,d1}$. For flutter, theory predicts that decreasing f and increasing c_b both have a stabilizing effect. This is exactly what is observed in the table with $u_{cr,fl,2}$ being higher for the model with present coefficients. Third mode flutter is not observed for the model with present force coefficients. Since the results show, in general, a higher critical flow velocity for flutter, this may lead to the occurrence of third mode flutter at a dimensionless flow velocity higher than $u = 12$, which is the maximum velocity used in the code. The results of the linear model for the cantilevered cylindrical system with the presently calculated force coefficients demonstrate similar dynamics as observed in the experiments, especially the coalesced first mode divergence and second mode flutter as the coupled-mode flutter (combination of the two modes leads to an asymmetric response also observed in Figs. 2.32 and 2.33 in Chapter 2). Hence, it can be stated that the linear model with the presently calculated force coefficients predicts the dynamics of the system better than the one with the previously used force coefficients.

Table 3.4 presents the comparison of critical velocities of cantilevered cylinder in water and air flows employing the previous force coefficients. Considering the models in water and air flows, it is seen that $u_{cr,d1}$ is the same for both models, which means that divergence is independent of β , as observed by Païdoussis (2004). However, a drop in $u_{cr,fl2}$ for the model in air flow can be seen. This is due to the inherent lower viscous damping of air. This also enables the cylinder in air flow to oscillate with higher frequency. In addition, the cylinder does not develop third mode flutter in air flow up to the maximum dimensionless flow velocity, i.e., $u = 12$, used

in the code. It may be inferred that the energy transfer from air to the cylinder is not sufficient enough to excite it in third mode.

3.13. Summary

In this chapter, after the general introduction of the problem under consideration, two-dimensional linear equations of motion, governing the cantilevered cylinder dynamics, in dimensional and dimensionless forms, and the methods of solution were presented followed by the solutions of the models in water flow using the MATLAB code. The mass ratio was then modified for the cantilevered cylinder case in air flow. Effects of confinement on the dynamics of cantilevered cylinder in water and air flows were then studied. Force coefficients present in the equation of motion were then recalculated based on the present geometrical and flow parameters matching the experimental ones, and with the presently calculated coefficients, the equations of motion were solved again for the cantilevered cylinder model using MATLAB code. Finally, the model results were compared with the ones available in the literature and with each other.

First, the general equation of motion with the boundary conditions for cantilevered cylinder was presented followed by its dimensionless form. In order to transform or simplify the two-dimensional fourth order linear Partial Differential Equations (PDE) into second order Ordinary Differential Equation (ODE), extended Galerkin method was used due to its time dependent free end boundary condition. The ODE was further simplified to a first order eigenvalue problem. It was then solved for a range of flow velocities using a MATLAB code and the respective results were presented. The present code for cantilevered cylinder was then run for air flow by modifying the mass ratio, β , and the results were presented. Results pertaining to the effects of confinement on the critical velocities for cantilevered cylinder in water and air flows were later presented.

Force coefficients such as longitudinal viscous coefficient, c_T , normal viscous coefficient, c_N , base drag coefficient, c_b , and zero-flow normal coefficient, c , were recalculated based on the present physical parameters matching the experiment conditions. After substituting the presently calculated coefficients in the MATLAB code, solution for the cantilevered cylinder in water flow was obtained. Similarly, the effect of confinement on the critical velocities for cantilevered cylinder was then presented.

Finally, three sets of comparison were done. The first set compared the critical flow velocities for cantilevered cylinder obtained in the present model by using the previously used force coefficients with the ones in the literature. The second set compared the critical flow velocities using the previous force coefficients with the ones obtained by using the present force coefficients. The third set compared the critical flow velocities for the cantilevered cylinder in water flow with the ones in air flow.

Table 3.1. Values of α at different values of χ .

χ	α
1.01	14.1774
1.10	4.5826
1.20	3.3166
1.30	2.7689
1.40	2.4495
1.50	2.2361
1.60	2.0817
1.70	1.9640
1.80	1.8708
1.90	1.7951
2.00	1.7321

Table 3.2. Dimensionless critical flow velocities, u_{cr} obtained from present runs and by Païdoussis (1973) for a cantilevered cylinder in water flow.

Models/critical velocities	First mode divergence,	First mode re-stabilization,	Second mode flutter,	Second mode re-stabilization,	Third mode flutter,
	$u_{cr,d1}$	u_{r1}	$u_{cr,fl2}$	u_{r2}	$u_{cr,fl3}$
Present model	2.042	4.965	5.173	8.677	8.311
Païdoussis	2.04	4.9	5.16	8.6	8.17
% difference	0.10	1.33	0.24	0.90	1.73

Table 3.3. Dimensionless critical flow velocities, u_{cr} of cantilevered cylinder with previously used and presently calculated force coefficients.

Model with	Critical velocity and frequency/Instability	First mode divergence,	Second mode flutter,	Third mode flutter,
		$u_{cr,d1}$	$u_{cr,fl2}$	$u_{cr,fl3}$
Previous force coefficients	u_{cr}	2.042	5.173	8.311
	ω	--	10.47	32.46
Present force coefficients	u_{cr}	1.904	5.278 (coupled-mode)	--
	ω	--	3.92	--

Table 3.4. Dimensionless critical flow velocities, u_{cr} of cantilevered cylinder in water and air flows.

Fluid	Critical velocity and frequency/Instability	First mode divergence,	Second mode flutter,	Third mode flutter,
		$u_{cr,d1}$	$u_{cr,fl2}$	$u_{cr,fl3}$
Water	u_{cr}	2.042	5.173	8.311
	ω	--	10.47	32.46
Air	u_{cr}	2.042	3.470	--
	ω	--	13.57	--

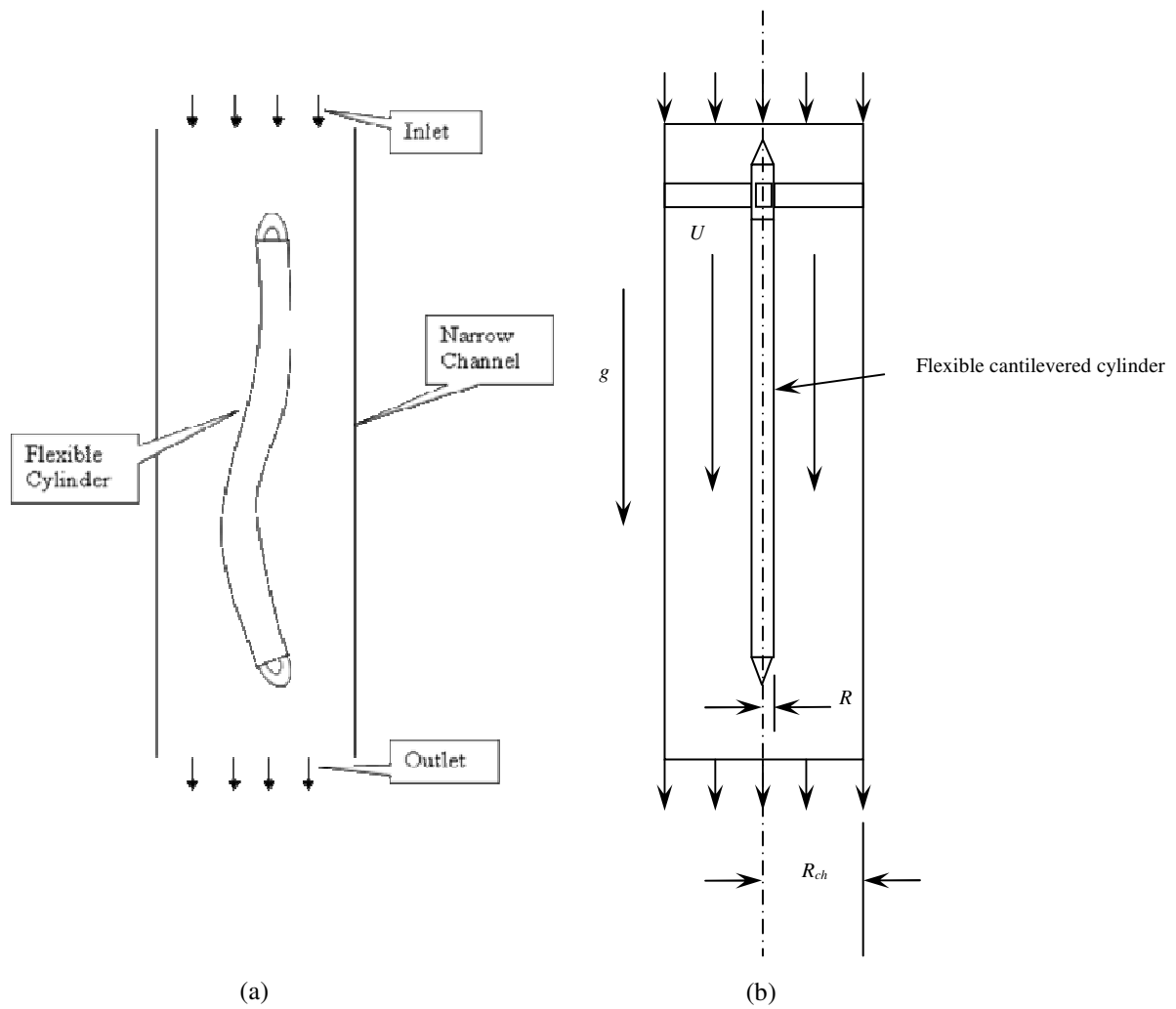


Fig. 3.1. (a) Schematic diagram of a flexible cylinder in a confined vertical axial flow (b) Diagrammatic view of a cantilevered cylinder in axial flow in the test-section of a circulating system.

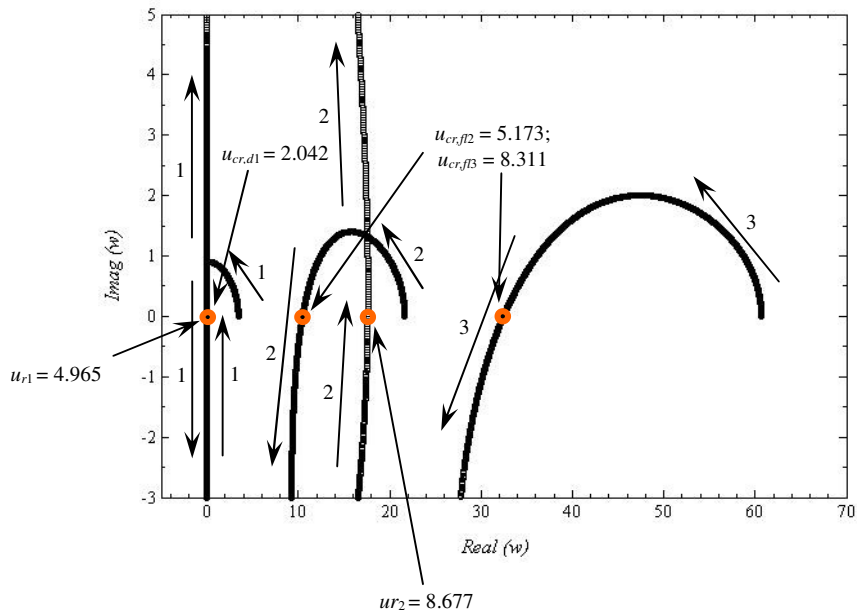


Fig. 3.2. Argand diagram of the dimensionless complex frequencies, ω of the lowest three modes of an isolated cantilevered cylinder with a tapered free end in unconfined axial water flow as function of u .

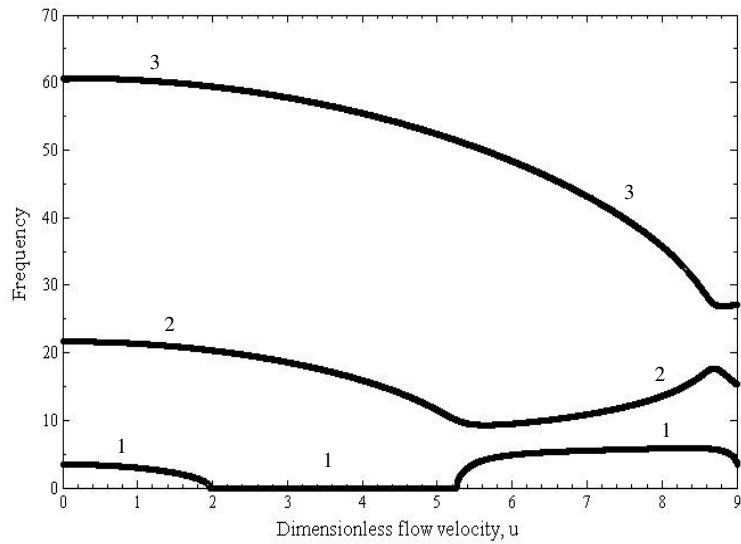


Fig. 3.3. Dimensionless oscillation frequency of the lowest three modes of an isolated cantilevered cylinder with a tapered free end in unconfined axial water flow as function of u .

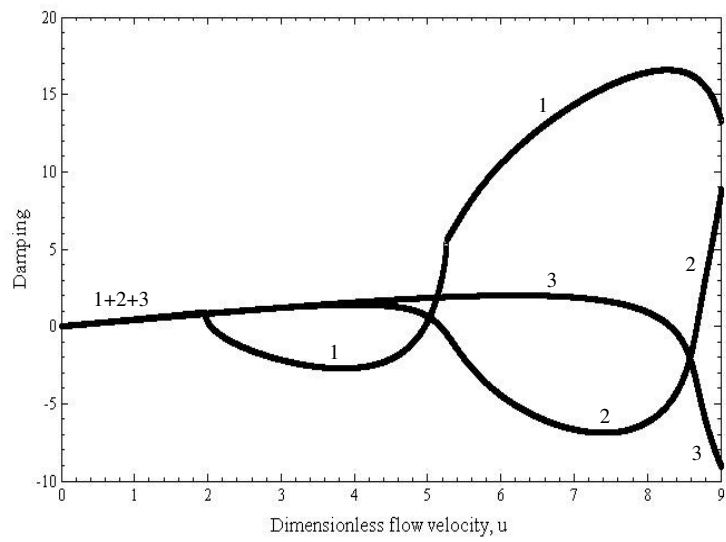


Fig. 3.4. Damping of the lowest three modes of an isolated cantilevered cylinder with a tapered free end in unconfined axial water flow as function of u .

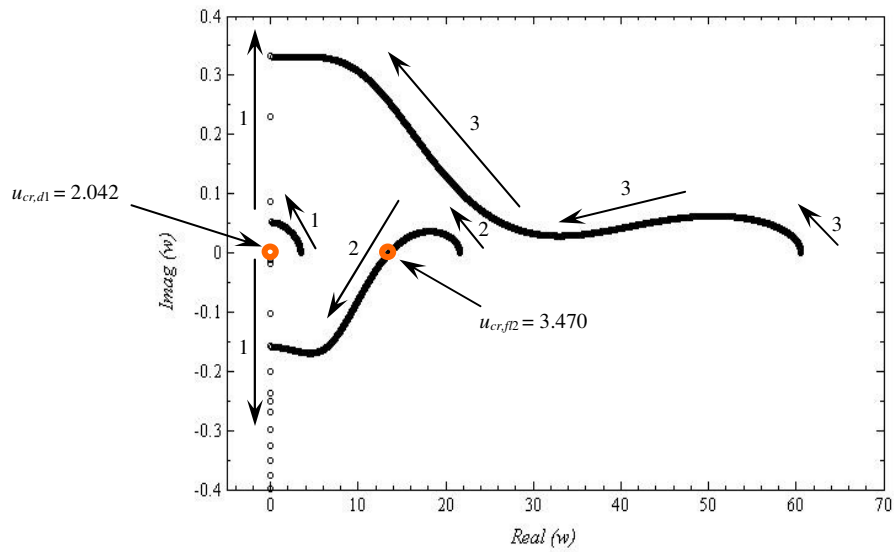


Fig. 3.5. Argand diagram of the dimensionless complex frequencies, ω of the lowest three modes of an isolated cantilevered cylinder with a tapered free end in unconfined axial air flow as function of u .

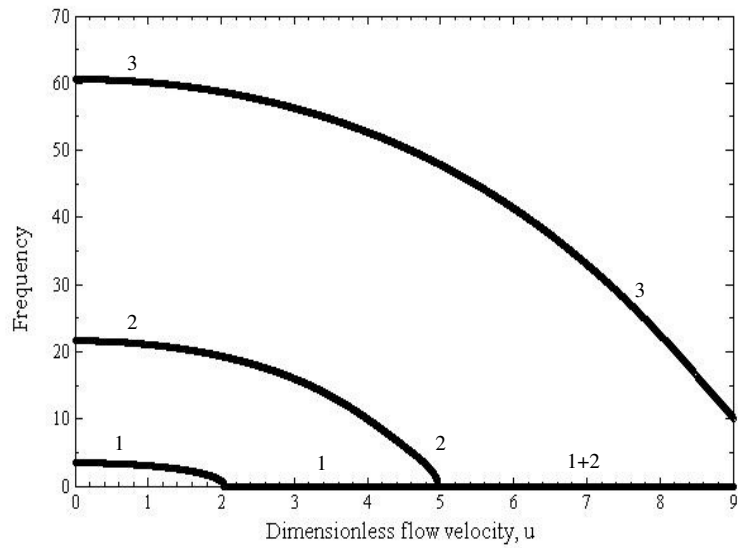


Fig. 3.6. Dimensionless oscillation frequency of the lowest three modes of an isolated cantilevered cylinder with a tapered free end in unconfined axial air flow as function of u .

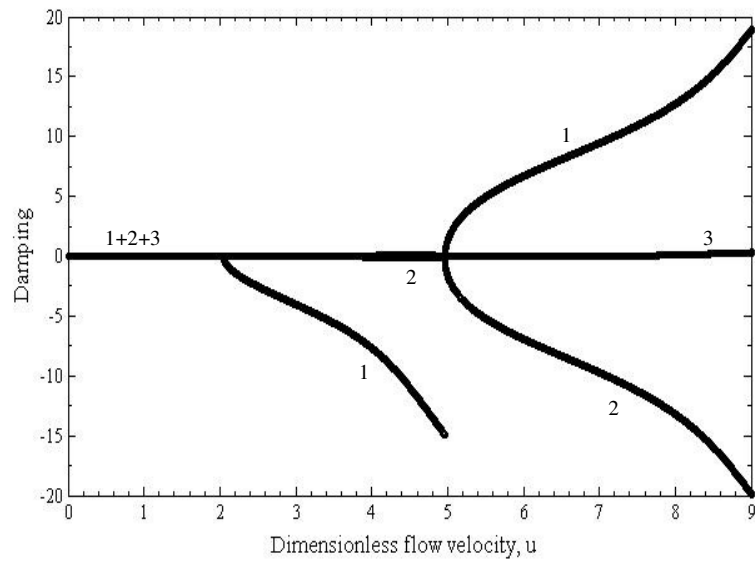


Fig. 3.7. Damping of the lowest three modes of an isolated cantilevered cylinder with a tapered free end in unconfined axial air flow as function of u .

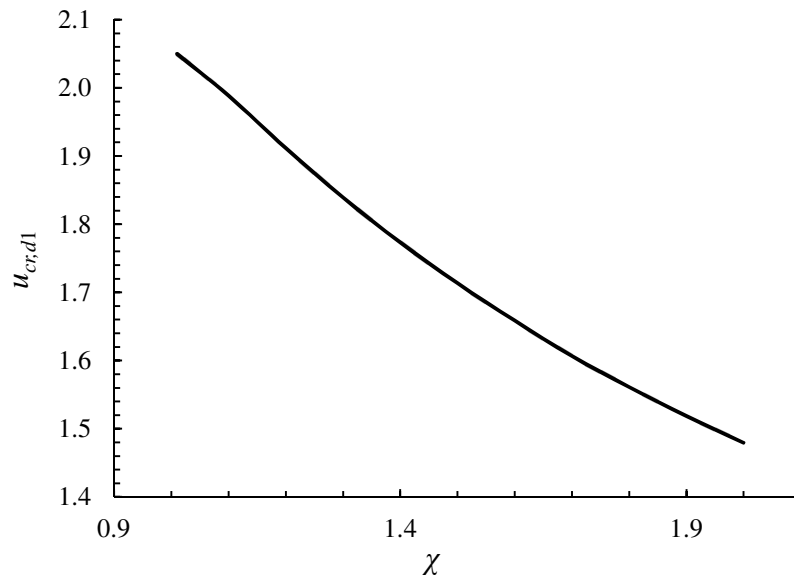


Fig. 3.8. Variation of critical flow velocity for divergence, $u_{cr,d1}$ with increasing confinement, χ , of model in water flow.

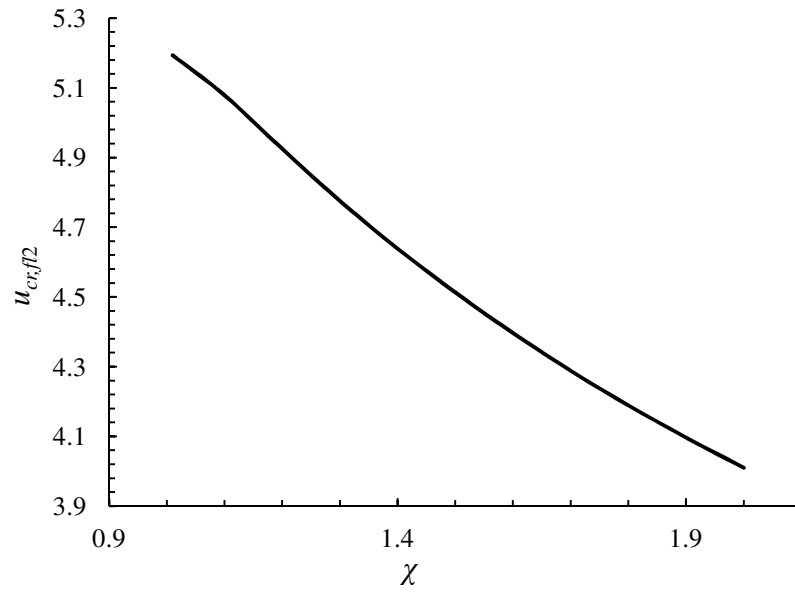


Fig. 3.9. Variation of critical flow velocity for flutter, $u_{cr,fl2}$ with increasing confinement, χ , of model in water flow.

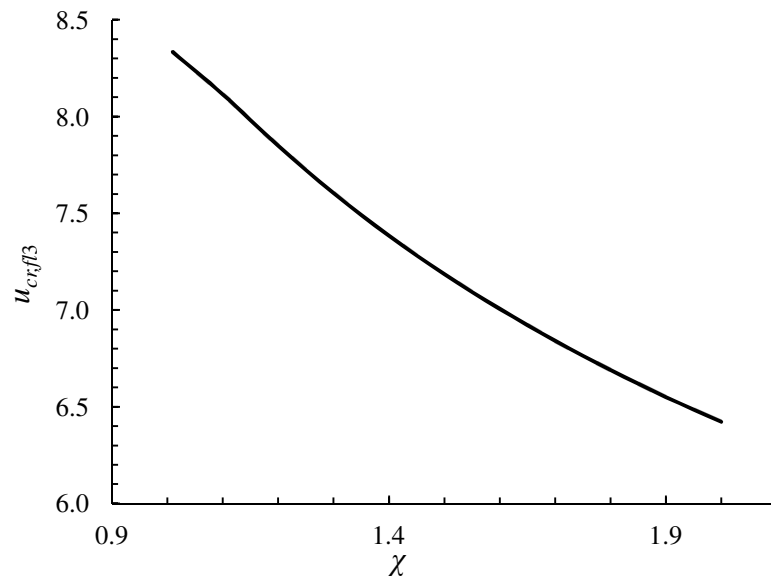


Fig. 3.10. Variation of critical flow velocity for flutter, $u_{cr,fl3}$ with increasing confinement, χ , of model in water flow.

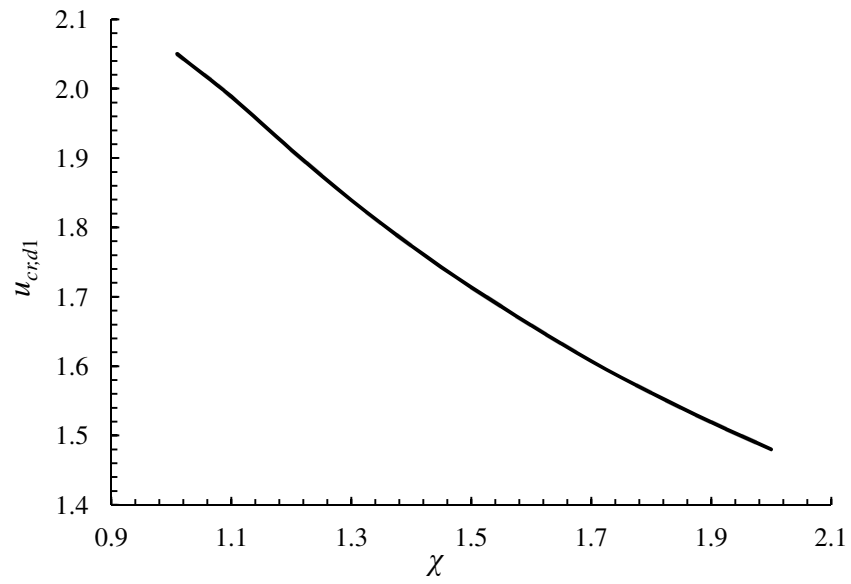


Fig. 3.11. Variation of critical flow velocity for divergence, $u_{cr,d1}$ with increasing confinement, χ , of model in air flow.

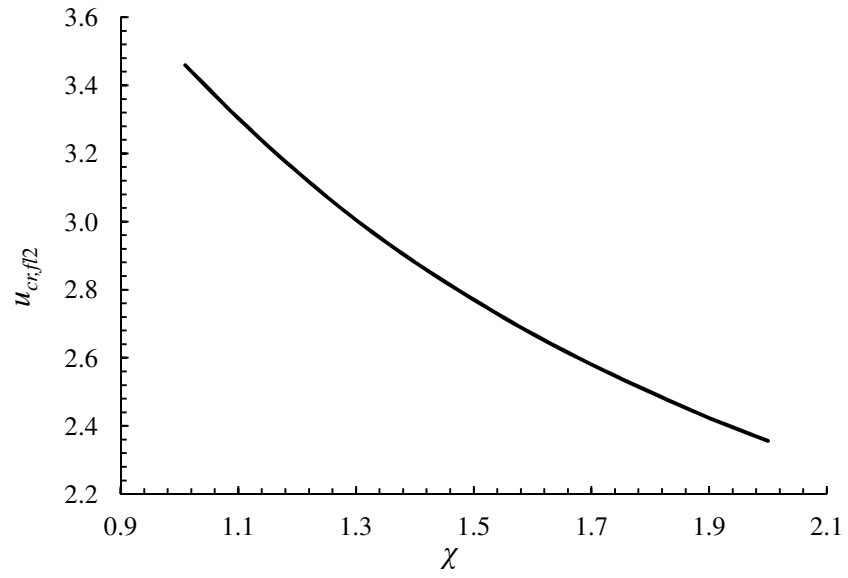


Fig. 3.12. Variation of critical flow velocity for flutter, $u_{cr,fl2}$ with increasing confinement, χ , of model in air flow.

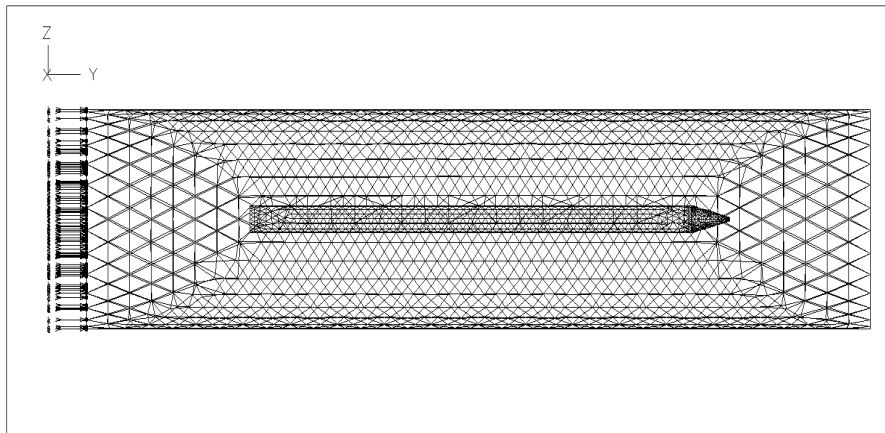


Fig. 3.13. Numerical mesh of the model to determine c_T .

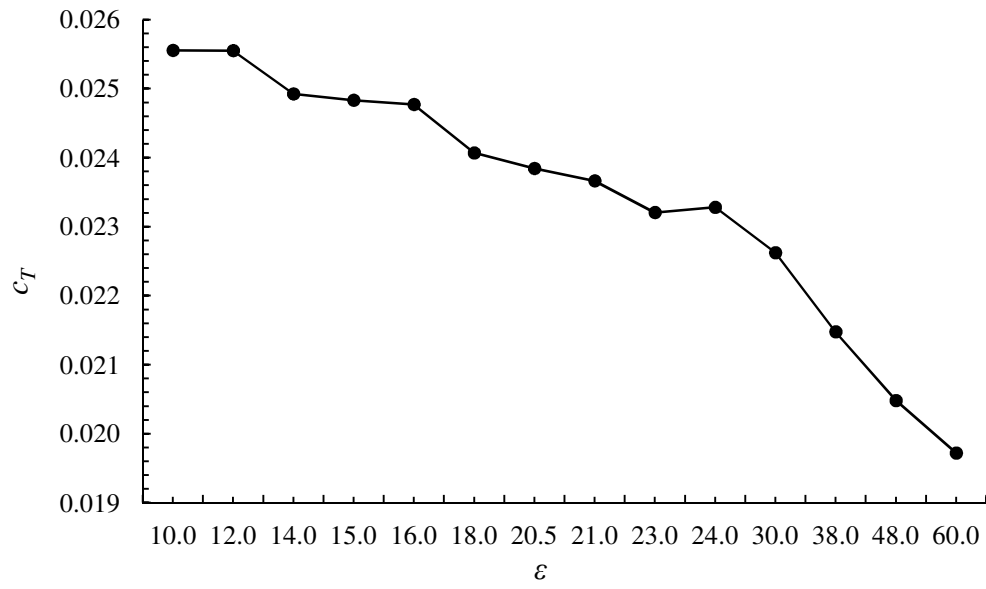


Fig. 3.14. Dimensionless longitudinal viscous coefficient, c_T as function of dimensionless length ε .

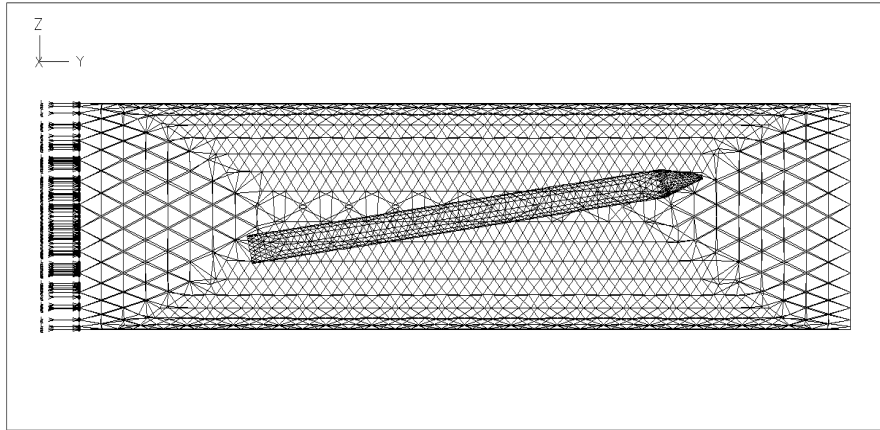


Fig. 3.15. Numerical mesh of the inclined cylinder model to determine c_N .

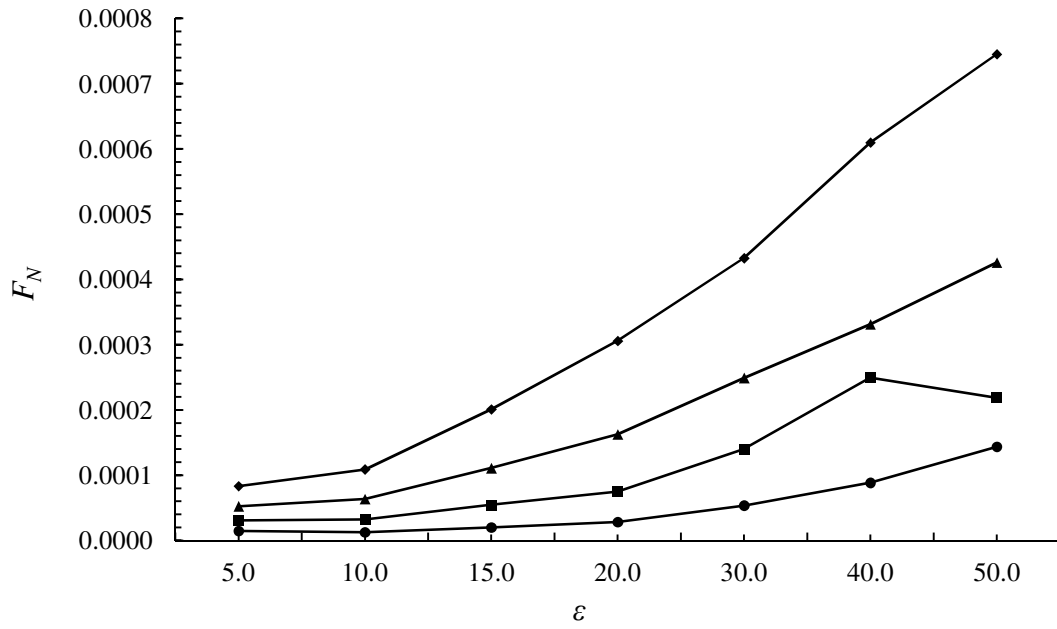


Fig. 3.16. Normal viscous force, F_N versus ε at different values of θ . \bullet , $\theta = 5^\circ$; \blacksquare , $\theta = 10^\circ$; \blacktriangle , $\theta = 15^\circ$; \blacklozenge , $\theta = 20^\circ$

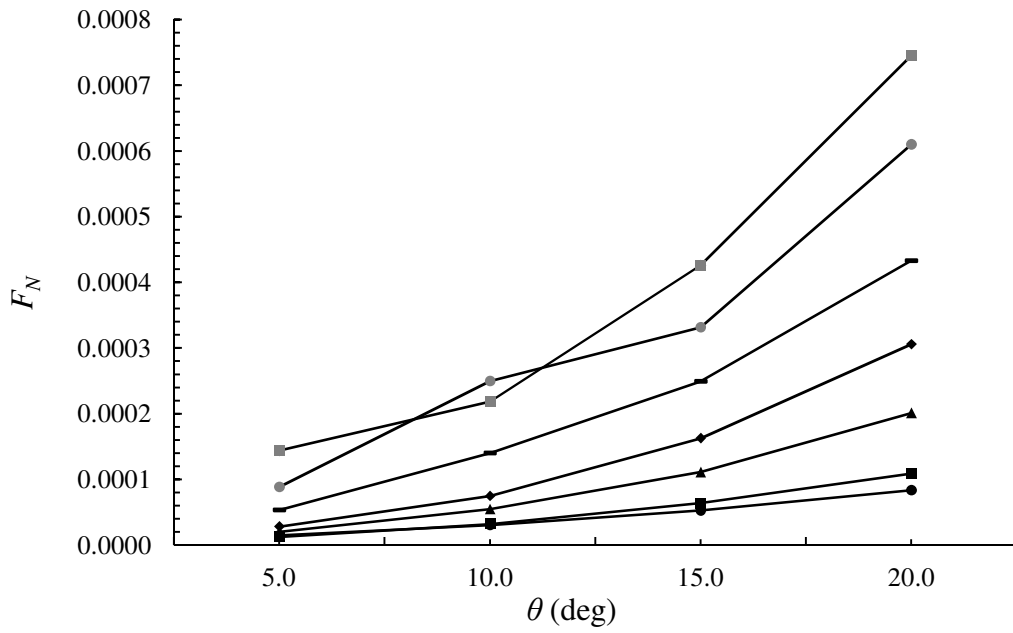


Fig. 3.17. Normal viscous force, F_N versus θ at different values of ϵ . \bullet , $\epsilon = 5$; \blacksquare , $\epsilon = 10$; \blacktriangle , $\epsilon = 15$; \blacklozenge , $\epsilon = 20$; $\bar{}$, $\epsilon = 30$; \bullet , $\epsilon = 40$; \blacksquare , $\epsilon = 50$.

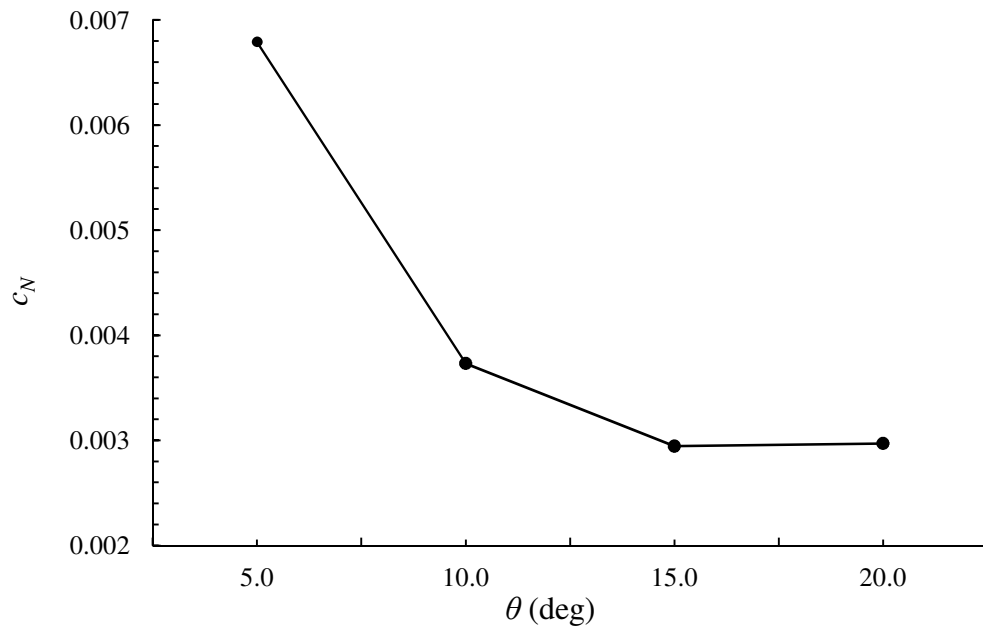


Fig. 3.18. Normal viscous coefficient, c_N as function of θ .

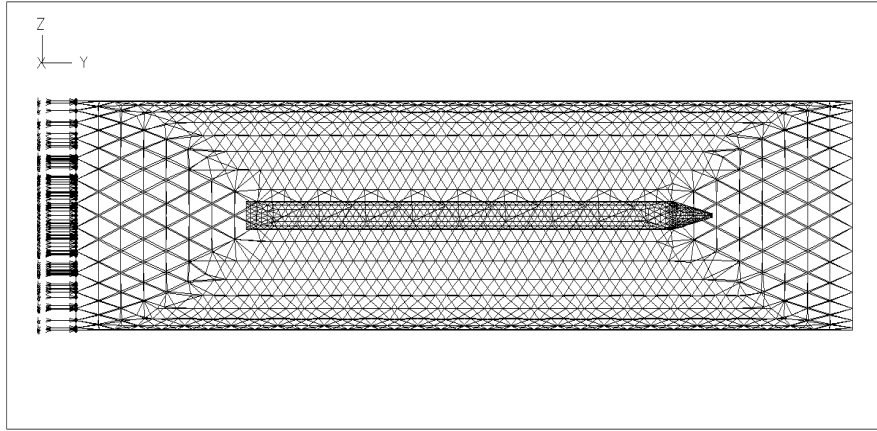


Fig. 3.19. Numerical mesh of the model to determine c_b .

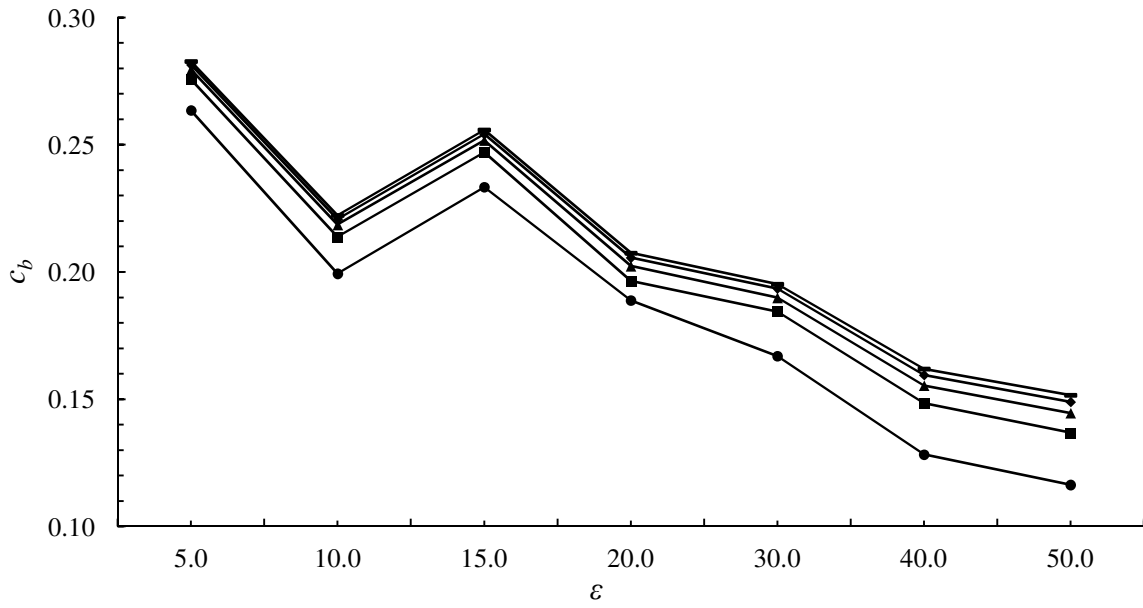


Fig. 3.20. Base drag coefficient, c_b versus ϵ at different values of u . \bullet , $u = 0.5$; \blacksquare , $u = 1.0$; \blacktriangle , $u = 1.5$; \blacklozenge , $u = 2.0$; \blacksquare , $u = 2.5$

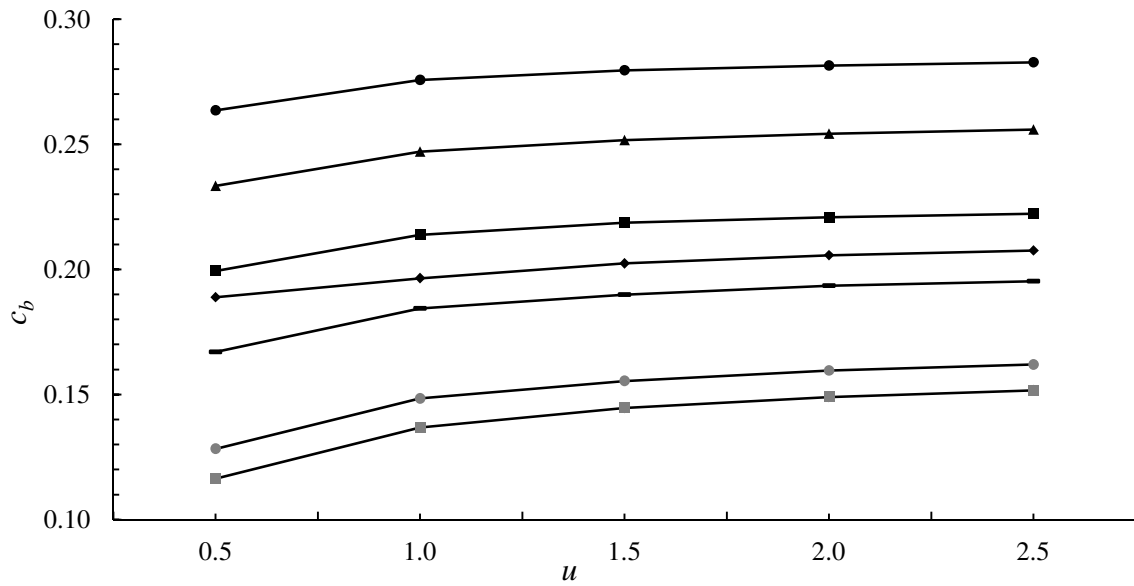


Fig. 3.21. Base drag coefficient, c_b Vs u at different values of ϵ . \bullet , $\epsilon = 5$; \blacksquare , $\epsilon = 10$; \blacktriangle , $\epsilon = 15$; \blacklozenge , $\epsilon = 20$; --- , $\epsilon = 30$; \bullet , $\epsilon = 40$; \blacksquare , $\epsilon = 50$.

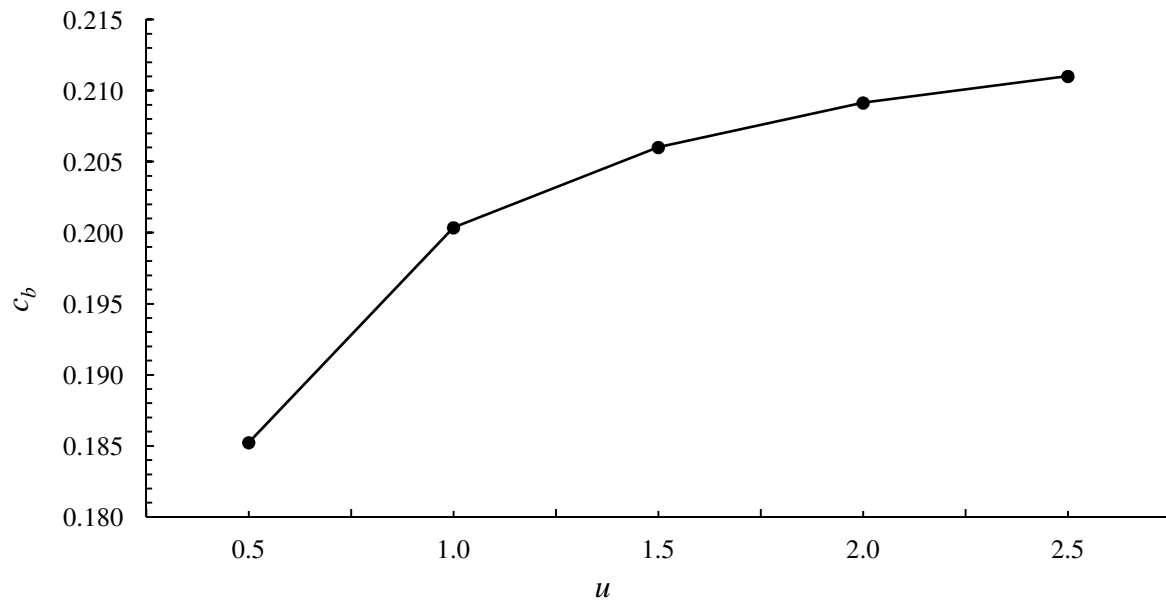


Fig. 3.22. Base drag coefficient, c_b as function of u .

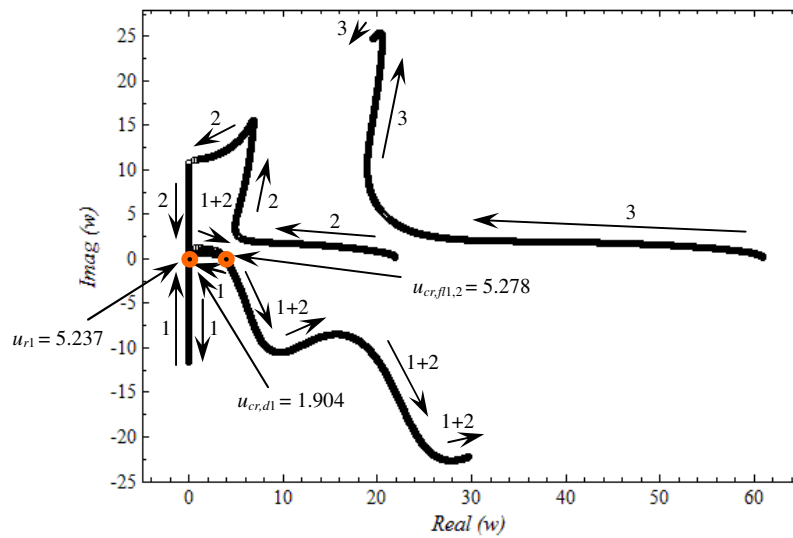


Fig. 3.23. Argand diagram of the dimensionless complex frequencies, ω of the lowest three modes of cantilevered cylinder with a tapered free end in water flow as function of u using the calculated force coefficients.

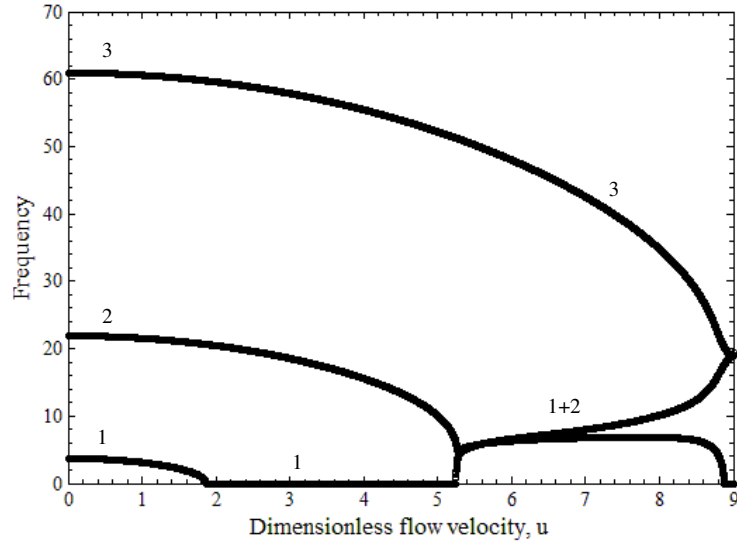


Fig. 3.24. Dimensionless oscillation frequency of the lowest three modes of cantilevered cylinder with a tapered free end in water flow as function of u using the calculated force coefficients.

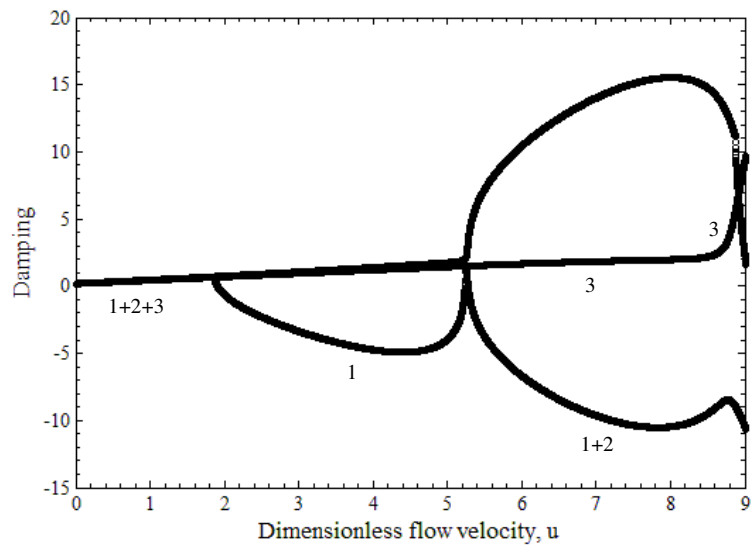


Fig. 3.25. Damping of the lowest three modes of cantilevered cylinder with a tapered free end in water flow as function of u using the calculated force coefficients.

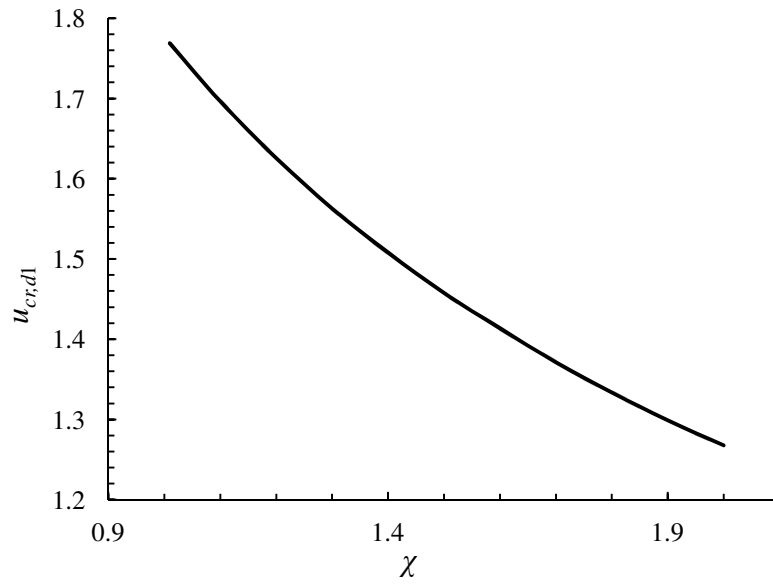


Fig. 3.26. Variation of critical flow velocity for divergence, $u_{cr,d1}$ with increasing confinement, χ of model with present force coefficients in water flow.

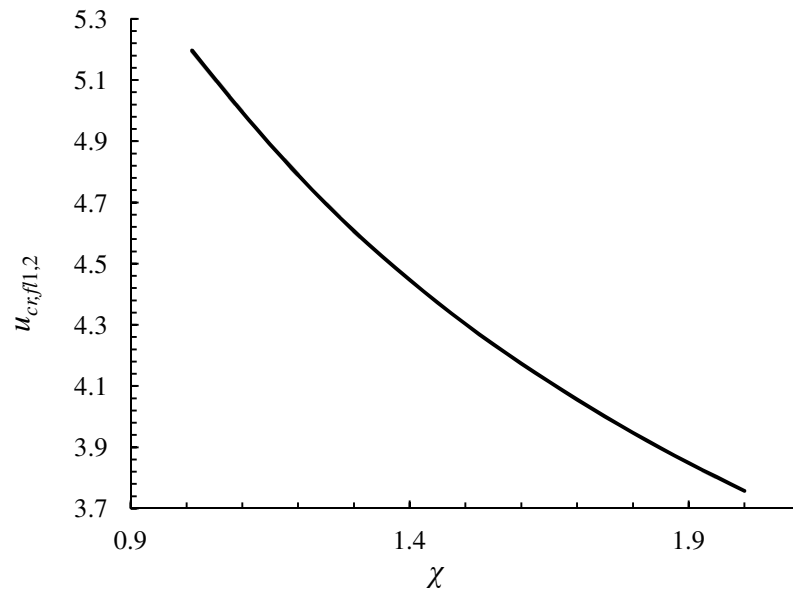


Fig. 3.27. Variation of critical flow velocity for flutter $u_{cr,fl1,2}$ with increasing confinement, χ of model with present force coefficients in water flow.

Chapter 4

Nonlinear Analysis

4.1. Introduction

As established earlier, a linear model can reliably predict the first point of instability of a flexible cylinder in axial flow, which is most of the time divergence (a static instability). The post-divergence dynamics of the cylinder, however, has to be confirmed through a nonlinear model (Païdoussis 1998, 2004; Modarres-Sadeghi 2006). It is also noted in the previous research work, presented in Chapter 1, utilizing the nonlinear models to describe the system dynamics of flexible slender cylinder in axial flow (Païdoussis et al. 2002; Modarres-Sadeghi 2005, 2007), the force coefficients were either chosen from a reasonable range or determined based on some simple relations. Therefore, there is a need to solve the nonlinear equation with the force coefficients, calculated in Chapter 3, incorporated in it in order to predict the nonlinear dynamics of the system.

In this Chapter, the dynamic response of a cantilevered cylinder in water flow, is studied again, this time a described by a nonlinear equation of motion. The system under consideration is similar to one studied in Chapter 3. The un-deformed cylinder axis coincides with the x -axis. The cantilevered cylinder is fitted with an ogival end-piece at the free end and considered to be short relative to the overall length of the cylinder. Furthermore, the fluid is supposed to be contained by boundaries sufficiently distant from the cylinder to have negligible influence on its motion. Similar assumptions are considered as in Chapter 3. First, the nonlinear model results are obtained by utilizing the force coefficients and other input parameters used by Semler et al. (2002). This is done so as to establish the adequacy of the present numerical method used for the solution by comparing the obtained results with those by Semler et al. (2002). Secondly, the presently calculated force coefficients from Chapter 3 are employed in the nonlinear equation and solved. Finally, the results obtained from the present work with previous and presently calculated force coefficients are compared with each other in order to see the effect of the force coefficients on the overall dynamics of the system.

4.2. Nonlinear Equation of Motion

Let us consider small lateral motions of the cylinder about its position of rest. Various fluid forces act on the cylinder namely inviscid hydrodynamic force, F_A , viscous forces per unit length in the normal and longitudinal direction, F_N and F_L , respectively, and hydrostatic forces in the x - and y - directions, F_{px} and F_{py} , respectively. The derivation of the equation of motion derived by Lopes et al. (2002) is via Hamilton's principle,

$$\delta \int_{t_1}^{t_2} \mathcal{L} dt + \int_{t_1}^{t_2} \delta W dt = 0, \quad (4.1)$$

where $\mathcal{L} = T_c - V_c$ is the Lagrangian, T_c and V_c being the kinetic and potential energies of the cylinder, respectively, and δW the virtual work by the fluid-related forces acting on the cylinder (Lopes et al. 2002). Finally the equation of motion of solitary cylinder in unconfined flow, given by Lopes et al. (2002), can be written as

$$\begin{aligned} & (m + M)\ddot{y} + 2MU\dot{y}'\left(1 + \frac{7}{4}y'^2\right) + MU^2y''\left(1 + \frac{5}{2}y'^2\right) - \frac{3}{2}M\dot{y}y'(\dot{y}' + Uy'') + \frac{1}{2}\rho DU^2C_N\left(y' + \frac{1}{2}y'^3\right) \\ & - \frac{1}{2}\rho DU^2C_T(L - s)\left(y'' + \frac{3}{2}y'^2y''\right) - Ap(L)(y'' + y'^2y'') + \left[\frac{1}{2}\rho DU^2C_T\left(\frac{D}{D_h}\right) + mg - \rho gA\right] \\ & \left[y' + \frac{1}{2}y'^3 - (L - s)\left(y'' + \frac{3}{2}y'^2y''\right)\right] + EI(y'''' + 4y'y''y''' + y''^3 + y''''y'^2) - \frac{1}{2}\rho DC_N\dot{y}\int_0^s y'y'ds \\ & + \frac{1}{2}\rho DU^2C_N\left(\frac{\dot{y}}{U} - \frac{1}{2}\frac{y'\dot{y}^2}{U^2} - \frac{1}{2}\frac{y'^2\dot{y}}{U} - \frac{1}{2}\frac{\dot{y}^3}{U^3}\right) + \frac{1}{2}\rho DU^2C_D\left(y'|y'| + \frac{y'|\dot{y}| + \dot{y}|y'|}{U} + \frac{\dot{y}|\dot{y}|}{U^2}\right) \\ & - m\dot{y}''\int_0^s \int_0^s (\dot{y}'^2 + y'\dot{y}')dsds + 2M(\dot{y}' + Uy'')\int_0^s y'y'ds - M\dot{y}''\int_s^L (\ddot{y}y' + 2U\dot{y}'y' + U^2y''y')ds \\ & + (m + M)y'\int_0^s (\dot{y}'^2 + y'\dot{y}')ds + y''\int_s^L \left\{Ap(L)y'y'' + \frac{1}{4}\rho DC_T\dot{y}^2\right\}ds \\ & + \frac{1}{2}\rho DU^2y''(C_T - C_N)\int_s^L \left(y'^2 + \frac{y'\dot{y}}{U}\right)ds + O(\varepsilon^5) = 0, \end{aligned} \quad (4.2)$$

where $(\dot{})' = \frac{\partial()}{\partial s}$, and $(\dot{}) = \frac{\partial()}{\partial t}$. (4.3)

All the symbols used in eq. (4.2) are defined in the Nomenclature and some in Chapter 3.

4.3. Boundary Conditions

The end-piece is assumed to be rigid, so that its motion is determined solely by the values of displacement and velocity at $s = L-l$. Hence, the boundary conditions for a cantilevered cylinder are

$$y = y' = 0 \quad \text{at } s = 0 \quad (4.4)$$

and

$$y'' = -EIy''' + [fM(\ddot{y} + U\dot{y}') + m\ddot{y}]s_e - fMU(\dot{y} + Uy') + (m - \rho A)gy's_e + \frac{1}{2}\rho DU^2 C_T \left(\frac{D}{D_h} \right) y's_e + \frac{1}{2}\rho DUC_N(\dot{y} + Uy')\bar{s}_e = 0, \quad \text{at } s = L-l \quad (4.5)$$

where

$$s_e = \frac{1}{A} \int_{L-l}^L A(s) ds, \quad (4.6)$$

$$\bar{s}_e = \frac{1}{D} \int_{L-l}^L D(s) ds, \quad (4.7)$$

Here $A = A|_{L-l}$, $D = D|_{L-l}$, $y' = y'|_{L-l}$, $\dot{y} = \dot{y}|_{L-l}$, and $M = \chi\rho A$ (Lopes et al. 2002).

4.4. Dimensionless Parameters

Using the expression given in eq. (3.7) of Chapter 3, one obtains the following dimensionless equation of motion (Lopes et al. 2002)

$$\begin{aligned}
& [1 + (\chi - 1)\beta]\dot{\eta} + 2u\sqrt{\beta}\chi\dot{\eta}'\left(1 + \frac{7}{4}\eta'^2\right) + u^2\chi\eta''\left(1 + \frac{5}{2}\eta'^2\right) - \frac{3}{2}\chi\dot{\eta}\eta'(\beta\dot{\eta}' + u\sqrt{\beta}\eta'') \\
& + \frac{1}{2}u^2\epsilon_N\left[\eta' + \frac{1}{2}\eta'^3\right] - \frac{1}{2}u^2\epsilon_T(1 - \xi)\left(\eta'' + \frac{3}{2}\eta'^2\eta''\right) - \frac{1}{2}c_b u^2(\eta'' + \eta'^2\eta'') + \left(\frac{1}{2}u^2\epsilon_T h + \gamma\right) \\
& \left[\eta' + \frac{1}{2}\eta'^3 - (1 - \xi)\left(\eta'' + \frac{3}{2}\eta'^2\eta''\right)\right] + \eta'''' + 4\eta'\eta''\eta''' + \eta'''^3 + \eta''''\eta'^2 - \frac{1}{2}\epsilon_N\beta\dot{\eta}\int_0^\xi \eta'\dot{\eta}'d\xi \\
& + \frac{1}{2}u^2\epsilon_N\left(\frac{\sqrt{\beta}}{u}\dot{\eta} - \frac{1}{2}\frac{\beta}{u^2}\dot{\eta}^2\eta' - \frac{1}{2}\frac{\sqrt{\beta}}{u}\dot{\eta}\eta'^2 - \frac{1}{2}\frac{\beta^{3/2}}{u^3}\dot{\eta}^3\right) + \frac{1}{2}u^2\epsilon_C\left[\eta'|\eta'| + \frac{\sqrt{\beta}}{u}(\dot{\eta}|\eta'| + \eta'|\dot{\eta}|)\right] \\
& \left. + \frac{\beta}{u^2}\dot{\eta}|\dot{\eta}|\right] \\
& - \eta''(1 - \beta)\int_0^\xi (\dot{\eta}'^2 + \eta'\dot{\eta}')d\xi d\xi + 2\chi(\beta\dot{\eta}' + u\sqrt{\beta}\eta'')\int_0^\xi \eta'\dot{\eta}'d\xi - \chi\eta''\int_\xi^1 \left(\frac{\beta\dot{\eta}\eta' + 2u\sqrt{\beta}\dot{\eta}'\eta'}{+ u^2\eta''\eta'}\right)d\xi \\
& + \eta'[1 + (\chi - 1)\beta]\int_0^\xi (\dot{\eta}'^2 + \eta'\dot{\eta}')d\xi + \eta''\int_\xi^1 \left(\frac{1}{2}c_b u^2\eta'\eta'' + \frac{1}{4}\epsilon_T\beta\dot{\eta}^2\right)d\xi + \frac{1}{2}u^2\eta''(\epsilon_T - \epsilon_N) \\
& \int_\xi^1 \left(\eta'^2 + \frac{\sqrt{\beta}}{u}\eta'\dot{\eta}\right)d\xi + O(\epsilon^5) = 0. \tag{4.8}
\end{aligned}$$

The corresponding dimensionless boundary conditions are

$$\eta = \eta' = 0 \quad \text{at } \xi = 0 \tag{4.9}$$

and

$$\begin{aligned}
& \eta'' = -\eta''' + \chi_e\left[1 + (\chi^f - 1)\beta\right]\dot{\eta} + \chi^f u\sqrt{\beta}\dot{\eta}' + \left(\frac{1}{2}\bar{\chi}_e\epsilon_N - \chi^f\right)(u\sqrt{\beta}\dot{\eta} + u^2\eta') \\
& + \left(\frac{1}{2}u^2\epsilon_T h + \gamma\right)\chi_e n' = 0, \quad \text{at } \xi = 1 \tag{4.10}
\end{aligned}$$

where

$$\left(\cdot\right)' = \frac{\partial(\cdot)}{\partial\xi}, \quad \left(\cdot\right) = \frac{\partial(\cdot)}{\partial\tau}, \quad \chi_e = \frac{s_e}{L}, \quad \bar{\chi}_e = \frac{\bar{s}_e}{L}. \tag{4.11}$$

4.5. Method of Solution

The nonlinear equation (eq. (4.8)) is correct to third order, $O(\epsilon^3)$; furthermore, the boundary conditions (eq. (4.10)) are time- and flow-velocity-dependent making the solution procedure rather complicated. For this, the ‘extended Galerkin method’ is used, which can be expressed as

$$F(\eta(\xi, \tau), u) + \delta(\xi - 1)B(\eta(\xi, \tau), u) = 0, \quad (4.12)$$

where $F(\eta)$ is the equation of motion, $B(\eta)$ is boundary condition, and $\delta(\xi - 1)$ is Dirac's delta function. Applying the procedure leads to a second-order ordinary differential equation given by Lopes et al. (2002) as

$$M_{ij}\ddot{q}_j + C_{ij}\dot{q}_j + K_{ij}q_j + r_{ijk}q_j|q_k| + \bar{s}_{ijk}|q_j|\dot{q}_k + \tilde{s}_{ijk}q_j|\dot{q}_k| + t_{ijk}\dot{q}_j|\dot{q}_k| + \alpha_{ijkl}q_jq_kq_l + \beta_{ijkl}q_jq_k\dot{q}_l + \gamma_{ijkl}q_j\dot{q}_k\dot{q}_l + \eta_{ijkl}\dot{q}_j\dot{q}_k\dot{q}_l + \mu_{ijkl}q_jq_k\ddot{q}_l = 0. \quad (4.13)$$

M_{ij} , C_{ij} , and K_{ij} are the mass, damping, stiffness matrices, respectively, while α_{ijkl} , β_{ijkl} , γ_{ijkl} , η_{ijkl} , μ_{ijkl} , r_{ijk} , \bar{s}_{ijk} , \tilde{s}_{ijk} , t_{ijk} are related to the nonlinear terms. The mass, damping, and stiffness matrices are defined as

$$M_{ij} = [1 + (\chi f - 1)\beta]\chi_e\phi_i(1)\phi_j(1) + [1 + (\chi - 1)\beta]\delta_{ij}, \quad (4.14)$$

$$C_{ij} = \left(\frac{1}{2}\bar{\chi}_e\epsilon c_N - \chi f\right)u\sqrt{\beta}\phi_i(1)\phi_j(1) + \chi fu\sqrt{\beta}\chi_e\phi_i(1)\phi_j'(1) + 2\chi u\sqrt{\beta}b_{ij} + \frac{1}{2}u\epsilon c_N\sqrt{\beta}\delta_{ij}, \quad (4.15)$$

$$K_{ij} = \left(\chi\chi_e + \frac{1}{2}u^2(\epsilon c_N\bar{\chi}_e + \epsilon c_T h\chi_e) - \chi fu^2\right)\phi_i(1)\phi_j'(1) + \chi u^2 c_{ij} + \left(\frac{1}{2}u^2\epsilon c_T(1 + h) + \gamma\right)(d_{ij} - c_{ij}) + \left(\frac{1}{2}u^2\epsilon(c_N + c_T h) + \gamma\right)b_{ij} + \lambda_j^4\delta_{ij} - \frac{1}{2}u^2 c_b c_{ij}, \quad (4.16)$$

where the constants b_{ij} , c_{ij} , and d_{ij} are already defined in chapter 2 and the nonlinear coefficients α_{ijkl} , β_{ijkl} , γ_{ijkl} , η_{ijkl} , μ_{ijkl} , r_{ijk} , \bar{s}_{ijk} , \tilde{s}_{ijk} , and t_{ijk} are defined by Lopes et al. (2002).

Equation (4.8) may be used for an isolated cylinder in unconfined axial flow by considering $\chi \rightarrow 1$ and $h \rightarrow 0$. The method adopted to solve eq. (4.13) is Houbolt's Finite Difference Method (FDM), which is an initial value problem solver and is used to solve the second-order ordinary differential equation directly without any need to recast it in first-order form (Modarres-Sadeghi 2006). The numerical solution is obtained using FORTRAN code developed by Modarres-Sadeghi (2006) that is based on the Houbolt's FDM. Six Galerkin modes are considered in both the axial and transverse directions in the solution.

4.6. Model in Water Flow with Previously Used Force Coefficients

4.6.1. Adequacy of the Nonlinear Solution

Adequacy of the nonlinear solution is established by solving the nonlinear equation especially for this purpose and comparing the critical flow velocity for the onset of first mode divergence, $u_{cr,d1}$, with that obtained by Semler et al. (2002). The solution of the nonlinear equation yields $u_{cr,d1} = 2.18$. The value of $u_{cr,d1}$ obtained by Semler et al. (2002) is 2.10. The difference is 3.8%, which may be considered acceptable. Complete comparison is presented in Section 4.8.

4.6.2. Results

First, the results obtained with the force coefficients and other dimensionless parameters implemented in the nonlinear equation of motion, previously used by Semler et al. (2002), are presented. These are $\beta = 0.47$, $f = 0.7$, $c_N = 0.0244$, $c_T = 0.0244$, $c_b = 0.3$, $c_d^1 = 0.0$, $\chi = 1$, and $\varepsilon \approx 20.47$. The results are obtained in the dimensionless flow velocity range of $0 \leq u \leq 8.0$. It is known that for linear theory to be applicable for post-divergence dynamics, the motion must be small in the vicinity of the equilibrium state. No such condition is required for nonlinear theory. Therefore, nonlinear theory unconditionally gives reasonably accurate dynamical behaviour of the system. Figure 4.1 illustrates the typical bifurcation diagram of the generalized coordinate, q_1 versus the dimensionless flow velocity, u . The critical flow velocity for the onset of static instability, i.e., divergence, with the help of the parameters such as the generalized coordinates and dimensionless displacements describing the state of the system sometimes is difficult to identify precisely. The reason is that the divergence does not occur abruptly but evolves gradually from the equilibrium state of the system. But in this case, looking at Fig. 4.1, it seems to be very clear. The value of q_1 remains essentially zero until at $u_{cr,d1} = 2.18$, it becomes non-zero, i.e., a pitchfork bifurcation occurs and the system loses stability by divergence in first mode; q_1 then increases with u . For $u \approx 3.2$, q_1 begins to decrease, reaches zero, and then becomes negative over a small range of u . Before q_1 crosses the horizontal axis, the mode shape of the system is transformed from first mode shape to second mode at $u_{cr,d2} \approx 4.4$. This value is approximate since the transformation is not abrupt but gradual and it is very difficult to precisely

¹ Semler et al. (2002) used the symbol c_d to represent zero-flow normal coefficient. In the present work, the same parameter is represented by the symbol c , as also indicated in Chapter 3.

locate the critical velocity. The negative q_1 indicates that the second mode shape is enhanced to the extent that q_1 crosses the equilibrium position, i.e., the horizontal axis. Subsequently, at $u_{r2} = 5.41$, the system is re-stabilized over a short range of u . At $u_{cr,fl2} = 5.55$, the solution loses stability again through a Hopf bifurcation, which results in flutter in the second mode. At higher flow velocity, the solution shows in first increasing and then decreasing q_1 . There might be some unstable solutions beyond $u_{cr,fl2}$, but the FDM code only gives stable solutions.

The results are obtained using 100,000 sample points in 100 dimensionless time units, τ . Figure 4.2 shows the time history and phase-plane plot of the system at $u = 1.9$. Both figures are obtained by plotting q_1 and \dot{q}_1 against $\tau \leq 16$ since a stable solution is obtained even before this time and there is no need to extend it up to $\tau = 100$. Both plots clearly demonstrate a stable system; the system returning to equilibrium position after initial perturbation. Figure 4.3 shows the time history, phase-plane plot, and the mode shape at $u = 2.6$. All three plots clearly demonstrate that the system has undergone a static instability, i.e., divergence. The saddle point is shifted to a new location. Figure 4.4 demonstrate second-mode shape divergence of the system at $u = 5.0$ with the help of time history, phase-plane plot, and mode shape. The dynamically unstable system in second mode flutter is shown in Fig. 4.5 at $u = 6.3$ with the help of time history, Fast Fourier Transform (FFT), Power Spectral Density (PSD), phase-plane plot, Poincaré map, and the mode shape. The phase-plane plot is obtained by plotting \dot{q}_1 versus q_1 ; \dot{q}_1 is the derivative of q_1 with respect to the dimensionless time τ . The Poincaré map is obtained by plotting \dot{q}_1 versus q_1 whenever the time derivative of second generalized coordinate, $\dot{q}_2 = 0$. The system oscillates around the original equilibrium position demonstrating periodic response. This is confirmed by the phase-plane plot showing, eventually, a stable limit cycle and the Poincaré map showing all the data points located at only two positions. It means that whenever the condition of $\dot{q}_2 = 0$ is met, q_1 is located at the same positions in the upper and lower halves of the periodic oscillation cycles with the same corresponding \dot{q}_1 in one or the other direction. The negative and positive values of q_1 and \dot{q}_1 are based on the sign convention for differentiation. The initial transient response is omitted in the Poincaré map. The flutter frequency, f_{fl2} , is 1.89 Hz. $3f_{fl2}$ is a multiple of the fundamental frequency as shown by PSD in Fig. 4.5 (c).

4.7. Model in Water Flow with Presently Calculated Force Coefficients

4.7.1. Adequacy of the Nonlinear Solution

Adequacy of the nonlinear solution with the presently calculated force coefficients is established by solving the nonlinear equation especially for this purpose and comparing the critical flow velocity for the onset of first mode divergence, $u_{cr,d1}$, with the experimental one. The solution of the nonlinear equation yields $u_{cr,d1} = 1.89$. The measured critical flow velocity, $u_{cr,d1}$, in experiments is 1.87 (Chapter 2). The difference is 1.07%, which is in good agreement.

4.7.2. Results

The force coefficients, calculated in Chapter 3, are going to be used in the nonlinear model instead of the previously used ones by Semler et al. (2002) since these are calculated based on the parameters of the cantilevered cylinder case under investigation and represent more precisely the fluid forces acting on the cylindrical system. The results thus obtained with these presently calculated force coefficients are presented in this section. To remind the reader, these force coefficients are longitudinal viscous coefficient, $c_T = 0.0234$ [$c_T = 0.0244$], normal viscous coefficient, $c_N = 0.0041$ [$c_N = 0.0244$], base drag coefficient, $c_b = 0.2024$ [$c_b = 0.3$], and zero flow normal coefficient, $c = 0.0510$ [$c_d = 0.0$], with the coefficients used previously by Semler et al. (2002) shown in square brackets. Other parameters are $\beta = 0.5$, $f = 0.8$, $\gamma = 1.23$, and $\chi = 1$. The dimensionless cylinder length, ε is equal to 20.7283. The results are obtained for the dimensionless flow velocity range of $0 \leq u \leq 7.2$. Six Galerkin modes are used in the solution. In this case too, the first bifurcation is clear and the onset of first point of instability can be obtained without much difficulty, as can be seen in Fig. 4.6, which illustrates the typical bifurcation diagram of the generalized coordinate, q_1 against the dimensionless flow velocity, u . The system first loses stability by first mode divergence via pitchfork bifurcation at $u_{cr,d1} = 1.89$. This is shown by the increase in q_1 . With increasing flow velocity, the plot shows an ascend in q_1 . Later, q_1 start to descend at $u = 2.9$ and eventually crosses the equilibrium position and becomes negative at $4.76 < u < 4.77$. Before this happens, the first mode divergence transforms gradually into second mode at $u_{cr,d2} \approx 4.4$. The system again returns to equilibrium state at $u_{r2} = 5.25$. This is indicated by q_1 becoming zero. The system remains stable over a short range of u and then becomes dynamically unstable by coupled-mode flutter at $u_{cr,f1,2} = 5.29$. This coupled-mode

flutter involves first and second cylinder modes and is observed in the forthcoming results. At $u > 7.2$, unstable solutions also co-exist and the dynamics of the system becomes more intricate.

These results also are obtained using 100,000 sample points in 100 dimensionless time units, τ . Figure 4.7 shows the time history and phase-plane plot of the system at $u = 1.8$. Both figures are obtained by plotting q_1 and \dot{q}_1 against $\tau \leq 16$ since a stable solution is obtained even before this time and there is no need to extend it up to $\tau = 100$. Both plots clearly demonstrate a stable system; the system returning to equilibrium position after initial perturbation. Figure 4.8 shows the diverged system in first mode with the help of time history, phase-plane plot, and the mode shape at $u = 2.6$. Figure 4.9 shows the diverged system in second mode at $u = 5.1$. In Figs 4.8 (b) and 4.9 (b), q_1 moves to new fixed points, i.e., saddle points. Dynamic instability of the system is shown with the help of time history, FFT, PSD, phase-plane plot, Poincaré map, and the mode shape in Fig. 4.10 at $u = 5.8$. The flutter frequency at this flow velocity is, $f_{f1,2} = 1.95$ Hz. $3f_{f1,2}$ is the multiple of the fundamental frequency as shown in Fig. 4.10 (c). The phase-plane plot, as shown in Fig. 4.10 (d), depicts a stable limit cycle. The Poincaré map, as shown in Fig. 4.10 (e), confirms periodic motion of the system. The coalesced first and second modes are observed in the mode shape of the system presented in Fig. 4.10 (f). It means the cylinder oscillates in its second mode around a diverged position leading to an asymmetric response.

4.8. Comparison of the Results

The results in terms of critical velocities obtained in present work are compared with those obtained by Semler et al. (2002) in Table 4.1. The present results are obtained by solving the nonlinear equation of motion numerically using Houbolt's FDM, whereas Semler et al. used two different numerical schemes namely FDM and AUTO. The software AUTO is based on a collocation method. It is adapted to solving continuation and bifurcation problems for differential equations. The small difference in the results is due to different numerical schemes used. In other words, the difference is attributed to numerical error of the schemes. Overall, the agreement is good.

The models employing previously used and presently calculated force coefficients are compared in Table 4.2, which shows a salient difference in the post-divergence dynamics depicting coupled-mode flutter in the model employing the presently calculated force coefficients, i.e., the system oscillates in second beam mode around first beam mode buckled

position. In other words, the first and second modes coalesce and leave the axis with finite q_1 indicating the onset of coupled-mode flutter. Other observation is that the divergence of the system with present force coefficients occur at lower $u_{cr,d1}$ (13.3 % lower) and $u_{cr,fl1,2}$ (4.68 % lower) than with previous ones. It can be reasoned by looking at the values of the present force coefficients and establishing how these affect the dynamics of the system. It is noticed that the presently calculated force coefficients c_T , c_N , and c_b are smaller, whereas the coefficient c is bigger than the previous ones. These present values affect the system by reducing its damping and stiffness through eqs. (4.15) and (4.16). The eventual result is that the system diverges in first mode and oscillates in second mode at relatively lower critical flow velocities, $u_{cr,d1}$ and $u_{cr,fl1,2}$, respectively. The results of the nonlinear model with the presently calculated force coefficients demonstrate similar dynamics as observed in the experiments, especially the combined first mode divergence and second mode flutter as the coupled-mode flutter (such type of flutter leads to an asymmetric response, as shown in Fig. 4.10(f) and also observed in Figs. 2.32 and 2.33 in Chapter 2). Hence, it can be inferred that the nonlinear model with the presently calculated force coefficients predicts the dynamics of the system better than the one with the previously used force coefficients.

4.9. Summary

In this chapter, the nonlinear equation of motion, governing the dynamics of cantilevered cylinder and derived by Lopes et al. (2002), was solved numerically using Finite Difference method (FDM). Six Galerkin modes were used for the solution. The downstream free end of the cylinder was terminated by an ogival end-piece. Two cases were studied; one with the previously used force coefficients and the other with the presently calculated ones. Results were obtained for a velocity range of $0 \leq u \leq 8.0$ and $0 \leq u \leq 7.2$ for the cases with previous and present force coefficients, respectively.

The first case showed that the system first lost stability by first mode divergence. At higher flow velocity, the divergence transformed form first-mode shape to second-mode shape. As the velocity increased further, the system stabilized by returning to the equilibrium position for a short range of flow velocity. Then it lost stability by second mode flutter. Results showed that the flutter exhibited periodic response. The second case (present force coefficients) showed more or less the same system dynamics with an eminent difference that the post-divergence

flutter was in fact of the coupled-mode type, i.e., the combination of first divergence and second mode flutter. This chapter presented the results in view of the fact established earlier in the work by Païdoussis (2004) that nonlinear theory predicts the post-divergence dynamics of the system more accurately than the linear theory.

Finally, the results obtained by the present work with previously used force coefficients were compared with those by Semler et al. (2002) and then with the ones using the presently calculated coefficients. The first comparison showed reasonable agreement.

Table 4.1. Dimensionless critical flow velocities, u_{cr} obtained by present work and Semler et al. (2002) for a cantilevered cylinder.

System coefficients	First mode divergence, $u_{cr,d1}$	Second mode re-stabilization, u_{r2}	Second mode flutter, $u_{cr,fl2}$
Present model with previously used force coefficients	2.18	5.41	5.55
Model with previously used force coefficients by Semler et al.	2.10	> 5.25	5.5
Percent difference	3.81	\approx 3.05	0.91

Table 4.2. Dimensionless critical flow velocities, u_{cr} of cantilevered cylinder with previously used and presently calculated force coefficients.

System coefficients	Divergence		Re-stabilization	Flutter
	$u_{cr,d1}$	$u_{cr,d2}$	u_{r2}	$u_{cr,fl2}$
Model with previously used force coefficients	2.18	≈ 4.4	5.41	5.55
Model with presently calculated force coefficients	1.89	≈ 4.4	5.25	5.29 (coupled-mode)
Percent difference	13.3	0.0	2.96	4.68

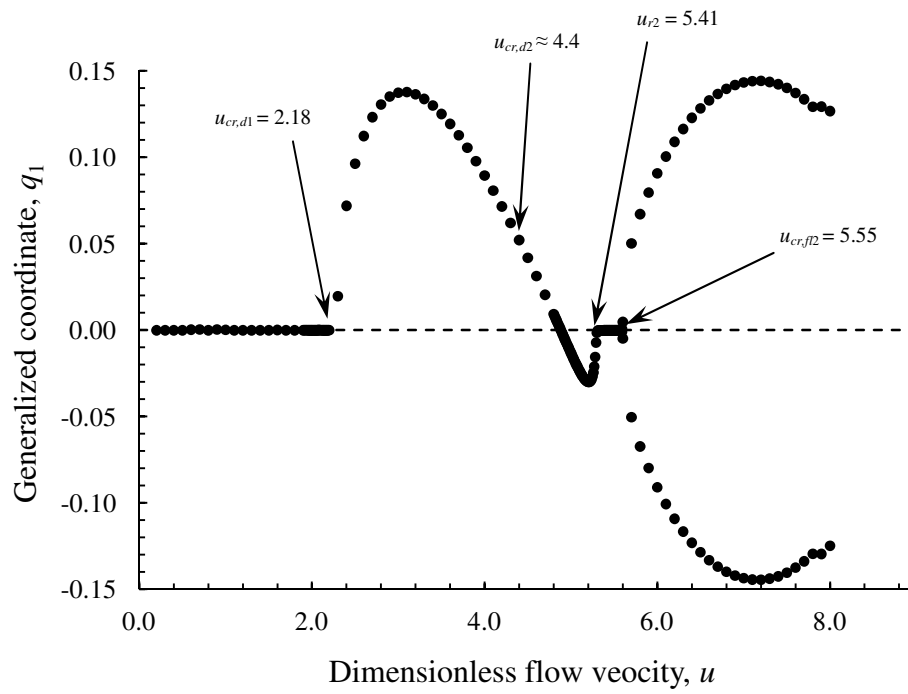


Fig. 4.1. Bifurcation diagram for cantilevered cylinder showing first generalized coordinate, q_1 as function of u .

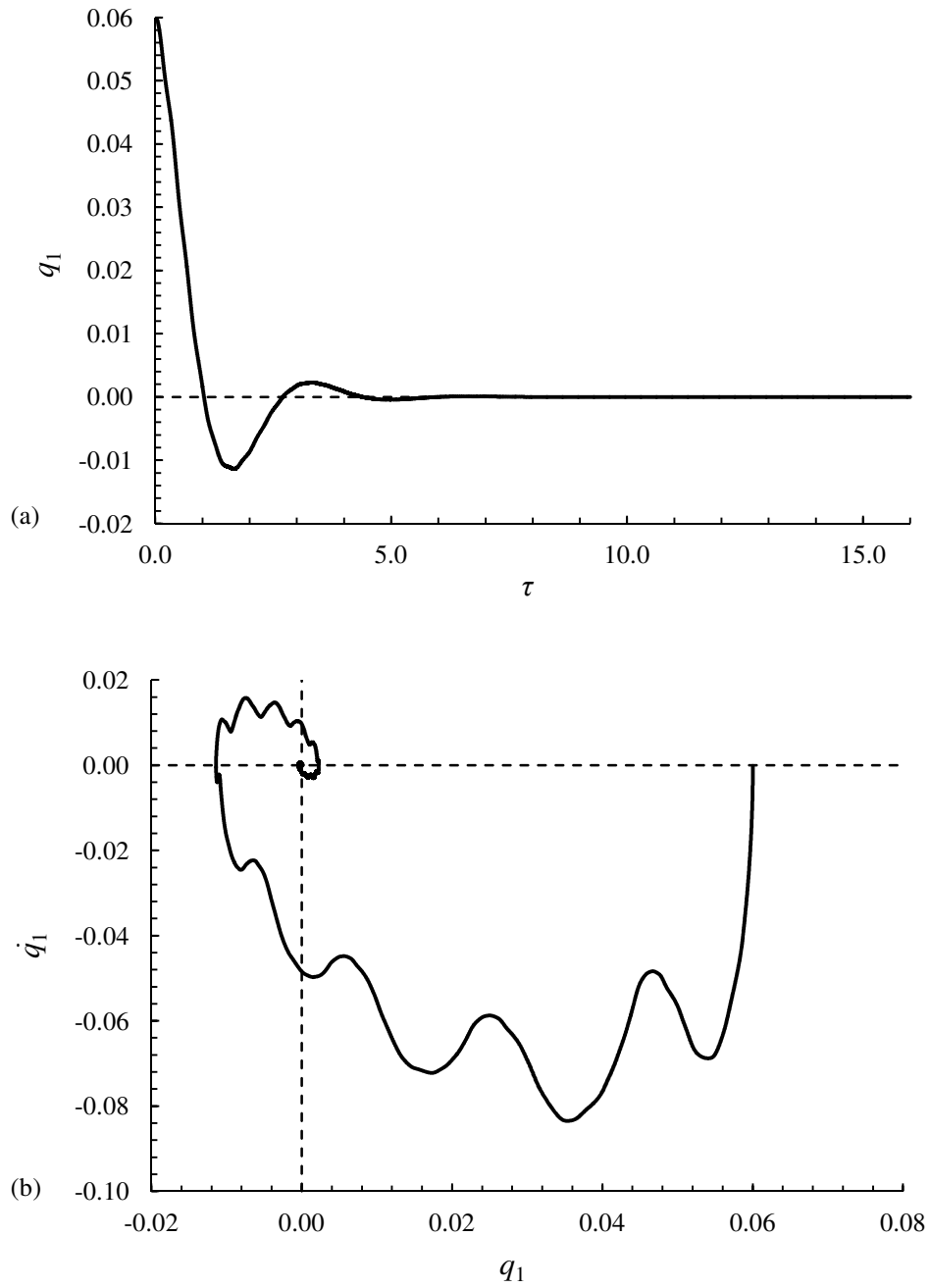


Fig. 4.2. (a) Time history and (b) phase-plane plot of cantilevered cylinder in stable state at $u = 1.9$.

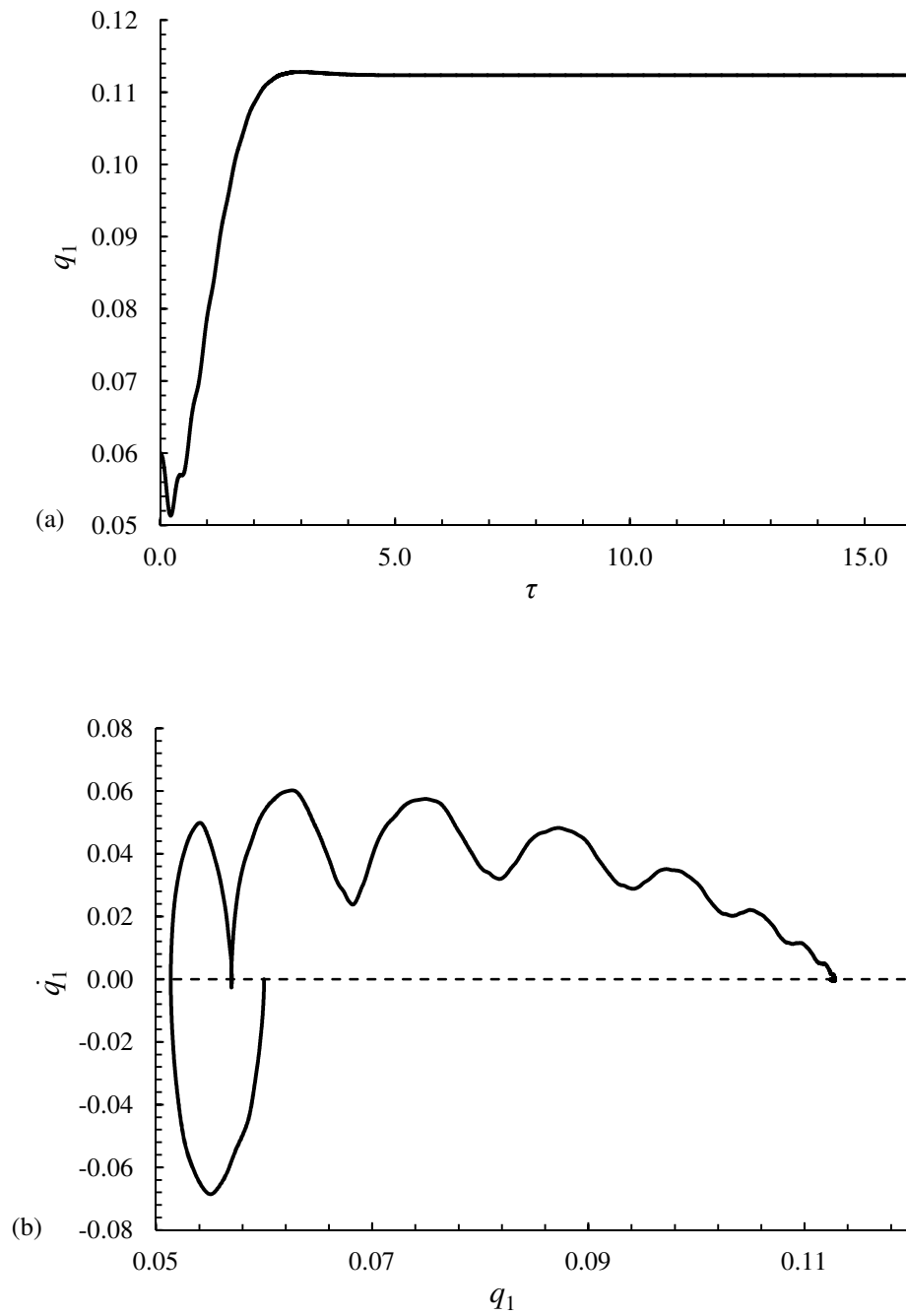


Fig. 4.3. (a,b). Caption on next page.

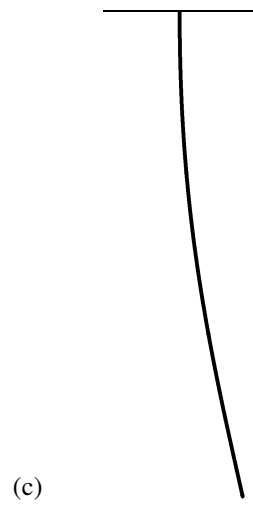


Fig. 4.3. (a) Time history, (b) phase-plane plot, and (c) mode shape of cantilevered cylinder in first mode divergence at $u = 2.6$.

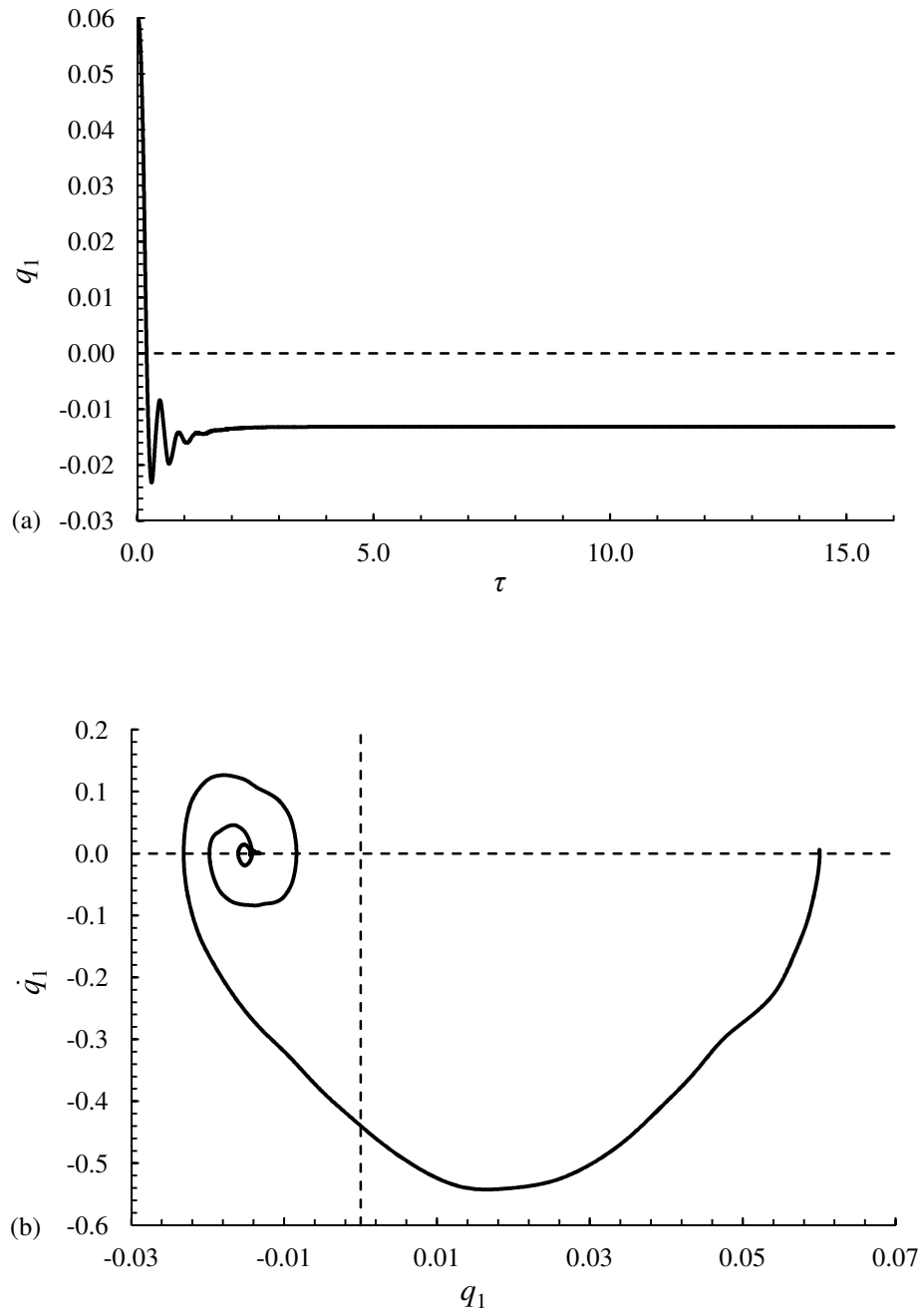


Fig. 4.4. (a,b). Caption on next page.

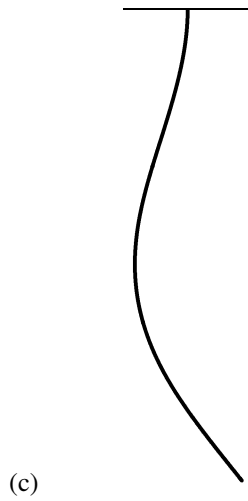


Fig. 4.4. (a) Time history, (b) phase-plane plot, and (c) mode shape of cantilevered cylinder in second mode divergence at $u = 5.0$.

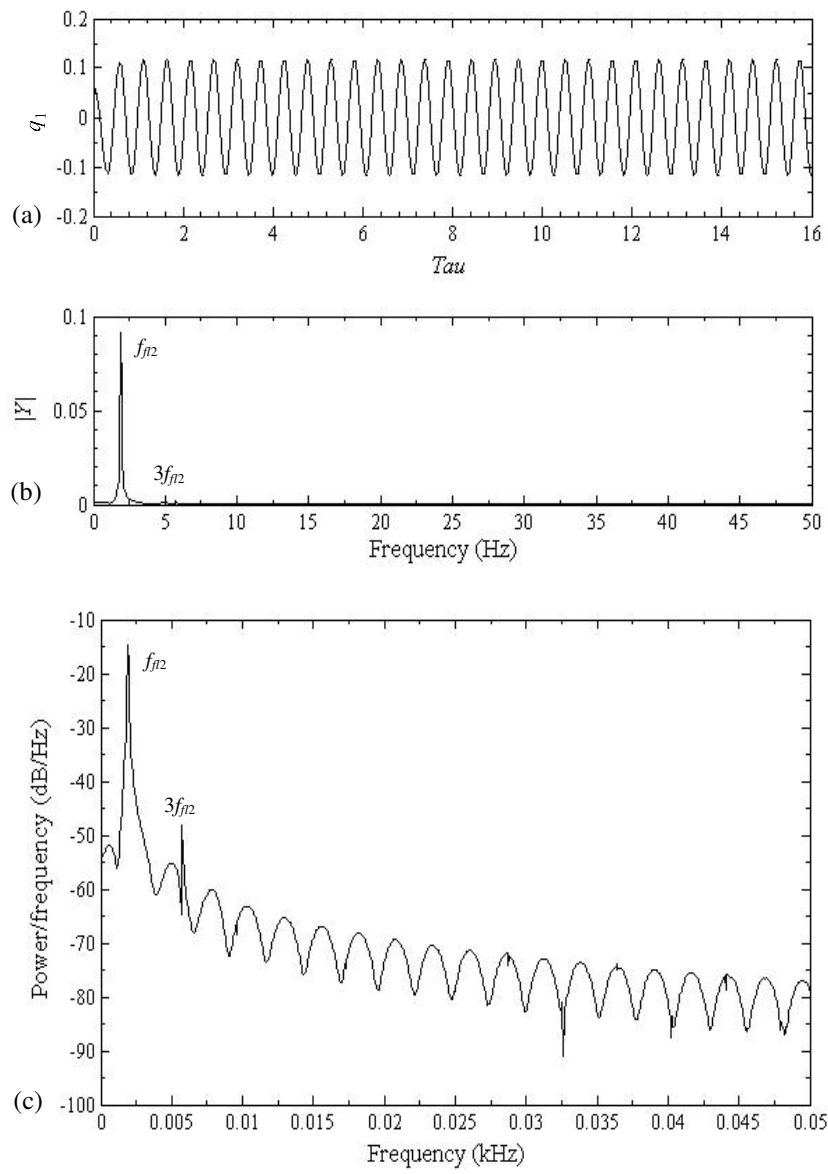


Fig. 4.5. (a,b,c). Caption on next page.

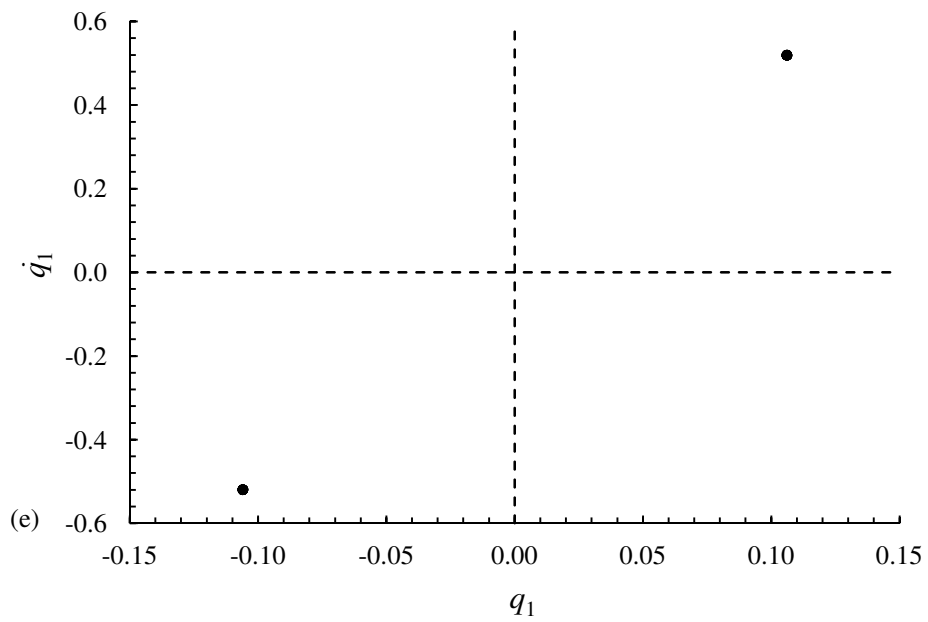
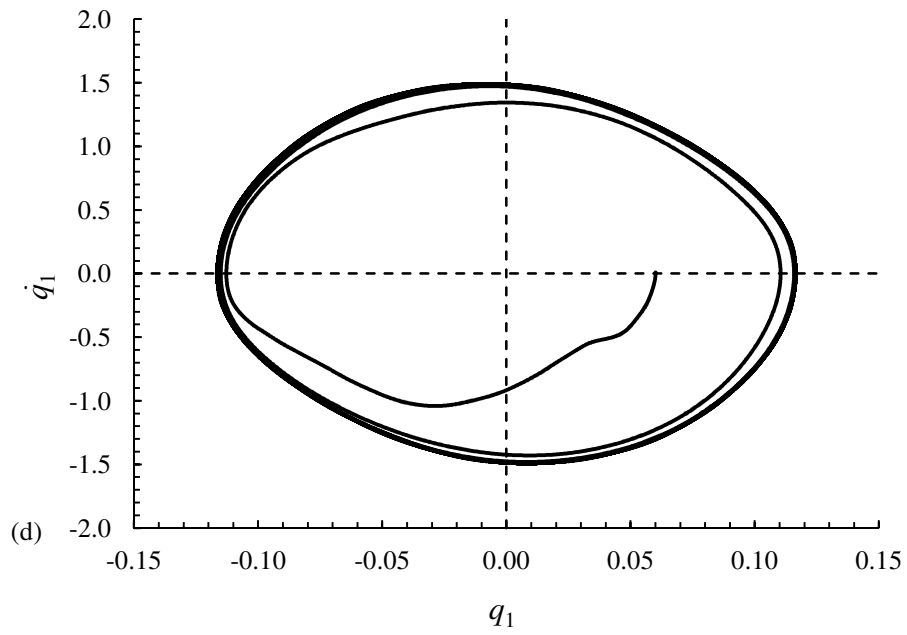


Fig. 4.5. (d,e). Caption on next page.

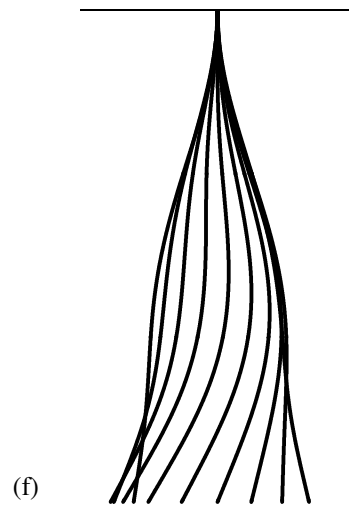


Fig. 4.5. (a) Time history, (b) FFT, (c) PSD, (d) phase-plane plot, (e) Poincaré map, and (f) mode shapes of cantilevered cylinder in second mode flutter at $u = 6.3$.

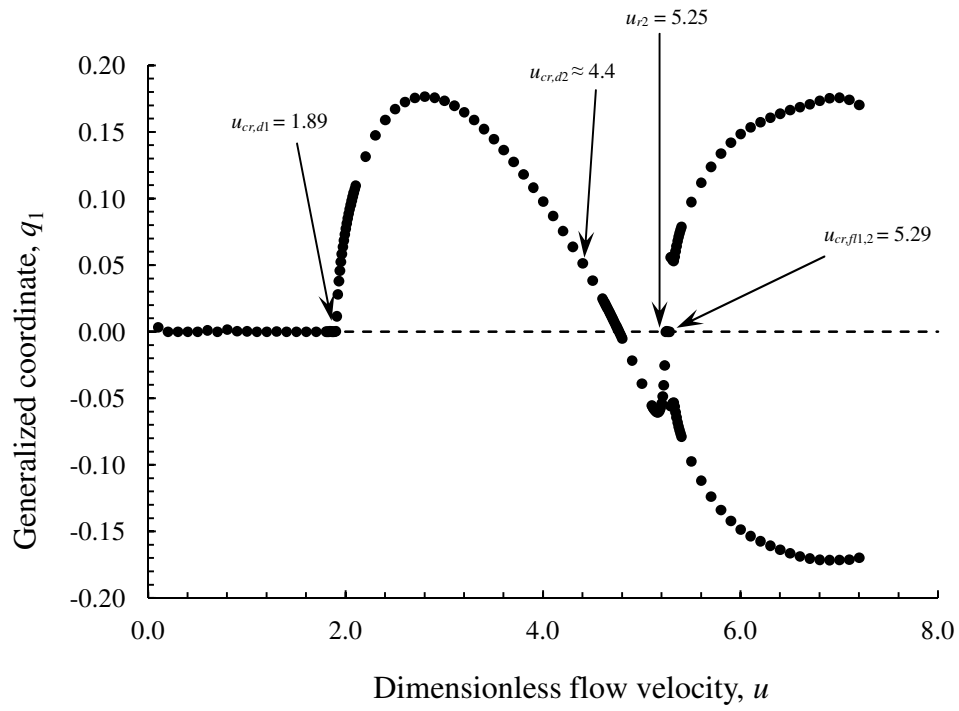


Fig. 4.6. Bifurcation diagram for cantilevered cylinder obtained with presently calculated force coefficients showing first generalized coordinate, q_1 as function of u .

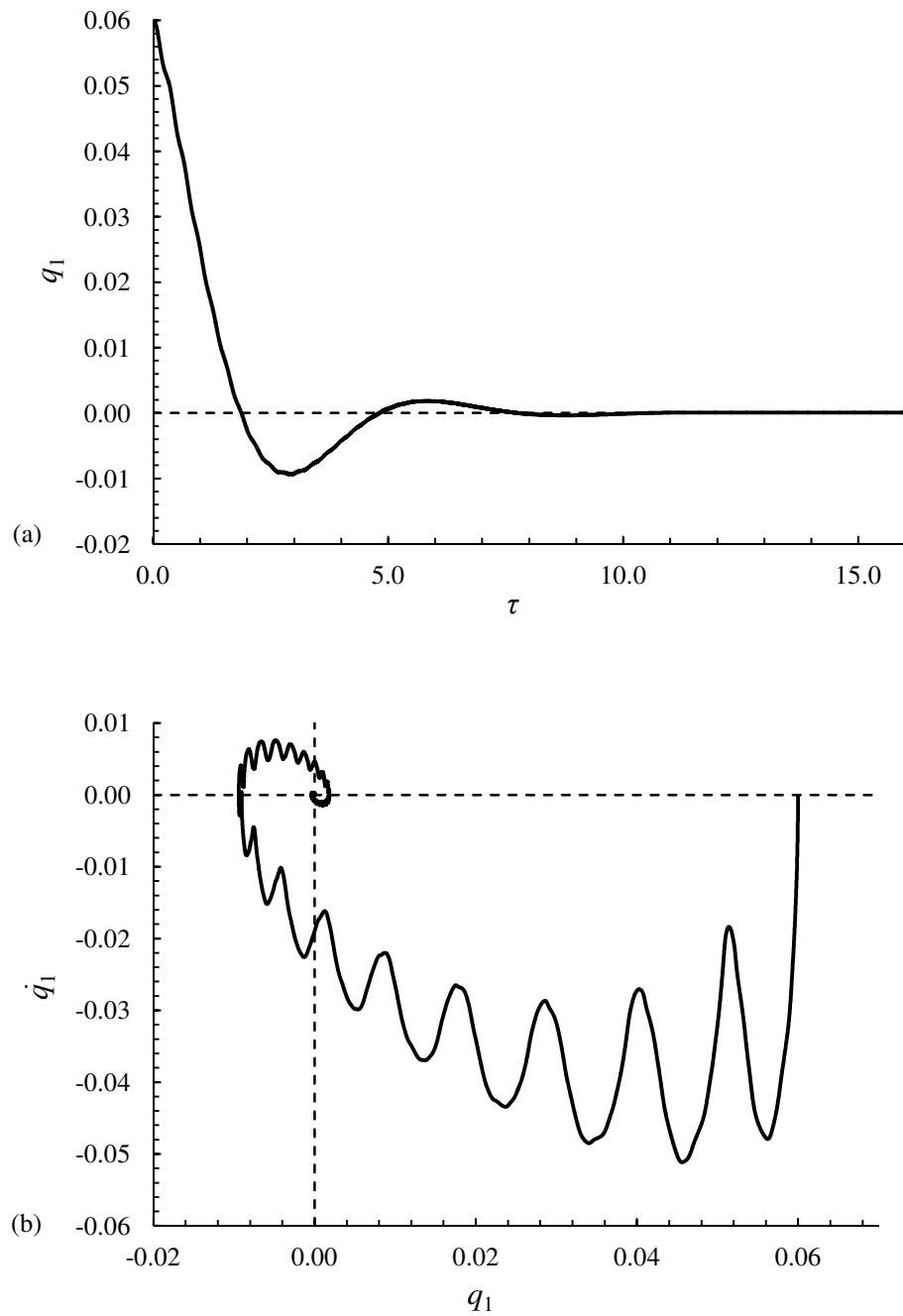


Fig. 4.7. (a) Time history and (b) phase-plane plot of cantilevered cylinder obtained with presently calculated force coefficients in stable state at $u = 1.8$.

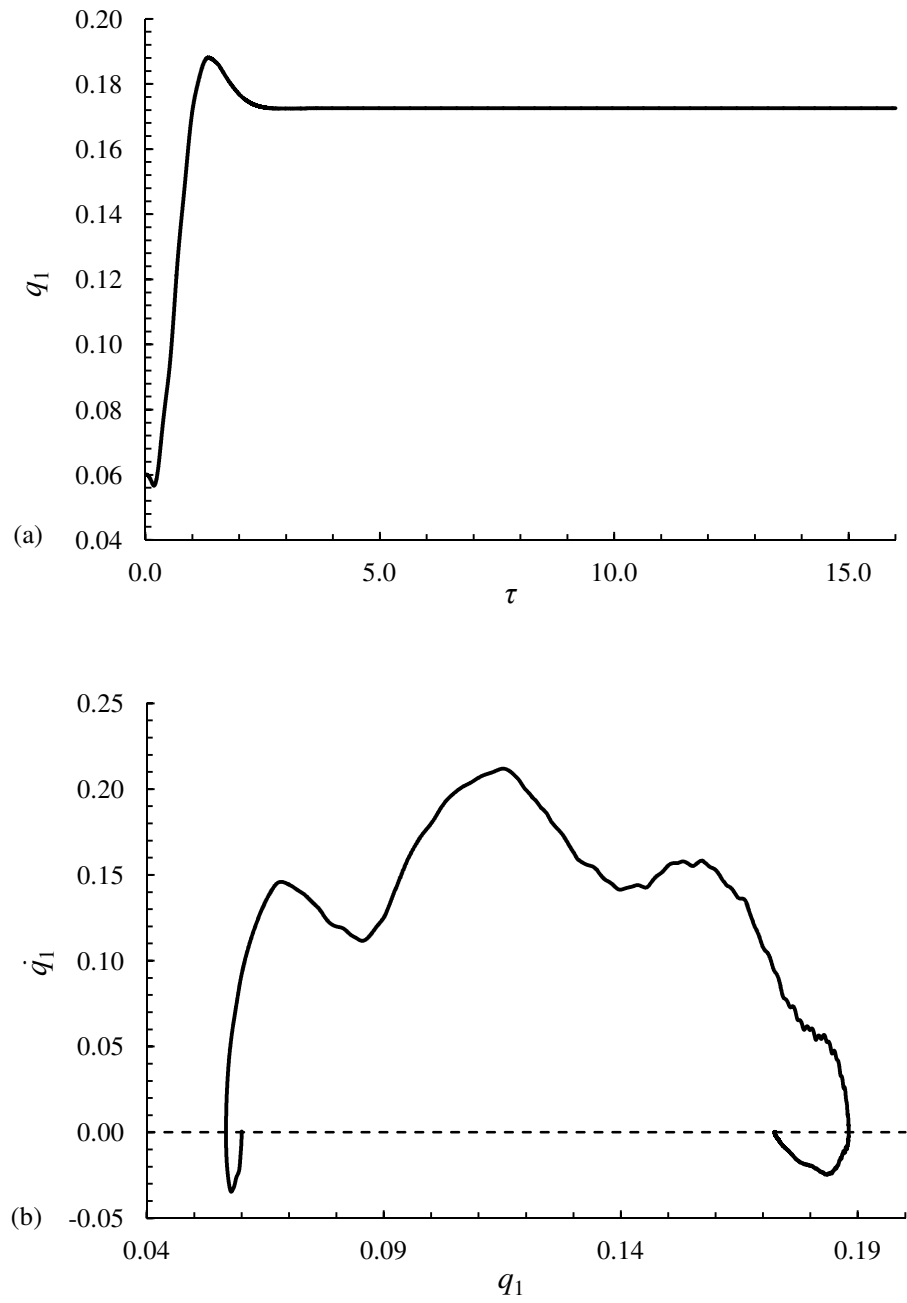


Fig. 4.8. (a,b). Caption on next page.

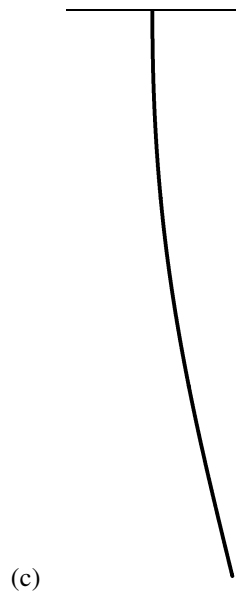


Fig. 4.8. (a) Time history and (b) phase-plane plot, and (c) mode shape of cantilevered cylinder obtained with presently calculated force coefficients in third mode flutter at $u = 2.6$.

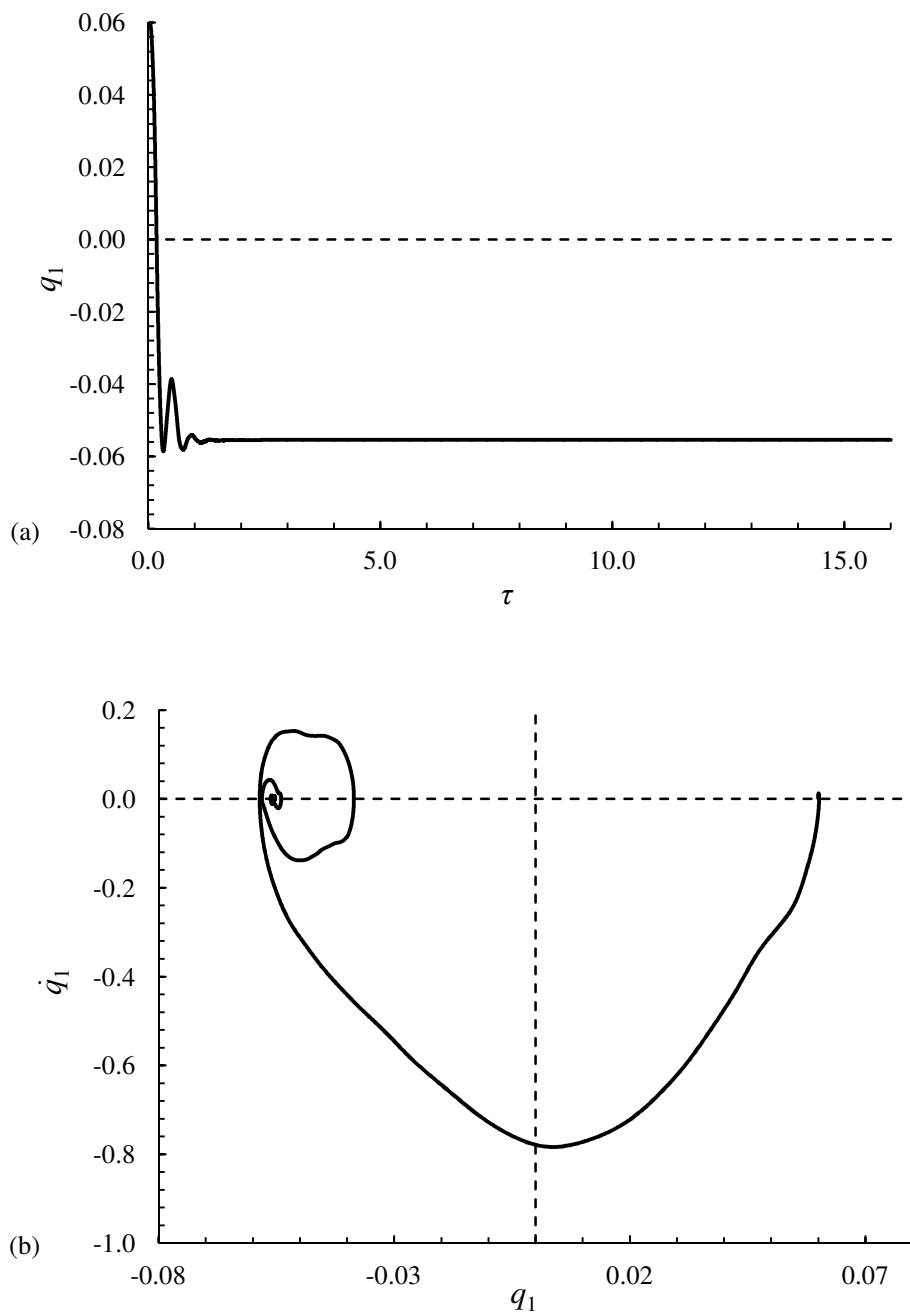


Fig. 4.9. (a,b). Caption on next page.

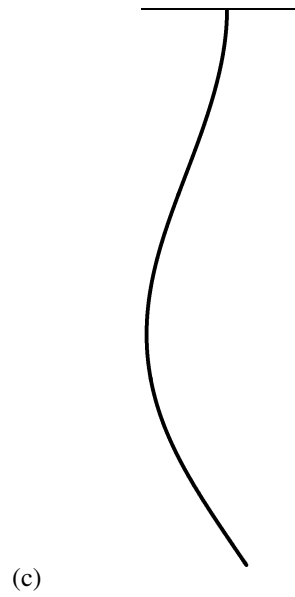


Fig. 4.9. (a) Time history, (b) phase-plane plot, and (c) mode shape of cantilevered cylinder obtained with presently calculated force coefficients in third mode flutter at $u = 5.1$.

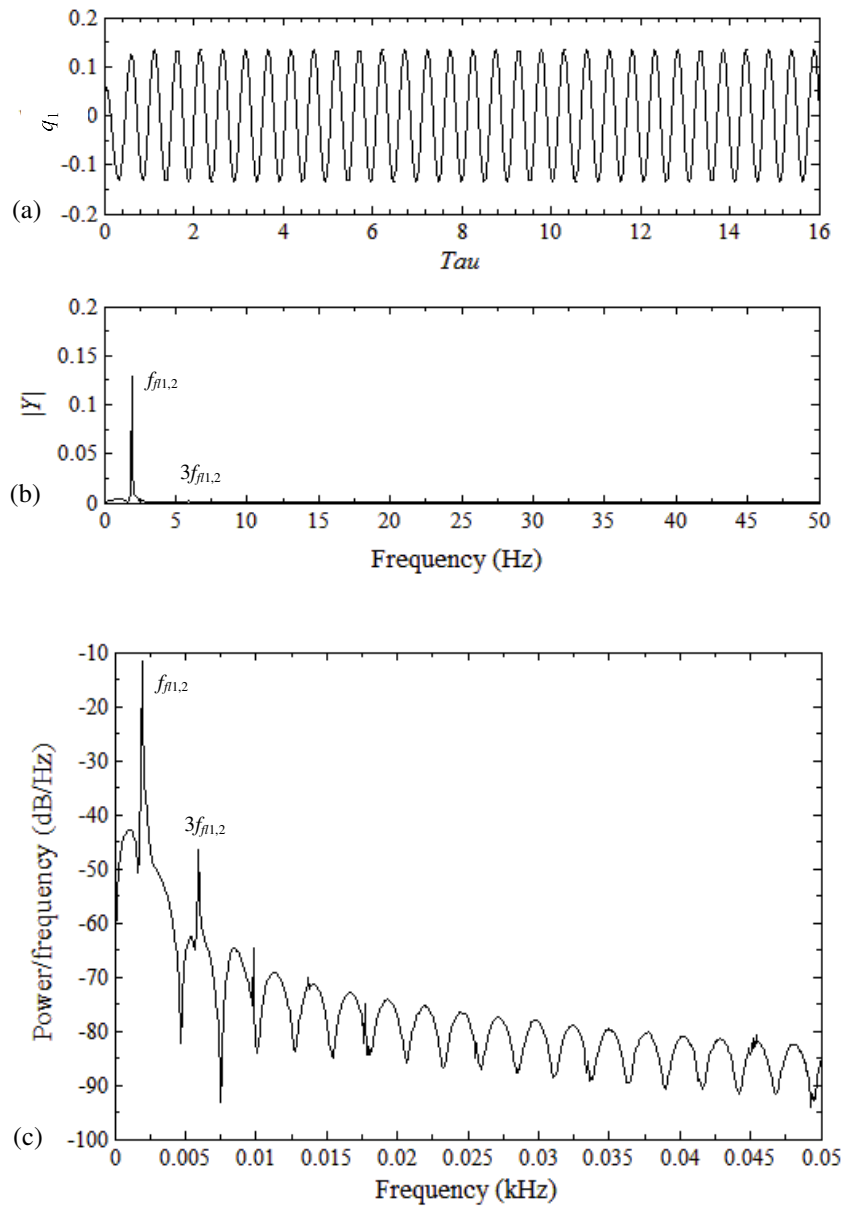


Fig. 4.10. (a,b,c). Caption on next page.

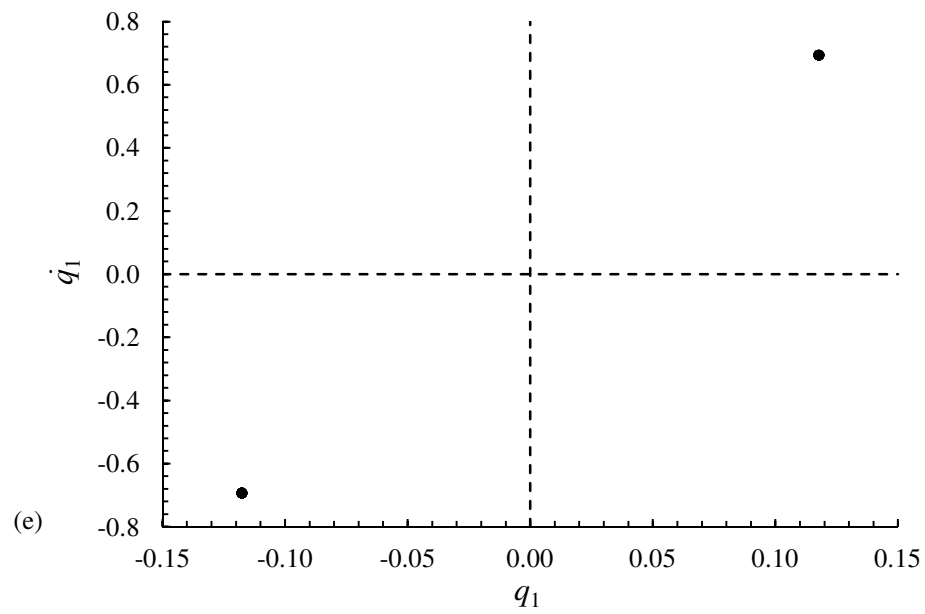
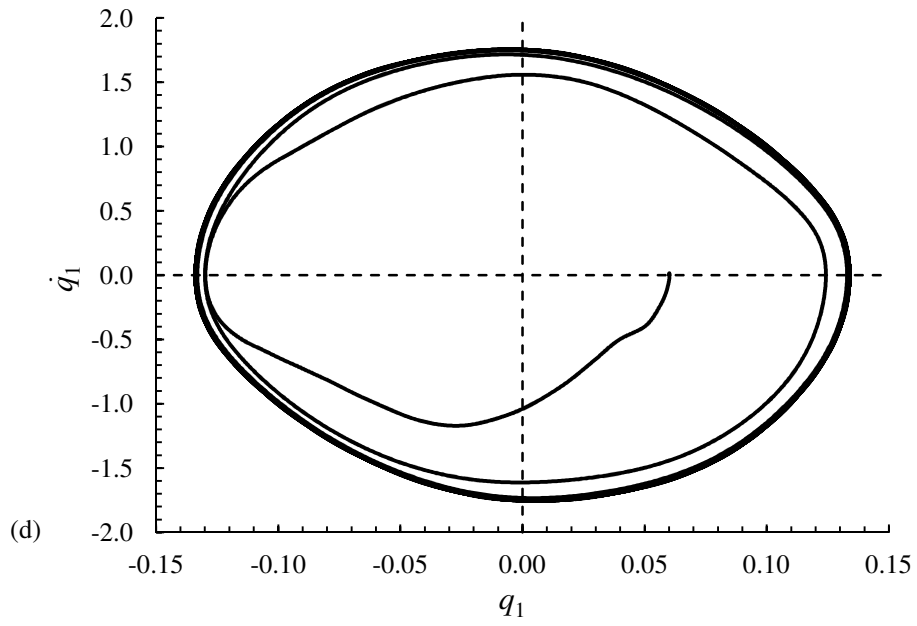


Fig. 4.10. (d,e). Caption on next page.

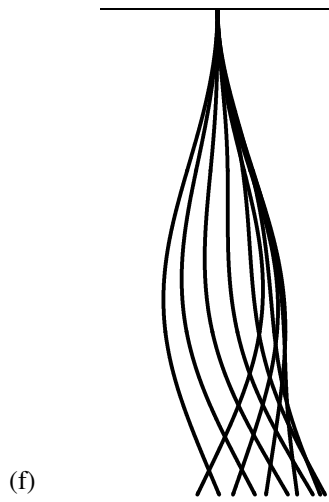


Fig. 4.10. (a) Time history, (b) FFT, (c) PSD, (d) phase-plane plot, (e) Poincaré map, and (f) mode shapes of cantilevered cylinder obtained with presently calculated force coefficients in coupled-mode flutter at $u = 5.8$.

Chapter 5

Numerical Simulations

5.1. Introduction

In all the practical applications and previously conducted experiments relevant to flexible slender cylindrical structures in axial flow, mentioned in Chapter 1, the dynamical behaviour observed is three-dimensional. Not only this but the path described by the cylinder end was observed in one of the experiments (Païdoussis et al. 2002) to be orbital instead of circular. Lack of knowledge to account for the three-dimensional behaviour, especially the non-symmetry found in the cylinder motion, important for the safe operation of the engineering and health delivery processes, is the motivation behind the present work, which is aimed at developing a three-dimensional coupled nonlinear model for a confined flexible cylindrical structure in axial flow in an FEM based modelling and simulation package called ADINA.

In addition to the solutions of the linear and nonlinear equations of motion obtained by the analytical and numerical techniques, respectively, ADINA is also utilized to solve the problem under investigation. ADINA is a finite element analysis solver and Simulation software package for various physics and engineering applications, especially multiphysics or coupled phenomena such as Fluid-Structure Interaction (FSI). ADINA offers FSI capabilities in one single program for the solution of problems where the fluids are fully coupled to general structures that can undergo highly nonlinear response due to large deformations, contact with the surrounding boundaries, and temperature-dependency. A fully coupled fluid-structure interaction means that the response of the solid is strongly affected by the response of the fluid, and vice versa. From the fluid point of view, the Navier-Stokes flow can be incompressible, slightly compressible, low-speed or high-speed compressible. From the structural point of view, all available element types can be used (i.e. shell, two-dimensional and three-dimensional solid, beam, iso-beam, contact surfaces, etc.) as well as all available material models. Once any part of the computational domain deforms, the Eulerian description of the fluid flow is no longer applicable. Therefore, ADINA solves the governing equations of fluid flow using an Arbitrary-Lagrangian-Eulerian (ALE) formulation (ADINA 2012). One of the benefits in developing the ADINA model is that it gives three-dimensional visualization of the results.

5.2. Validation of ADINA

To check the adequacy of ADINA, results from the well known benchmark problems are compared with the experimental and numerical results obtained previously by other investigators. If the results obtained from ADINA show good agreement with the previous results, then it will be considered fit to be used for further analysis. Therefore, the following four different models were developed: (a) two-dimensional pipe flow model; (b) backward facing step mode; (c) point load deflection model; (d) three-dimensional point load deflection model.

5.2.1. Two-Dimensional Pipe Flow Model

The validation of ADINA is commenced with a very fundamental fluid mechanics boundary layer model, i.e., a two-dimensional pipe flow model. Two parameters, the length of the pipe required to achieve fully developed flow, i.e., the entrance length, and the pressure drop, Δp across the pipe of given length. The model of a horizontal pipe of diameter, $D_{ch} = 0.05$ m is generated in ADINA. Water enters the pipe from the left at a uniform flow velocity, $v = 0.01$ m/sec as shown in Fig. 5.1. Standard Temperature and pressure (STP) conditions of water are considered. The resulting Reynolds number Re , is 500, indicating laminar flow. The flow profile is checked across the cross-sections of the pipe along its length. The distance from the pipe entrance at which a fully developed parabolic flow profile is obtained is marked as the entrance length, L_{ent} . The resulting dimensionless value, L_{ent}/D_{ch} , comes out to be 29.8. Then, the standard relation for the entrance length in laminar pipe flow is considered (Shaughnessy et al. 2005)

$$\frac{L_{ent}}{D_{ch}} = 0.06 Re . \quad (5.1)$$

For a Re of 500, the dimensionless entrance length, L_{ent}/D_{ch} , is 30. The difference between the ADINA and theoretical result is 0.67 %.

In order to determine the pressure drop, Δp , in a two-dimensional pipe of given length, a similar model with the same flow parameters as used for the entrance length is considered in ADINA. The length of the pipe L_{ch} is prescribed as 1 m. Simulation of the model in ADINA gives Δp of 0.126 Pa. The standard relation of pressure drop across a pipe is given by (Shaughnessy et al. 2005)

$$\frac{p_1 - p_2}{\rho} = f_D \frac{L_{ch}}{D_{ch}} \frac{v_k^2}{2} \quad (5.2)$$

or

$$\Delta p = f_D \frac{L_{ch}}{D_{ch}} \frac{\rho v_k^2}{2}, \quad (5.3)$$

where f_D is the Darcy-Weisbach friction coefficient. For laminar flow, it is equal to $64/Re$. For a flow velocity of 0.01 m/s, the theoretical value of Δp obtained from eq. (5.3) is equal to 0.128 Pa. The difference between ADINA and theoretical values is 1.56 %.

5.2.2. Backward Facing Step Model

The validity of ADINA is further verified by comparing the results for backward facing step in a rectangular duct model with the experimental and numerical results. The model developed in ADINA is shown in Fig. 5.2. Flow enters the inlet from left. Flow separation occurs right after the flow passes over the backward facing step of height s_h . It reattaches to the duct bottom wall after a certain distance x . Therefore, the parameter selected for comparison is the reattachment length x of the fluid flow with the duct wall. Figure 5.3 shows the flow velocity profile development with the help of velocity vectors and velocity contours on the duct cross-sections along the length of the duct.

The first comparison is carried out with the results of Nie and Armaly (2003). They performed numerical simulations for incompressible three-dimensional laminar forced convection flow adjacent to backward facing step in a rectangular duct in order to examine the reattachment region of the separated flow on the stepped wall. They selected the dimensions of the duct in such a way that the flow at the inlet section of the duct ($x/s_h = -2$) was not affected significantly by the sudden expansion in the geometry at the step, and the flow at the exit section ($x/s_h = 50$) was fully developed. It was also insured through measurements that the flow was laminar and steady for Reynolds number less than 600. Considering $Re = 400$, they obtained the dimensionless reattachment length, $x/s_h = 7.6$. Similar initial and boundary condition have been adopted in the ADINA model. The dimensionless reattachment length, x/s_h thus obtained is 7.5. The difference is 1.32 %.

The other comparison is with the experimental result of the same parameter, i.e., flow reattachment length, obtained by Williams and Baker (1996). They considered a three-dimensional backward facing step model and ran numerical simulations at different Reynolds number, Re to compare with the work of Armaly et al. (1983). For $Re = 800$, they obtained the dimensionless reattachment length, $x/s_h = 14$. Simulating the same model in ADINA gives value of $x/s_h = 13.122$. The difference is 6.27 %.

5.2.3. Point Load Deflection Model

ADINA has also been tested for the purely structural mechanics part. A two-dimensional horizontal beam model of length, $l_{beam} = 1$ m, height, $b = 0.02$, infinite width, subjected to a vertical concentrated point load, $W = 1$ N at the tip of the beam is generated in ADINA as shown in Fig. 5.4. The beam material is steel with modulus of elasticity, $E = 2.07 \times 10^{11}$ Pa and second moment of area, $I = 1.33 \times 10^{-8}$ m⁴. The beam tip deflects 1.20773×10^{-4} m downwards. Increasing the point load to 300 N results in a tip deflection of 3.623×10^{-2} m. The relation of maximum beam deflection under a concentrated point load at the tip is given by (Ryder 1969)

$$\delta_{max} = -\frac{Wl_{beam}^3}{3EI}. \quad (5.4)$$

The negative sign signifies downward deflection, in negative y -direction. Substituting the parameters of the ADINA beam model, values of $\delta_{max} = 1.21 \times 10^{-4}$ m and 3.632×10^{-2} m for point loads of 1 N and 300 N, respectively, are obtained. The corresponding differences between theory and ADINA are 0.19 % and 0.25 %, respectively.

5.2.4. Three-Dimensional Point Load Deflection Model

A horizontal circular flexible silicone rubber of cylinder length, $l = 0.483$ m, diameter, $D = 0.0254$ m, modulus of elasticity, $E = 2.76 \times 10^6$ Pa, and second moment of area, $I = 2.0435 \times 10^{-8}$ m⁴ subjected to a vertical concentrated tip load, $W = 0.1$ N, in the negative y -direction is considered. The model generated in ADINA is shown in Fig. 5.5. The maximum deflection of the cylinder end, δ_{max} , thus obtained is 6.61×10^{-2} m. Making use of eq. (5.4) and substituting in the same parameters, δ_{max} thus obtained is 6.66×10^{-2} m. The discrepancy between theory and ADINA is 0.75 %.

The good agreement displayed in the above validation tests between ADINA and analytical results have built up confidence that the ADINA model can safely be used to develop, simulate, and analyze the FSI model of the problem under consideration in this thesis.

5.3. Model Description

The three-dimensional FSI flexible cantilevered cylinder model is generated in ADINA in its two modules namely ADINA CFD and ADINA Structures. Dealing first with the fluid part of the model in ADINA CFD, a circular channel of diameter, $D_{ch} = 0.203$ m and length, $L_{ch} = 0.77$ m is generated. Then the outlines of the cylinder and the upstream supports are generated. The cylinder outline serves as an FSI boundary across which the information of fluid forces and solid motion/deformation is passed and the support outline serves as rigid wall. The fluid domain of the FSI model is first discretized. This is done by dividing the surfaces of the fluid domain into segments ranging from 10 to 60, resulting in a mesh density of around 5.6×10^6 elements/m³. An unstructured mesh is then generated by the option available in the software. This creates the meshed fluid domain as shown in Fig. 5.6 (a). For model's solid part in ADINA Structures, the cylinder and the upstream support are generated in such a way that the physical surfaces of these structures match the surfaces of the same in the model's fluid part. In a similar way, the cylinder surface is set as the FSI boundary whereas the support as a rigid wall. This matching consistency ensures two-way continuity of information flow across the boundaries and helps ADINA to develop coupling between the fluid and solid domains. The cylinder material is silicone rubber, with modulus of elasticity, $E = 2.76 \times 10^6$ Pa, flexural rigidity, $EI = 5.6391 \times 10^{-2}$ N m², density, $\rho = 1120$ kg/m³, diameter, $D = 0.0254$ m, and length, $L = 0.52$ m. The cylinder is terminated by a conical end-piece of length, $l = 0.037$ m and end-shape factor, $f \approx 0.48$; the procedures to calculate f is given in Appendix A. The upstream support consists of four perpendicular arms. These are designed in such a way as to keep the flow past the support as streamlined as possible. The material of the support is taken as steel with $E = 2.0 \times 10^{11}$ Pa. The solid domain of the FSI model is then discretized. This is done by dividing the surfaces of the solid domain into the same number of segments as the fluid domain surfaces in order to match the nodes on all the common surfaces of both the domains. The resulting mesh density of solid domain obtained is around 7.8×10^7 elements/m³. Similar to fluid domain, an unstructured mesh is generated. The meshed solid domain is shown in Fig. 5.6 (b). The values of χ (defined in Chapter 2) and α (defined in

Chapter 3) for the present model are equal to 1.03 and 7.99, respectively. As indicated earlier, the value of χ arrow 1 (Chapter 2) and $\alpha \gg 1$ (Chapter 3) indicates the case of an unconfined flow. Therefore, the present model, as pointed out by the values of χ and α , is essentially the case of an unconfined flow.

ADINA simulations are carried out for two different fluids, namely water and air. Different dynamics of the cylinder is obtained for the two fluids. A model without the upstream support arms is also generated and simulated for velocities beyond the critical velocity for flutter in water flow and for the entire velocity range in air flow as shown in Fig 5.7. The faces of the model are divided into segments ranging from 5 to 30 resulting in mesh densities of around 5.2×10^5 and 7.2×10^6 elements/m³ in CFD and solid parts, respectively. Such mesh densities also produce reasonable results. The results of both simulations are presented and compared hereunder.

5.4. CFL Condition

The Courant–Friedrichs–Lewy (CFL) condition is a necessary condition for convergence while solving certain partial differential equations numerically. It arises in the numerical analysis of time-marching schemes, when these are used for the numerical solution. The time step must be less than a certain time in many time-marching computer simulations; otherwise the simulation will produce incorrect results. The CFL condition is commonly prescribed for those terms of the finite-difference approximation of general partial differential equations, which model the advection phenomenon (Courant et al. 1967). The Courant number, in fact, reflects the portion of a cell that a fluid particle will traverse by advection in one time step. For a one-dimensional case, the CFL has the form

$$C = \frac{U\Delta t}{\Delta x} \leq C_{max}, \quad (5.5)$$

where U is the dimensional flow velocity, Δt is the time step, Δx is the length interval, and C is the Courant number. C_{max} is the maximum value of Courant number that helps in determining the minimum value of time step. The value of C_{max} changes with the method used to solve the discretized equation. If a time-marching solver is used, then typically $C_{max} = 1$. Δt can be determined by re-adjusting eq. (5.5) as

$$\Delta t = \frac{C\Delta x}{U}. \quad (5.6)$$

Since $C = 1$, the equation becomes

$$\Delta t = \frac{\Delta x}{U}. \quad (5.7)$$

The simulation has been run for flow velocities up to 6.41 m/s. In order to obtain one consistent value of Δt for the entire simulation, a mean value of flow velocity is considered, i.e., $U = 3.21$ m/s; the corresponding dimensionless velocity is $u = 5.0$. With the unstructured mesh in both fluid and solid domains, the minimum and maximum length intervals, Δx , are found to be 0.0039 m and 0.0425 m, respectively. Substituting U and the terminal values of Δx in eq. (5.7) gives $0.001 \leq \Delta t \leq 0.01$ s. It is good to have a value of Δt close to the lower limit especially at the initial stages of the simulation and cylinder higher frequency modes, because of the conditions being unsteady and developing, and changes in the parameters taking place mode rapidly. But limitations are imposed on the use of the value of Δt smaller than a certain limit. The reason being that for a three-dimensional model, smaller Δt increases the simulation time many folds and makes the size of the output file beyond the capabilities of many powerful systems with large memories. For this reason, $\Delta t = 0.01$ s is selected.

5.5. Model in Water Flow

5.5.1. Adequacy of the Numerical Solution

Adequacy of the numerical solution is established by simulating the numerical model especially for this purpose and comparing the critical flow velocity for the onset of first mode divergence, $u_{cr,d1}$, with the experimental one. The results of the numerical model yield $u_{cr,d1} = 1.80$. The measured critical flow velocity, $u_{cr,d1}$, in experiments is 1.87 (Chapter 2). The difference is 3.74 %, which may be considered acceptable.

5.5.2. Numerical Results

First, the flexible cantilevered cylinder model is considered in water flow. The physical properties of water at Standard Temperature and Pressure (STP) are input in ADINA. A flow

velocity range of $0.064 \leq U \leq 8.97$ m/s is utilized for the simulation runs. The relation used to render the flow velocity dimensionless is

$$u = \left(\frac{\rho A}{EI} \right)^{1/2} UL, \quad (5.8)$$

as given by Païdoussis (2004). Substituting the input parameters simplifies the relation as $u = 1.56 U$, which gives the corresponding dimensionless velocity range as $0.1 \leq u \leq 14.0$. Utilizing the relation for Re gives its range as $1.3 \times 10^4 \leq \text{Re} \leq 1.81 \times 10^6$. The $k-\omega$ turbulence model is used for water flow.

Figure 5.8 shows the dimensionless mean cylinder tip displacement, $\eta^*(1) = \bar{y}(L)/D$, as a function of u . The figure illustrates the dynamics of the cylinder up to static instability, i.e., divergence. It is also clear from the figure that divergence does not develop abruptly. Therefore, it becomes rather difficult to locate the critical velocity for divergence, precisely. For this reason, a rougher but reliable criterion of $\eta^*(1)$ surpassing a threshold is used. This threshold is arbitrarily chosen as $\eta^*(1) = 0.023$. Physically, this criterion corresponds to about twice the cylinder diameter. At $u_{cr,d1} = 1.80$, $\eta^*(1)$ surpasses the threshold and thus marks the onset of divergence in its first mode as shown in Fig 5.9 (a). At higher flow velocities, the cylinder amplitude varies; later, gradually the first mode divergence transforms into second mode at $u_{cr,d2} \approx 4.30$ as shown in Fig. 5.9 (b). The second mode divergence is based on visual inspection. The results are shown in Table 5.1. As the flow velocity increases, one expects the cylinder to become dynamically unstable with relatively large amplitude oscillations or flutter, which has been observed previously by Païdoussis et al. (2002) and Semler et al. (2002) in their analytical and experimental work at $5.16 \leq u \leq 5.5$. In fact, reaching the same or even higher values of u does not produce any flutter in the cylinder in the ADINA simulations, as can be seen in Figs 5.10 (b) and (c). A possible reason might be due to the inherent numerical damping imposed in ADINA on the solid that damps out the higher mode oscillations.

ADINA employs a conditionally stable algorithm. A conditionally stable algorithm necessitates that the size of the time step used be inversely proportional to the highest frequency of the system. In fact, this is a strict limitation, as accuracy in the lower modes can be attained with time steps which are very large compared with the period of the highest mode. When only low mode response is of interest, it is often advantageous for an algorithm to have some form of

numerical dissipation or damping, which stabilizes the numerical integration scheme by damping out the unwanted high frequency modes (Hilber et al. 1977). As for ADINA, numerical damping works well at lower mode static instabilities but introduces a substantial damping effect on the higher modes, which is not desirable. This inherent unwanted damping effect makes the cylinder remain in the second mode buckled shape at $u \approx 5.10$ as shown in Fig. 5.10 (a); it remains there for the supposedly post-flutter velocities, $u = 5.5$ and 5.6 (Figs. 5.10 (b) and (c)). At further higher dimensionless flow velocity of 8.0 , the cylinder develops third mode shape but the dynamic response is still damped as shown in Fig. 5.10 (d) by the same damping present in the algorithm. For this velocity and all higher velocities, the upstream support arms are removed in order to nullify any of their possible effects on the dynamics of the cylinder. A practical way to reduce its contribution in the overall system damping as much as possible at higher frequency modes is to decrease the time step. By doing so, the ADINA simulation becomes very expensive in terms of simulation execution time (it could reach up to a couple of weeks) and size of the output file (it might reach up to 100 Gigabyte). There are no powerful computing systems at hand, which can open and post-process the output data of files of such size. For this reason, no attempt is made to use very small Δt in the model to handle the numerical damping and obtain second and third cylinder mode flutter.

In addition to the inherent numerical damping imposed on the system in the software, it is important to also look into physical aspect such as vortex-induced vibration. Blevins (1990) explains the underlying physics generating structural vibration subjected to vortex shedding as: “As a fluid particle flows toward the leading edge of a cylinder, the pressure in the fluid particle rises from the free stream pressure to the stagnation pressure. The high fluid pressure near the leading edge impels flow about the cylinder as boundary layers develop about both sides. However, the high pressure is not sufficient to force the flow about the back of the cylinder at high Reynolds numbers. Near the widest section of the cylinder, the boundary layers separate from each side of the cylinder surface and form two shear layers that trail aft in the flow and bound the wake. Since the innermost portion of the shear layers, which is in contact with the cylinder, moves much more slowly than the outermost portion of the shear layers, which is in contact with the free flow, the shear layers roll into the near wake, where they fold on each other and coalesce into discrete swirling vortices. A regular pattern of vortices, called a vortex street, trails aft in the wake. The vortices interact with the cylinder and they are the source of the effects

called vortex-induced vibration”. Therefore, velocity and pressure contours are obtained at the cross-sections 0.71 m (7.5 cylinder diameters downstream of cylinder free end) and 0.715 m (7.7 cylinder diameters downstream of cylinder free end) from the channel inlet at dimensionless turbulent flow velocities $u = 5.6$ and 8.0 , respectively. These contours are shown in Figs. 5.11 and 5.12. Both figures clearly show low velocity and high pressure in the wake region and relatively high velocity and low pressure in the swirling flow on either sides of the channel centreline. The apparent swirling flow seems to be part of the vortices. These vortices at the same cross-sections at both the flow velocities are monitored throughout the simulation but no vortex shedding advancing with time in either case is detected. This might also be another reason for the system to have no oscillations because of the absence of vortex shedding. From these results, a strong need is felt to verify experimentally the presence of vortex shedding in the present model and to see whether it contributes to the cylinder dynamics.

One of the effective experimental methods to observe the vortex shedding is the particle Image Velocimetry (PIV). Through PIV, the velocity field across the channel cross-section at different times can be obtained. It measures the velocity field by taking images shortly after each other and calculating the distance individual particles travelled within the time intervals. From the known time difference and the measured displacements, the velocity of each particle is calculated. This experimental method is beyond the scope of the present investigation and can be done later as a separate investigation.

5.6. Model in Air Flow

5.6.1. Numerical Results

In addition to the simulations in water flow, the flexible cantilevered cylinder model has also been considered in air flow. The slender cylinder subjected to air flow is the limiting case of a practical application of a long train with the last carriage having a tapered end inside a tunnel. The physical properties of air at Standard Temperature and Pressure (STP) are input in ADINA. A velocity range of $5 \leq U \leq 65$ m/s is utilized for the simulations. Substitution of the input parameters in eq. (5.8) yields $u = 0.054 U$, so that the corresponding dimensionless velocity range as $0.27 \leq u \leq 3.51$. Utilizing the expression for Re gives its range $6.715 \times 10^4 \leq Re \leq 8.73 \times 10^5$. The $k-\omega$ turbulence model is used for air flow. It is noticeable that the dimensional

velocity corresponding to a dimensionless value of, say, $u = 3.51$ for air is far higher than its counterpart for water. This is because the relation to render the velocity dimensionless involves the density of fluid, and water is about 1000 times denser than air. The multiplying factor of the velocity conversion relation in the case of water is 28.9 times larger than of air. As indicated in Section 5.3, a cantilevered cylinder model without upstream support arms is used for simulation in air flow. The reason for that is to eliminate any slight possibility of flow disturbance from the support arms, especially at higher flow velocities at which flutter may possibly occur.

Figure 5.13 shows the dimensionless mean cylinder tip displacement, $\eta^*(1)$, as a function of u . The figure illustrates the dynamics of the cylinder up to static instability, i.e., divergence. Similar to the model in water flow, the cylinder tip magnitudes are very small and the onset of divergence is gradual. Therefore, a threshold is arbitrarily chosen as $\eta^*(1) = 0.04$. Any displacement surpassing this value marks the onset of divergence, which is achieved at $u_{cr,d1} = 1.62$. Figure 5.14 (a) shows the orthographic and isometric views of the cylinder first mode. At higher flow velocities, the cylinder amplitude varies and later, gradually, the first mode divergence evolves into second mode shape at $u_{cr,d2} \approx 3.02$. The diverged second mode of the cylinder is shown in Fig. 5.14 (b). The same results are also presented in Table 5.2.

The onset of flutter is identified by obtaining the r.m.s. amplitude, $\eta(1)_{r.m.s.}$, of the cylinder end-piece tip response and the PSDs of the vibration signal at increasing flow velocities. Figure 5.15 shows a typical diagram of $\eta(1)_{r.m.s.}$ versus u , used to locate flutter. The steep rise of $\eta(1)_{r.m.s.}$ before $u_{cr,fl2}$ does not correspond to a stable solution; the oscillations seem to be in transition phase. Therefore, any of these values cannot be considered for the flutter critical velocity. A stable solution for the Hopf bifurcation is obtained at $u_{cr,fl2} = 3.20$, which leads to flutter in the second mode. The reduction in amplitude, after a high of $0.0362 D$ is reached, reflects gradual changes in modal shape with increasing u . $\eta(1)_{r.m.s.}$ values are also tabulated in Table 5.3. Figure 5.16 shows the PSDs of the vibration signal at $u = 1.08, 3.08,$ and 3.20 . Figures 5.16 (a) and (b) show PSDs before first mode divergence and after second mode divergence, respectively, and display no dominant frequency; whereas Fig. 5.16 (c) shows the PSD at the onset of second mode flutter and displays a dominant frequency, $f_{cr,fl2} = 3.52$ Hz. The corresponding dimensionless value ($\omega_{cr,fl2} = 18.96$) is obtained from the expression given in Païdoussis (2004).

5.7. Comparison of the Results

The critical velocities marking the onset of static and dynamic instabilities of the models in water and air flow are compared in Table 5.4. Third mode flutter for the model in air flow is not obtained due to the system's limitations. The word 'static' in the case of the water flow model is included to indicate inability of the software to exhibit oscillations due to the damping effect as already explained. The numerical model in air flow shows lower $u_{cr,d1}$, $u_{cr,d2}$, and $u_{cr,fl2}$ than their counterparts for the model in water flow. One of the possible reasons for the lower $u_{cr,d1}$ for the numerical model in air flow is the criterion of the threshold value chosen to mark the onset of divergence, which can vary based on the judgment. For all the models, the second mode divergence is evolved from the first mode before the onset of flutter. Since $u_{cr,fl2}$ for the numerical model in air flow is lower than for the models in water flow, this makes the $u_{cr,d2}$ for the numerical model lower too. The reason for the lower $u_{cr,fl2}$ for the numerical model in air flow is due to the inherent lower viscous damping of air, as also indicated in Chapter 3. It is also observed in both the numerical models that the cylinder displacement and oscillation magnitudes for the entire velocity range are minuscule. It seems that the negative damping of the system somehow does not increase considerably in ADINA resulting in small magnitudes of cylinder motion. The numerical and analytical model results in terms of the critical flow velocities for the onset of instabilities for water and air flows are compared in Chapter 6.

5.8. Summary

In this chapter, after the introduction of the numerical simulation software ADINA, it was validated followed by the determination of CFL condition for numerical stability. The cantilevered cylinder in axial flow was then modeled in ADINA FSI and simulated to study its dynamics in water and air flows. Finally, the two models were compared.

The chapter started with the general introduction of ADINA and its solution capabilities in various multiphysics phenomena. The software was then validated by developing two-dimensional pipe model, backward facing step model, point load deflection model, and three-dimensional point load deflection model in ADINA and comparing their results with the experimental and theoretical results found in the literature. All showed reasonable agreements.

CFL condition was also utilized to determine the time step range necessary for numerical stability.

The problem under consideration, i.e., cantilevered cylinder in axial flow was modeled in ADINA with the dimensions and input parameters nearly equal to the experimental values. Two such models one with upstream support arms and finer mesh and the other without the support arms and coarser mesh were developed with both models having cylinder downstream ends terminated by end-pieces. The model was first simulated in water flow and the mean displacements of cylinder tip at increasing velocities were recorded. Unfortunately, the simulations could show only the static instability, i.e., divergence in first and second modes even at velocities beyond $u_{cr,fl2}$ determined by experiments. Possible explanation is given in Section 5.5. The model without support arms was then simulated in air flow. Mean values of cylinder dimensionless tip displacements and their r.m.s. values plotted against dimensionless flow velocities, u , helped determining the critical velocities for divergence, $u_{cr,d1}$ and $u_{cr,d2}$ and flutter, $u_{cr,fl2}$, respectively. Finally, the models in water and air flows were compared for critical flow velocities and the results revealed that the critical flow velocities for the model in air flow were lower than the one in water flow.

Table. 5.1. The dimensionless mean displacement of the free-end tip of the cylinder, $\eta^*(1)$, as a function of increasing dimensionless flow velocity, u , in water flow.

Dimensionless velocity, u	Dimensional velocity, U (m/s)	Reynolds number, Re	Dimensionless mean tip displacement, $\eta^*(1)$
0.1	0.064	1.30×10^4	2.35×10^{-4}
0.2	0.128	2.59×10^4	8.35×10^{-4}
0.4	0.256	5.18×10^4	3.36×10^{-3}
0.6	0.385	7.78×10^4	7.74×10^{-3}
0.8	0.513	1.04×10^5	1.00×10^{-2}
1	0.641	1.30×10^5	1.33×10^{-2}
1.4	0.897	1.81×10^5	2.12×10^{-2}
1.8	1.154	2.33×10^5	2.37×10^{-2}
1.9	1.218	2.46×10^5	2.24×10^{-2}
2.0	1.280	2.59×10^5	2.26×10^{-2}
2.1	1.350	2.73×10^5	2.27×10^{-2}
2.2	1.410	2.85×10^5	2.32×10^{-2}
2.3	1.474	2.98×10^5	2.16×10^{-2}
2.4	1.540	3.11×10^5	2.18×10^{-2}
2.5	1.602	3.24×10^5	2.14×10^{-2}
2.6	1.670	3.38×10^5	2.09×10^{-2}
2.7	1.730	3.50×10^5	2.04×10^{-2}
2.8	1.790	3.62×10^5	1.91×10^{-2}
3.0	1.920	3.88×10^5	1.87×10^{-2}
3.2	2.050	4.14×10^5	1.82×10^{-2}
3.3	2.120	4.29×10^5	1.77×10^{-2}
3.4	2.180	4.41×10^5	1.72×10^{-2}
3.5	2.240	4.53×10^5	1.68×10^{-2}
3.6	2.310	4.67×10^5	1.64×10^{-2}
3.7	2.370	4.79×10^5	1.57×10^{-2}
3.8	2.440	4.93×10^5	1.54×10^{-2}
3.9	2.500	5.06×10^5	1.51×10^{-2}
4.0	2.560	5.18×10^5	1.46×10^{-2}
4.1	2.630	5.32×10^5	1.42×10^{-2}
4.2	2.690	5.44×10^5	1.39×10^{-2}
4.3	2.760	5.58×10^5	1.37×10^{-2}
4.4	2.820	5.70×10^5	1.39×10^{-2}
4.5	2.880	5.82×10^5	1.36×10^{-2}
4.6	2.950	5.96×10^5	1.37×10^{-2}
4.7	3.010	6.09×10^5	1.32×10^{-2}
4.8	3.080	6.23×10^5	1.33×10^{-2}
4.9	3.140	6.35×10^5	1.33×10^{-2}
5.0	3.210	6.49×10^5	1.33×10^{-2}

Table. 5.2. The dimensionless mean displacement of the free-end tip of the cylinder, $\eta^*(1)$, as a function of increasing dimensionless flow velocity, u , in air flow.

Dimensionless velocity, u	Dimensional velocity, U (m/s)	Reynolds number, Re	Dimensionless mean tip displacement, $\eta^*(1)$
0.270	5.0	6.72×10^4	3.44×10^{-3}
0.540	10.0	1.34×10^5	1.21×10^{-2}
1.080	20.0	2.69×10^5	3.18×10^{-2}
1.620	30.0	4.03×10^5	4.12×10^{-2}
2.160	40.0	5.37×10^5	4.00×10^{-2}
2.700	50.0	6.72×10^5	3.39×10^{-2}
2.970	55.0	7.39×10^5	3.06×10^{-2}
3.024	56.0	7.52×10^5	2.98×10^{-2}
3.078	57.0	7.66×10^5	2.99×10^{-2}
3.132	58.0	7.79×10^5	2.87×10^{-2}
3.159	58.5	7.86×10^5	2.76×10^{-2}
3.164	58.6	7.87×10^5	3.07×10^{-2}

Table. 5.3. The r.m.s. amplitude of cylinder end-piece tip vibration, $\eta(1)_{\text{r.m.s.}}$, versus u , in air flow.

Dimensionless velocity, u	Dimensional velocity, U (m/s)	Reynolds number, Re	r.m.s. amplitude of tip vibration, $\eta(1)_{\text{r.m.s.}}$
0.270	5.0	6.72×10^4	2.63×10^{-4}
0.540	10.0	1.34×10^5	7.41×10^{-4}
1.080	20.0	2.69×10^5	3.09×10^{-3}
1.620	30.0	4.03×10^5	5.61×10^{-3}
2.160	40.0	5.37×10^5	6.94×10^{-3}
2.700	50.0	6.72×10^5	6.77×10^{-3}
2.970	55.0	7.39×10^5	6.59×10^{-3}
3.024	56.0	7.52×10^5	6.33×10^{-3}
3.078	57.0	7.66×10^5	6.52×10^{-3}
3.132	58.0	7.79×10^5	6.64×10^{-3}
3.159	58.5	7.86×10^5	6.54×10^{-3}
3.164	58.6	7.87×10^5	1.28×10^{-2}
3.170	58.7	7.88×10^5	1.44×10^{-2}
3.175	58.8	7.90×10^5	1.68×10^{-2}
3.181	58.9	7.91×10^5	2.14×10^{-2}
3.186	59.0	7.92×10^5	2.61×10^{-2}
3.191	59.1	7.94×10^5	3.46×10^{-2}
3.197	59.2	7.95×10^5	3.46×10^{-2}
3.202	59.3	7.96×10^5	3.53×10^{-2}
3.213	59.5	7.99×10^5	3.58×10^{-2}
3.224	59.7	8.02×10^5	3.64×10^{-2}
3.229	59.8	8.03×10^5	3.62×10^{-2}
3.294	61.0	8.19×10^5	3.62×10^{-2}
3.510	65.0	8.73×10^5	3.23×10^{-2}

Table. 5.4. Comparison of critical flow velocities for instabilities between models in water and air flows.

Fluid/instabilities	First mode divergence, $u_{cr,d1}$	Second mode divergence, $u_{cr,d2}$	Second mode flutter, $u_{cr,fl2}$	Third mode flutter, $u_{cr,fl3}$
Water	1.80	≈ 4.30	≈ 5.10 (static)	≈ 8.0 (static)
Air	1.62	≈ 3.02	3.20	--

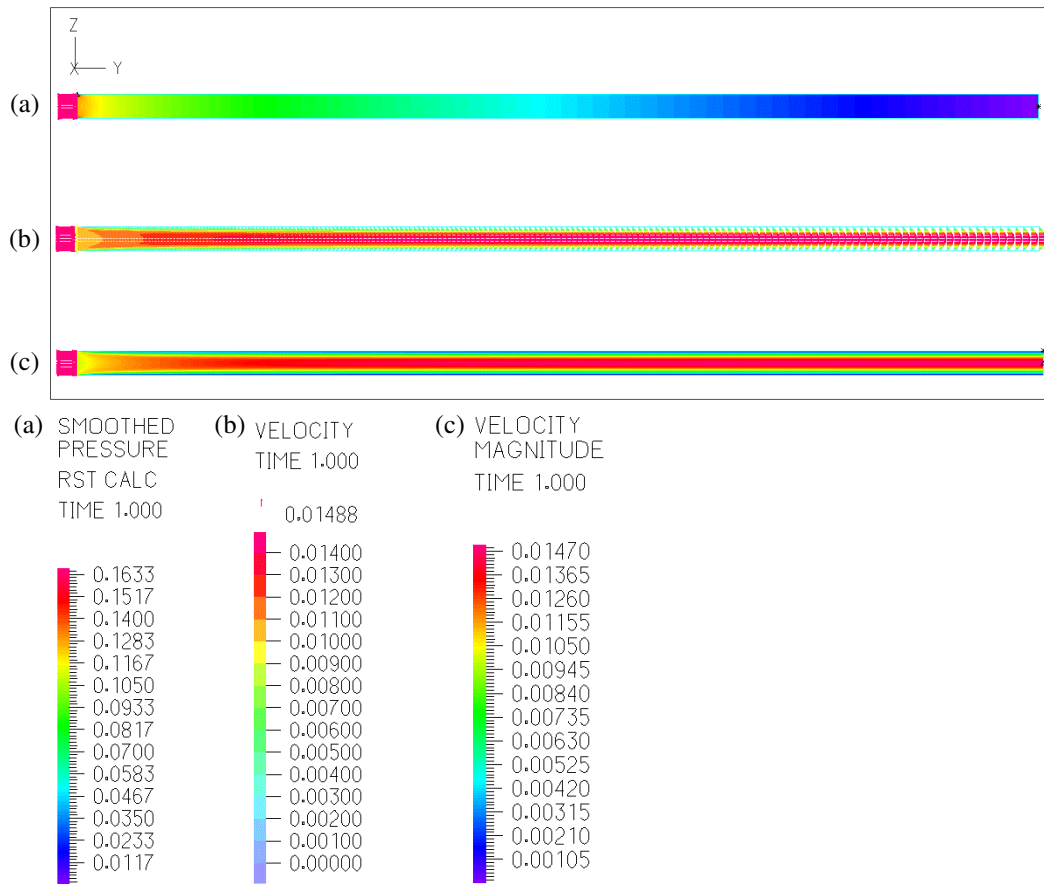


Fig. 5.1. Two-dimensional flow model in ADINA showing (a) pressure contours, (b) velocity vectors, and (c) velocity contours.

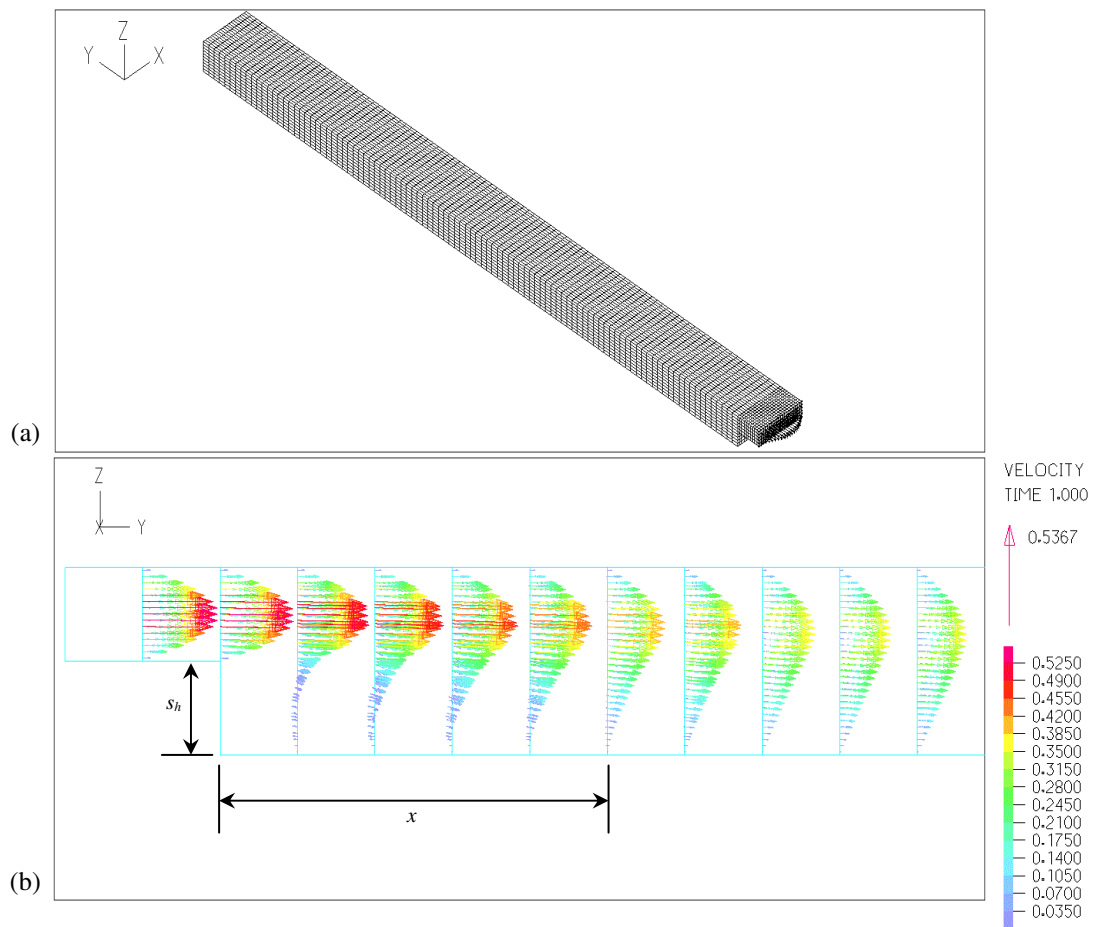


Fig. 5.2. (a) Mesh of the backward facing step in rectangular duct model in ADINA; (b) development of the flow velocity profile and reattachment in the rectangular duct.

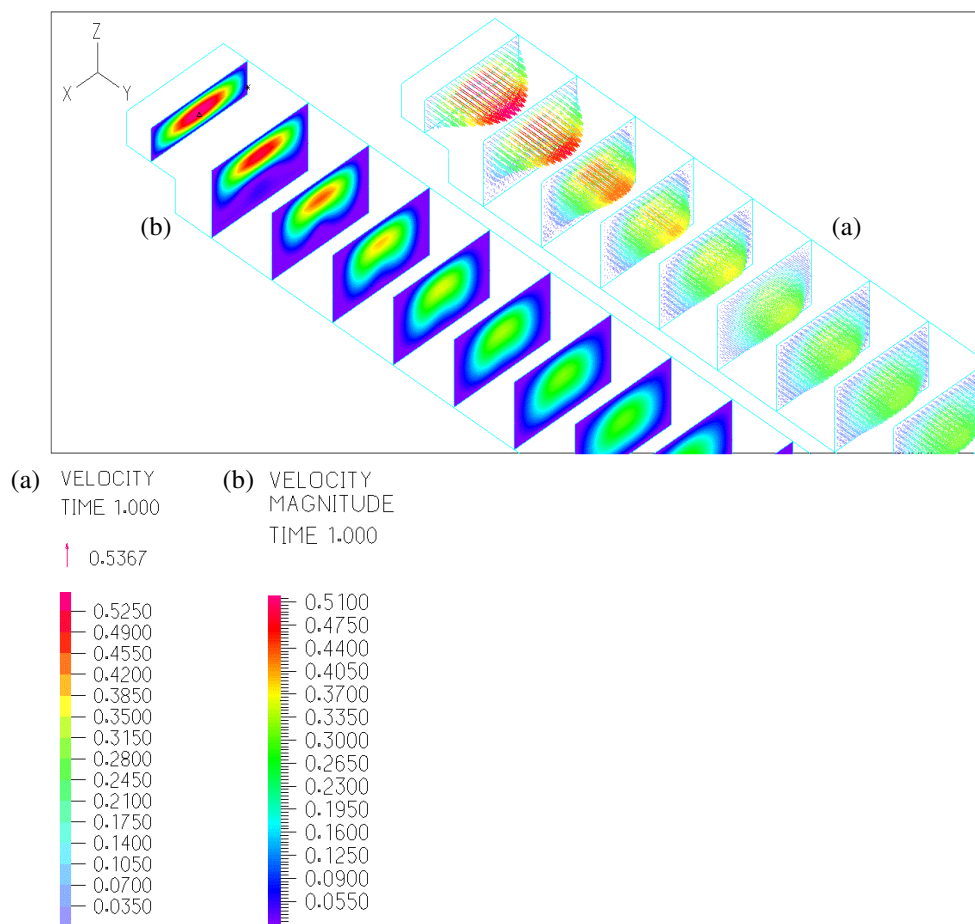


Fig. 5.3. Development of the flow velocity profile shown by velocity vectors and velocity contours.

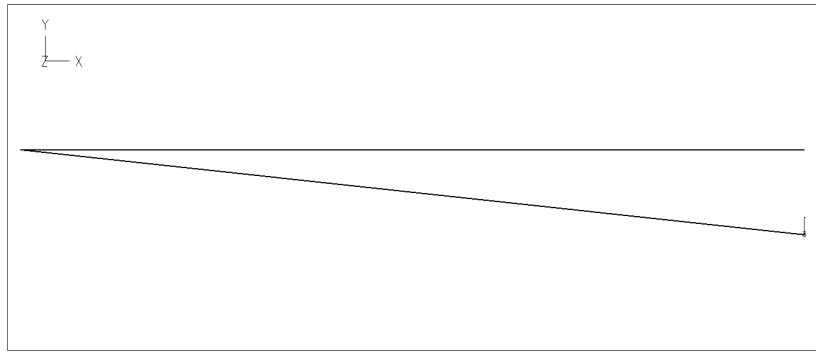


Fig. 5.4. Two-dimensional point force deflection beam model.

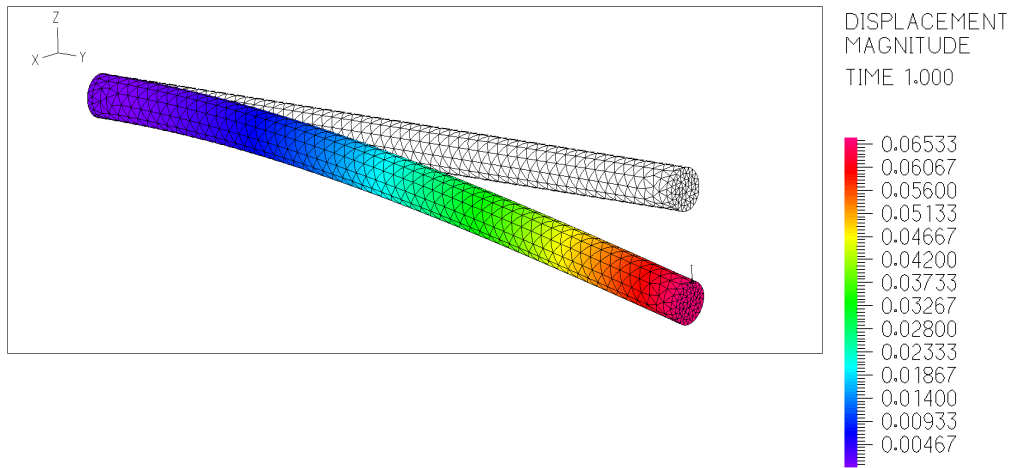


Fig. 5.5. Three-dimensional point force deflection cylinder model.

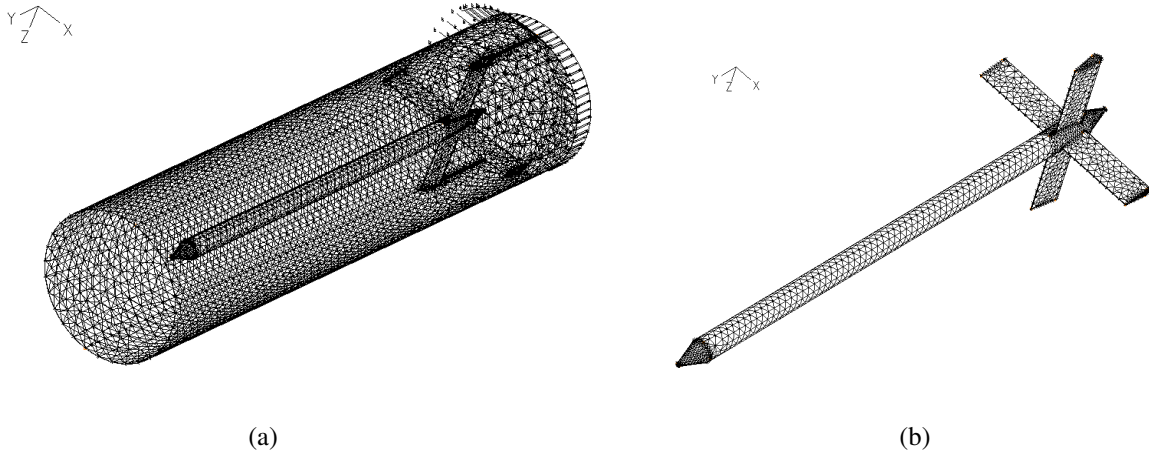


Fig. 5.6. (a) Fluid domain in ADINA CFD; (b) solid domain in ADINA Structures.

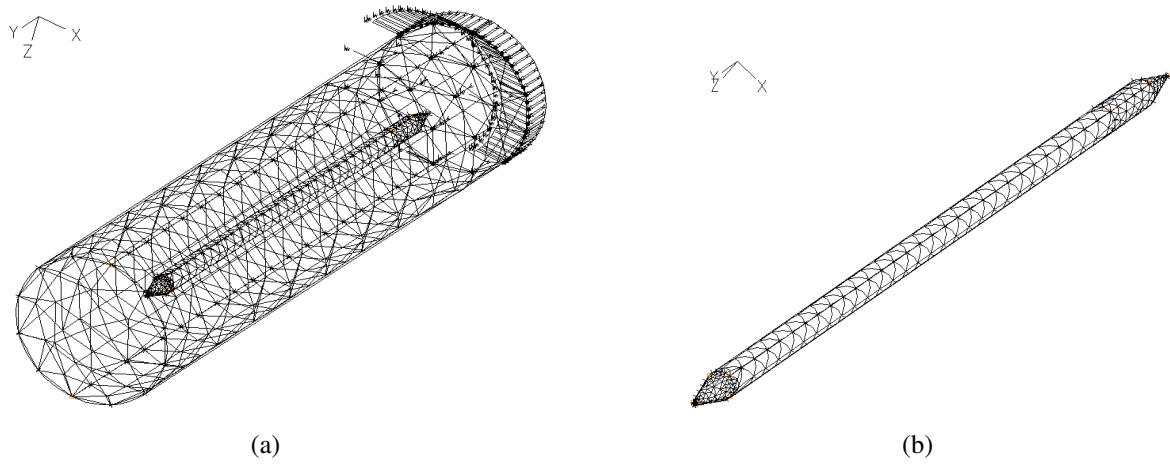


Fig. 5.7. (a) Fluid domain in ADINA CFD; (b) solid domain in ADINA Structures.

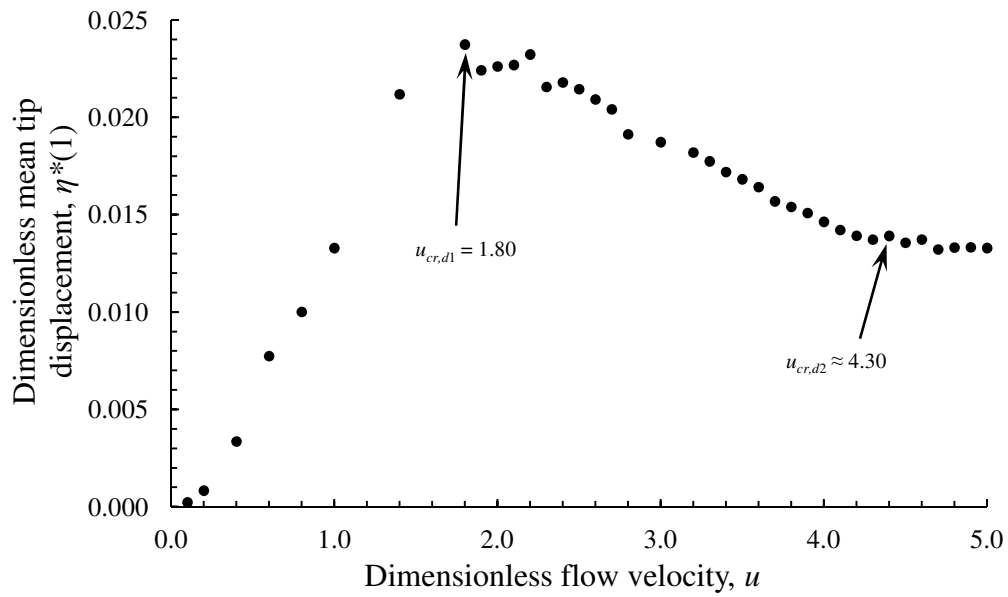


Fig. 5.8. The dimensionless mean displacement of the free-end tip of the cylinder, $\eta^*(1)$, as a function of increasing dimensionless flow velocity, u , in water flow showing the development of divergence.

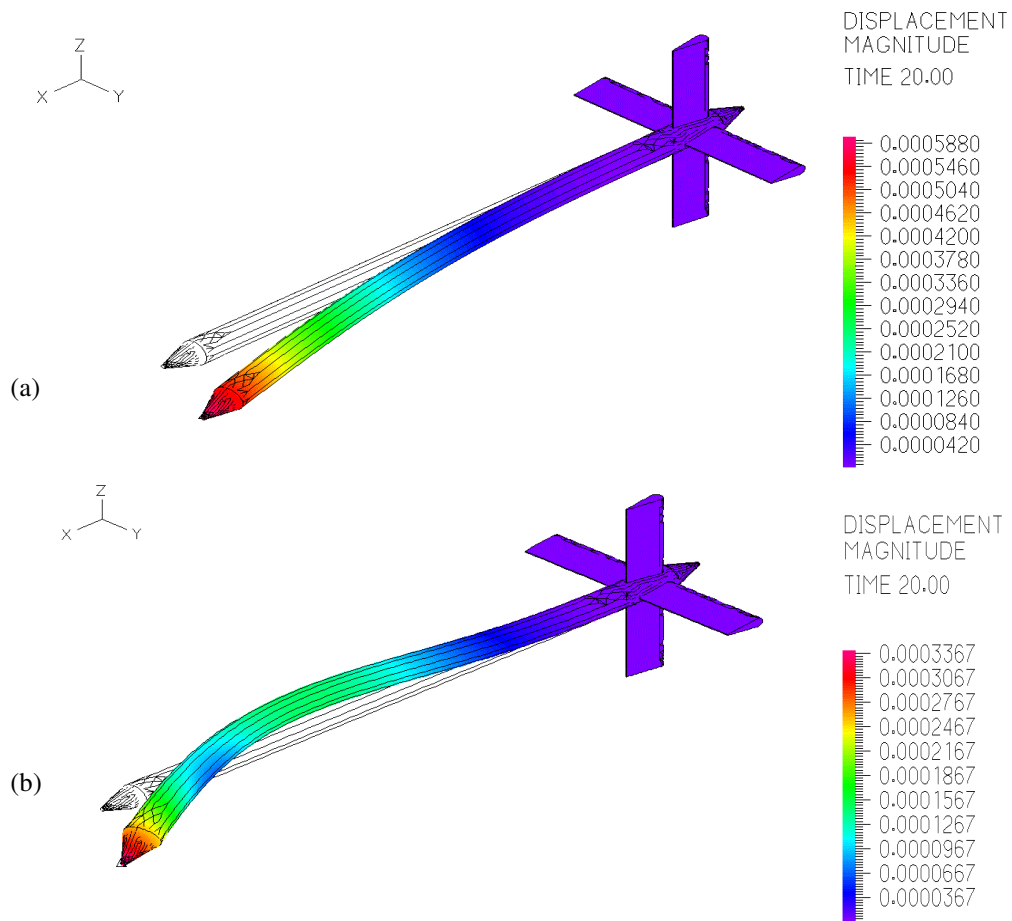


Fig. 5.9. Cylinder mode shapes at (a) $u_{cr,d1} = 1.8$; (b) $u_{cr,d2} = 4.3$ in water flow.

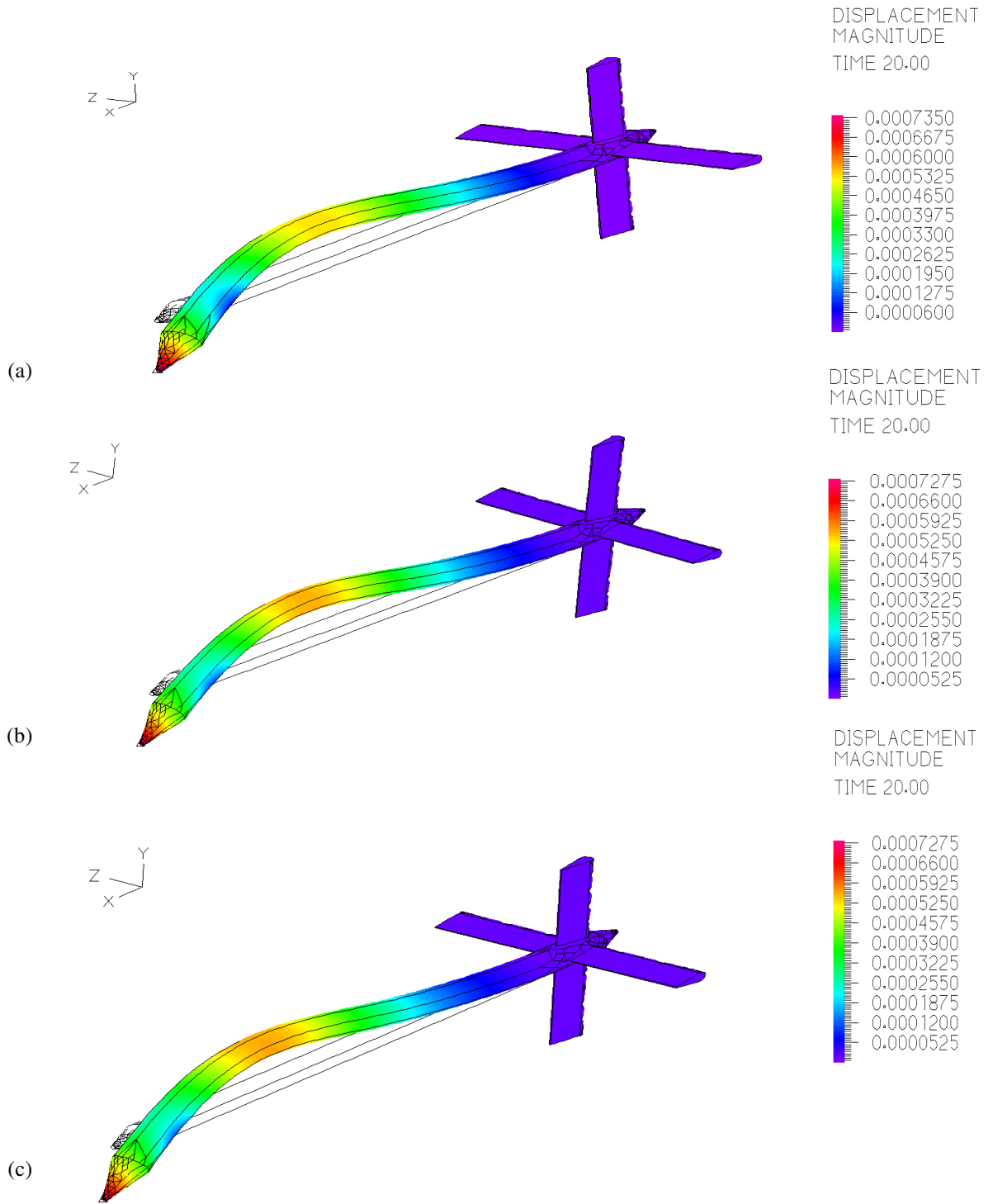


Fig. 5.10. (a,b,c). Caption on next page.

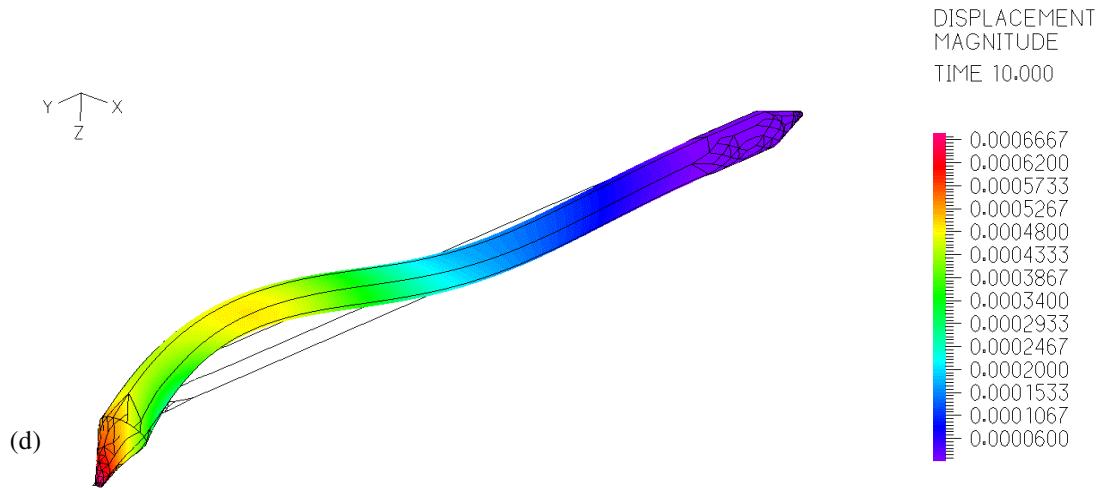


Fig. 5.10. Cylinder mode shapes at (a) $u = 5.1$; (b) $u = 5.5$; (c) $u = 5.6$; (d) $u = 8.0$ in water flow.

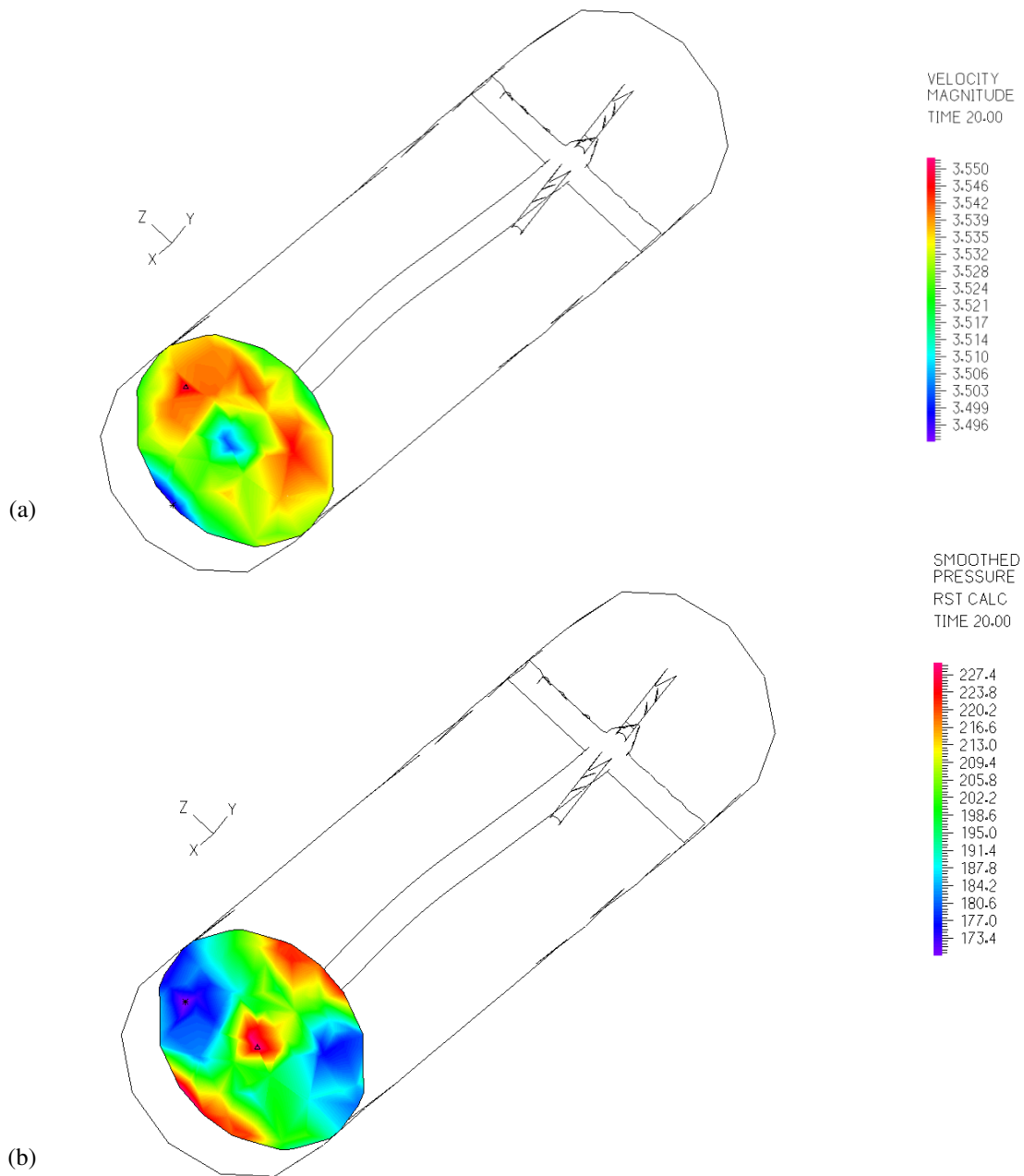


Fig. 5.11. (a) Velocity contours and (b) pressure contours at a distance of 0.71 m from the channel entrance at $u = 5.6$ in water flow.

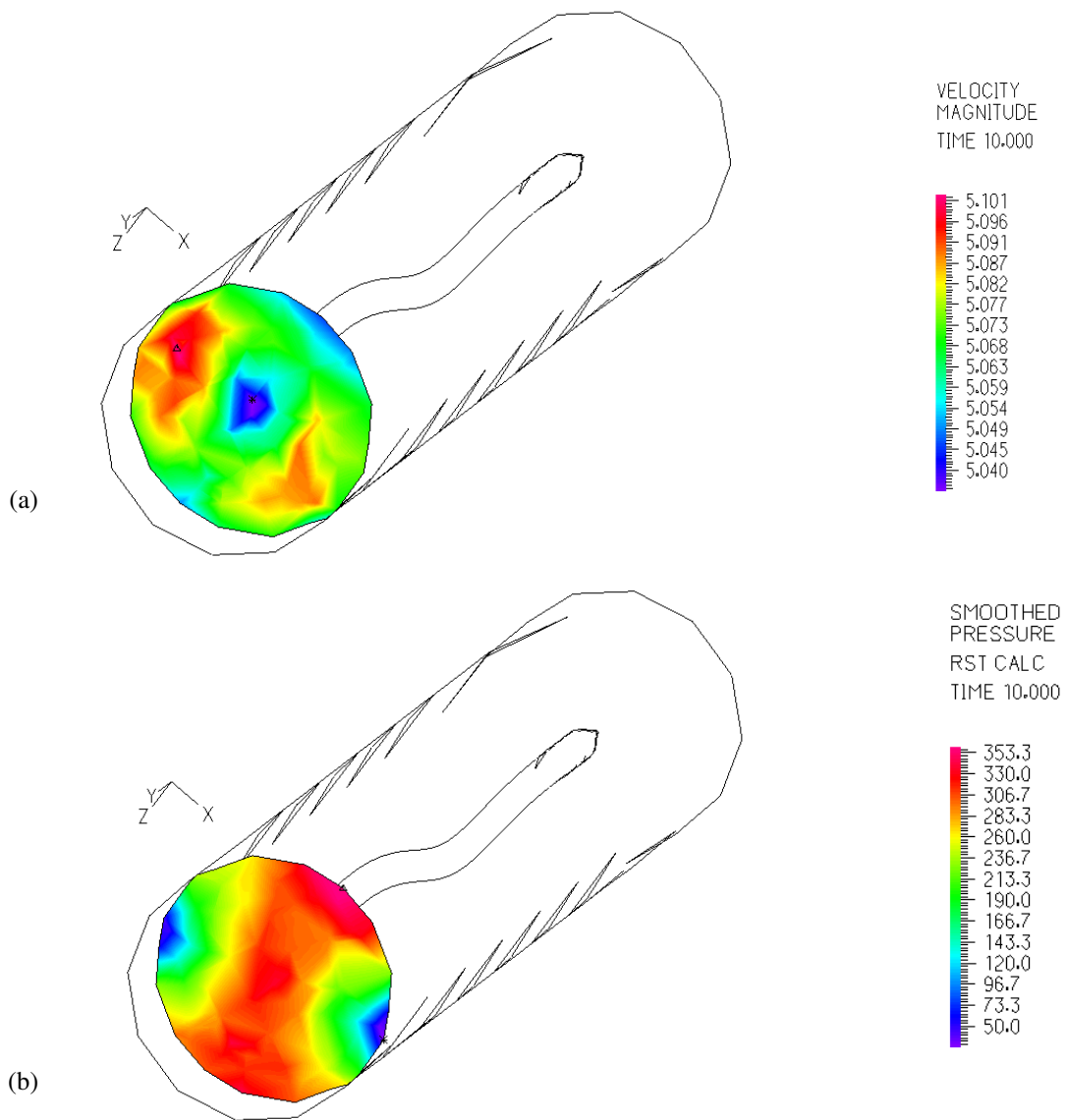


Fig. 5.12. (a) Velocity contours and (b) pressure contours at a distance of 0.715 m from the channel entrance at $u = 8.0$ in water flow.

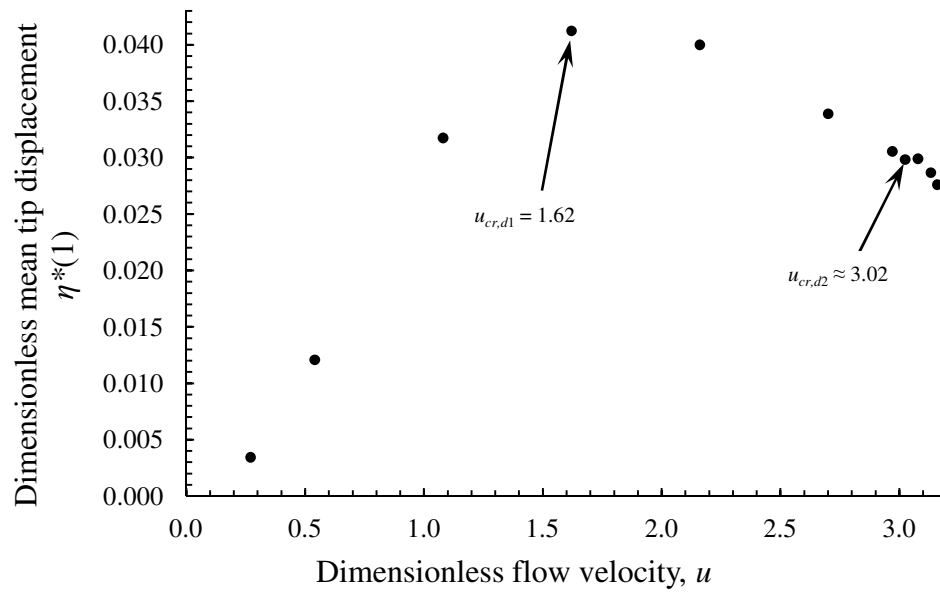


Fig. 5.13. The dimensionless mean displacement of the free-end tip of the cylinder, $\eta^*(1)$, as a function of increasing dimensionless flow velocity, u , in air flow showing the development of divergence.

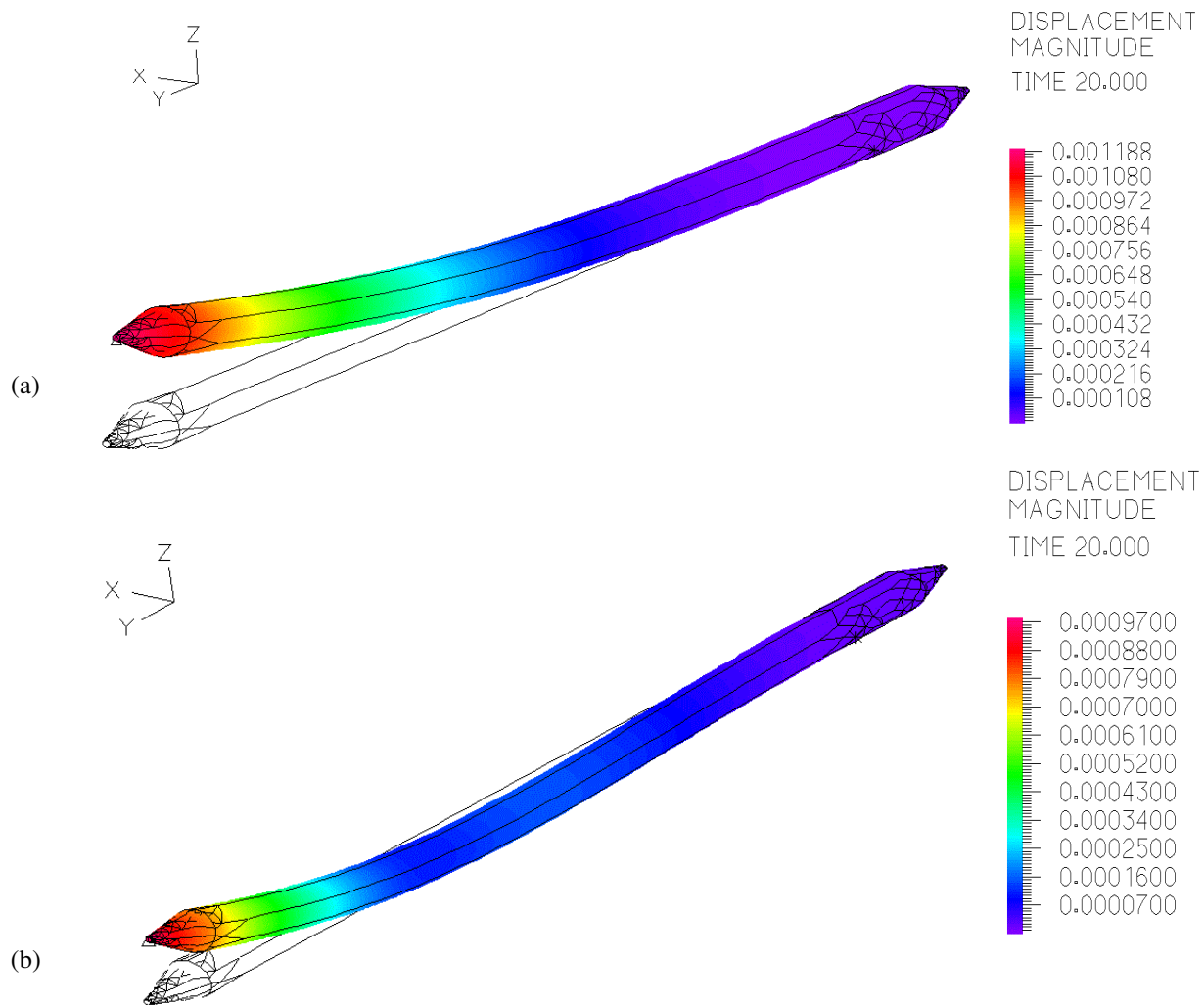


Fig. 5.14. Cylinder mode shapes at (a) $u_{cr,d1} = 1.62$; (b) $u_{cr,d2} = 3.02$ in air flow.

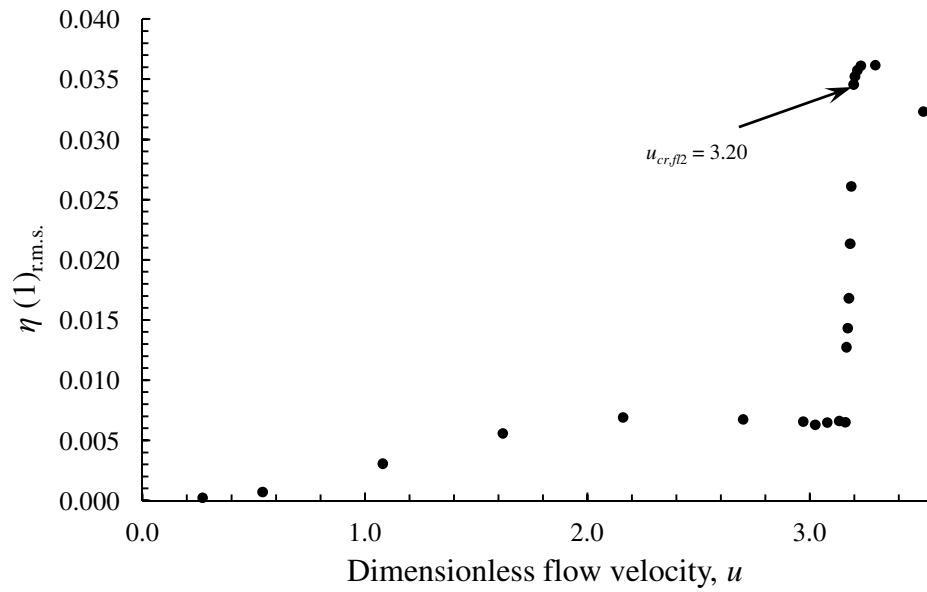


Fig. 5.15. The r.m.s. amplitude of cylinder end-piece tip vibration, $\eta(1)_{r.m.s.}$, versus u , in air flow showing the onset of second mode flutter.

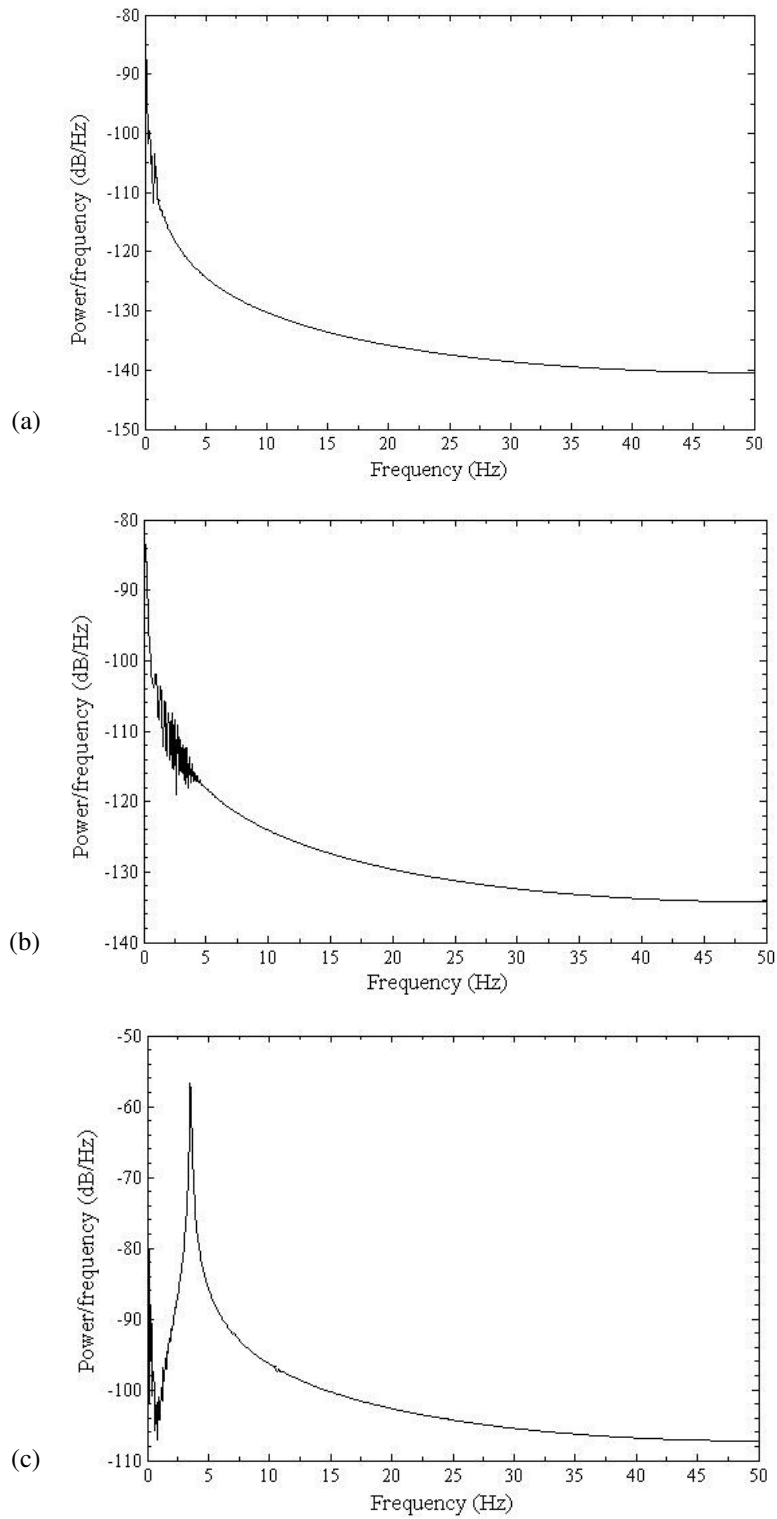


Fig. 5.16. PSD of cylinder oscillations at (a) $u = 1.08$, (b) $u = 3.08$, and (c) $u = 3.20$.

Chapter 6

Comparison of the Models

6.1. Introduction

In this chapter, the results in terms of critical flow velocities for the onset of static and dynamic instabilities obtained from linear and nonlinear models, experiments and the numerical model in water and air flows using the previously used and presently calculated force coefficients are compared with each other. All the models are run for a cantilevered cylinder with an end-piece at the downstream end. Experiments were conducted in a vertical test-section water tunnel. The comparison gives a good picture of the dynamics of cantilevered cylinders in axial flow investigated by different models and helps to understand the phenomena better by reasoning any discrepancies present in the results.

6.2. Comparison of the Linear and the Nonlinear Models in Water and Air Flows with Previously Used Force Coefficients

The results of linear and nonlinear models employing the force coefficients previously used by Païdoussis (1973) are compared with each other in this section. The results of the linear and nonlinear models employing the previous force coefficients are presented and discussed in Chapters 2 and 3, respectively. Table 6.1 shows these results in terms of critical flow velocities for the onset of static and dynamic instabilities. Qualitatively, quite similar dynamical behaviors of the cylinder are observed in the linear and nonlinear solutions subjected to water flow with the exception of the evolution of second mode divergence not observed in the linear model. Third mode flutter is not observed in the nonlinear results but one can expect it to occur after the flow velocity, i.e., $u = 7.70$. For the linear model in air flow, third mode flutter is not observed. It may be inferred that the energy transfer from air to the cylinder is not sufficient to excite the cylinder in third mode.

Quantitatively, for models in water flow, the linear model exhibits higher critical flow velocity for first mode divergence, $u_{cr,d1}$, i.e., 2.042 as compared to 1.95 for the nonlinear one, whereas nonlinear model shows higher $u_{cr,fl2}$, i.e., 5.18 as compared to 5.173 for the linear one. The overall maximum deviation is not more than 4.7 %. Linear model in air flow has the same

$u_{cr,d1}$, whereas lower $u_{cr,fl2}$ than the one in water flow. These observations are explained in Chapter 3. Finally, the results of the model in air flow show the occurrence of second mode divergence at $u_{cr,d2} > u_{cr,fl2}$. This late occurrence of second mode divergence is explained in Chapter 3. The comparison of the model results in water flow is also illustrated in Fig. 6.1.

6.3. Comparison of the Models in Water and Air Flows with Presently Calculated Force Coefficients

The results from linear and nonlinear models, experiments, and numerical models in water flow are compared in this section. In addition, numerical model results in air flow are also presented. All the results, in this section, are obtained by employing the presently calculated force coefficients. The present force coefficients are calculated using a three-dimensional model generated in ADINA based on the input parameters matching those of experiments, meaning that the coefficients represent closely the experiment conditions. That is why the results of experiments and numerical model of ADINA are included in the comparison here in this section. Table 6.2 shows these results in terms of critical flow velocities for the onset of static and dynamic instabilities. Qualitatively, the linear and nonlinear models show coupled-mode flutter. For both models, third mode flutter is not observed. One possible reason is that the linear model becomes less accurate in predicting the dynamics well especially at high flow velocities, whereas the nonlinear model solution becomes unstable at such high velocities to predict third mode flutter. In addition, linear model does not show the transformation of first mode divergence into the second mode. Also, second mode flutter is not observed in the numerical model; the reason being the inherent numerical damping imposed on the cylinder, damping out the oscillations. For the numerical model in air flow, third mode flutter is not observed up to the flow velocity, $u = 3.51$. It is expected to observe it as the flow velocity increases further but at flow velocities higher than 3.51, the solution becomes more prone to becoming numerically unstable and the program crashes.

Quantitative comparison show that $u_{cr,d1}$ for models in water flow show good agreement with discrepancies up to 3.74 %. The critical flow velocities, $u_{cr,d2}$, for the models are reasonably close with the maximum deviation up to 7.7 %. The critical flow velocities for coupled-mode flutter, i.e., $u_{cr,fl1,2}$, for the linear and nonlinear models are in good agreement with each other. However, $u_{cr,fl2}$ from experiments differs substantially. For experiments and numerical model,

$u_{cr,d1}$ is obtained by arbitrarily choosing a threshold value of $\eta^*(1)$. The numerical model in air flow shows lower $u_{cr,d1}$, $u_{cr,d2}$, and $u_{cr,fl2}$ than their counterparts for the models in water flow. This is explained in Chapter 5. The comparison of the model results in water flow is also illustrated in Fig. 6.2.

It is known that the cantilevered cylinder is a non-conservative system. Such a system is an open dissipative system, which means that mechanical energy may enter or leave the system. The state of the system depends on how the system is subjected to the forces such as the inviscid non-conservative and frictional forces. The frictional forces transform a small part of the mechanical energy of the system such as the kinetic energy into heat, which leaves the system and is lost. Therefore, the mechanical energy is not conserved when non-conservative forces are present. The dynamics of the cantilevered cylinder depends on how these forces are formulated and solved. The linear model of such cantilevered system has these forces formulated by considering only the linear terms, making it less accurately predictive specifically in the post-divergence velocity range. In nonlinear cylinder model, these forces are formulated, more accurately by considering the nonlinear terms too, making it a better predictive tool for the dynamics than the linear model. The numerically simulated model in ADINA is also nonlinear with relatively less control on the formulation of the forces and any modification in the model equation. Experiments, on the other hand, have no simplifying assumptions. The numerical schemes employed to solve the nonlinear and the numerical models also have some inherent numerical error, which cannot be totally eliminated. Also, the linear and nonlinear models account for the fluid forces in two-dimensions only, whereas the ADINA simulations and the experiments consider the fluid forces in all three-dimensions. In addition, for the experiments, the onset of divergence is not abrupt and the values chosen for the onset of flutter depend on the increments of fluid velocity chosen for data recording. Hence, the above factors can possibly explain the small discrepancies present in the model results.

The linear equation solution does not give the displacement amplitudes directly; rather the results are in terms of the complex eigenfrequencies and the instabilities are identified by the imaginary part. In the case of the nonlinear model, the results show the state of the system in terms of the generalized coordinate, q_1 . However, in the case of the experiments and the numerical model, the displacement is represented by η^* , the mean dimensionless displacement or $\eta_{r.m.s.}$, the r.m.s. value of the dimensionless displacement. Experimental results show that $\eta_{r.m.s.}$ of

second mode flutter either stays relatively constant or decreases with increasing flow velocity by up to approximately 13 % at $u = 7.4$. Hence, it is observed that numerical model results show far smaller values of $\eta^*(1)$ than those of experiments. A possible reason as explained earlier in Chapter 5 is that the negative damping of the system somehow does not increase considerably in ADINA, resulting in small magnitudes of cylinder motion.

The frequencies of flutter of the models are now compared. The linear model directly provides the dimensionless frequency as the real part of the complex eigenfrequency, whereas nonlinear and numerical models and experiments first provide the dimensional frequency, which is rendered dimensionless by using eq. (3.62). The Experimental results show that dimensionless second mode flutter frequency either stays relatively constant or decreases with increasing flow velocity by up to approximately 5 % at $u = 6.9$, whereas the third mode flutter frequency stays relatively constant with a minuscule variation of 0.2 %. It is observed that the dimensionless frequencies obtained from linear model are far higher than the ones obtained from other models. The reason is that the real part of the eigenfrequency is in fact the resonant frequency of the system. On the other hand, the frequencies observed by experiments and nonlinear and numerical models are the ones at which the system oscillates in that particular mode and flow velocity.

Lastly, observing the results of the linear and nonlinear models in water flow with previous and present force coefficients reveal that for models with the present force coefficients, divergence occurs earlier than for the models with the previous coefficients used by Païdoussis (1973). For flutter, the models with the present force coefficients show a coupled-mode flutter occurring at higher critical flow velocity than that for the models with the previous coefficients. This can be explained with the help of the end shape factor, f , and the base drag represented by c_b . As mentioned earlier in Chapter 3, a decrease in f and an increase in c_b have opposing effects on divergence while the same on flutter, i.e., decreasing f stabilizes the system for both divergence and flutter, while increasing c_b destabilizes and stabilizes for divergence and flutter, respectively. Since the model with the present force coefficients has same f (0.8) and higher c_b (0.2024) than that with the previous force coefficients ($c_b = 0.0$), we can say that the opposing effect of increasing c_b on divergence and flutter causes the system with the present force coefficients to destabilize by divergence at lower $u_{cr,d1}$ and by flutter at higher $u_{cr,fl2}$. In addition to this, the coalescing of first and second modes in the coupled-mode flutter also contributes in the delay.

6.4. Summary

In this chapter, the critical velocities, u_{cr} , obtained from linear and nonlinear models, experiments, and numerical model in water and air flows using the previous and present force coefficients were compared. Results from the models in water flow with the previous force coefficients showed that linear and nonlinear models had the respective critical flow velocities quite close to each other except that the nonlinear model could not go beyond $u = 7.70$ to show third mode flutter because of numerical instability issues. The results of the models in water flow with the present force coefficients showed reasonable agreement with each other except the value of $u_{cr,fl2}$ for experiments. In each of the linear and nonlinear models with present force coefficients, a coupled-mode flutter was observed. In the numerical model and experiments, the emergence of first mode divergence was not abrupt and some threshold had to be chosen to help obtaining the critical flow velocities. The second mode divergence in nonlinear and numerical models in water and air flows, and experiments in water flow was mainly based on visual inspection. However, second and third mode flutters in the models could be precisely located with the help of r.m.s. values of the dimensionless displacements and the frequencies of oscillations. It was also noticed that for the linear models with the previous and the present force coefficients, evolution of second mode divergence was not observed at all.

Table 6.1. Comparison of critical flow velocities of instability for different models in water and air flows using previous force coefficients.

Fluid	Models/instabilities	First mode divergence, $u_{cr,d1}$	Second mode divergence, $u_{cr,d2}$	Second mode flutter, $u_{cr,fl2}$	Third mode flutter, $u_{cr,fl3}$
Water	Linear	2.042	--	5.173	8.311
	Nonlinear	2.04	≈ 4.40	5.18	--
Air	Linear	2.042	4.965	3.470	--

Table 6.2. Comparison of critical flow velocities of instability for linear and nonlinear models in water flow using present force coefficients.

Fluid	Models/instabilities	First mode divergence, $u_{cr,d1}$	Second mode divergence, $u_{cr,d2}$	Second mode flutter, $u_{cr,fl2}$	Third mode flutter, $u_{cr,fl3}$
Water	Experimental	1.87	≈ 4.66	5.92	7.70
	Linear [prev.] (impr. from prev.)	1.904 [2.04] (80.12 %)	--	5.278 [5.16] (coupled-mode) (15.51 %)	--
	Nonlinear [prev.] (impr. from prev.)	1.89 [2.10] (91.30 %)	≈ 4.40	5.29 [5.5] (coupled-mode) (-50 %)	--
	Numerical	1.80	≈ 4.30	--	--
Air	Numerical	1.62	≈ 3.02	3.20	--

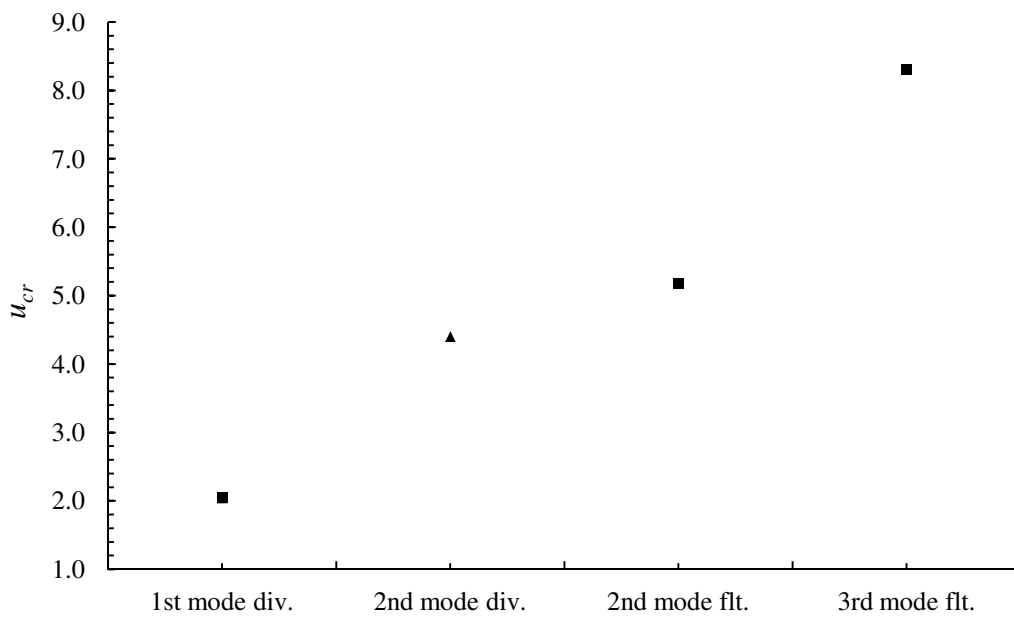


Fig. 6.1. Critical flow velocities, u_{cr} versus the instabilities for different models in water flow using previous force coefficients. ■, linear model; ▲, nonlinear model.

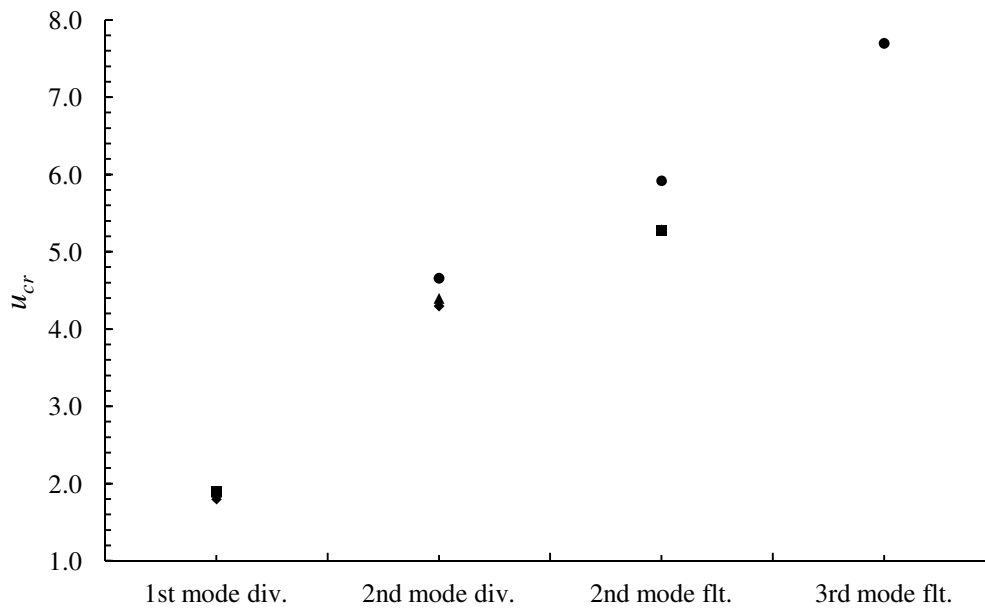


Fig. 6.2. Critical flow velocities, u_{cr} versus the instabilities for different models in water flow using present force coefficients. •, experiments; ■, linear model; ▲, nonlinear model; ◆, numerical model.

Chapter 7

Conclusions

7.1. Overview

In this thesis, the nonlinear dynamics of a slender flexible cantilevered cylinder subjected to external axial flow was studied, both theoretically and experimentally. An extensive literature review in Chapter 1 revealed that a three-dimensional coupled nonlinear model for the flexible cylinder had not been developed. The motivation behind the present research work was to account for the three-dimensional nonlinear behaviour, important in the practical applications such as nuclear power production, heat exchangers, undersea geological survey, and biomedical science. In addition, the fluid force coefficients used previously by Païdoussis (1973) and Semler et al. (2002) were re-evaluated to find out if these coefficients actually were suitable for the present model.

The objectives outlined in Chapter 1 were achieved by solving the linear and nonlinear equations, simulating numerical models, and conducting experiments. Also, the force coefficients were recalculated based on the present experimental input parameters and then implemented in the linear and nonlinear equations. The linear and nonlinear equations, with these presently calculated force coefficients incorporated, were then solved. In addition, the effect of confinement on the dynamics of linear model was also investigated. To complement the linear and nonlinear models, three-dimensional model of flexible cylinder with cantilevered boundary conditions was developed in a Finite Element Method (FEM) based multiphysics simulation software called ADINA. Finally, experiments were conducted and the results obtained from analytical linear, nonlinear, and numerical models, all in water flow, were then validated by comparing them with those from the experiments. The results showed reasonable agreement. Some special runs of linear and numerical models were also conducted in air flow. The model results were also compared with each other.

7.2. Summary of the Work

In the previous section, steps taken to achieve the objectives were mentioned briefly, while in this section, a detailed enumeration is presented.

Series of experiments were conducted on the confined cantilevered cylinder in a vertical test section of a water tunnel. Water flowed from top to bottom of the test section. The downstream free end of the cylinder was fitted with a rigid ogival end-piece. The upstream end was clamped to a central rigid cylindrical support with four perpendicular arms extending to the wall of the test section. Before the experiments were conducted, the laser sensors, utilized to record the displacements of the cylinder in the experiments, were calibrated for known linear distances and their calibration curves were obtained. The essential parameters such as flexural rigidity, EI , logarithmic decrements, δ_n , hysteretic damping constant, $\bar{\mu}^*$, and the dimensionless viscoelastic damping constant, $\bar{\alpha}^*$ of the cylinder were then determined experimentally. The flexural rigidity was determined by first exciting the cylinder in its first mode and finding out the first mode natural frequency. Using this frequency and the set of expressions and table given by Païdoussis and Des Trois Maisons (1969), EI was calculated. In order to obtain the logarithmic decrements, the cylinder was excited in its first, second, and third modes. The first mode excitation was done the same way as done for EI . However, the second and third cylinder modes were excited mechanically with the help of a crank-slider mechanism and hence the respective natural frequencies were determined. The natural logarithm of the displacement data for each mode was then plotted versus time and the slope of the decrement was calculated. Later dividing the slopes by the respective frequencies led to δ_1 , δ_2 , and δ_3 . $\bar{\mu}^*$ and $\bar{\alpha}^*$ were then calculated using the expressions and the plots given by Païdoussis and Des Trois Maisons (1969).

The controller ATR141 for the differential-pressure transducer (Huba-692) connected to the Venturi flow meter on the main flow pipe and the centrifugal pump speed in terms of r.p.m. were calibrated using a pitot-static tube and a mercury manometer. The pitot-static tube was carefully inserted through the lower test section window to align its tip with the centre-line of the test section. Its static and stagnation pressure ports were connected to the mercury column manometer. In addition to this, readings of the pressure transducers across the Venturi meter, fitted in the water tunnel, were also recorded with the help of the controller ATR141. The tunnel was then run at given pump r.p.m. A calibration curve, establishing the relationship between the ATR141 readings and the flow velocity, was finally obtained. The velocity profile inside the test section was also obtained experimentally using Laser Doppler Anemometry (LDA). In order to establish the velocity profile in close proximity to the test section wall, law of the wall for turbulent flow was utilized. Finally, in order to determine $u_{cr,d1}$ and $u_{cr,d2}$, the laser beam was

horizontally pointed on the cylinder near its downstream free end. Mean dimensionless displacements were plotted against u and the critical velocities were determined by choosing a threshold value. The critical flow velocities $u_{cr,fl2}$ and $u_{cr,fl3}$ were determined by placing the laser head horizontally near the cylinder upstream end. The r.m.s. values of the cylinder dimensionless displacements led to distinct critical flow velocities for flutter. At the end, the path traced by the cylinder was also mapped.

The calibration curves of the laser sensors were linear. The calibration curve of ATR141 readings and the flow velocity was of sixth order polynomial. The half-symmetric flow velocity profile had some mismatching between the experiment and the theoretical values at $y = 0.0029$ m due to the inherent experimental errors such as difficulty in controlling the uniform density of the seeding particles in the flow, laser beam diffraction due to different fluid and solid media. In addition to these, rounding off the data of both the experimental and theoretical results to some significant figures also made the values differ from each other. The theoretical model did not give the exact true values of velocity due to the imprecise usage of the relations in the viscous sub-layers, which do not have distinct boundaries. While recording and observing the evolution of cylinder displacements at increasing flow velocity, it was obvious that the onset of first and second mode divergences were not abrupt. Therefore, a threshold value had to be chosen, especially for $u_{cr,d1}$, which ensured significant displacements and hence could confidently be considered as the onset of divergence. For flutter, the r.m.s. values of the dimensionless displacements showed substantial variation of the values at the onsets of second and third mode flutters. The overall response of the cylinder showed the onset of first instability by first mode divergence followed by a gradual evolution into second mode divergence. The cylinder then lost stability again by second mode flutter and later by third mode flutter. The path traced by the cylinder in both second and third mode flutters was observed to be quasi-circular path. In third mode flutter, the difference between the major and minor axes of the path was found to be more than in second mode flutter, making the quasi-circular path more pronounced in the third mode flutter.

Linear equation of motion, derived by Païdoussis (1973), was considered for a slender flexible cylinder with cantilevered boundary conditions, having the downstream free end of the cylinder terminated by an ogival end-piece. The equation was then simplified to second-order Ordinary Differential Equation (ODE) and finally to an eigenvalue problem. In order to accommodate the time- and flow velocity-dependent free end boundary condition, a procedure

namely the ‘extended Galerkin method’ was adopted. The eigenvalue problem was then coded in MATLAB and solved, using six Galerkin modes, for the complex eigenfrequencies comprising of the resonant frequency as its real part and the damping as its imaginary part. The force coefficients previously used by Païdoussis (1973) were used. The results in the form of critical flow velocities for the onset of instabilities were obtained for water flow. The effect of confinement on the cylinder dynamics was also studied. The solution of the equation in air flow was also obtained. Furthermore, the fluid forces such as inviscid hydrodynamic forces, frictional or viscous forces, and hydrostatic or pressure forces acting on the cantilevered cylinder were considered and the associated viscous force coefficients such as longitudinal viscous coefficient, c_T , normal viscous coefficient, c_N , base drag coefficient, c_b , and zero-flow normal coefficient, c were recalculated. The values of the present force coefficients were found to be within their respective suitable ranges suggested by Païdoussis (2004). These present force coefficients were incorporated into the linear equation and obtained the results. The effect of confinement on the dynamics of the cylinder with the present force coefficients was also investigated. Finally, the present model results with previously available force coefficients were compared with those of Païdoussis (1973) who solved the equation by a different method. A comparison was also done between the results obtained with the previous and present force coefficients and then between the results with water and air flows.

The results for an isolated unconfined cantilevered cylinder showed that the free motions were damped at small dimensionless flow velocity, u . At sufficiently high u , however, the cylinder first loses stability by divergence in its first mode followed by re-stabilization and then single second mode flutter. At further higher u , the model lost stability again by third mode flutter. The results for the model in air flow showed that at sufficiently high u , it lost stability by first mode divergence followed by second mode flutter. At further higher u , third mode flutter did not occur rather second mode divergence and third mode divergence occurred. Increasing confinement of the model in water flow resulted in a decrease in $u_{cr,d1}$ as well as $u_{cr,fl2}$. For the model in air flow, increasing confinement resulted in the same trend as in water flow. The results of the model with present force coefficients showed that with increasing u , the model first lost stability by first mode divergence followed by re-stabilization. Later, it lost stability again by coupled-mode flutter. The cylinder did not become unstable in the third mode. As for the effect of confinement with present force coefficients, the model exhibited the same trend of $u_{cr,d1}$ and

$u_{cr,fl2}$ as observed in the model with previous force coefficients. The comparison of the results of present model with the ones reported by Païdoussis (1973), both having the previous force coefficients, showed good agreement. Previous and present force coefficient results were also compared. The results revealed that the model with the presently calculated force coefficients exhibit similar dynamics as observed in the experiments, especially the coalesced first mode divergence and second mode flutter as the coupled-mode flutter (combination of the two modes leads to an asymmetric response also observed in Figs. 2.32 and 2.33 of Chapter 2). Hence, it can be concluded that the linear model with the presently calculated force coefficients predicts the dynamics of the system better than the one with the previously used ones. The comparison of model in water flow with the one in air flow showed similar values of $u_{cr,d1}$. However, $u_{cr,fl2}$ for the model in air flow was lower than that in water flow.

The nonlinear equation of motion, derived by Lopes et al. (2002), was considered for a confined slender flexible cylinder with cantilevered boundary conditions, having the downstream free end of the cylinder terminated by an ogival end-piece. Hamilton's principle was utilized for the derivation. Due to the time- and flow velocity-dependent free end boundary condition, 'extended Galerkin method' was used to transform the PDE into ODE. The force coefficients previously used by Semler et al. (2002) were used. The obtained equation was then solved using Houbolt's Finite Difference Method (FDM) using a FORTRAN code. Six Galerkin modes were considered in both the axial and transverse directions in the solution. The presently calculated force coefficients were then incorporated into the nonlinear equation and the results sought.

It was observed in the results with the previous coefficients that with increasing u , the cylinder first lost stability by first mode divergence followed by a gradual evolution into second mode. The cylinder then re-stabilized for short range of u and again became unstable by second mode flutter. Instability in third mode was not observed. The results of the present model were compared with those obtained by Semler et al. (2002), both with previous force coefficients, and showed good agreement. Finally, the present models with previous and present coefficients were compared to understand how the force coefficients affect the critical flow velocities. The results of the model with the present force coefficients showed similar sequence of instability occurrences as for the model with the previously used force coefficients except that the former model had higher critical flow velocities, typically 13.30 % and 4.68 % higher for divergence and flutter, respectively, than the latter one.

A cantilevered cylinder model, possessing the same input parameters as for the model in experiments, was developed in ADINA. The cylinder had its downstream free end terminated by an end piece. The upstream support had two configurations one with the support arms and the other without. The study started by first validating the software with the help of theoretical and experimental results of the benchmark problems reported in the earlier work. The solution time step range was then determined using the CFL condition. The simulations of the model were first done in water flow followed by the simulations in air flow. The model in water flow had the upstream support arms attached to the central rigid cylindrical support, whereas the model in air flow was devoid of those. Finally, a comparison was done between both the models.

The results of all the benchmark problems obtained from ADINA were in good agreement with the ones previously reported. The dynamics of the cylinder in water flow showed that, with increasing flow velocity, the cylinder first lost stability by divergence in first mode followed by the evolution of second mode. Flutter did not occur even at very high flow velocity. The model without support arms in water flow was also tested to see if flutter occurs but the results were the same. A possible reason might be due to the inherent numerical damping imposed in ADINA on the solid that damped out the oscillations. The dynamics of the cylinder in air flow was the same except that in this case the second mode flutter was actually observed. The value of $u_{cr,fl2}$ was decided based on the r.m.s. values of the dimensionless amplitudes of the cylinder, which was sustained over sufficient period of time. Finally, the models in water and air flow were compared. It was observed that all critical velocities in air flow were lower than their counterparts in water flow.

The results in the form of the critical flow velocities of linear and nonlinear models, experiments, and numerical model in water and air flows using the previous and present force coefficients were compared with each other. It was noticed that for the linear model in water flow, evolution of second mode divergence was not observed at all. The results of the models in water flow with the present force coefficients showed reasonable agreement with each other except the value of $u_{cr,fl2}$ for experiments. In each of the linear and nonlinear models with present force coefficients, a coupled-mode flutter was observed. In the numerical model and experiments, the emergence of first mode divergence was not abrupt and some threshold had to be chosen to help obtaining the critical flow velocities. The second mode divergence for nonlinear and numerical models in water and air flows, and experiments in water flow was

mainly based on visual inspection. However, second and third mode flutter in the models could be precisely located with the help of r.m.s. values of the dimensionless displacements and the frequencies of oscillations. The results, overall, showed reasonable agreement.

7.3. Suggestions for Future Work

The main goal of this thesis was to investigate the dynamics of a cantilevered cylinder in water and air flows with the help of analytical and numerical models, supported by experiments. Due to the wide scope of the present research work, some suggestions for future research in the same area can be given.

There is little or no work done on the experiments pertaining to investigating the dynamics of a slender flexible cylinder in confined axial flow. Confinement can be achieved either by considering the cylinder in the presence of adjacent cylinders or in close proximity to the flow-containing channel. It is known that with increased confinement, pressure drop is clearly not negligible and viscous effects of fluid on the cylinder and on the flow channel become more pronounced. In fact, confinement case is often present in many practical applications such as nuclear fuel rods bundled together, heat exchanger tubes, and angioplasty. Therefore, it is worth investigating this area with different boundary conditions such as cantilevered, pinned-pinned, and clamped-clamped.

Eccentricity is encountered in many applications possessing enclosed slender cylinders. In angioplasty, it is almost impossible to keep the slender flexible catheter concentric inside the artery. Also, in the drilling operations of oil and gas wells, mud is pumped from a surface mud tank via the drill pipe (several kilometers in length), through nozzles in the rotating drill bit, and back to the mud tank through the annular space between the well bore wall and the drill pipe. It is extremely difficult to keep the drill pipe concentric inside the well bore. Since mud flows upward out of the well bore, any eccentricity present in the annulus can induce motion in the drill pipe and can seriously affect the drilling operation. Therefore, it is important to investigate, both experimentally and theoretically, how the dynamical behavior of the slender flexible cylinder is affected by eccentricity. With eccentricity, the eccentric annulus causes the fluid forces acting on the cylinder to be non-symmetric and, therefore, an appropriate coordinate system must be adopted to resolve these forces. A bipolar coordinate system is the most suitable for this purpose.

The other way to account for the eccentricity was adopted by Mateescu et al. (1994), who used a coordinate transformation factor to account for the circumferential variation of the annulus.

It is also worth investigating the combined effects of confinement and eccentricity on the response of a slender flexible cylindrical system placed inside a channel subjected to axial flow, both experimentally and theoretically. Both cases (confinement and eccentricity), combined, are expected to restrict the motion of the cylinder.

It is also suggested to investigate other boundary conditions for the flexible cylindrical structure such as clamped-pinned as limiting case, both experimentally and theoretically. The above mentioned boundary conditions can be swapped or the flow direction reversed to see if there is any variation in the response of the cylinder from the first condition.

References

ADINA. 2012. *ADINA Research and Development*. Massachusetts:

<http://www.adina.com/index.shtml>.

AML Oceanographic. 2013. *Seismic Array*. Sidney:

http://www.amloceanographic.com/Technical-Demo/Seismic-Array_2.

Armaly, B.F., Durst, F., Pereira, J.C.F., and Schönung, B. 1983. Experimental and theoretical investigation of backward-facing step flow. *Journal of Fluid Mechanics* **127**, 473-496.

Batchelor, G.K. 1967. *An Introduction to Fluid Dynamics*. Cambridge: Cambridge University Press.

Ben-Gal, Y., Weisz, G., Collins, M.B., Genereux, P., Dangas, G.D., Teirstein, P.S., Singh, V.P., Rabbani, L.E., Kodali, S.K., Sherman, W., Leon, M.B., and Moses, J.W. 2010. Dual catheter technique for the treatment of severe coronary artery perforations. *Catheterization and Cardiovascular Interventions* **75** (5), 708-712.

Blevins, R.D. 1984. *Applied Fluid Dynamic Handbook*. New York: Van Nostrand Reinhold.

Blevins, R.D. 1990. *Flow-Induced Vibration* 2nd Edition. Malabar: Krieger Publishing company.

Bungartz, H. and Schäfer, M. eds. 2006. *Fluid-Structure Interaction: Modelling, Simulation, Optimization*. Berlin, Heidelberg: Springer Verlag.

Chen, S.S. 1978. Cross-flow induced vibrations of heat exchanger tube banks. *Nuclear Engineering and Design* **47**, 67-86.

Chen, Y.N. 1970a. Turbulence-induced instability of fuel rods in parallel flow. *Sulzer Technical Review, Special Issue*, 72-84.

Chen, Y.N. 1970b. *Flow-Induced Vibration in Heat Exchangers*, p. 57. New York: ASME.

Chen, S.S. and Wambsganss, M.W. 1972. Parallel-flow-induced vibration of fuel rods. *Nuclear Engineering and Design* **18**, 253-278.

Cook, R.D., Malcus, D.S., and Plesha, M.E. 1989. *Concepts and Applications of Finite Element Analysis*. New York: Wiley.

- Courant, R., Friedrichs, K, and Lewy, H. 1967. On the partial difference equations of mathematical physics. *IBM Journal of Research and Development* **11** (2), 215-234.
- Dantec Dynamics. 2004. *Flowlite Installation and User's Guide*. Skovlunde.
- De Langre, E., Païdoussis, M.P., Doare, O., and Modarres-Sadeghi, Y. 2007. Flutter of long flexible cylinders in axial flow. *Journal of Fluid Mechanics* **571**, 371-389.
- Dowling, A.P. 1988. The dynamics of towed flexible cylinders. Part 1: neutrally buoyant elements. *Journal of Fluid Mechanics* **187**, 507-532.
- Drain, L.E. 1980. *The Laser Doppler Technique*. New York: John Wiley & Sons.
- Fujita, K. and Ohkuma, A. 2010. Effect of structural and fluid characteristics on dynamic stability of an elastic beam subjected to axial flow in a narrow passage. *Proceedings of ASME 2010 3rd joint US-European Fluids Engineering Summer Meeting and 8th International Conference on Nanochannels, Microchannels, and Minichannels FEDSM2010-ICNMM2010*, Montreal, Canada.
- Fujita, K. and Shintani, A. 1999. Flow-induced vibration of the elastic rod due to axial flow: Unstable phenomena of continuous flexible rod as the axisymmetric body. *ASME Flow Induced Vibration*, PVP **389**, 199-206.
- Fujita, K. and Shintani, A. 2001. Axial leakage flow-induced vibration of the elastic rod as the axisymmetric continuous flexible beam. *Journal of Pressure Vessel Technology* **123**, 421-428.
- Fujita, K., Morikazu, H., and Shintani, A. 2007. A consideration on pre-and post-instability of an axisymmetric elastic beam subjected to axial leakage flow. *Journal of Fluids and Structures* **23**, 463-478.
- Gagnon, J.O. and Païdoussis, M.P. 1994a. Fluid coupling characteristics and vibration of cylinder clusters in axial flow. Part 1: Theory. *Journal of Fluids and Structures* **8**, 257-291.
- Gagnon, J.O. and Païdoussis, M.P. 1994b. Fluid coupling characteristics and vibration of cylinder clusters in axial flow. Part 2: Experiments. *Journal of Fluids and Structures* **8**, 293-324.

- Gorman, D.J. 1969. *The Role of Turbulence in the Vibration of Reactor Fuel Elements in Liquid Flow*. Atomic Energy of Canada Report AECL-3371.
- Gorman, D.J. 1971. An analytical and experimental investigation of the vibration of cylindrical reactor fuel elements in two-phase parallel flow. *Nuclear Science and Engineering* **44** (3), 277-290.
- Hannoyer, M.J. 1977. *Instabilities of Slender, Tapered Tubular Beams Induced by Internal and External Axial Flow*. Ph. D. Thesis, McGill University, Montreal, Canada.
- Hannoyer, M.J. and Païdoussis, M.P. 1978. Instabilities of tubular beams simultaneously subjected to internal and external axial flows. *ASME Journal of Mechanical Design* **100**, 328-336.
- Hawthorne, W.R. 1961. The early development of the Dracone flexible barge. *Proceedings of the Institution of Mechanical Engineers* **175**, 52-83.
- Hilber, H.M., Hughes, T.J.R., and Taylor, R.L. 1977. Improved numerical dissipation for time integration algorithms in structural dynamics. *Earthquake Engineering and Structural Dynamics* **5**, 283-292.
- Hoerner, S.F. 1965. *Fluid Dynamic Drag*, 2nd Edition. Brick Town, New Jersey: Hoerner Fluid Dynamics.
- Idel'chik, I.E. 1966. *Handbook of Hydraulic Resistance*. Translated from Russian, AEC-tr-6630, Springfield, VA: United States Department of Commerce. Also 1986, New York: Hemisphere.
- Kaneko, S., Nakamura, T., Inada, F., and Kato, M. 2008. *Flow-Induced Vibrations: Classifications and Lessons from Practical Experiences*. Amsterdam, Boston, London: Elsevier.
- Ko, P.L. 1997. Wear of power plant components due to impact and sliding. *Applied Mechanics Reviews* **50**, 387-411.
- Langthjem, M.A. and Nakamura, T. 2007. Influence of swirl on the stability of a rod in annular leakage flow. *Journal of Fluids and Structures* **23**, 329-337.

- Langthjem, M.A., Morita, H., Nakamura, T., and Nakano, M. 2006. A flexible rod in annular leakage flow: Influence of turbulence and equilibrium offset, and analysis of instability mechanisms. *Journal of Fluids and Structures* **22**, 617-645.
- Lee, D. and Kennedy, R.M. 1985. A numerical treatment of a mixed type dynamic motion equation arising from a towed acoustic antenna in the ocean. *Computers & Mathematics with Applications* **11**, 807-816.
- Li, D.-W., Kaneko, S., and Hayama, S. 2002. A study on annular leakage-flow-induced vibrations. *Journal of Fluids and Structures* **16** (7), 909-930.
- Lighthill, M.J. 1960. Note on the swimming of slender fish. *Journal of Fluid Mechanics* **9**, 305-317.
- Lopes, J.L., Païdoussis, M.P., and Semler, C. 2002. Linear and nonlinear dynamics of cantilevered cylinders in axial flow. Part 2: The equations of motion. *Journal of Fluids and Structures* **16** (6), 715-737.
- Mateescu, D. and Païdoussis, M.P. 1985. The unsteady potential flow in an axially variable annulus and its effect on the dynamics of the oscillating rigid center-body. *Journal of Fluids Engineering* **107**, 421-427.
- Mateescu, D. and Païdoussis, M.P. 1987. Unsteady viscous effects on the annular-flow-induced instabilities of a rigid cylindrical body in a narrow duct. *Journal of Fluids and Structures* **1**, 197-215.
- Matlab help file 2010. MATLAB 64 bit version 7.10.0.499.
- Miller, S.L. and Childers, D.G. 2004. *Probability and Random Processes: with Applications to Signal processing and Communications*. Boston: Elsevier Academic Press.
- Modarres- Sadeghi, Y. 2006. *Nonlinear Dynamics of a Slender Flexible Cylinder to Axial Flow*. Ph. D. Thesis, McGill University, Montreal, Canada.
- Modarres-Sadeghi, Y., Païdoussis, M.P., and Semler, C. 2005. A nonlinear model of an extensible slender flexible cylinder subjected to axial flow. *Journal of Fluids and Structures* **21**, 609-627.

- Modarres-Sadeghi, Y., Païdoussis, M.P., and Semler, C. 2007. The nonlinear behavior of a slender flexible cylinder pinned or clamped at both ends and subjected to axial flow. *Computers and Structures*, **85**, 1121-1133.
- Morgan, R.A. and Walser, E. 2010. *Handbook of Angioplasty and Stenting Procedures*. London: Springer-Verlag.
- Naudascher, E. and Rockwell, D. 1990. *Flow-Induced Vibrations – An Engineering Guide (C) Movement-Induced Excitation*, Sonderforschungsbereich 210, “Strömungsmechanische Bemessungsgrundlagen für Bauwerke” SFB 210/A/65, Universität Karlsruhe.
- Naudascher, E. and Rockwell, D. 1994. *Flow-Induced Vibrations: An Engineering Guide*. Rotterdam: A. A. Balkema.
- Ni, C.C. and Hansen, R.J. 1978. An experimental study of the flow-induced motions of a flexible cylinder in axial flow. *ASME Journal of Fluids Engineering* **100**, 389-394.
- Nie, J.H. and Armaly, B.F. 2003. Reattachment of three-dimensional flow adjacent to backward-facing step. *Transactions of the ASME* **125**, 422-428.
- Ortloff, C.R. and Ives, J. 1969. On the dynamic motion of a thin flexible cylinder in a viscous stream. *Journal of Fluid Mechanics* **38**, 713-720.
- Païdoussis, M.P. 1966a. Dynamics of flexible slender cylinders in axial flow. Part 1: Theory. *Journal of Fluid Mechanics* **26**, 717-736.
- Païdoussis, M.P. 1966b. Dynamics of flexible slender cylinders in axial flow. Part 2: Experiments. *Journal of Fluid Mechanics* **26**, 737-751.
- Païdoussis, M.P. 1973. Dynamics of cylindrical structures subjected to axial flow. *Journal of Sound and Vibration* **29** (3), 365-385.
- Païdoussis, M.P. 1974. The dynamical behavior of cylindrical structures in axial flow. *Annals of Nuclear Science and Engineering* **1**, 83-106.
- Païdoussis, M.P. 1979. The dynamics of clusters of flexible cylinders in axial flow: Theory and experiments. *Journal of Sound and Vibration* **65** (3), 391-417.

- Païdoussis, M.P. 1980. *Flow-Induced Vibrations in Nuclear Reactors and Heat Exchangers Practical Experiences and State of Knowledge*. Berlin, Heidelberg, New York: Springer Verlag.
- Païdoussis, M.P. 1981. Fluidelastic vibration of cylinder arrays in axial and cross flow: State of the art. *Journal of Sound and Vibration* **76** (3), 329-360.
- Païdoussis, M.P. 1983. A review of flow-induced vibrations in reactors and reactor components. *Nuclear Engineering and Design* **78** (1), 31-60.
- Païdoussis, M.P. 1987. Flow-induced instabilities of cylindrical structures. *Applied Mechanics Reviews* **40** (2), 163-175.
- Païdoussis, M.P. 1993. 1992 Calvin Rice lecture: Some curiosity-driven research in fluid structure interactions and its current applications. *Transactions of the ASME* **115**, 2-14.
- Païdoussis, M.P. 1998. *Fluid-Structure Interactions: Slender Structures and Axial Flow*, Vol. 1. London: Elsevier Academic Press.
- Païdoussis, M.P. 2004. *Fluid-Structure Interactions: Slender Structures and Axial Flow*, Vol. 2. London: Elsevier Academic Press.
- Païdoussis, M.P. 2008. The canonical problem of the fluid-conveying pipe and radiation of the knowledge gained to other dynamics problems across applied mechanics. *Journal of Sound and Vibration* **310**, 462-492.
- Païdoussis, M.P. and Curling, L.R. 1985. An analytical model for vibration of clusters of flexible cylinders in turbulent axial flow. *Journal of Sound and Vibration* **98**, 493-517.
- Païdoussis, M.P. and Pettigrew, M.J. 1979. Dynamics of flexible cylinders in Axisymmetrically confined axial flow. *Journal of Applied Mechanics* **46**, 37-44.
- Païdoussis, M.P. and Suss, S. 1977. Stability of a cluster of flexible cylinders in bounded axial flow. *Journal of Applied Mechanics* **44**, 401-408.
- Païdoussis, M.P., Chaubernard, J.P., Genadry, M.R., and El Barbir, K.N. 1983b. Dynamics of a cluster of flexibly interconnected cylinders. Part 2: In axial flow. *Journal of Applied Mechanics* **50**, 429-435.

- Païdoussis, M.P., El Barbir, K.N., Genadry, M.R., and Chaubernard, J.P. 1983a. Dynamics of a cluster of flexibly interconnected cylinders. Part 1: In vacuum. *Journal of Applied Mechanics* **50**, 421-428.
- Païdoussis, M.P., Grinevich, E., Adamovic, D., and Semler, C. 2002. Linear and nonlinear dynamics of cantilevered cylinders in axial flow. Part 1: physical dynamics. *Journal of Fluids and Structures* **16** (6), 691-713.
- Païdoussis, M.P., Issid, N.T., and Tsui, M. 1980a. Parametric resonance oscillations of flexible slender cylinders in harmonically perturbed axial flow. Part 1: Theory. *Journal of Applied Mechanics* **47**, 709-714.
- Païdoussis, M.P., Issid, N.T., and Tsui, M. 1980b. Parametric resonance oscillations of flexible slender cylinders in harmonically perturbed axial flow. Part 2: Experiments. *Journal of Applied Mechanics* **47**, 715-719.
- Païdoussis, M.P., Mateescu, D., and Sim, W.G. 1990. Dynamics and stability of a flexible cylinder in a narrow coaxial cylindrical duct subjected to annular flow. *Journal of Applied Mechanics* **57**, 232-240.
- Pao, H.P. 1970. Dynamical stability of a towed thin flexible cylinder. *AIAA Journal of Hydronautics* **4**, 144-150.
- Pope, S.B. 2000. *Turbulent Flows*. New York: Cambridge University Press.
- Quinn, E.P. 1962. *Vibration of Fuel Rods in Parallel Flow*. U.S. Atomic Energy Commission Report GEAP-4059.
- Reavis, J.R. 1967. WVI-Westinghouse vibration correlation for maximum fuel-element displacement in parallel flow. *Transactions of the American Nuclear Society* **10**, 369-371.
- Reavis, J.R. 1969. Vibration correlation for maximum fuel-element displacement in parallel turbulent flow. *Nuclear Science and Engineering* **38** (1), 63-69.
- Rinaldi, S. 2009. *Experiments on the dynamics of cantilevered pipes subjected to internal and/or external axial flow*. M. Eng Thesis, McGill University.

- Ryder, G.H. 1969. *Strength of Materials*, 3rd Edition. Hong Kong: English Language Book Society/Macmillan.
- Schlichting, H. and Gersten, K. 2000. *Boundary-Layer Theory*, 8th Edition. Berlin, Heidelberg, New York: Springer Verlag.
- Semler, C., Lopes, J.L., Augu, N., and Païdoussis, M.P. 2002. Linear and nonlinear dynamics of cantilevered cylinders in axial flow. Part 3: Nonlinear dynamics. *Journal of Fluids and Structures* **16** (6), 739-759.
- Shaughnessy Jr., E.J., Katz, I.M., and Schaffer, J.P. 2005. *Introduction to Fluid Mechanics*. New York: Oxford University Press.
- Sinyavskii, V.F., Fedotovskii, V.S. and Kukhtin, A.B. 1980. Oscillation of a cylinder in a viscous liquid. *Prikladnaya Mekhanika* **16**, 62-67.
- Strang, G. 1994. Wavelets. *American Scientist* **82** (3), 250-255.
- Sudarsan, K., Bhattacharyya, S.K., and Vendhan, C.P. 1997. An experimental study of hydroelastic instability of flexible towed underwater cylindrical structures. *Proceedings of 16th OMAE Conference*, Yokohama, Japan **A**, 73-80.
- Tang, L. 2007. *The dynamics of two-dimensional cantilevered flexible plates in axial flow and a new energy-harvesting concept*. Ph. D. Thesis, McGill University.
- Taylor, G.I. 1952. Analysis of the swimming of long and narrow animals. *Proceedings of the Royal Society of London. Series A, Mathematical and Physical Sciences* **214**, 158-183.
- Triantafyllou, G.S. and Chryssostomidis, C. 1985. Stability of a string in axial flow. *ASME Journal of Energy Resources Technology* **107**, 421-425.
- Wang, L. and Ni, Q. 2009. Vibration of slender structures subjected to axial flow or axially towed in quiescent fluid. *Advances in Acoustics and Vibration* **2009**, 1-19.
- White, F.M. 1974. *Viscous Fluid Flow*. London: McGraw-Hill, Inc.
- White, F.M. 2003. *Fluid Mechanics*. New York: McGraw-Hill, Inc.

- Williams, P.T. and Baker, A.J. 1996. Incompressible computational fluid dynamics and the continuity constraint method for the three-dimensional Navier-Stokes equations. *Numerical heat transfer, Part B* **29**, 137-273.
- Yeh, Y. and Cummins, H.Z. 1964. Localized fluid flow measurements with He-Ne laser spectrometer. *Applied Physics Letters* **4** (10), 176-178.
- Zdravkovich, M.M. 2003. *Flow around Circular Cylinders, Applications*, Vol. 2. Oxford: Oxford University Press.

Appendix A

A.1. Determination of End-Shape Factor, f

In the experiment, the cantilevered cylinder downstream end is fitted with an ogival end-piece. Païdoussis (1966b, 2002) investigated, experimentally and theoretically, the effect of the end-piece shape on the cylinder instability pattern. He found both experimentally and theoretically that transforming the end-piece from a well streamlined shape to a blunt shape stabilizes the system for both divergence and flutter. He characterised the perfectly streamlined shape by the end-shape factor, $f = 1$ and the perfectly blunt one by $f = 0$. Since the shape of the end-pieces represented by the end-shape factor, f , it becomes important to find the value of f both for theoretical models and experiments. Hannover and Païdoussis (1978) proposed the expression

$$f = \frac{4s_e^2}{4s_e^2 + (D_o - D_i)^2}, \quad (\text{A.1})$$

where s_e is the axial variation in the end-piece cross-sectional area. s_e is dimensional quantity and has the unit of length, i.e., m; D_i and D_o being the inner and outer diameters of a pipe conveying fluid, respectively. In order to render eq. (A.1) dimensionless, the expressions

$$\chi_e = \frac{s_e}{L}, \quad (\text{A.2})$$

$$\varepsilon = \frac{L}{D_o}, \quad (\text{A.3})$$

and

$$\bar{\delta} = \frac{D_i}{D_o} \quad (\text{A.4})$$

are used (Païdoussis 2004). D_o is the external diameter of a pipe or cylinder. The dimensionless form thus obtained is

$$f = \frac{4\varepsilon^2 \chi_e^2}{4\varepsilon^2 \chi_e^2 + (1 - \bar{\delta})^2}. \quad (\text{A.5})$$

For a cylinder, $\bar{\delta} = 0$ and $(D_o - D_i)^2$ in eq. (A.1) is replaced by D_o^2 . Hence, the dimensional and dimensionless expressions for a cylinder become

$$f = \frac{4s_e^2}{4s_e^2 + D_o^2} = \frac{4\epsilon^2 \chi_e^2}{4\epsilon^2 \chi_e^2 + 1}. \quad (\text{A.6})$$

The end-piece used in the experiments resembles closest to an ellipsoidal shape. Hence, for an ellipsoidal end-piece, Païdoussis (2004) defined se as

$$s_e = \frac{2}{3}l. \quad (\text{A.7})$$

Here, l is the length of the end-piece. D_o is the same as D as used in the present case as both represent the external diameter of the cylinder. For the present experiments, the parameters involved in determining f are $L = 0.5265$ m, $D_o = 0.0254$ m, and $l = 0.03462$ m. Substituting the values in the above expressions gives $f = 0.8$. This value of f is also going to be used in the linear and nonlinear models.